DOCTOR OF PHILOSOPHY

Observations and modelling of the western Irish Sea gyre

Horsburgh, Kevin J.

Award date:
1999

Awarding institution:
Bangor University

OBSERVATIONS AND MODELLING OF THE WESTERN IRISH SEA GYRE

A thesis submitted in accordance with the requirements of the University of Wales for the degree of Doctor of Philosophy

by

Kevin J. Horsburgh

University of Wales, Bangor
School of Ocean Sciences
Menai Bridge
Anglesey LL59 5EY
United Kingdom

June 1999

ABSTRACT

Observations from 1995 and 1996 described the seasonal evolution of the three-dimensional density field in the western Irish Sea. A cold, dense pool flanked by strong nearbed density gradients was present from May until October. Temperature had the dominant effect on density from June onwards. The trajectories of 55 satellite-tracked drifters defined the full spatial extent of the cyclonic circulation that is the western Irish Sea gyre. Several distinct recirculation paths were observed and drifter speeds were in good agreement with geostrophic calculations based on the observed density field. The existence of such organised, baroclinic flows in shelf seas demands that coastal ocean models should reproduce their dynamics correctly, if the models are to be useful as environmental management tools. One such model, ECOMsi, was applied to the study area and results from seasonal simulations were compared with the observations. A new technique was developed to perform quantitative comparisons between modelled and observed flow fields.

The model successfully reproduced the three-dimensional temperature structure throughout the seasonal simulations, and also predicted the cyclonic, near-surface residual circulation of the gyre. The model demonstrated conclusively that the gyre is density-driven and revealed the same recirculation paths that were visible in the drifter tracks. The vertical structure of the modelled density-driven flow confirmed the geostrophic nature of the currents and emphasised the important dynamical role of sharp density gradients near the bed (bottom fronts). A quantitative comparison of different model runs identified the critical parameterisations and forcing quantities for this application. An accurate specification of air temperature over the sea region was required for the model to achieve the correct timing of the stratification breakdown. During this phase, convective cooling at the surface was seen to be as important as the mixing by autumnal winds in eroding the density structure. The possibility of a seasonal reversal in density-driven flow along the east coast of Ireland was also identified. A new interaction between the wind and the density field, which could define where the strongest currents in the gyre are to be found, is described.

The model is now considered to be sufficiently well tested to use in a predictive capacity and for biological transport studies. This work highlights the benefits that can be obtained using high quality spatial and temporal field observations in the critical testing of numerical models, and furthermore suggests that shelf seas are the perfect location for such tests to be performed.

Acknowledgements

I would like to express my gratitude to Dr. Ed Hill for his invaluable supervision, and for what is nowadays termed 'expert tutelage'. His encouragement and advice assisted the completion of this work in no small measure, and his enthusiasm for dynamical oceanography has forged a lifelong interest for me. I also thank the other members of my research committee - John Simpson, Alan Elliott and Ian James - for their guidance during the course of this work.

The observations described here were made possible by the dedication of the officers and crews of the research vessels *Prince Madog*, *Cirolana* and *Corystes*. Technical support on *Prince Madog* cruises was provided by Nigel Mathers, Dave Boon, Anne Hammerstein and Ray Wilton, who are gratefully acknowledged. Thanks also to all those willing (or otherwise) participants in the 1995/1996 cruise program. I am grateful to Juan Brown and Liam Fernand at CEFAS for selected Scanfish data and for inviting my participation in rewarding collaborative work.

I am indebted to Alan Blumberg of Hydroqual Inc. for providing me with the source code for ECOMsi. Thanks also to Alan Davies and Jiuxing Xing at Proudman Oceanographic Laboratory for supplying the bathymetry, and for useful discussions. The satellite image in chapter 6 was processed by the NERC Remote Sensing Data Analysis Service, Plymouth. The meteorological data used in the model simulations were courtesy of the Irish Meteorological Service.

Over the past four years I have made many good friends and colleagues and I would like to thank in particular Des Barton, Alan Davies, Karen Wild-Allen, Teri Navarro-Perez, Jonathan Malarkey, Maria Angelico and Ricardo Torres for their companionship and conversation. Special thanks also to Rich Garvine, whose stimulating company I enjoyed during his sojourn in Menai Bridge. Finally, I express my immense gratitude to my partner, Frances Kellie, for her patience, love and support which have helped so much in the completion of this thesis.

This work was funded by an award, GR3/9601, from the U.K. Natural Environmental Research Council. The CEFAS contribution was funded by the Ministry of Agriculture, Fisheries and Food. Rich Garvine provided Argos drifters and participated in the 1995 observations whilst on sabbatical leave from the University of Delaware, during which time he received support from the US National Science Foundation under Grant INT-9413299 and the Sir Kirby Laing Fellowship of the School of Ocean Sciences, University of Wales, Bangor.

To Fran

Table of contents

List of Figures

Chapter 1

Chapter 2

Chapter 3

Chapter 4

Chapter 5

Chapter 6

Chapter 7

List of Tables

Chapter 2

Chapter 3

Chapter 4

Chapter 5

Chapter 6

Chapter 1. Introduction

1.1 Background

Numerical modelling has proven itself to be a valuable tool in shelf sea oceanographic research over the past three decades. During this time two-dimensional, depth-averaged models (e.g. Flather, 1976) have provided reliable tide and storm-surge forecasting for coastal regions. Many coastal engineering problems (e.g. sediment transport) require information on the vertical structure of the flow and recent increases in computing power have facilitated the development of three-dimensional barotropic (constant density) models (for a review of three-dimensional tidal models see Davies *et al.*, 1996). As models have become more sophisticated then new problems have emerged to challenge them. The most difficult challenge currently faced by shelf sea models is the realistic simulation of long term circulation, so that model results can be used for water quality manangement and for understanding the influence of regional circulations on marine ecosystems. To meet these (and other) challenges the present generation of coastal ocean models must include baroclinic forcing mechanisms that give rise to density-driven circulation.

The importance of baroclinic processes (due to buoyancy inputs) in shelf seas is reviewed by Hill (1998) and there is a growing body of evidence (Hill *et al.*, 1997b; Horsburgh *et al.*, 1998; Brown *et al.*, 1999) to suggest the existence of significant, mesoscale density-driven circulations in British shelf seas (the first two papers cited above are included as appendices to this thesis). The seasonality of many baroclinic flows, and their dependence on spatial variations in density, implies a likely sensitivity to relatively small annual changes in climatic forcing. A thorough understanding of these phenomena as indicators of the response of shelf seas to decadal climate change is therefore necessary (Boelens, 1995). Density-advecting, coastal ocean models must succeed in reproducing baroclinic flows if they are to have credibility in supplying the hydrodynamical framework for coupled biological, regional ecosystem models (e.g. Bartsch, 1993; Nihoul *et al.*, 1993; Skogen *et al.*,

1995) as is increasingly the case. The foregoing provides sufficient motivation for performing a critical test by using one such numerical model in an attempt to reproduce a baroclinic feature whose details have been established through observations. One such well-observed feature is the seasonal gyre in the western Irish Sea (Hill *et al.*, 1997a).

Previous observations in the western Irish Sea (Hill *et al.*, 1994; Hill *et al.*, 1997a) have revealed the existence of a cyclonic, near-surface gyre. The gyre is present in spring and summer each year when stratification isolates a dome of cold, dense water beneath a strong thermocline. This cold water pool is surrounded by warmer, well-mixed water and the resulting horizontal density gradients provide the baroclinicity that drives the cyclonic flow (Fig. 1.1). Hill (1993) has given details of five other locations on the European shelf where isolated bodies of dense water associated with topographic depressions have been identified; in each case, observations or numerical modelling suggest a circulation which is consistent with cyclonic, density-driven flow. Observations of cold water masses in other parts of the world consistently imply an associated cyclonic component of baroclinic flow, for example in the Middle Atlantic Bight (Houghton *et al.*, 1982), the Adriatic Sea (Henderschott and Rizzoli, 1976; Rizzoli and Bergamasco, 1983) and the Yellow Sea (Hu *et al.*, 1991). Baroclinicity can equally well be generated by a local increase in tidal mixing over a topographic elevation, producing an anticyclonic density-driven flow in the northern hemisphere which is in the same sense as barotropic residual flows resulting from the well-known mechanism of tidal rectification (Huthnance, 1973; Loder, 1980). The circulation around Georges Bank is discussed by Loder (1980) and Loder and Wright (1985) who noted a doubling of the anticyclonic flow in summer when horizontal density gradients were stronger, implying a significant baroclinic component.

Baroclinic gyres have biological and environmental implications. The western Irish Sea gyre provides a physical retention mechanism for the commercially valuable Norway Lobster, *Nephrops norvegicus* (Brown *et al.*, 1995; Hill *et al.*, 1996) and

also for pelagic juvenile fish (Dickey-Collas *et al.*, 1997). The same mechanism could act to retain contaminants in the event of a summertime spill. Furthermore, the isolation of the dense water mass has consequences for the local distribution and interseasonal variability of heat and nutrients. Seasonal gyres form part of an emerging picture of organised, mesoscale, baroclinic circulation in shelf seas. Hill *et al.* (1997b) reported the recirculation of part of the Scottish coastal current around an intrusion of dense, saline Atlantic water in the Minch and Horsburgh *et al.* (1998) have identified strong baroclinic flows associated with the Celtic Sea tidal mixing front. A feature common to all of these flows is the existence of strong density gradients near the sea bed, or bottom fronts.

Although the Irish Sea has been extensively modelled over the past twenty years, the emphasis has been on its response to winds and, in particular, storm surges for which barotropic models are adequate. Fine resolution barotropic models of the Irish Sea (Proctor, 1981; Davies and Jones, 1992; Davies and Aldridge, 1993; Davies and Lawrence, 1994a) do not predict the pattern of residual currents which constitute the western Irish Sea gyre which is further evidence of the baroclinic nature of the gyre. The cyclonic circulation in the western Irish Sea was first simulated using a diagnostic model (Hill *et al.*, 1996; Hill *et al.*, 1997a) which demonstrated the importance of the heating-stirring balance in controlling the pattern of stratification and the resulting circulation. Diagnostic techniques are extremely useful and provide insight into the dynamics governing the steady-state flow but do not evolve the flow field dynamically. To properly simulate time-dependent, density-driven flow in response to seasonal heating, tidal currents and wind forcing requires a three-dimensional, primitive equation model that treats density prognostically. Only recently have density-advecting models been applied to British shelf seas. Proctor and James (1996) simulated the seasonal cycle of stratification in the southern North Sea with a fine-resolution (~2.4 km), three-dimensional model. Elsewhere, Schrum (1997) has modelled the density-driven flow due to salinity gradients in the German Bight using the model of Backhaus (1985).

As yet, the western Irish Sea gyre has not been simulated with any primitive equation model. This work will apply ECOMsi (Estuarine Coastal and Ocean Model, semi-implicit), which is a semi-implicit version of the Princeton Ocean Model (Blumberg and Mellor, 1987), to the western Irish Sea. The model will be initialised from data and forced with real winds and solar insolation. The seasonal evolution of the gyre will then be modelled and compared with extensive hydrographic and drifter data obtained in 1995 and 1996. The model will be used to demonstrate unequivocally that the cyclonic circulation in the western Irish Sea is density-driven. It will also provide insight into those dynamical mechanisms which are important in the maintenance, and seasonal evolution, of the density structure.

1.2 The western Irish Sea gyre

Knowledge of non-tidal currents in the Irish Sea has improved gradually since Bowden (1950) inferred a weak (~1 cm s^{-1}), northward residual flow on the basis of salinity distribution. This long-term, basin-wide circulation has been confirmed by subsequent tracer observations and modelling studies (Wilson, 1974; Heaps, 1979; Prandle, 1984). Attempts to provide a detailed map of regional currents in the Irish Sea have been made (Ramster and Hill, 1969) but many of the current meter records used would have been too short to give a useful estimate of the long-term flow (Hill *et al.*, 1997a). A deficiency of Eulerian techniques (current measurements at a fixed point in space) is that many instruments are required to resolve the circulation pattern. Where current meter records do exist for the Irish Sea they typically provide a time series of vertical structure for a limited number of points (e.g. Lavin-Peregrina, 1984; Sherwin, 1987; Brown and Gmitrowicz, 1995). Furthermore, intense fishing activity in the area makes moored instrument arrays difficult to maintain. Substantial improvements in our understanding of the Irish Sea circulation have come from Lagrangian drifter observations (Hunter, 1972; Hill *et al.*, 1994).

The dynamics of the Irish Sea (Fig. 1.2) are dominated by the semi-diurnal tide which takes the form of a standing wave with a real amphidrome between Islay and Kintyre, to the north of the North Channel and a degenerate amphidrome near Wicklow in south east Ireland. Tidal currents in most of the Irish Sea are of the order 1 m s^{-1} and tidal ellipses are predominantly rectilinear (see Fig. 1.3a). The velocity node of the standing wave occurs to the west of the Isle of Man at around 54° N, 6° W and here (Fig. 1.3b) tidal currents are relatively weak (~ 20 cm s^{-1}). As can be seen from the bathymetric contours of Fig. 1.2, this region of weaker tidal currents coincides with a deep (>100 m) water channel. The western Irish Sea stratifies in spring and summer each year because the combination of weak tides and deep water produces insufficient tidally-generated vertical mixing to overcome the input of surface buoyancy due to solar heating (Simpson, 1971; Simpson and Hunter, 1974).

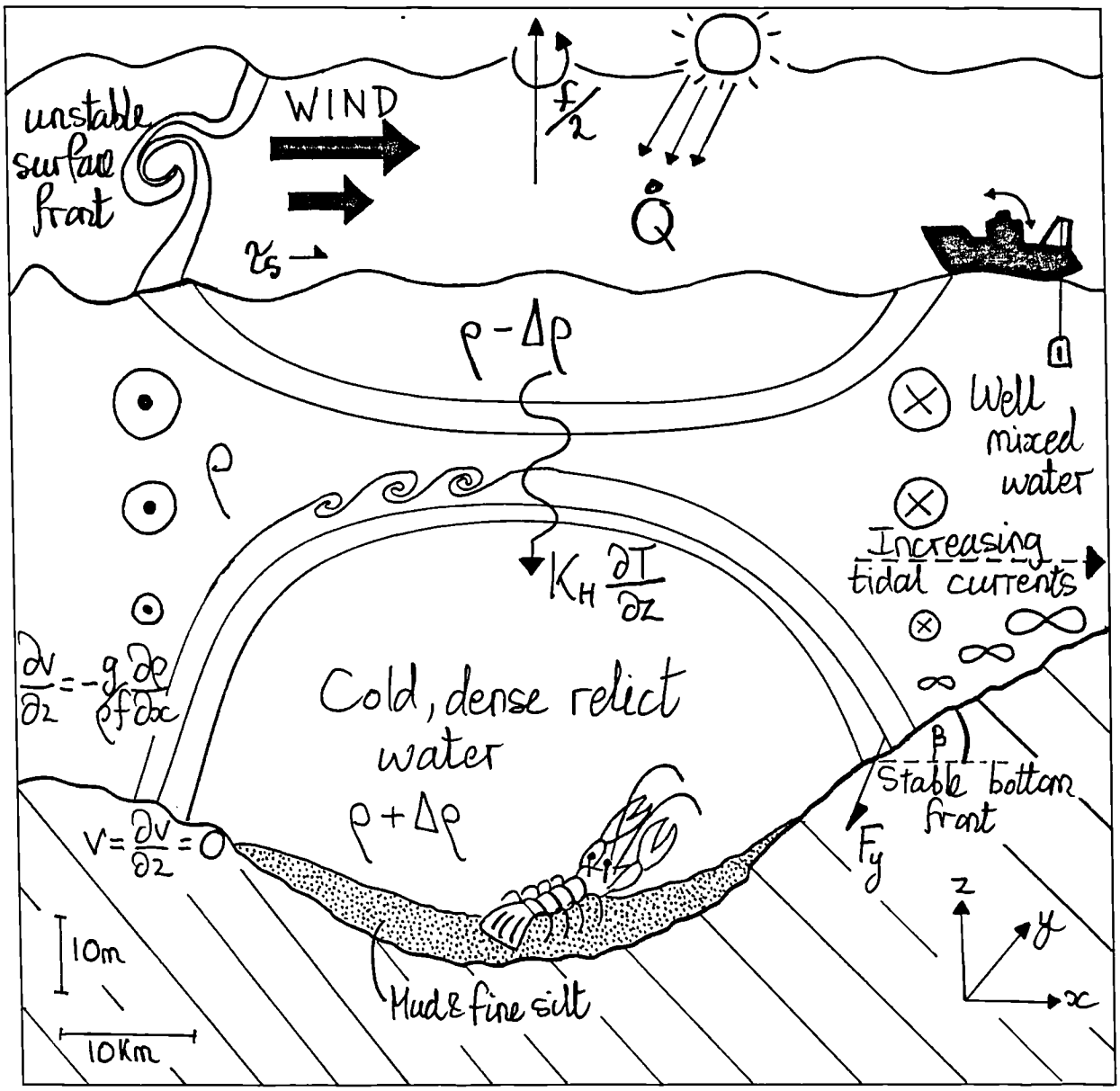

Fig. 1.1 Schematic representation of a baroclinic gyre indicating some of the dynamical mechanisms that are important in its formation and maintenance. The flow around the dense dome is cyclonic (in the northern hemisphere), dotted and crossed circles denoting flow out of and into the page, respectively.

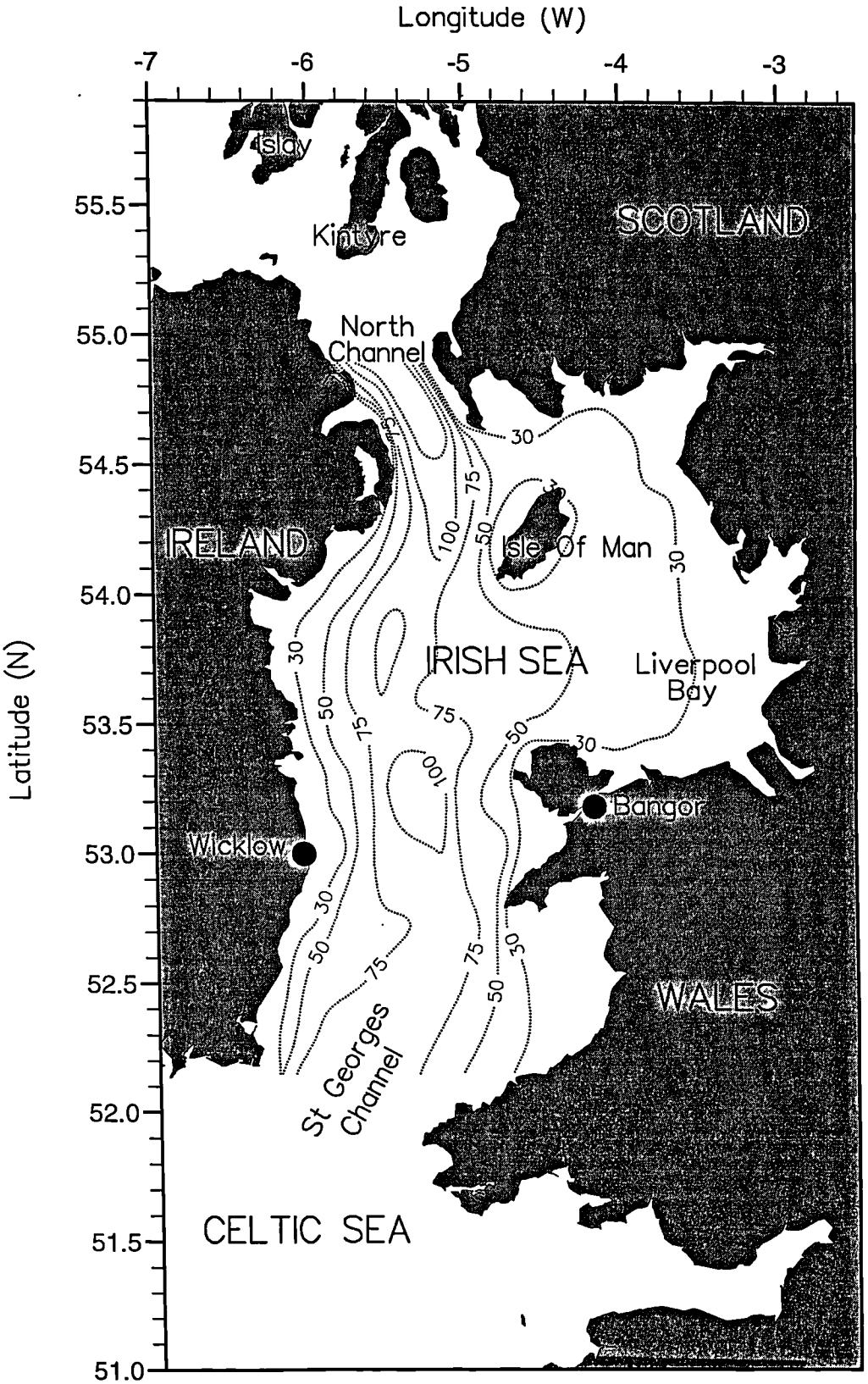

Fig. 1.2 Location map showing places referred to in the text. The dotted lines show contours of bathymetry (m) for the Irish Sea.

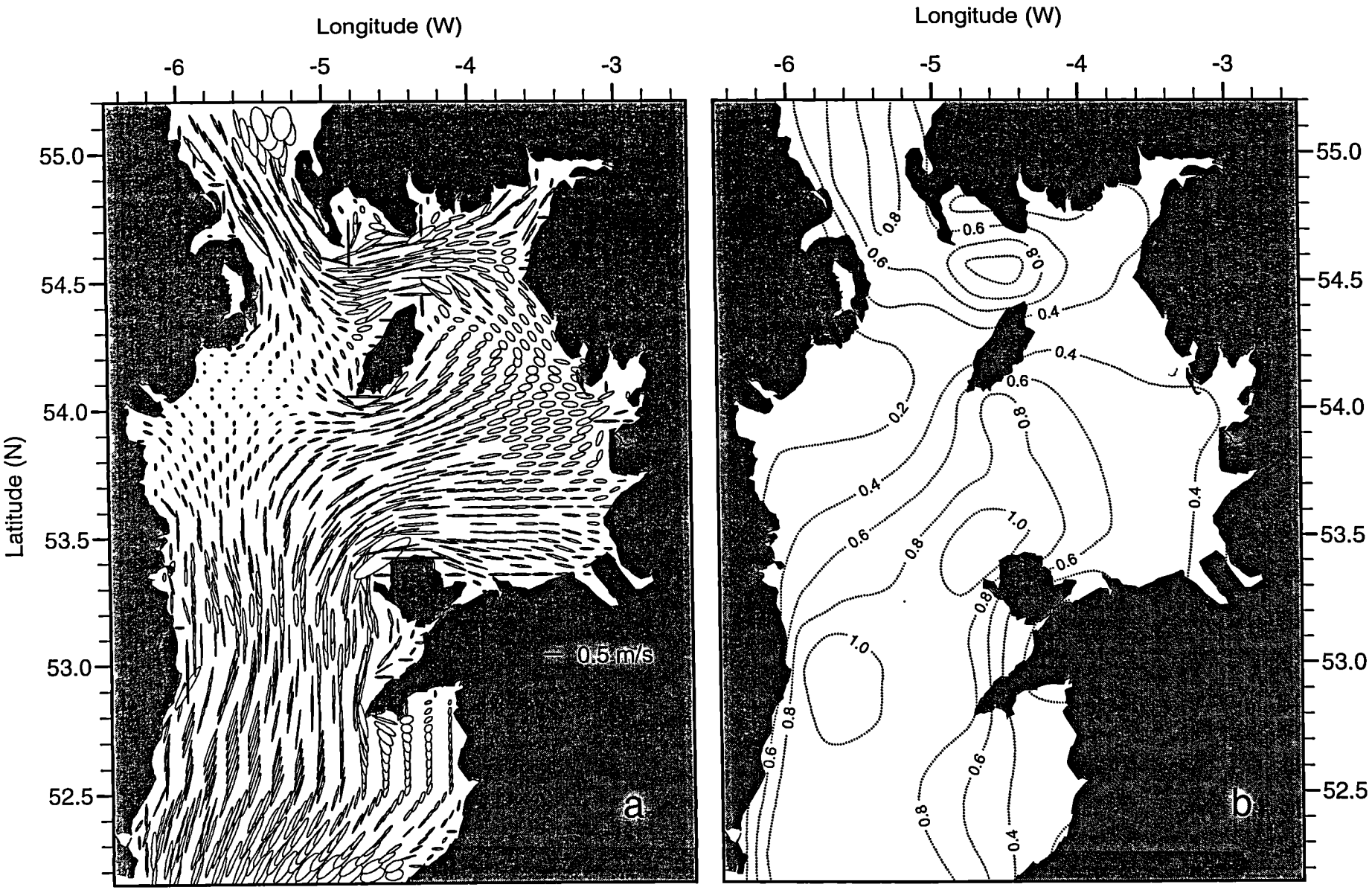

Fig. 1.3 (a) Depth-averaged M_2 current ellipses at every second grid point of the numerical model (ECOMsi) used in this thesis. (b) contours of depth-averaged M_2 current amplitude (ms^{-1}).

Observations of this area prompted the formulation of the well-known h/u^3 criterion for the location of tidal mixing fronts (Simpson and Hunter, 1974).

Beneath the seasonal thermocline, which is usually found at 20 - 40 m, is a dome-shaped mass of cold water, trapped after the onset of stratification. The suppression of vertical mixing by stratification means that this water warms only very slowly and is therefore a persistent feature over the heating season. Limited exchange of the cold water is also implied by dissolved oxygen minima (Davies, 1972). A typical density section across the dome is shown in Fig. 1.4. The pattern of isopycnals is consistent with a large database of hydrographic results (Slinn, 1974; Simpson, 1981; Lavin-Peregrina, 1984; Hill *et al.*, 1994; Hill *et al.*, 1997a) which show the cold dome to be a regular feature from year to year. The transition from vertically mixed to stratified water occurs rapidly (over ~10 km) at tidal mixing fronts which are located at critical contours of h/u^3 (Simpson and Hunter, 1974). These frontal density gradients drive a baroclinic flow which is geostrophic to a first approximation. Dynamical considerations (described in the next section and shown schematically in Fig. 1.1) predict a cyclonic circulation near the surface (i.e. the flow is parallel to isopycnals with the denser water to the left).

Evidence of this circulation was first provided by the release of two radio-tracked drifters (Hunter, 1972) whose drogue centres were at 27 m depth. One of these drifters described an anticlockwise loop centred at 53° 55' N, 5° 30' W. Geostrophic calculations from dynamic topography (Davies, 1972) also suggested a cyclonic circulation, weakening towards the bed. Confirmation of the gyre came with the release of nine satellite-tracked Decca-Argos buoys drogued at 15m depth in July 1990 (Hill *et al.*, 1994). The drifter trajectories clearly demonstrated cyclonic surface flow in the western Irish Sea (see Fig. 1.5) with mean speeds of 5 cm s^{-1}. Residual current vectors from ADCP records contemporaneous with the drifter deployments also showed cyclonic circulation in the region (Hill *et al.*, 1994).

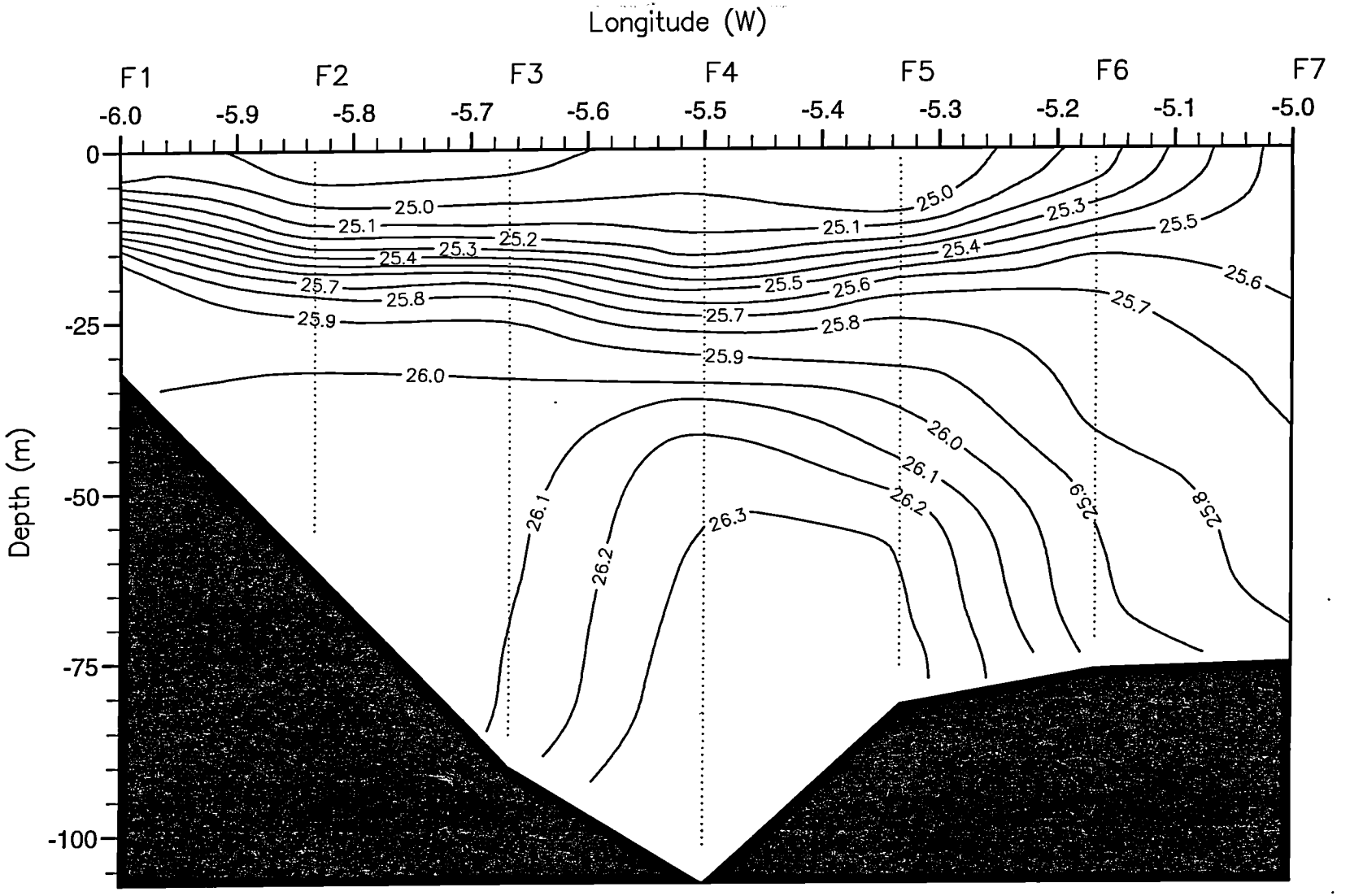

Fig. 1.4 Vertical section through the dense dome in the western Irish Sea along line of latitude 53° 40' N, taken on 25 July 1995. Contours are of σ_t (ρ - 1000) kg m^{-3}. F1-F7 denote the positions where CTD casts were made.

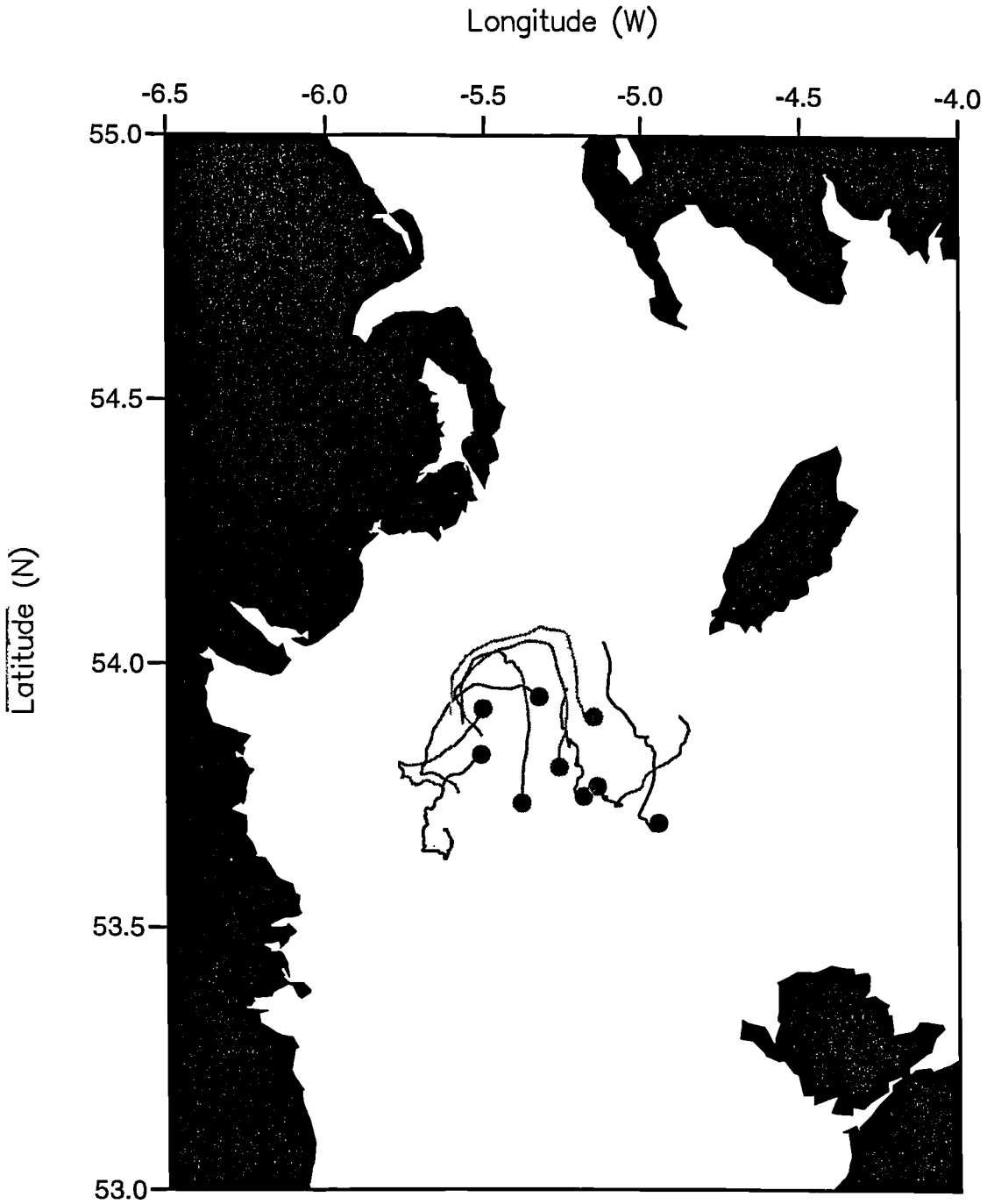

Fig. 1.5 Cyclonic trajectories of nine satellite-tracked Decca-Argos drifters released in July 1990 (Hill *et al.*, 1994). The tracks have been lowpass filtered to remove tidal fluctuations. Solid circles denote release points.

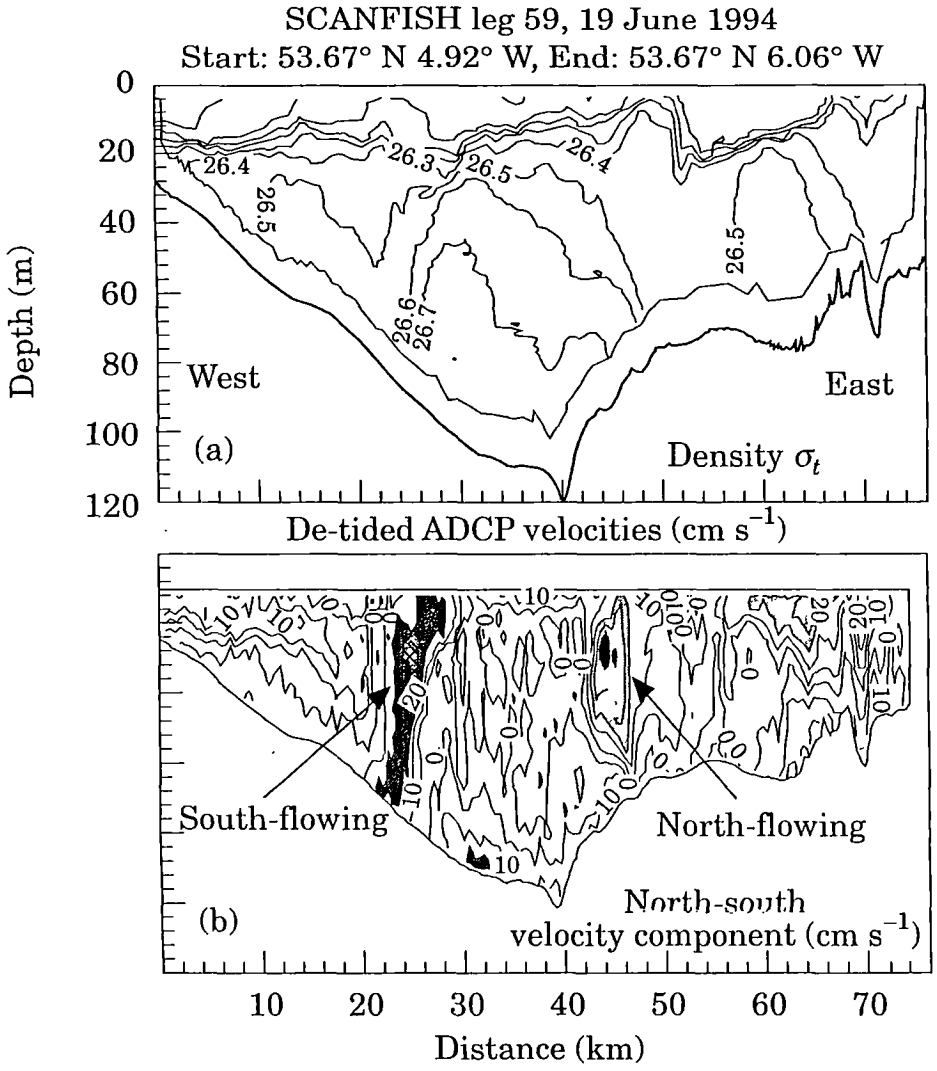

Fig. 1.6 Density and residual currents along latitude 53° 40' N from 19 June 1994 (from Hill *et al.*, 1997a). Panel (a) shows contours of σ_t derived from undulating CTD observations. Panel (b) shows detided ADCP velocities normal to the section.

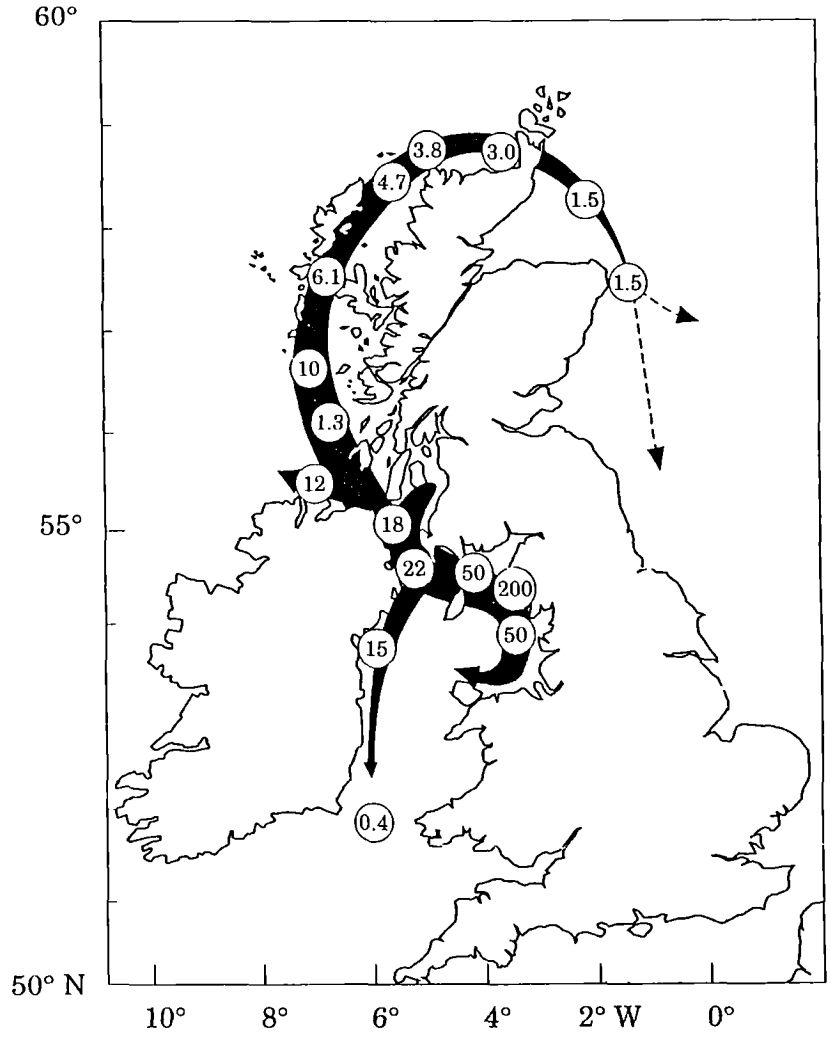

Fig. 1.7 Concentrations (pCi l^{-1}) in May-July 1972 and inferred pathways of the radio-isotope ^{137}Cs (from Jeffries *et al.*, 1973).

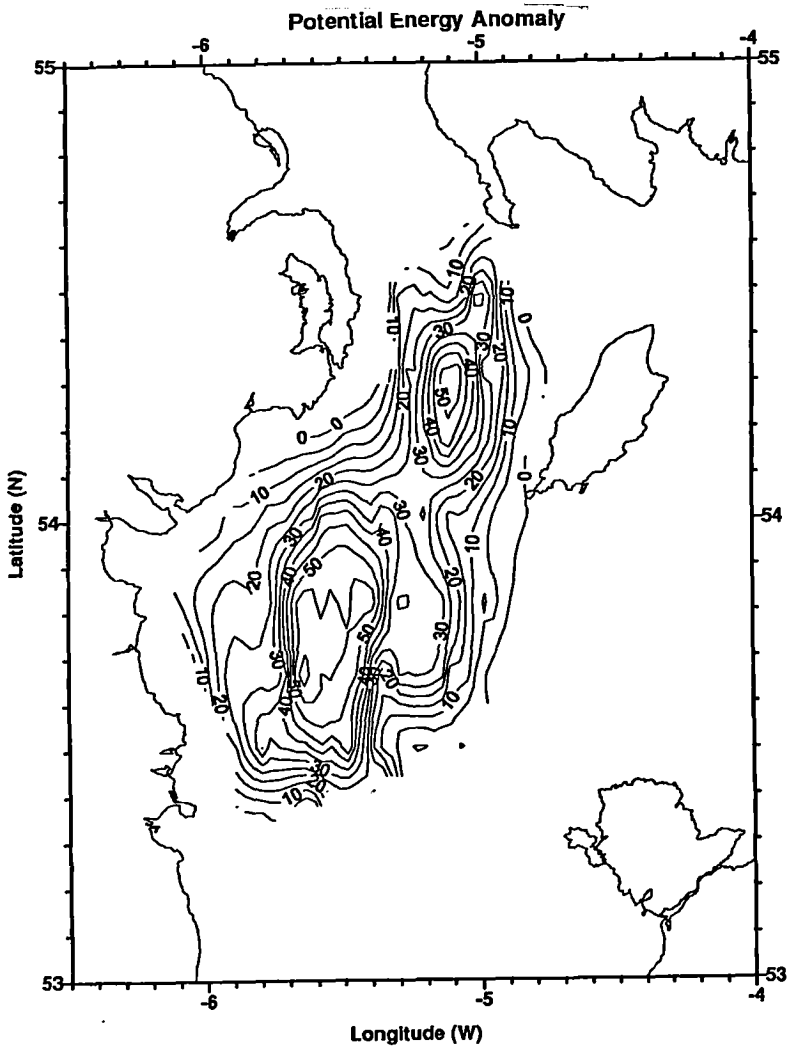

Fig. 1.8 Spatial pattern of potential energy anomaly, φ, for the period 18-22 June 1994 (from Hill *et al.*, 1997a). Note the two local maxima of stratification.

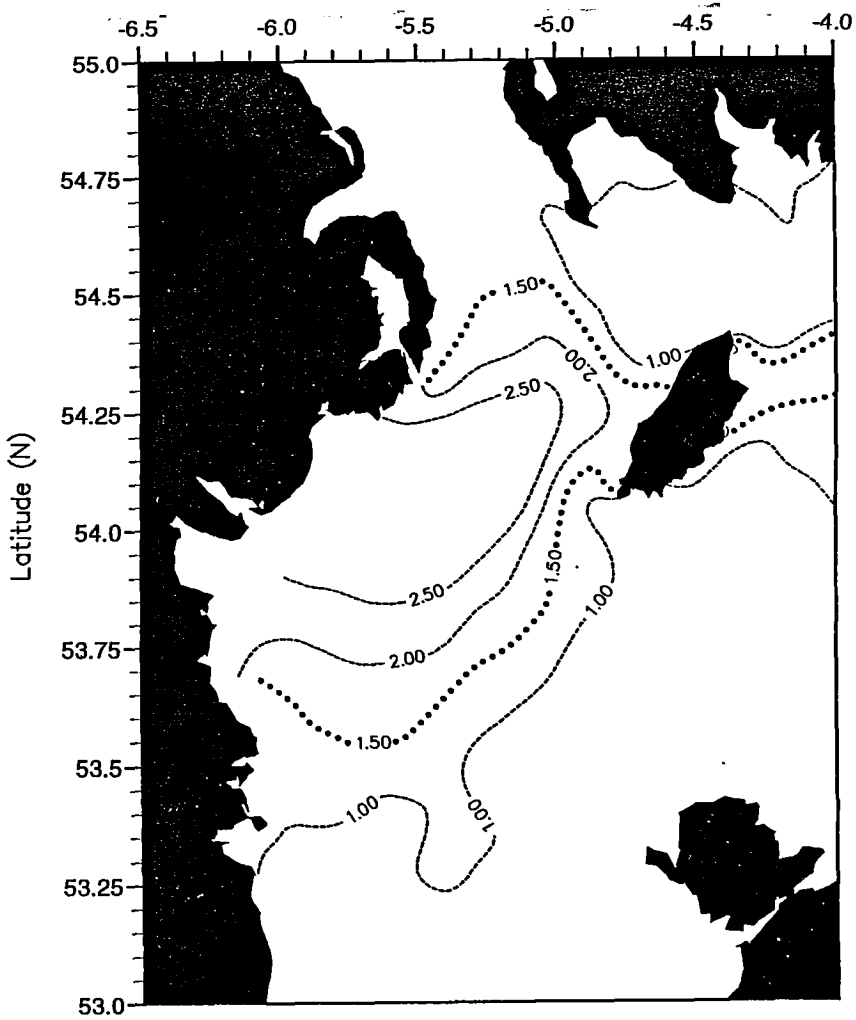

Fig. 1.9 Contours of $S = \log_{10}(h / C_D |u|^3)$ after Pingree and Griffiths (1978) but using values from ECOMsi. Stratified conditions exist where $S > 2$; $S = 1.5$ predicts the positions of fronts.

Limited drifter deployments in 1993 and 1994 (Hill *et al*, 1997a) provided further evidence for the gyre. A simultaneous survey across the gyre using the Scanfish undulating CTD (Brown *et al.*, 1996) and bottom mounted ADCP was made in 1994 (Hill *et al.*, 1997a) and the results show cyclonic flows of up to 20 cm s^{-1} concentrated in jet-like cores at the base of the pycnocline and immediately above the flanks of a well-defined dome of dense water (Fig. 1.6).

Indirect support for the existence of the gyre comes from the implied pathway (see Fig. 1.7) for the soluble radio-isotope ^{137}Cs (Jeffries *et al.*, 1973). An alternative explanation for this southward flow is that it represents a coastal current due to freshwater input along the Irish coast or is due to a North Channel inflow (Brown and Gmitrowicz, 1995). However, fresh water runoff is not a significant dynamical factor in the summer months and it seems likely that the inferred transport path for radio-caesium is at least in part due to the western flank of the gyre. Recent analyses of ^{137}Cs levels in *Fucus vesiculosus* (Bladderwrack) along the east coast of Ireland (Pollard *et al.*, 1996) confirm the pathway shown in Fig. 1.7.

Although fresh water input along the Irish coast may contribute to the local dynamics and density distribution in the spring, in summer the density field in the Irish Sea is primarily temperature controlled. A useful measure of stratification is the potential energy anomaly, ϕ, which is the amount of energy required to completely vertically mix a water column of unit area. Simpson (1981) defines ϕ as

$$\phi = \frac{1}{h}\int_{h}^{0}(\overline{\rho} - \rho)gz\,dz \qquad where \qquad \overline{\rho} = \frac{1}{h}\int_{-h}^{0}\rho\,dz \tag{1.1}$$

and h is the total water depth with ρ the *in-situ* density.

The spatial distribution of ϕ is a vertically-integrated measure of horizontal density differences and might therefore be expected to provide information about the density-driven flows. Fig.1.8 shows the distribution of ϕ for the western Irish Sea in June

1994 (Hill *et al.*, 1997a), derived from the Scanfish undulating CTD. Two centres of high stratification are apparent which has interesting implications for the residual circulation, as shown herein. This pattern of stratification persists until strong autumn winds erode the thermal structure. Since all observations suggest the baroclinic component of flow to be of the same order as the maximum tidal currents in the area, it is fair to say that the gyre dominates the near-surface circulation in the summer months.

1.3 Gyre dynamics

Baroclinic gyres in shelf seas share many aspects of their dynamics with tidal mixing fronts (indeed, a simplified conceptual model of a gyre is an axisymmetric frontal system). The dynamics of fronts are discussed in detail by Garrett and Loder (1981), van Heijst (1986), Simpson and James (1986) and Hill *et al.* (1993). Huthnance (1995) provides a thorough review of different types of fronts and their implications for cross-frontal exchange.

A property of fundamental importance in rotating fluids is the Rossby number, defined as $Ro = U / fL$ where U and L are, respectively, typical velocity and length scales and f is the Coriolis parameter. Large along-front scales imply a small Rossby number and if frictional effects are small then the basic dynamical balance at fronts is geostrophic, the vertical shear in the along-front current being related to the cross-front density gradient through the thermal wind equation :

$$\frac{\partial v}{\partial z} = -\frac{g}{\rho f}\frac{\partial \rho}{\partial x} \tag{1.2}$$

where v is the along-front current, g is gravitational acceleration, ρ is density and $\partial\rho/\partial x$ is the cross-front density gradient. For an axisymmetric gyre one must, more precisely, consider a cyclostrophic balance (i.e. include the effect of centrifugal

accelerations, v^2/R, where v is the azimuthal velocity and R is the radius of curvature). The Rossby number can also be utilised to express the relative importance of centrifugal and Coriolis terms. For the Irish Sea gyre (taking $U = 0.1$ m s^{-1}, $f = 10^{-4}$ s^{-1} and $R = 20$ km), $Ro = 0.05$ and a geostrophic balance may still be assumed to a first approximation. Large isopycnal slopes and the presence of significant bottom slopes means that quasigeostrophic theory (Pedlosky, 1979) cannot be readily applied to baroclinic gyres, although Hill (1996) has succesfully used a two-layer quasigeostrophic model to demonstrate the spin-up of cyclonic upper layer flow. Cushman-Roisin (1986) exchanged the quasigeostrophic constraint of small interface slope for restrictions on the length scale of the motion and thus devloped the frontal geostrophic equation which can be used to model certain types of front and Gulf Stream rings. Hoskins (1975) retained the ageostrophic velocity in the advective terms of the momentum equation to develop the semigeostrophic equations which have proven useful in atmospheric (Duffy, 1976) and oceanic (Flagg and Beardsley, 1978) stability analyses. However, the high levels of mixing that occur at shelf sea fronts dictate that frictionally-induced ageostrophic motions be explicitly represented in dynamical models of baroclinic gyres and tidal mixing fronts.

Internal friction due to the along-front flow results in an unbalanced component of the cross-frontal pressure gradient. This residual pressure field drives a weak, secondary circulation in the cross-frontal plane which can be thought of as the slow gravitational spreading of the front. The cross-frontal circulation implies upwelling of cold water on the mixed side of the front and surface flow convergence near the front (Simpson and James, 1986; Hill *et al.*, 1993). Our knowledge of the transverse circulation stems largely from two-dimensional models (James, 1978; Garrett and Loder, 1981; James, 1984; Wang, 1984) although indirect evidence of surface convergence includes observations of surface slicks and the accumulation of debris and seaweed near tidal mixing fronts (e.g. Pingree *et al.*, 1974). Observed surface temperature minima on the mixed side (Simpson *et al.*, 1978) provide support for the upwelling of cold water.

All geostrophic flows are indeterminate (unless the pressure field is known) since any pressure field can satisfy the governing equations of momentum and continuity, subject to the condition of small *Ro*. The thermal wind equation (1.2) predicts only vertical shear and a level of known motion is required if absolute velocities are to be determined. Garrett and Loder (1981) presented a semi-analytic, diagnostic model for frontal flows in which the cross-frontal velocity component is related to along-front friction by:

$$f u = \partial(A_v \partial v/\partial z)/\partial z \qquad (1.3)$$

If bottom stress is assumed to be linearly related to velocity and surface stress is taken as zero then 1.3 can be integrated over depth to give a cross-frontal Ekman transport

$$f \int_{-h}^{0} u\, dz \equiv f U_x = \int_{-h}^{0} \frac{\partial}{\partial z}\left(A_v \frac{\partial v}{\partial z}\right) dz = -\left(A_v \frac{\partial v}{\partial z}\right)_{-h} \equiv -k\rho v_{-h} \qquad (1.4)$$

where the subscript *-h* implies evaluation at the bed. The condition of a zero cross-frontal volume flux implies $v = 0$ at the bed which provides a physical basis for obtaining absolute velocities from the thermal wind equation. Garrett and Loder's (1981) model provides evidence for the validity of the assumption, particularly for low Ekman number (low friction) and for strong bottom fronts. For the density structure shown in Fig. 1.4, integration of the thermal wind equation subject to the condition of zero along-front current at the bed predicts a cyclonic, near-surface, along-front jet. The ADCP observations shown in Fig. 1.6 provide further support for the assumption.

For typical frontal density gradients, along-front jets of the order 20 cm s^{-1} are expected. Jet-like flows of these magnitudes are reliably predicted by models (James, 1978; Garrett and Loder, 1981; Wang, 1984) but have generally proven to be elusive in observational studies (e.g. Simpson *et al.*, 1978). Part of the difficulty in

observing frontal jets is that they are relatively narrow phenomena (as seen from the ADCP isopleths in Fig. 1.6) whose spatial location varies with the density field. Hill *et al.* (1993) noted the difficulty of making long-term measurements in a dynamically active frontal zone. Observations are further hindered by the non-persistent nature of fronts themselves. Satellite images of sea surface temperature reveal that nearly all surface fronts are unstable (van Heijst, 1986), baroclinic instabilities giving rise to large-scale meanders and detached eddies such as those observed in the Celtic Sea by Simpson and Pingree (1978). As well as modifying the density structure, the horizontal mixing that results from these eddies has important biological consequences (Savidge, 1976).

The laboratory experiments of Griffiths and Linden (1981; 1982) demonstrate how instabilities form at a sharp surface density gradient in a two-layer rotating system. Griffiths and Linden (1981) were unable to produce a stable surface front; waves grew rapidly, became asymmetric and were observed to form a characteristic hammerhead shape before breaking into a vortex dipole (containing a cyclone and an anticyclone). The Rossby radius of deformation is a fundamental parameter of rotating, stratified fluids and is the scale at which Coriolis forces balance gravitational (or buoyancy) forces. It is defined as

$$R_D = \sqrt{(g'H)}/f \qquad (1.5)$$

where g' is the reduced gravity, $g\Delta\rho/\rho$, and $\Delta\rho$ is the density difference between layers. Griffiths and Linden (1982) showed that the most unstable wavelength, λ, for surface fronts could be expressed as $\lambda / 2\pi R_m \approx 1.1$, where R_m is the geometric mean of the upper and lower Rossby radii of deformation. Killworth *et al.* (1984) gave a theoretical value of $\lambda / 2\pi R_m = 1.15$. The length scales of perturbations favoured by baroclinic instability exceed the deformation radius (Pedlosky, 1979) and it is this type of instability that is most readily observed in these experiments. In all cases, the most unstable wavelengths are in reasonable agreement with the classical Eady

(1949) model which predicts a wavelength of four Rossby deformation radii. Numerical simulations of frontal instability (James, 1984; James, 1989) generated eddies resembling the vortex dipoles of tank experiments but it was found that both bed friction and topography tend to suppress eddy formation. James (1981) has also shown how values of vertical eddy viscosity typical of unstratified tidal flows tend to suppress baroclinic eddy formation in a coastal front.

There is considerable evidence to suggest that bottom fronts are more stable than their surface counterparts. Pedlosky (1979) noted that sufficiently strong topographic slopes can restrict the range of motions possible and reduce baroclinic instability, regardless of the available potential energy of the basic state. Linden and van Heijst (1984) created unstable bottom fronts but noted that bottom Ekman layers can dissipate the kinetic energy of longer baroclinic waves and stabilise these disturbances. Stable, dense water vortices have been produced in the laboratory experiments of Saunders (1973), van Heijst (1986) and Mory *et al.* (1987) subject to some critical Burger number, given by Saunders (1973) as $\theta = (R_D / R)^2$, where R is the initial radius of the dense cylinder of water. Saunders (1973) obtained stable vortices for $\theta > 1.8$ and Mory *et al.* (1987) produced stable eddies on a sloping bottom for $\theta > 2$. Flagg and Beardsley (1978) used a semigeostrophic approximation to perform a stability analysis of a two-layer front over steep topography. The effect of increasing the bottom slope was to reduce sharply the growth rates of all unstable modes. They noted that the *e*-folding times of the unstable modes increased from 2-5 days over a flat bottom to as much as 75 days over slopes characteristic of the US continental shelf.

Surface fronts in shelf seas are also affected significantly by the wind (Simpson and Bowers, 1981; Lavin-Peregrina, 1984) and can be rapidly eroded by convective instability (Wang *et al.*, 1990) if denser water is advected over less dense water on the stratified side. Observations in the North Sea (van Aken *et al.*, 1987) and in the

Irish Sea (Allen, 1979; Lavin-Peregrina, 1984; Hill *et al.*, 1994) confirm that surface fronts are usually less pronounced than bottom fronts. The dynamical significance of bottom fronts explains the stability and persistence of the western Irish Sea gyre and also explains why the gyre was not predicted sooner by maps of h/u^3 (Simpson and Hunter, 1974). Fig. 1.9 follows the approach of Pingree and Griffiths (1978) who used tidal amplitudes derived from a numerical model to predict frontal locations around the British Isles. With the exception of the western flank, along the Irish coast, the extent of the gyre is in good agreement with frontal positions predicted by the h/u^3 criterion. Residual currents greater than 1-2 cm s^{-1}, parallel to density gradients, would cause frontal positions to deviate from those predicted (Simpson, 1981) but cross-frontal flows are weak and the along-front flows are parallel to isopycnals and therefore do not invalidate the h/u^3 model. However, h/u^3 only predicts the transition from vertically mixed to stratified water. As Fig. 1.4 shows, stratification near the Irish coast does not preclude the existence of the near-bed fronts required for baroclinic flow.

The structure and position of tidal mixing fronts are influenced by a variety of forcing mechanisms over a wide range of timescales. Tidal mixing power is modulated over spring-neap cycles and one might expect a periodic, non-linear movement of the frontal position (Simpson and Bowers, 1981) along with an intensification of density gradients at springs. Diagnostic models predict the sharpening of density gradients and increased velocities at springs (Garrett and Loder, 1981). However, observations suggest only a small (but significant) change in frontal position over the fortnightly spring-neap cycle (Lavin-Peregrina, 1984) and in Wang *et al.*'s (1990) model of the Celtic Sea front there was no change in frontal position despite a six-fold change in u^3 between springs and neaps. Advection and tidal straining during a tidal cycle are also important processes in the evolution and maintenance of the density structure. Allen (1979) surveyed the structure of a tidal mixing front over a single tidal cycle using an undulating CTD and found that the slope of isotherms varied significantly, with maximum steepness around low water. In non-rotating laboratory experiments,

Linden and Simpson (1988) showed that cross-gradient flow was strongest when background turbulence was low. However, in a rotating system any baroclinic relaxation will adjust geostrophically over an inertial timescale and become a component of the along-front flow.

It is not yet fully understood to what extent the cross-frontal circulation, through the advection of density, modifies the density structure at the front. Garrett and Loder (1981) compare five cross-frontal transfer mechanisms and find the most important to be the frictionally induced mean flow. Shear dispersion due to semi-diurnal tides or inertial oscillations was shown to depend mainly on the eddy Prandtl number, $Pr = A_v/K_v$ (the ratio of vertical eddy viscosity to diffusivity). Since the eddy Prandtl number is usually large in stratified conditions, shear dispersion associated with tides or inertial oscillations is less significant than the mean flow flux, although shear dispersion due to low-frequency cross-frontal winds was found to be significant. Garrett and Loder (1981) found that a steady along-front wind of only 4 m s^{-1} gave rise to a cross-frontal Ekman flux comparable with the mean flow flux in the surface layer. These results allow the relative importance of frontal dynamic processes to be assessed but they neglect the continuous modification of the density field due to the combined effect of solar heating and vertical mixing due to wind and tide. Cross-frontal flows cause a relaxation of isopycnals and therefore a decrease in potential energy. However, potential energy *is* constantly replenished as vertical mixing ensures that the well-mixed water warms faster than that isolated beneath the thermocline on the stratified side. In terms of a particular isopycnal, cross-frontal fluxes act to make it horizontal whilst mixing due to wind and tide tend to make it vertical. The gyre is maintained so long as the horizontal density gradients persist near the bed. Observations (Lavin-Peregrina, 1984) and model studies (James, 1978) show that density gradients at the bed exceed those near the surface once stratification is well established. Lavin-Peregrina (1984) found temperature differences across a bottom front in the western Irish Sea to be 3.5° C by mid-June,

compared to a difference of only 1.5° C at a corresponding surface front.

No clear picture of the seasonal development of cyclonic flow in the gyre has yet emerged. Hill (1996) used a quasi-geostrophic model to show that under realistic shelf sea conditions, dense domes quickly come to rest and cyclonic circulation is induced in the upper layer through vortex stretching. The inclusion of bottom friction distinguishes this approach from inviscid models such as that of Nof (1983) which predict only anticyclonic flow in the lower layer. Laboratory experiments (van Heijst, 1986; Mory *et al.*, 1987; Whitehead *et al.*, 1990) illustrate the spin-up of cyclonic motion in the fluid overlying dense domes. In a three-layer experiment, van Heijst (1986) observed that the upper-layer flow is governed by the lower-layer density gradient which dominates the thermal wind balance. Neither quasi-geostrophic theory nor laboratory models fully reflect the complex evolution of gyral circulation in shelf seas but they do demonstrate final conditions which are in agreement with observed flow patterns. Hill (1996) also showed how an initially barotropic flow can adjust to a baroclinic one with cyclonic motion in the surface layer only. In shelf seas, one would expect the cyclonic flows to increase throughout the heating season, as density gradients near the bed sharpen, and to then diminish in the autumn when strong winds and convective mixing due to surface cooling erode the density structure. This development has been observed in diagnostic models (Hill, 1993). In the absense of restorative mechanisms, Garrett and Loder (1981) gave the timescale for decay of a continuously stratified front as $T = f^2 L^2 / A_v N^2$ where f is the Coriolis parameter, N the buoyancy frequency, L a length scale for the width of a front and A_v the vertical eddy viscosity. Taking f^2/N^2 as 5×10^{-5}, L as 20 km and A_v as 10^{-2} m^2 s^{-1} implies a decay time of just 20 days. In the western Irish Sea, strong autumnal winds are likely to play at least as important a role in the decay of the gyre and other processes which might contribute to increased mixing are inertia currents (Sherwin, 1987) and breaking internal waves (Lavin-Peregrina and Sherwin, 1985).

1.4 Aims of this study

Previously reported observations (Hill *et al.*, 1994; Hill *et al.*, 1997a) described a limited number of drifter trajectories of relatively short duration (up to 24 days). Whilst these demonstrated the cyclonic circulation, a larger set of Lagrangian observations was required to provide a comprehensive description of the strength of the residual flow, its spatial extent and its seasonal evolution. An extensive cruise program in the spring and summer of 1995 and a smaller cruise program in 1996 provided this dataset. The overall program combined the largest ever deployment of satellite-tracked Argos drifters in European inshore waters with frequent hydrographic measurements at 60 stations in the western Irish Sea. Previous observations at the western Irish Sea front (Allen, 1979; Lavin-Peregrina, 1984), concerned with the temporal variability of stratification, have concentrated on two-dimensional sections across the front. Remote sensing has been used to chart the movement of surface fronts (e.g. Bomback, 1974) but, until now, no observational program has provided a picture of the development of the three-dimensional density field in the western Irish Sea. Such measurements are necessary in order to rigorously test the predictive capabilities of the latest generation of coastal ocean models.

Numerical models have provided a great deal of knowledge about the physical oceanography of the Irish Sea, particularly its response to storm surges (e.g. Davies and Jones, 1992; Davies and Lawrence, 1994a). The existence and environmental implications of organised, baroclinic flows now demand that numerical models used in shelf sea management are able to correctly reproduce density-driven flows. The gyre thus both poses a challenge to the present generation of coastal ocean models and represents a useful test case. This work proceeds to focus on the numerical modelling of the western Irish Sea gyre and those dynamical mechanisms which affect its seasonal development. The model used is a semi-implicit version of the Princeton Ocean Model (Blumberg and Mellor, 1987) incorporating a level 2½

turbulence closure scheme (Mellor and Yamada, 1982). Comparisons of modelled three-dimensional density and velocity fields will be made with the hydrographic and drifter observations. The modelling work will also elucidate features of the gyre not amenable to observation, such as the response of the density field to sudden wind events and the flow field during the autumn/winter transition when sea conditions make drifter deployments impractical. Specific objectives of this thesis are :

- To present results of the 1995 and 1996 drifter releases. These tracks prove the existence of the western Irish Sea gyre beyond doubt as well as defining the gyre's spatial extent and showing seasonal changes in the circulation. The trajectories also provide the first observational evidence of a persistent along-front jet at a tidal mixing front.

- To present observations of the seasonal evolution of the three-dimensional density field in the western Irish Sea over the full heating season.

- To develop and apply ECOMsi to the western Irish Sea on a 3km grid with suitable bathymetry and boundary conditions and to validate the model against established models of the Irish Sea and a range of baroclinic test problems.

- To demonstrate that the model reproduces the observed density structure and flow fields over a spring-to-autumn simulation and to investigate the effect of key parameterisations on these results.

- To use the model to gain further insight into the dynamics of frontal circulation and of the interaction between the wind and the gyral circulation.

1.5 Thesis Plan

This thesis contains the results of observations carried out during two years and the results of an applied numerical modelling study using a three-dimensional, primitive equation model. The thesis is organised as follows :

Chapter 1. An introduction to the western Irish Sea gyre is presented along with a review of the relevant dynamics. The objectives of this work are given.

Chapter 2. The observational program is described along with the instruments used to collect the data and the methods employed in its analysis.

Chapter 3. The results of the hydrographic surveys are presented and the seasonal development of stratification is described. Drifter trajectories are presented and correlations with the observed winds are performed. Drifter tracks are then manipulated to obtain an Eulerian picture of the spring and summer flow fields.

Chapter 4. An overview of previous modelling studies in the Irish Sea is provided. A technical description of several, currently popular coastal ocean models is given, with a concentration on those numerical schemes used in the Princeton Ocean Model and its derivative, ECOMsi, used here. A complete description of ECOMsi is provided, from the governing equations to previous applications of the model.

Chapter 5. The configuration of the model for the western Irish Sea is described. The model is then validated in a number of ways. Firstly, its tidal performance is compared with well-established models of the Irish Sea. Secondly, baroclinic aspects of the model are tested against steady-state and streamfunction frontal models, and finally comparisons are made with laboratory experiments on baroclinic instability.

Chapter 6. Results from seasonal simulations of the temperature distribution and circulation in the western Irish Sea are presented. The sensitivity of results to the choice of horizontal advection scheme is explored, along with the influence of prescribed horizontal diffusivity. Density-driven residual circulations are isolated and compared quantitatively with flow fields derived from drifter data. The model is used to show that strong wind events can sharpen density gradients near the bed, leading to stronger currents in certain parts of the gyre. The dependency of the model on accurate prescriptions of air temperature, if it is to correctly simulate the autumnal phase of stratification decay, is demonstrated with a simple experiment.

Chapter 7. The model results are compared rigorously with observations, and the performance of the different model runs is compared. The choice of numerical schemes and aspects of model configuration for the successful prediction of flows in baroclinic systems are discussed. New aspects of the dynamics of baroclinic gyres, suggested by the modelling work are highlighted. An outline of future modelling and observational projects prompted by the findings of this study is given.

Chapter 2. Observational program, instrumentation and techniques

2.1 Introduction

The observational program was designed to reveal the seasonal evolution of the three-dimensional density field in the western Irish Sea and to provide a better understanding of the spatial extent and strength of the cyclonic gyre. The project represents the most comprehensive survey of the region to date. As well as providing a definitive hydrographic dataset, the observations enable detailed comparisons with three-dimensional, numerical models to be made. The work described in this thesis was part of a larger collaborative project involving the University of Wales Bangor (UWB), the Centre for Environmental, Fisheries and Aquaculture Sciences (CEFAS) and the University of Delaware (UD). In 1995, eleven cruises spanning the months of May to November were made; most of these involved UWB's research vessel the *Prince Madog* but observations were also made from CEFAS research vessels *Corystes* and *Cirolana*. Three further cruises were made in 1996. Hydrographic data were obtained on most cruises with profiling CTDs. During CEFAS cruises, the Scanfish undulating CTD (Brown *et al.*, 1996) was employed and on two of the *Prince Madog* cruises, data were obtained using the UWB undulating CTD, Searover (Bauer *et al.*, 1985).

Prince Madog was equipped with a hull-mounted, 300 kHz RD Instruments Acoustic Doppler Current Profiler (ADCP) and *Corystes* carried an RD Instruments broadband, 153.6 kHz ADCP. These ADCPs were operated in bottom-tracking mode for all cruises. Detailed analysis of the ADCP and Scanfish data are reported elsewhere (Fernand, 1998). Free-drifting, satellite-tracked buoys were deployed and recovered opportunistically during the various cruises. Finally, meteorological data for the duration of the project were collected from four weather stations surrounding the western Irish Sea (Bangor Harbour (Co.Down), Point of Ayre, Ronaldsway airport and Dublin airport, see Fig. 2.1).

2.2 Observational area and cruise summary

The areal extent of the hydrographic observations is shown in Fig. 2.1. The east-west CTD lines were separated by 10' of latitude (~18.5 km) and individual stations within a line were mostly 10' of longitude (~10 km) apart. Appendix 1 provides the exact position of each CTD station and the approximate water depths. These key CTD sections are referred to throughout as lines A to H (e.g. line E refers to all stations at latitude 53° 50' N). Details of the cruise sequence, stations visited and activities conducted during each cruise are given in Table 2.1. The observational strategy for *Prince Madog* cruises was simply to visit as many CTD stations as time and weather permitted. CEFAS cruises were more complicated due to the necessary inclusion of biological sampling - only the hydrographic elements of CEFAS cruises are mentioned here.

Table 2.1 Cruise durations, activities and CTD stations occupied.

Cruise identifier	Vessel	Duration	Activities	Stations occupied
Cor5b/95	*Corystes*	4-19 May 1995	Scanfish	All lines
PM1/95	*Prince Madog*	30 May - 2 June 1995	CTD	Lines A,C,E,G Stations D3, F3, H2
PM2/95	*Prince Madog*	12-16 June 1995	CTD Searover	Lines C,D,E,F,G,H
PM3/95	*Prince Madog*	20-22 June 1995	CTD	Stations B2-B5, C3, D4, E5, F2-F5, G4
Cir5/95	*Cirolana*	22-24 June 1995	Scanfish	Lines C,D,E,F,G,D1-C7
PM4/95	*Prince Madog*	17-21 July 1995	CTD	Lines A-H
PM5/95	*Prince Madog*	24-27 July 1995	CTD	Lines C,F,G Stations D4, H3
PM6/95	*Prince Madog*	14-19 August 1995	CTD	All stations
PM7/95	*Prince Madog*	28-31 August 1995	Searover	Lines A,B,C,D,F,G
PM8/95	*Prince Madog*	21 September 1995	CTD	Line E
Cor10/95	*Corystes*	29 September - 13 October 1995	Scanfish	Lines D,E,F,D3-C7, C3-B6
PM9/95	*Prince Madog*	31 October - 2 November 1995	CTD	Stations C3,D4,E5,F2-F6
Cor9/96	*Corystes*	4-17 July 1996	Scanfish	All lines
PM1/96	*Prince Madog*	22-26 July 1996	CTD	All stations
PM2/96	*Prince Madog*	29 July - 2 August 1996	CTD	Lines E,G Stations C3,D4,H3

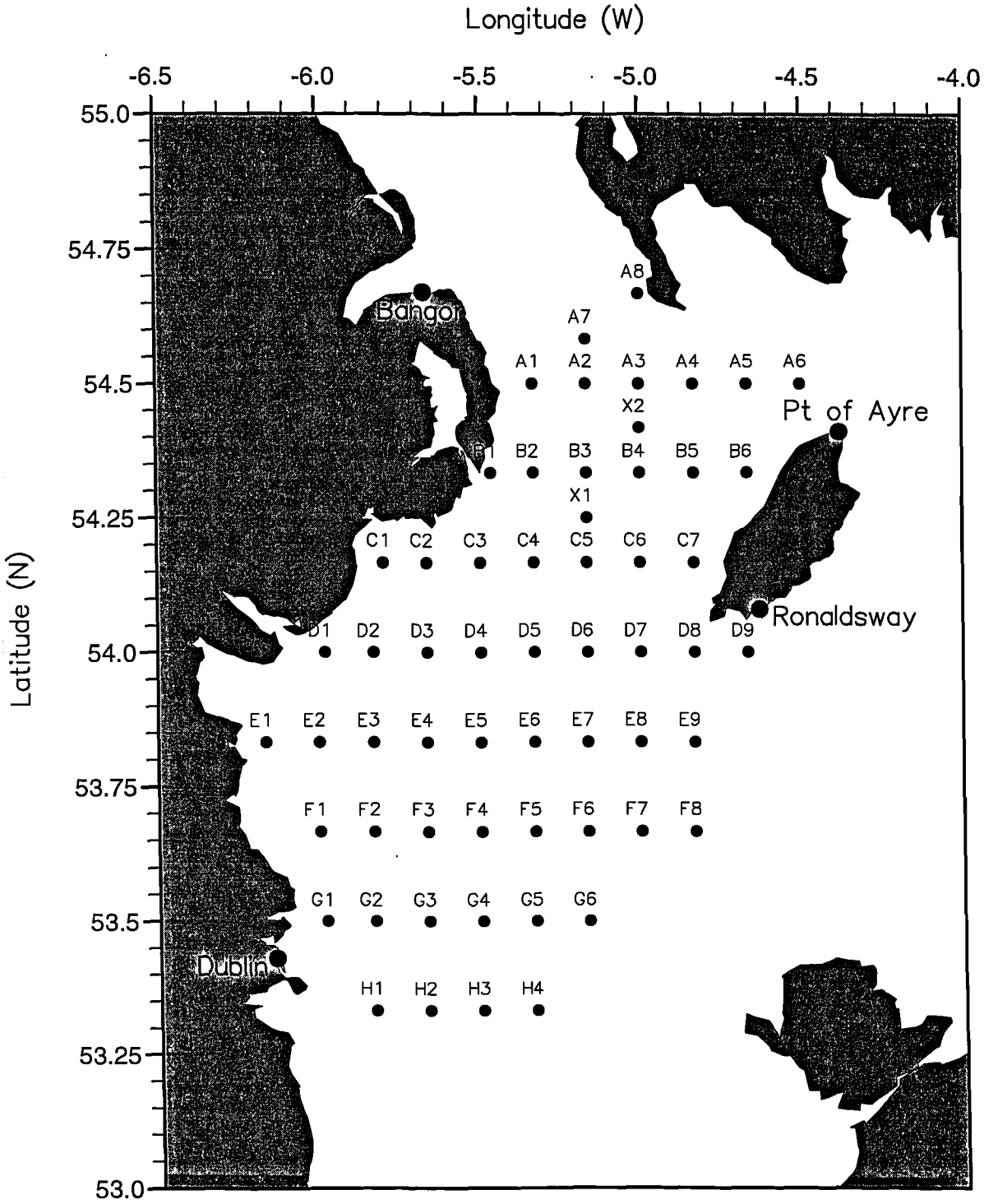

Fig. 2.1. Grid of CTD stations occupied during the 1995 and 1996 cruises. Also shown are the stations where meteorological data were collected.

2.3 Profiling CTDs

On *Prince Madog* cruises, vertical profiles of pressure, temperature and conductivity were obtained using a Neil Brown Mk III CTD. Data were collected with EG&G data acquisition module, version 2.02 and were then checked for unreliable values and averaged into 1 m depth bins using EG&G post-processing module, version 1.22. The instrument used on cruise PM6/95 was a Seabird SBE19 CTD and the two 1996 cruises employed a Seabird 911+ CTD. For these instruments data were collected and post-processed with Seasoft, version 4.211. The pressure-averaged values of temperature and conductivity were used to calculate salinity following the international standard procedures for seawater (Unesco, 1981). Density was calculated using the same procedures after calibration corrections had been applied to temperature and salinity. Salinities in this thesis have been determined on the practical salinity scale (Unesco, 1978) and are quoted without units.

2.3.1 Calibration

Temperature was calibrated against reversing, platinum resistance, digital thermometers (accurate to 0.001° C). Salinity was calibrated with water samples which were subsequently analysed in the laboratory using an Autosal model 8400A salinometer. For each cruise, r.m.s. errors for temperature and salinity are given in Table 2.2. Simple linear regressions were performed to obtain the calibration coefficients given in Table 2.2 which were then applied universally to correct for temperature and salinity according to the equations:

$$T_{correct} = a\,T_{CTD} + b$$

$$S_{correct} = c\,S_{CTD} + d$$

2.4 Searover

Cruise PM7/95 made use of UWB's towed, undulating CTD, Searover (Seasonal and Regional Ocean Variability Explorer) which has been described by Bauer *et al.*

(1985) and Leach *et al.* (1987). The vehicle was equipped with a Meerestechnik Elektronik CTD (Durazo-Arvizu, 1993) which was calibrated in a similar manner to profiling CTDs. At calibration sites, the vehicle was lowered to the desired depth where simultaneous readings were made on precision reversing thermometers and water samples were taken for analysis on the laboratory salinometer. Calibration coefficients for the Searover are given in Table 2.2.

Searover was towed at 4-8 knots behind the vessel and undulated to depths of 70 m which provided a horizontal sampling resolution equivalent to a conventional CTD cast every 1 km. Transects were chosen to lie east-west (along lines of latitude) for ease of comparison with profiling CTD data from the grid in Fig.2.1. A program was written to synchronise position data from ADCP bottom-tracking with the hydrographic data (sampled at 16 Hz) from Searover.

Table 2.2 CTD accuracy (r.m.s. error), and calibration coefficients used to correct for CTD derived temperature and salinity.

Cruise	Type of CTD	TEMPERATURE			SALINITY		
		r.m.s. error (°C)	Coefficients a	b	r.m.s. error	Coefficients a	b
PM1/95	Neil Brown MkIII	0.016	0.998	0.034	0.027	0.973	0.422
PM2/95	Neil Brown MkIII	0.014	1.000	0.014	0.029	0.973	0.641
PM3/95	Neil Brown MkIII	0.018	0.998	0.040	0.029	0.974	0.611
PM4/95	Neil Brown MkIII	0.016	0.998	0.031	0.030	0.980	0.388
PM5/95	Neil Brown MkIII	0.018	0.999	0.026	0.030	0.989	0.156
PM6/95	Seabird SBE19	0.007	1.004	-0.030	0.022	0.978	0.240
PM7/95	Searover	0.022	1.000	-0.013	0.024	1.000	0.270
PM8/95	Neil Brown MkIII	0.017	0.997	0.029	0.025	0.980	0.555
PM9/95	Neil Brown MkIII	0.016	0.999	0.035	0.022	0.990	0.268
PM1/96	Seabird 911+	0.005	0.996	0.043	0.009	0.994	0.022
PM2/96	Seabird 911+	0.005	0.996	0.043	0.009	0.994	0.022

2.5 Drifters

The observations reported here make extensive use of free-floating drifters which are satellite-tracked by Service Argos (hereafter referred to as Argos drifters). Lagrangian techniques can provide a better picture of coherent regional circulation than an equivalent number of Eulerian devices and satellite-tracking has removed many of the logistical problems associated with determining the positions of a large number of drifters. Argos drifters have been used to describe flow patterns over a large range of scales including global surface circulation (Sombardier and Niiler, 1994), North Atlantic recirculation (Brügge, 1995), slope currents (Burrows and Thorpe, 1998) and mesoscale eddy kinematics in the Bay of Biscay (Pingree, 1994) and the Rockall Trough (Booth, 1988). In shelf seas, drifters were instrumental in the discovery of the western Irish Sea gyre (Hunter, 1972; Hill *et al.*, 1994), have elucidated the clockwise, gyral circulation around Georges Bank (Limeburner and Beardsley, 1996) and have been used to estimate eddy diffusivities at tidal mixing fronts from single-particle statistics (Durazo-Arvizu, 1993; Hill *et al.*, 1993).

All Argos platforms carry a Platform Transmitter Terminal (PTT) which transmits a carrier frequency of 401.650 MHz ± 4kHz. This uplink signal is received by the Argos data collection system on the NOAA polar orbiting satellites. The position of an Argos drifter is calculated from the Doppler shift of the received frequency and the number of distinct messages received by the satellite determines the accuracy of the position, expressed as location "classes". The 1 standard deviation accuracies of the various classes are 1 km for Class 1, 350 m for Class 2 and 150 m for Class 3. Each polar orbiting satellite completes approximately fourteen revolutions per day and the sidelap between successive swaths increases with altitude. At 50° N each PTT is located independently 10-15 times per day.

For some shelf sea studies, where motions on scales of less than 1 km are of interest, greater location accuracy and temporal frequency may be required. Buoys

containing the Decca navigation locating system were designed for the North Sea Project (Roberts *et al.*, 1991) and GPS/Argos drifters are now widely available. This study was principally concerned with sub-tidal residual flows and therefore the spatial and temporal resolution provided by the Argos postioning system was considered adequate.

2.5.1 Drifter designs used in this study

All drifters used in this study comprised a free-drifting surface buoy equipped with an Argos PTT transmitting a 360 ms message at 90 s intervals. The 401.650 MHz uplink signal was also used for drifter recovery by means of a radio direction finder. The surface float was connected to a sub-surface holey sock drogue by means of a rope tether. Holey sock drogues have high drag coefficients and are an effective design for efficient coupling to the water column (Sybrandy and Niiler, 1991; Sombardier and Niiler, 1994). Two basic combinations of drifter and drogue were employed.

The University of Delaware supplied 20 drifters built to the CODE specification (Davis *et al.*, 1982) which has been shown to reduce wave rectification. The cylindrical surface unit derived its buoyancy from four floats attached to the drifter by thin rods. This was connected to a 0.7 m diameter, 2.5 m long holey sock drogue via a surface float which decoupled the drogue from the drifter. The UWB and CEFAS drifters comprised a pear-shaped fibreglass buoy similar to the Scottish Marine Biological Association (SMBA) design (Booth and Ritchie, 1983) connected to a 1.5 m diameter, 7 m long holey sock drogue. The drifter was designed to reduce windage, only the lid lying above the waterline. The tether included an elasticated section to decouple the surface unit and the drogue. The drag area ratios for both configurations were greater than the critical value of 45 which reduces wind slip to below 0.01 m s^{-1} in a wind of 10 m s^{-1} (Niiler *et al.*, 1995).

Due to the different shapes of the drifters and the absolute differences in drogue dimensions, an intercomparison of the two designs was carried out. One of each design was deployed for 120 hours (~10 tidal cycles) midway between Anglesey and the Isle of Man, where tidal stream amplitudes are of the order 0.7 m s^{-1} . The release and recovery details for the experiment are given in Table 2.3 below.

Table 2.3 Intercomparison mission for UD and UWB drifter designs

Drifter Number (design)	DEPLOYED		RECOVERED	
	Time	Position	Time	Position
17823 (UD)	Day 166 1300 GMT	53° 46.8' N 4° 39.0' W	Day 171 1310 GMT	53° 48.2' N 4° 38.9' W
24055 (UWB)	Day 166 1258 GMT	53° 46.9' N 4° 39.1' W	Day 171 1333 GMT	53° 46.9' N 4° 38.85' W

Initial separation was sufficient to avoid entanglement (~100 m) and the separation after 120 hours was 2.3 km, showing that the drifters diverged at a mean rate of 0.5 cm s^{-1}, less than 1% of the background flow. The observed separation can easily be accounted for by diffusive processes. On the basis of this result no further distinction is drawn between the two drifter designs.

All drogues were centred at 24 m depth (consistent with the base of the thermocline in previous observations) except for two of the 1996 releases whose drogues were centred at 8.5 m depth. The latter were deployed in a pairing with a standard drogued design to examine differences between surface flows and those at the thermocline. The UWB and CEFAS drifters carried temperature sensors and the UD drifters had temperature and conductivity sensors.

2.5.2 Drifter deployments

40 deployments were made in 1995 with a mean duration of 21 days and a maximum of 55 days. The time lines for each drifter are shown in Table 2.4 where the numbers immediately below the months are year days (times for all drifter analysis

are expressed in year days, yd, and GMT). Of the 40 releases 23 drifters were recovered safely and 17 were either lost or grounded.

Table 2.4 Drifter releases in 1995. Each column represents 5 days and the code in the final column refers to the eventual fate of the drifter (R=recovered, L=lost, G=grounded).

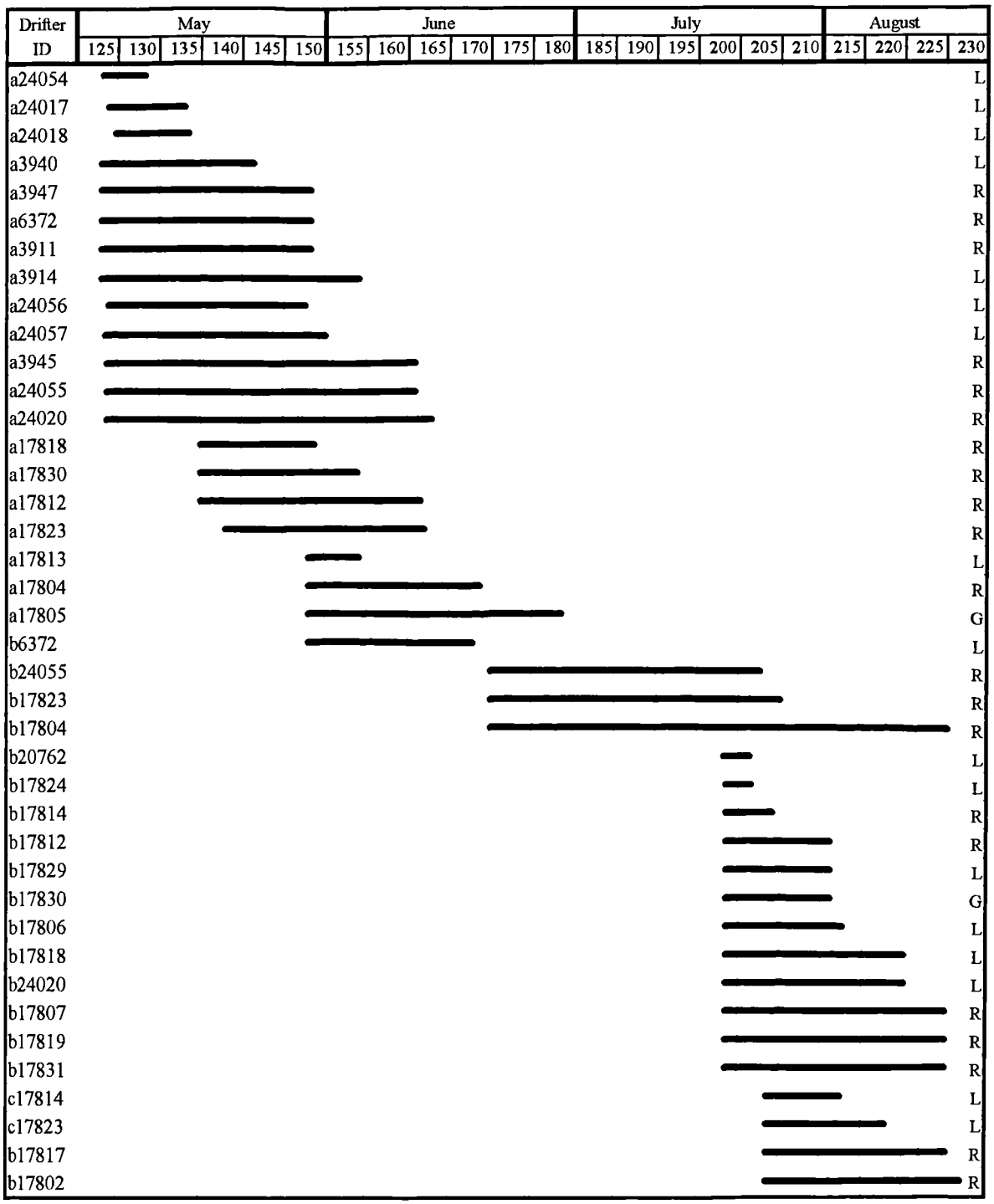

Nine further drifter releases took place in 1996 the details of which are presented in Table 2.5.

Table 2.5 Drifter releases in 1996. (R=recovered, L=lost, G=grounded, an asterisk indicates the drogue was centred at 8.5 m depth).

Drifter	April						May						June						July			
ID	105	110	115	120	125	130	135	140	145	150	155	160	165	170	175	180	185	190	195	200		
d24058	▬	▬	▬	▬	▬	▬																R
d24059	▬	▬																				L
d24019		▬	▬																			R
d24022		▬	▬																			R
f6373																	▬	▬	▬			R
f24017																	▬	▬	▬			R
f24056																	▬	▬	▬		*	R
f24062																	▬	▬	▬		*	R
f21575																	▬	▬	▬			R

Sophisticated algorithms to optimise drifter deployments (e.g. Hernandez *et al.*, 1995) were not necessary in this study since the extent of the gyre could be determined by hydrographic measurements (e.g. the spatial pattern of potential energy anomaly) which were then used to guide the drifter seeding strategy.

2.5.3 Data collection and processing

Drifter positions were obtained in standard format from the Argos data centre in Toulouse and were separated into individual files giving successive locations, location class and sensor data for each drifter. Since two NOAA satellites are involved in data reception it is occassionally possible for successive fixes to be in close temporal proximity. Where fixes were less than 1 hour apart the more accurate was used (in the case of equal accuracy the positions and times were averaged). In 1995 the mean interval between successive fixes was 2.8 hours and the mean number of locations per day was 8.6. Fig. 2.2 shows a histogram of location class for all 40 releases. For any drifter a 'mean class' can be obtained by multiplying the class by the number of occurrences and summing. The location class average for the 1995 dataset was 1.9.

Residual circulation is better observed when the tidal signal is removed from drifer tracks. Linear interpolation was used to transform latitude and longitude on to a uniform 3 hour time series (necessary for digital filtering). Linear interpolation can be used (e.g. Limeburner and Beardsley, 1996) as an alternative to cubic splines which, in tidal regimes, may introduce artifical loops in the reconstructed track (Durazo-Arvizu, 1993). A lowpass, Hamming window, finite impulse response (FIR) filter was designed (Proakis and Manolakis, 1992) to remove the tidal signal. The filter has N = 55 coefficients given by:

$$h(n) = 2f_c\,(0.54 + 0.46\cos[2\pi n/N]) \qquad n = 0$$

$$h(n) = 2f_c\,\sin(n\omega_c)\,(0.54 + 0.46\cos[2\pi n/N]) \,/\, (n\omega_c) \qquad n \neq 0$$

where f_c is the cutoff frequency (normalised by the sampling frequency of 8 day^{-1}) and ω_c is its angular equivalent. The cutoff used (f_c = 0.06) filters out the semidiurnal and diurnal frequencies (the latter being on the edge of the transition band). The frequency response of the filter is illustrated in Fig. 2.3 and its effectiveness in removing the tidal signal from a drifter track is demonstrated in Fig. 2.4. Each position in the regular time series is convoluted with the filter to obtain the smoothed trajectory. To avoid losing data at the beginning of a track, dummy values were supplied by N repetitions of the start coordinates.

Zonal (u) and meridional (v) residual velocities were obtained from central spatial differences of the filtered time series over 24 hours (i.e. over 8 intervals). Only drifters whose mean class was ≥ 2 were used to derive velocities. This gives a mean locational accuracy of ~350 m and ensures that the combined error in positions (after filtering) used in the finite difference calculations is restricted to ~1 km, implying errors in velocity of the order 1 cm s^{-1} . To provide a useful description of the flow field over the full extent of the gyre the velocities thus derived were averaged into cells of 4' of latitude by 3' of longitude (an approximate 7 km grid). This technique

was applied for ensembles of simultaneous drifter releases and gives a quasi-Eulerian view of the circulation from Lagrangian measurements. It also enables comparisons to be made with residual velocities predicted by the numerical model, since each grid cell contains four model cells.

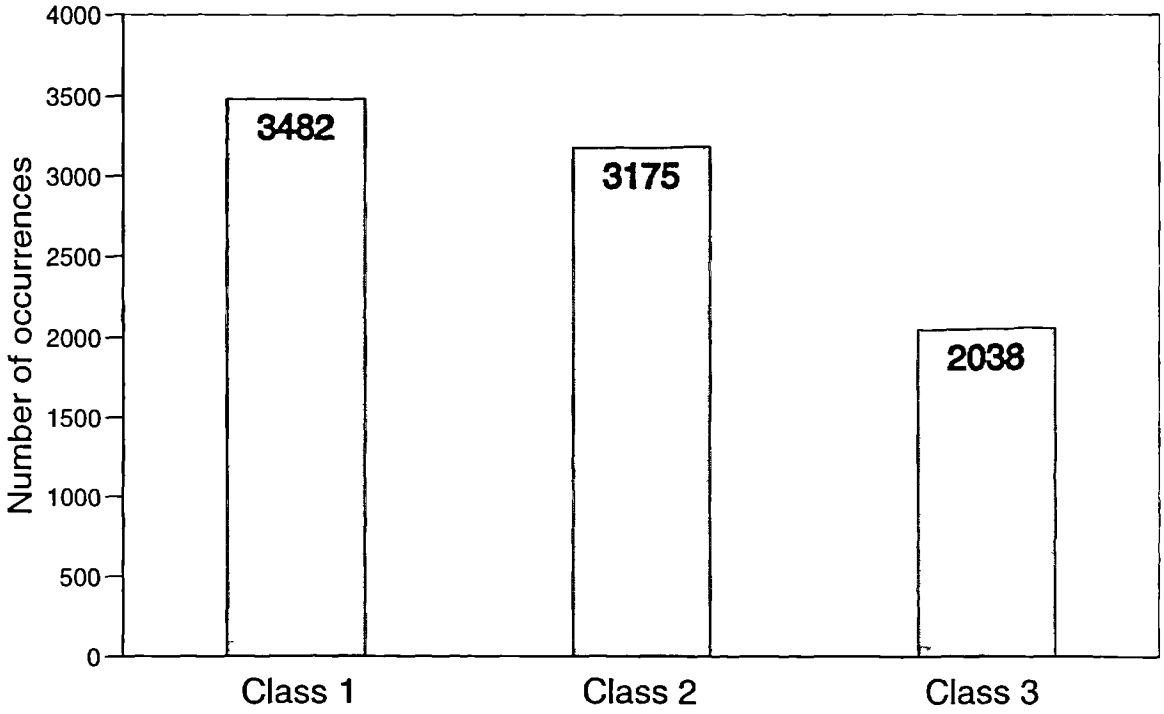

Fig. 2.2 Histogram of location class for all 40 drifter releases in the 1995 dataset.

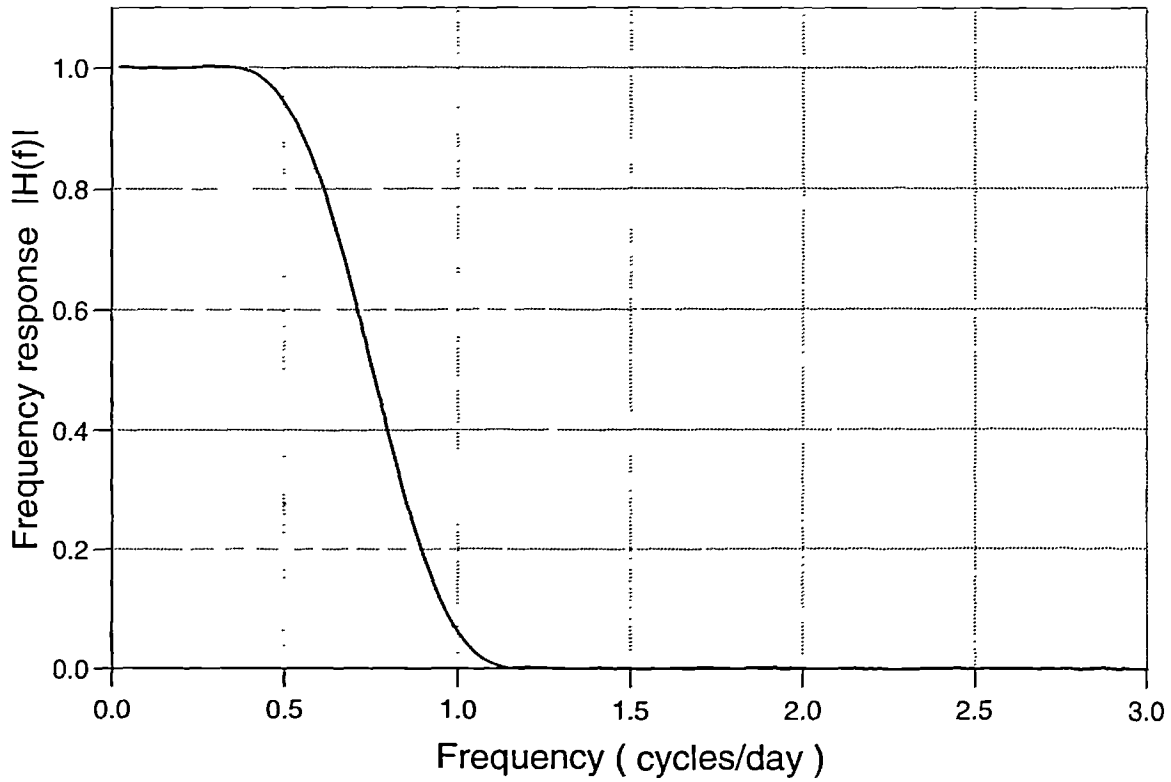

Fig. 2.3 Frequency response of the 55 coefficient FIR lowpass filter.

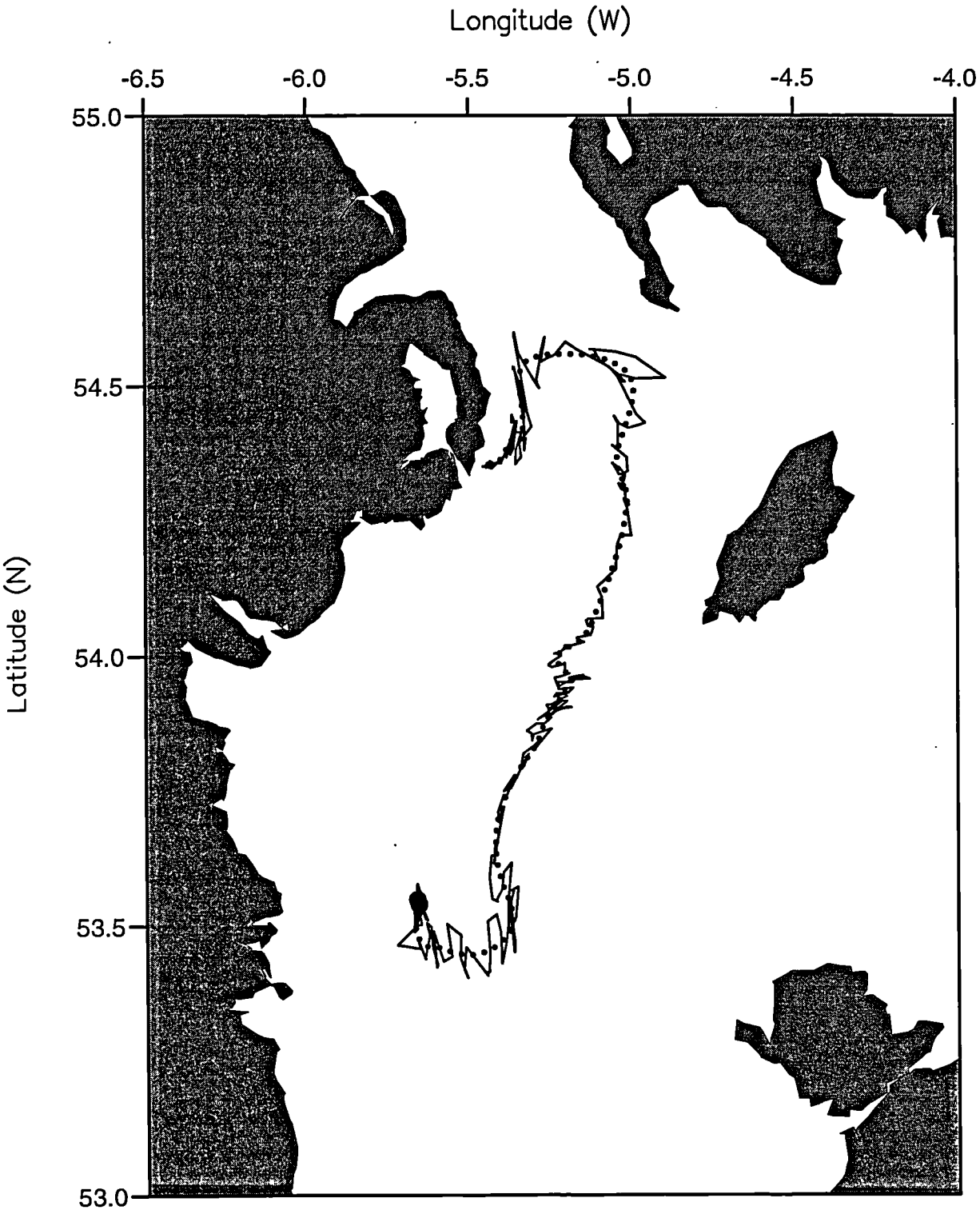

Fig. 2.4 Raw data (solid line) and filtered drifter track (dotted line) for a 33 day deployment in July 1995. The solid circle denotes the start position.

coastal wedge of fresher water had its maximum effect on stratification about 40 km offshore (note the 0.4 contour in Fig. 3.4c). By the end of June, salinity contributed negligibly to vertical structure (Fig. 3.4d) and, therefore, no further transverse sections of salinity are presented here. The horizontal distribution of salinity varied little over the study period as illustrated in Fig. 3.5 which shows depth-mean salinity for four cruises with high spatial coverage (more than 30 stations sampled). Salinity increased gradually from west to east (due to coastal freshwater input) and individual spot values ranged from 33.8 in surface water near Ireland to 34.5 in shallow waters during later cruises. The horizontal salinity gradient was strongest during PM1/95 (Fig. 3.5a) and then showed no significant changes throughout July and August (Figs. 3.5b-d).

The variation of temperature in the western Irish sea during the 1995 observations can be seen in Fig. 3.6. Surface, bottom and top-to-bottom temperature differences are presented (left, central and right panels respectively) for all cruises where more than 30 stations were visited. Searover was employed on cruises PM2/95 (Fig. 3.6b) and PM7/95 (Fig.3.6f) and the limitations of this instrument meant that (i) profiles were only available to 70 m depth and (ii) the coast could not be approached as closely as with conventional CTD profiles. For Searover surveys, bottom temperature is replaced by T_{70} which is the temperature at 70 m depth (or at the bottom, if shallower).

Temperature stratification was already evident (Fig. 3.6a) in the first cruise (PM1/95) with cold bottom water ($< 9°$ C) extending to the North Channel, except for a small, isolated patch of colder ($< 8.5°$ C) water at 53.8° N, 5.7° W. Fig. 3.6b(ii) reveals that by cruise PM2/95 (12 June) the isolated pool of cold water had enlarged (note that this cold dome could be inferred even though Searover only profiled to 70 m). By 17 July (Fig. 3.6c, PM4/95) the stratified region had extended to the north-west of the Isle of Man and strong gradients of temperature were seen at

the bed (Fig. 3.6c(ii)). Cruise PM5/95 (24 July) measured the largest vertical temperature difference of 6.7°C at station E5 but made no observations north of the C line so the northern limit of stratification could not be determined. By cruise PM6/95 (14 August) stratification was seen as far north as 54.5° N, close to the North Channel.

Figs. 3.6(b-e) illustrate that during the stratified season the loci of the surface and bottom fronts were notably different, the surface front intersecting the coast of Ireland at the latitude of the Isle of Man (cf. contours of h/u^3, see Fig. 1.9) whilst the bottom front extended northward from the Isle of Man towards the Scottish coast. Other points to note are that the gradients of temperature were generally stronger at the bed than at the surface and that closed contours of bottom temperature existed along the western side of the area (despite the absence of a surface front) providing a dynamical mechanism for a southward, density-driven flow which comprises the western part of the gyre. By 28 August (PM7/95, Fig. 3.6f), the strong thermal stratification had retreated back to an area similar to that in June (Fig. 3.6b) with vertical temperature differences to the north west of the Isle of Man of only 0.5°-1° C. This retreat may have been partly caused by increased cooling and mixing due to stronger northwesterly winds which were sustained from day 236 (24 August) onwards (see Fig. 3.7), although because Fig. 3.6f was derived from Searover data (i.e. only top 70 m of water column were sampled) the vertical differences would, in reality, have been larger. Terrestrial weather stations surrounding the study region are all sheltered from at least one significant wind direction, therefore a hybrid wind time series was synthesised by taking the higher value from the stations at Ronaldsway and Point of Ayre (see Fig. 2.1 for locations); these values were then vector averaged over 24 h to obtain the winds shown in Fig. 3.7.

The gradual warming of the isolated cold pool can be seen in the succession of central panels in Fig. 3.6. The coldest bottom temperatures were observed at stations

E4, E5 and F4 (see Fig. 3.1) which serve to define the centre of the cold pool. Surface and bottom temperatures from these stations are plotted in Fig 3.8 for the duration of the 1995 observations. The mean warming rate of the relict water can be estimated as 0.025 °C d^{-1} prior to day 205 (24 July) increasing to 0.04°C d^{-1} thereafter. Despite this warming the horizontal gradients of temperature at the bed did not change substantially (the maximum values remaining at ~1°C in 9 km). These observations confirm the stability and seasonal persistence of the central mass of cold, bottom water and the horizontal density gradients associated with it.

The dynamical significance of horizontal density gradients is emphasised by equation 1.2. The seasonal development of the three-dimensional density structure is now considered by presenting two principal transverse sections (see Fig. 3.1 for locations). Fig. 3.9 shows the temporal evolution of density (σ_t) along line F at latitude 53° 40'N. This priority line was sampled wherever possible on all cruises and where data from line F were unavailable (Figs. 3.9a and h) line E (latitude 53° 50'N) is shown in its place. Data from undulating CTDs (Figs. 3.9 b,c,g and i) are only contoured to the maximum profiling depth reached by the instruments.

The influence of freshwater on the density field was apparent near the Irish coast throughout the June observations (Figs. 3.9a,b and c). Temperature began to exert dominant control over density by the end of June as discussed. This is reinforced in Fig. 3.9c where a significant sharpening of the pycnocline can be observed. The dome of dense bottom water can be seen throughout the sequence of observations with maximum horizontal density gradients being reached in late July (Fig. 3.9e) on the eastern flank of the dome. Density gradients were generally stronger here than on the western side (Figs. 3.9d and e) except for those observations in June where the strongest gradients were found near the Irish coast. The locations of bottom fronts (taken to be the longitude of the strongest density gradients) changed little over the heating season, consistently occurring between 5° 15'W and 5° 25'W on the

eastern side and at approximately 5° 40'W on the west. Also, once the bottom front was established, its location was consistently offset by 10-20 km offset to the stratified side of the surface front (where isopycnals outcrop at the surface). The pycnocline depth remained at approximately 25 m from the beginning of June until the end of August. The beginning of a breakdown in stratification can be seen in Fig. 3.9g, confirming the conclusions drawn from the map of temperature differences (Fig. 3.6f(iii)), yet some residual stratification persisted until October as shown in Fig. 3.9i. By 31 October 1995 (cruise PM9/95, not shown) density was vertically mixed ($\sigma_t = 25.55$) at all stations visited.

Fig. 3.10 shows a sequence of density (σ_t) sections for a north-south line through the cold pool. The line is viewed from the east and passes through longitude 5° 30'W (Fig. 3.10b,c and e) or 5° 40'W (Fig. 3.10a). Where sufficient stations were visisted, an oblique section (southwest to northeast) through the stratified area was created (Figs. 3.10 d,f and g); a typical oblique line is shown in Fig. 3.1 but station numbers are shown on the top axes of the sections so it can be seen how they were compiled. Qualitatively, the shape of isopycnals in Figs. 3.10(a) and (b) suggests that salinity was again important at the northern limit of the area until June. The strengthening of the thermocline in late June due to surface heating is further evident in Fig 3.10c and the thermocline depth was consistently 20-30 m for the remaining observations. The southern boundary of the dense pool is seen to be between 53° 25'N and 53° 30'N. Those sections which pass through the entire stratified region (Figs. 3.10d and f) show that there were, in fact, two isolated density maxima near the bed, each with significant horizontal density gradients at its edges. The Searover survey of 30 Aug (Fig. 3.10g) was unable to provide further evidence of the two domes since profiles were limited to 70m depth. It is possible to construct regional flow fields from these density fields and such an approach, along with a comparison of ADCP data, is presented elsewhere (Fernand, 1999). Here, some geostrophic calculations are

presented in the next section to facilitate comparisons with speeds obtained from the Argos drifters.

Maps of potential energy anomaly (calculated from equation 1.1) from cruises PM1/95, PM4/95, PM5/95 and PM6/95 are presented in Fig. 3.11. Contours of ϕ provide a vertically integrated measure of horizontal density differences and might therefore be expected to behave as analogues to streamlines for the flow field. The calculation of ϕ is most sensitive to the large departures from mean density found near the surface and the bed and it is important, therefore, to obtain the fullest possible vertical profile of density since extrapolation will lead to inaccuracies. Consequently the parameter is only calculated from conventional CTD data on those cruises with high spatial coverage. Maximum values of ϕ of 120-130 J m^{-3} were obtained during cruises PM4/95 and PM5/95, decreasing to peak values of 100 J m^{-3} by PM6/95. It should be noted that because it is a vertically averaged quanitity the largest values of ϕ do not necessarily coincide with the largest top-to-bottom density differences. The distribution of potential energy anomaly confirms the existence of two distinct regions of stratification and, whilst bearing most resemblance to the contours of vertical temperature differences seen in Fig. 3.6 (panel iii), its advantage as a descriptive parameter is that its contours bear direct relation to the thermal wind equation. The closed contours of ϕ define the extent of the western Irish Sea gyre and also act broadly as contour lines for the residual circulation, as the Argos drifter tracks will show.

The consistent appearance of the cold pool from year to year is an important regional feature. Fig. 3.12 shows the two key transverse sections of density and the spatial pattern of potential energy anomaly from cruise PM1/96 (22-26 July 1996). The qualitative similarity between these vertical sections and their 1995 counterparts (Fig. 3.9d for line F and Fig. 3.9d for the north to south section) is obvious. The dense dome at latitude 53° 40'N can also be seen in the Scanfish section presented in

Fig. 1.6a. Observed temperatures in July 1996 were similar to those in July 1995 with values of 15° C at the surface and lowest temperatures of 9.6° C at the bed at station F4. Salinity was uniformly higher (34.6-34.7) along line F in 1996 resulting in higher maximum values of density (σ_t = 26.7). The extent of stratification and the existence of two distinct stratification centres seen in Fig. 3.12c agrees well with observations from previous years (cf. Fig. 3.11b and Fig. 1.8).

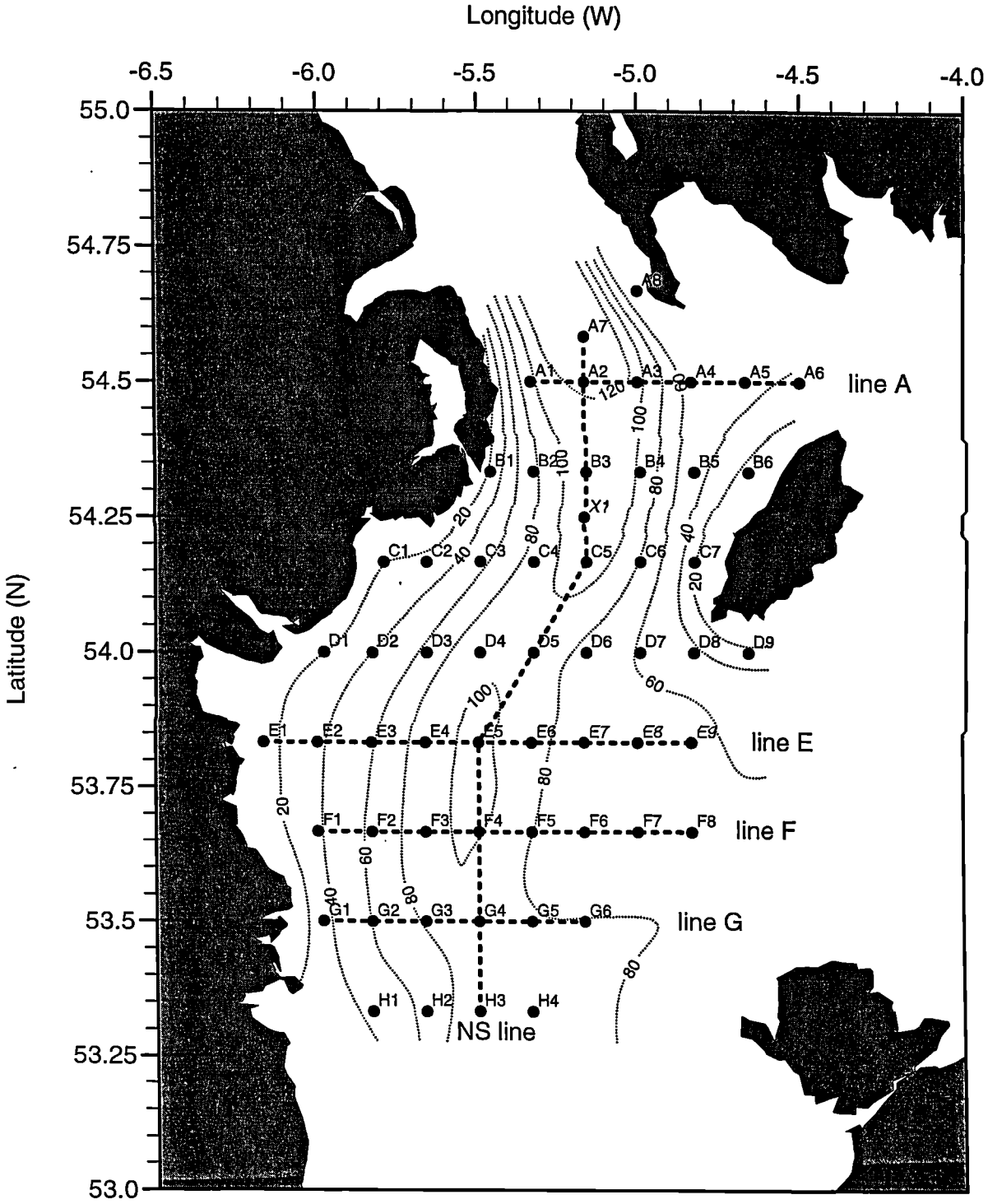

Fig. 3.1 Grid of CTD stations where observations were made. The dotted lines show depth contours (m) whereas the bold dashed lines show the location and orientation of transverse sections for which hydrographic variables are presented in this chapter.

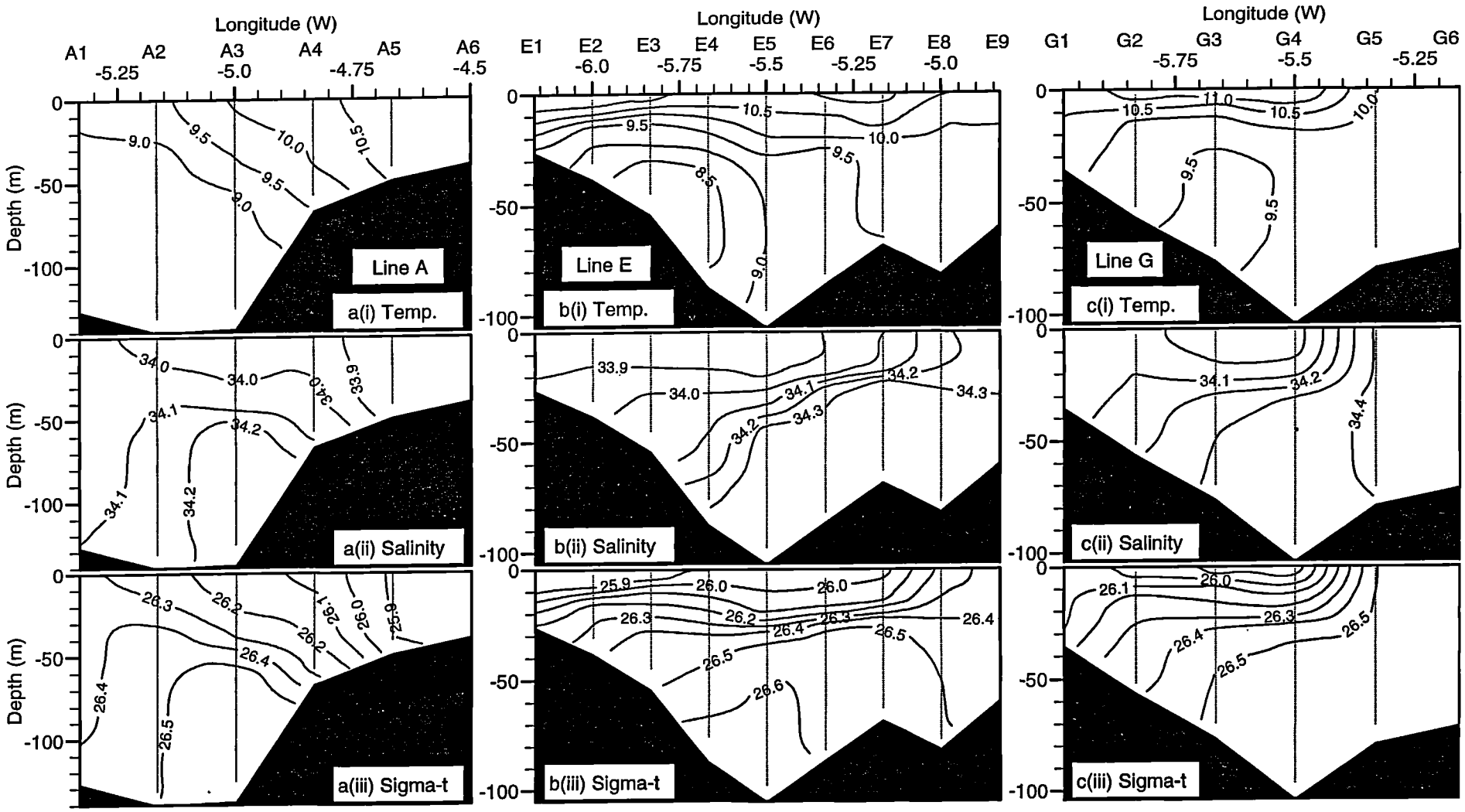

Fig. 3.2 Transverse sections from cruise PM1/95 for (a) line A at 54° 30'N, (b) line E at 53° 50'N and (c) line G at53° 30'N. In each case the upper panel (i) shows temperature (°C), the central panel (ii) is salinity and the lower panel (iii) displays density (σ_t). Vertical dotted lines denote the 1m resolution data points and the station numbers (see Fig. 3.1) are given at the top of each group of panels. Note the qualitative similarity between isopycnals and isohalines.

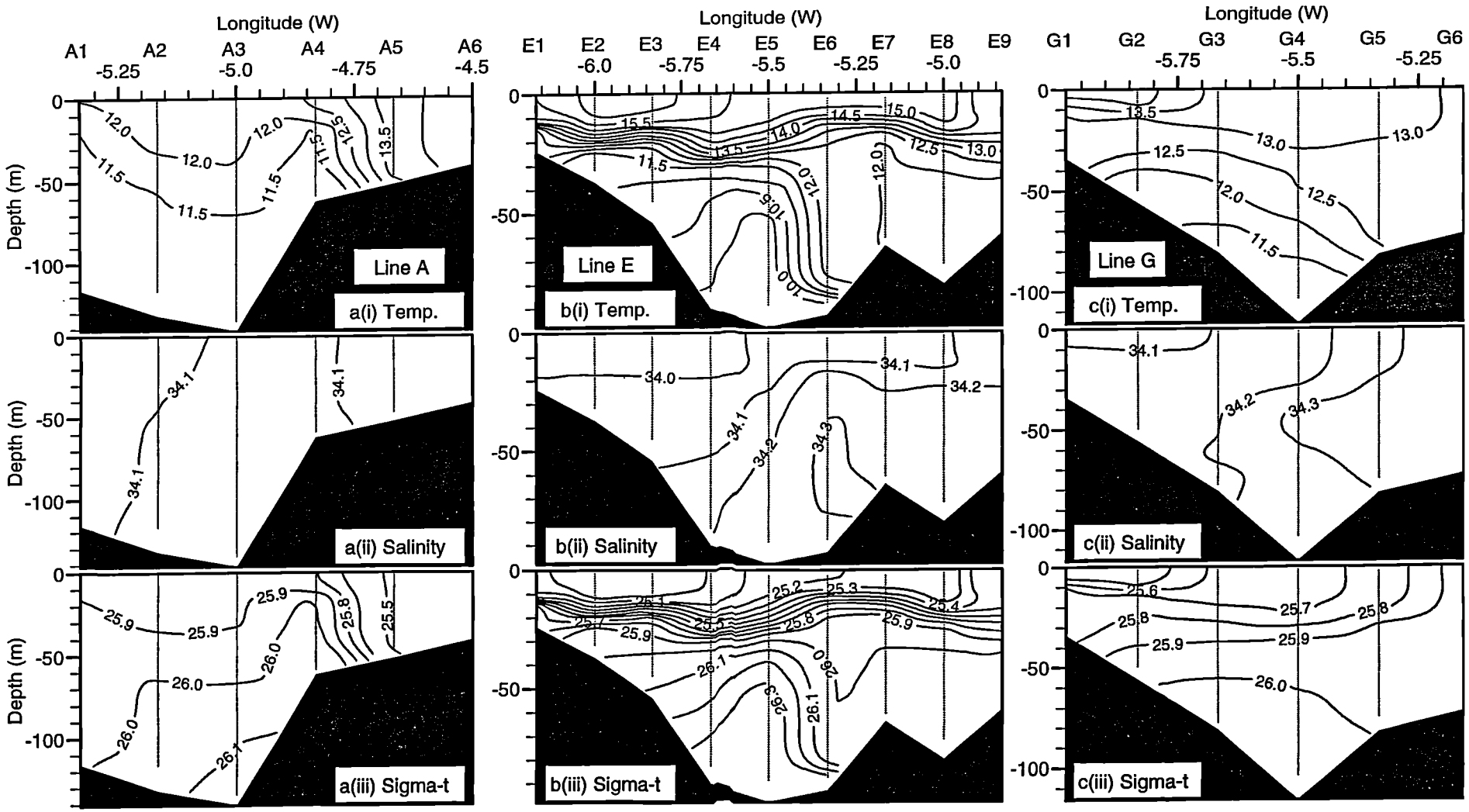

Fig. 3.3 Transverse sections from cruise PM4/95 for (a) line A at 54° 30'N, (b) line E at 53° 50'N and (c) line G at 53° 30'N. The panels are arranged as for Fig. 3.2 and annotations are identical. Note now the qualitative similarity between isopycnals and isothermals and also the greater range of temperature values compared to Fig. 3.2.

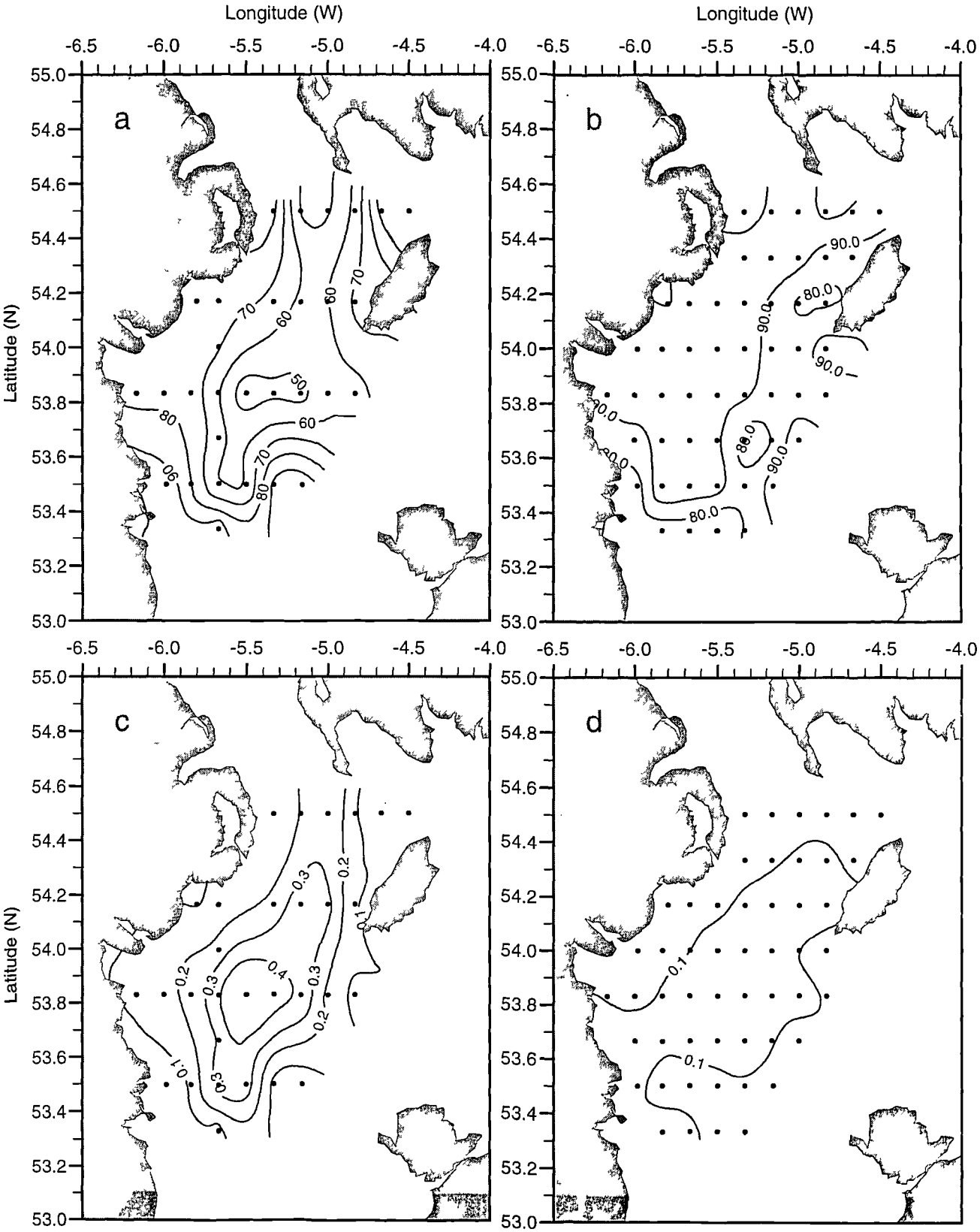

Fig. 3.4 (a) Spatial pattern of temperature control (%) on top-to-bottom density stratification for cruise PM1/95 and (b) for PM4/95. The corresponding top-to-bottom salinity differences are shown in (c) for PM1/95 and (d) for PM4/95. Dots denote those stations sampled.

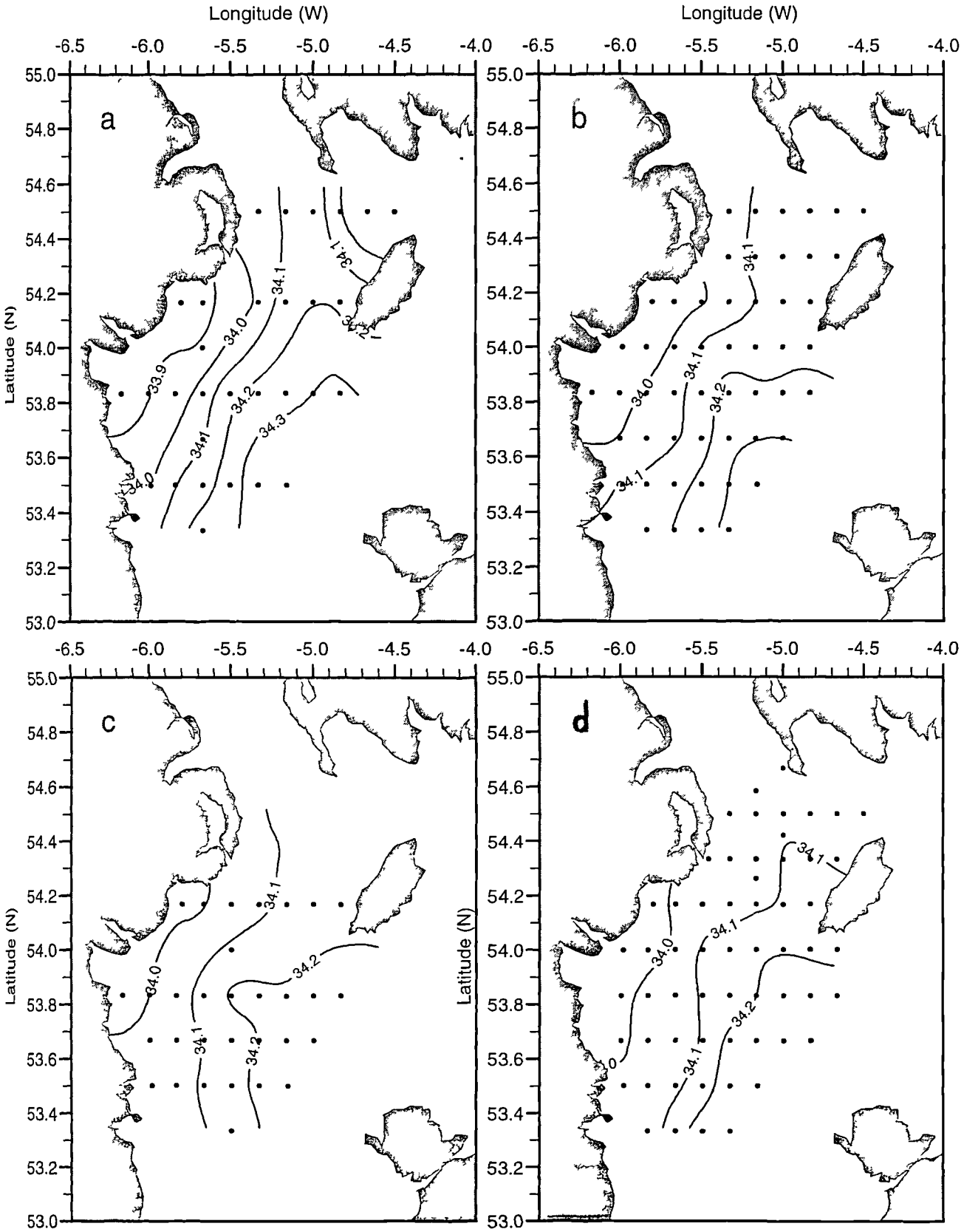

Fig. 3.5 Spatial pattern of vertically averaged salinity over the period May-August 1995 for all cruises where more than 30 stations were sampled: (a) PM1/95, (b) PM4/95, (c) PM5/95 and (d) PM6/95.

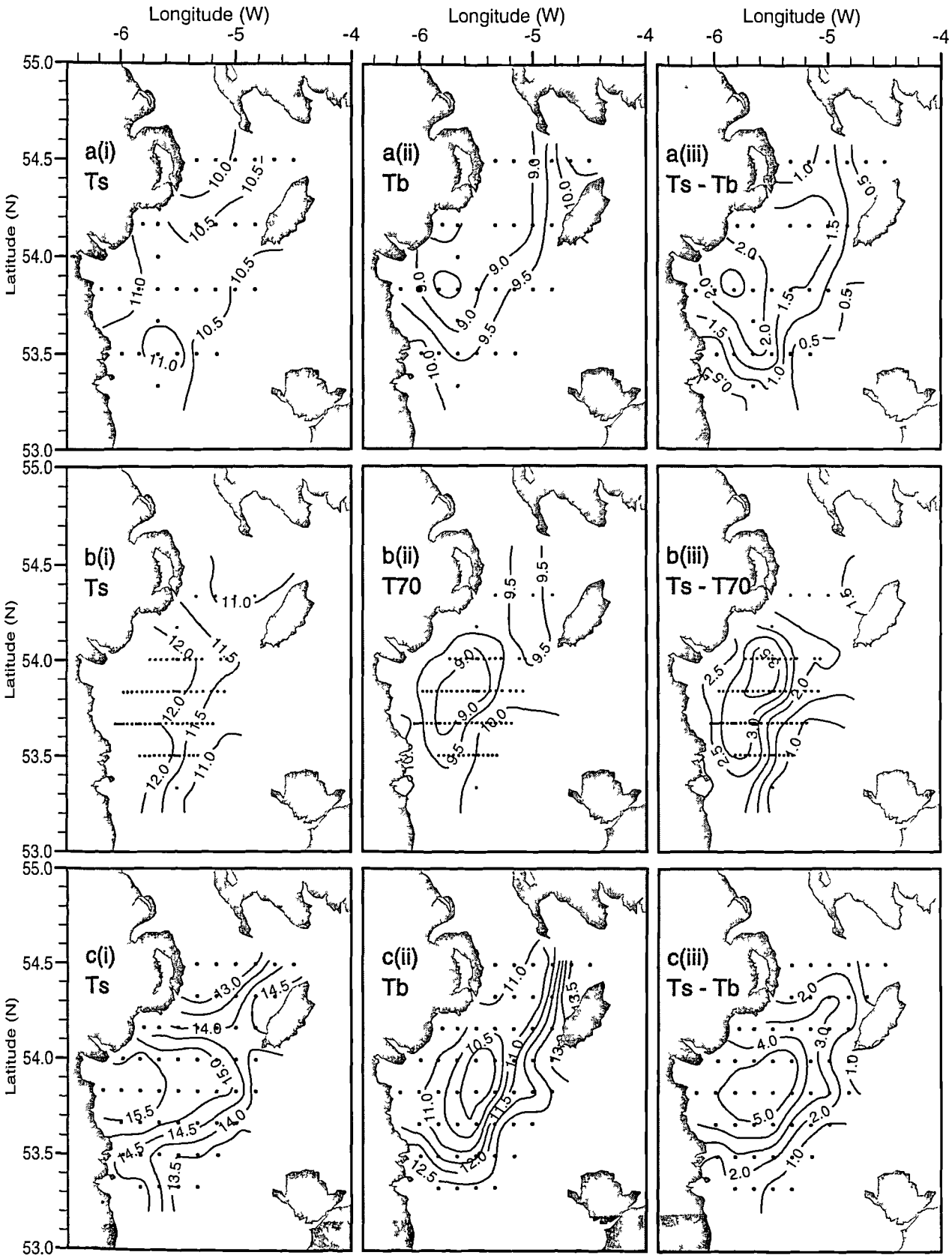

Fig. 3.6 Seasonal development of the temperature field (°C) for those cruises in 1995 with high spatial coverage: (a) PM1/95, (b) PM2/95, (c) PM4/95 and (next page) (d) PM5/95, (e) PM6/95 and (f) PM7/95. In each case (i) is surface temperature, (ii) the bottom temperature (continued overleaf).

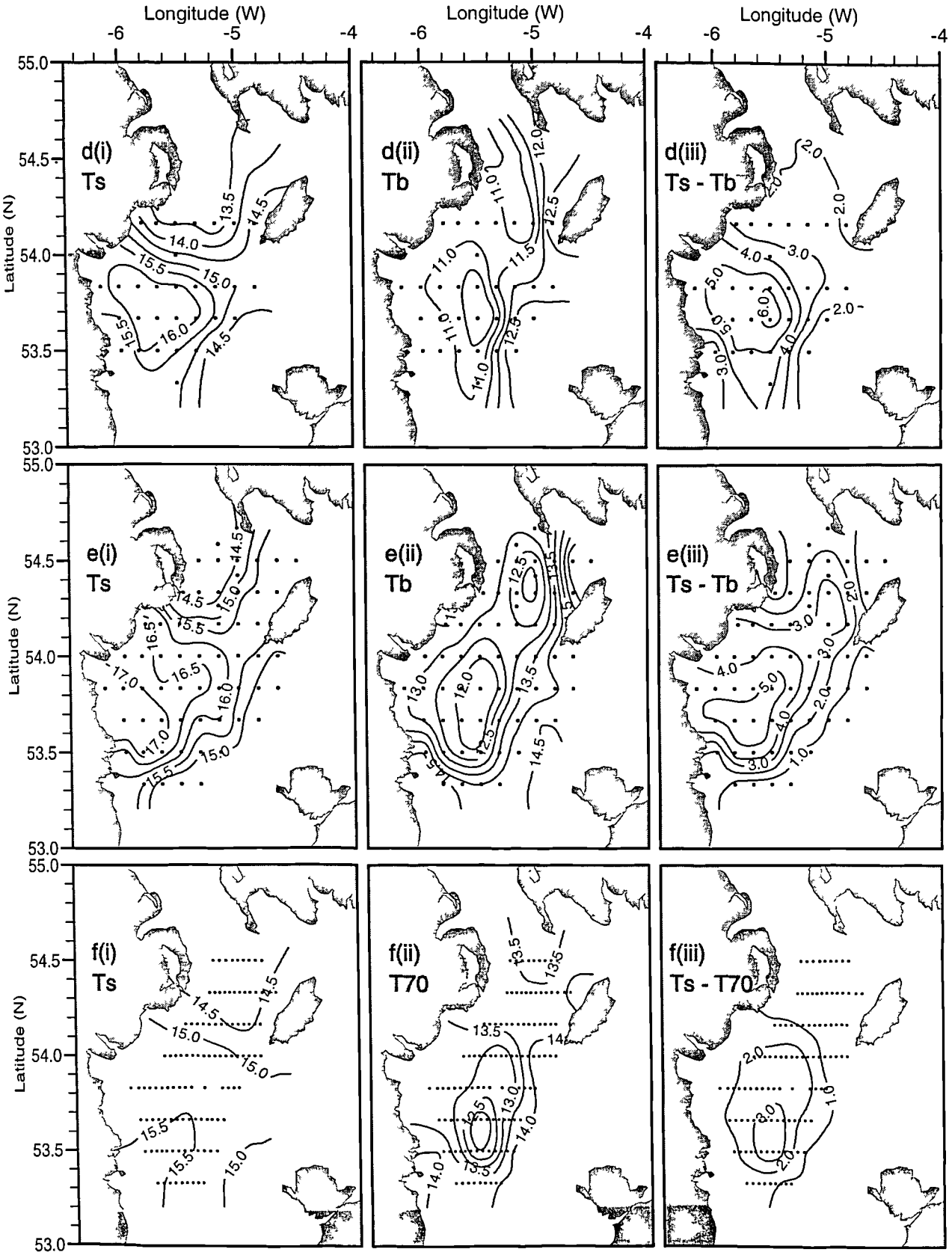

Fig. 3.6 (continued) and (iii) is the difference between the two except for Searover cruises (b & f) where temperature at 70m depth (T_{70}) replaces bottom temperature. Dots denote those stations sampled. Note the change of contour interval for temperature difference in Fig. 3.6c (iii).

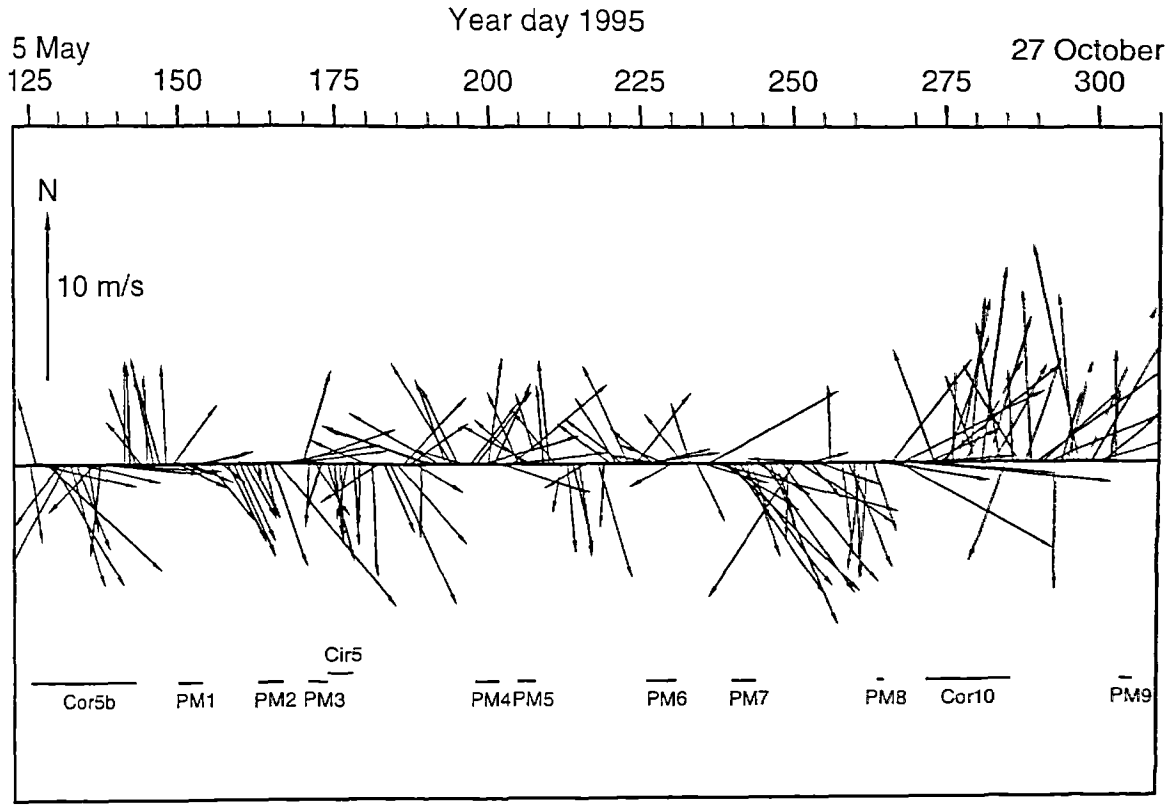

Fig. 3.7 Wind vectors (24 h means) obtained by taking the maximum value from Ronaldsway and Point of Ayre weather stations (see Fig. 2.1 for locations). Horizontal bars below the vectors depict cruise durations.

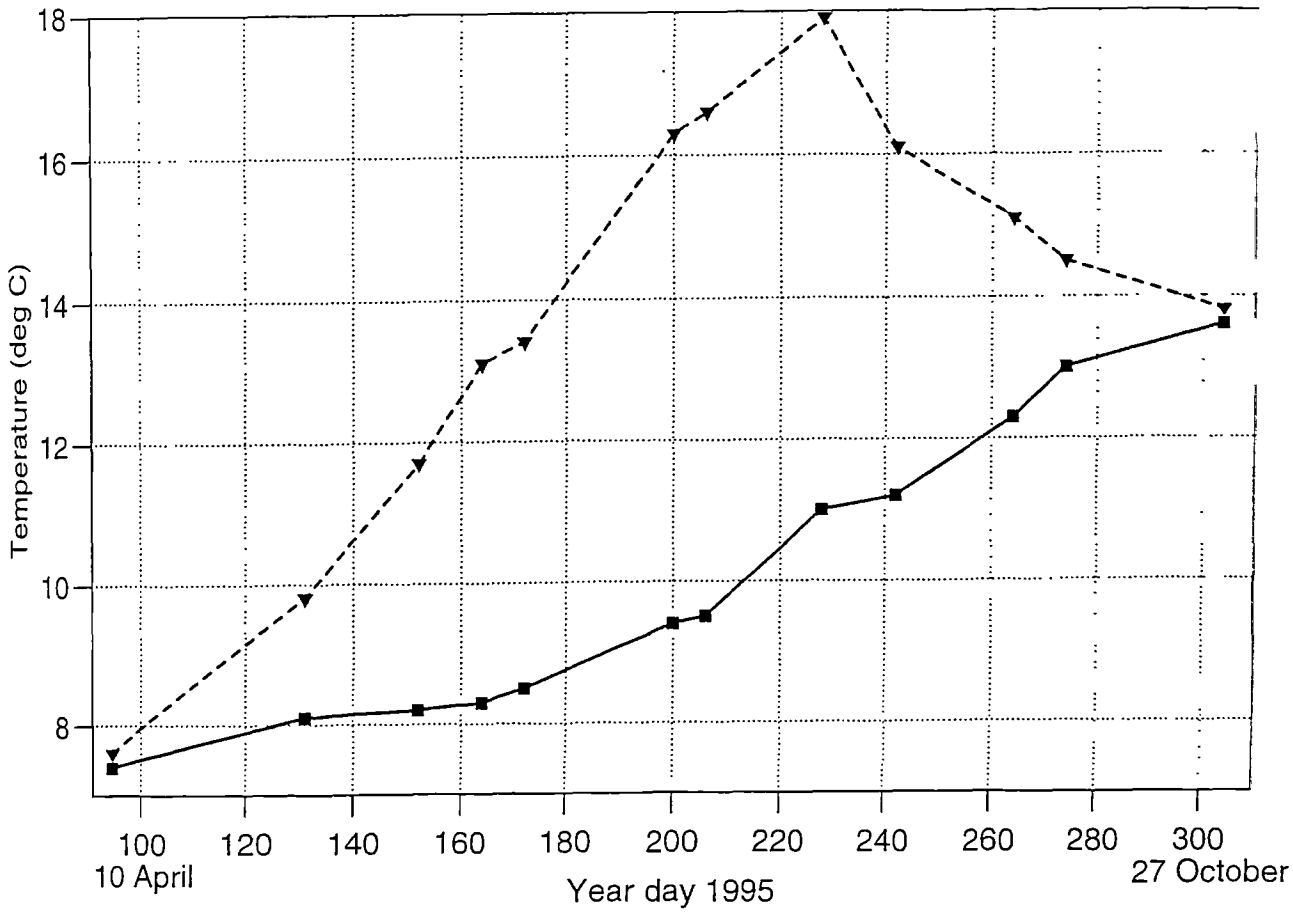

Fig. 3.8 Seasonal development of surface (dashed line) and bottom (solid line) temperatures for 1995 at station E4 (or F4, if E4 was not visited).

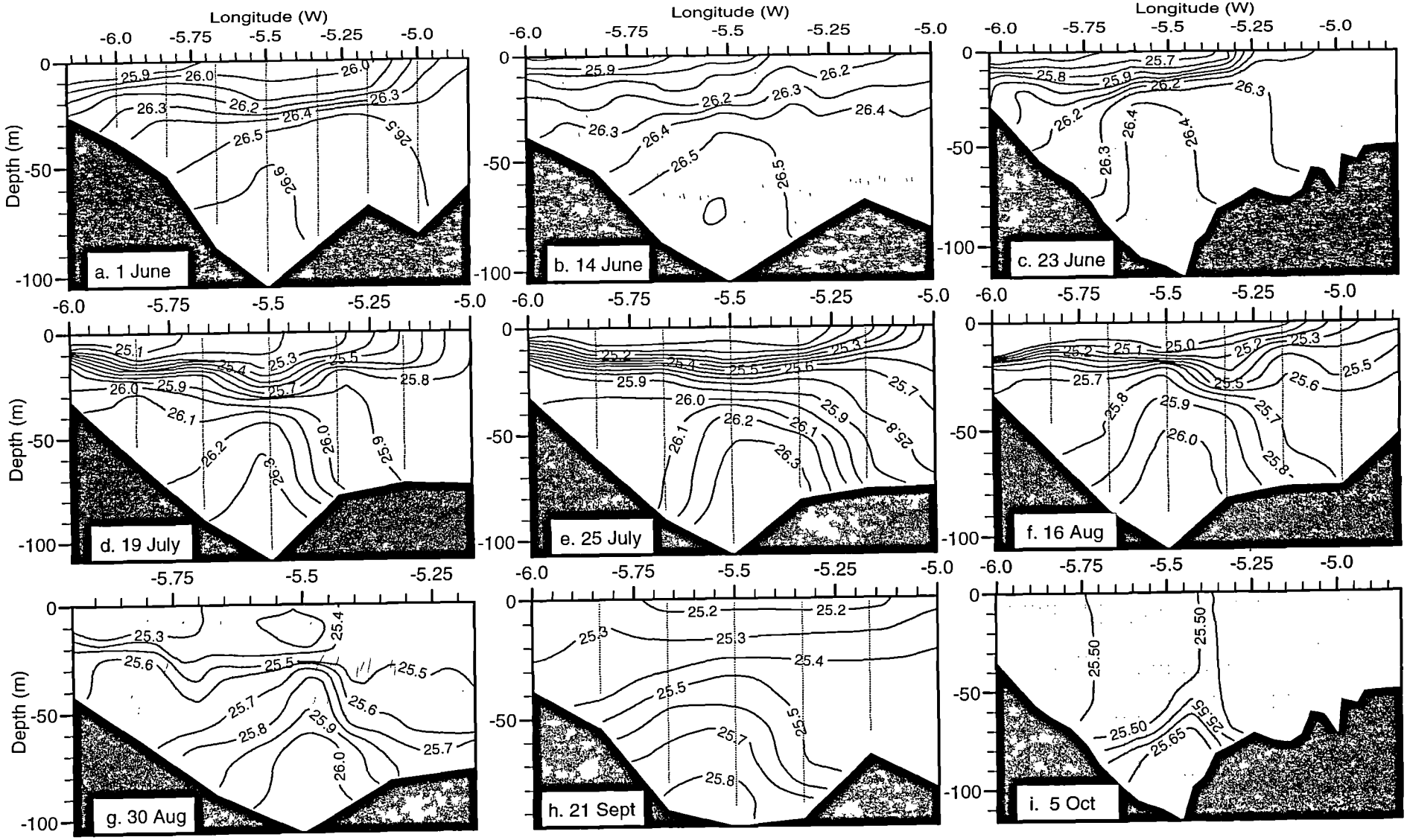

Fig. 3.9 Transverse sections of density (σ_t) through the cold dome at latitude 53° 40'N (line F) or, (a) and (h) where line F was not visited, latitude 53° 50'N (line E). Panels (a) to (i) show sequentially all available observations from cruises in 1995. Dates of the measurements are given inside each panel. Note the change of contour interval in (i).

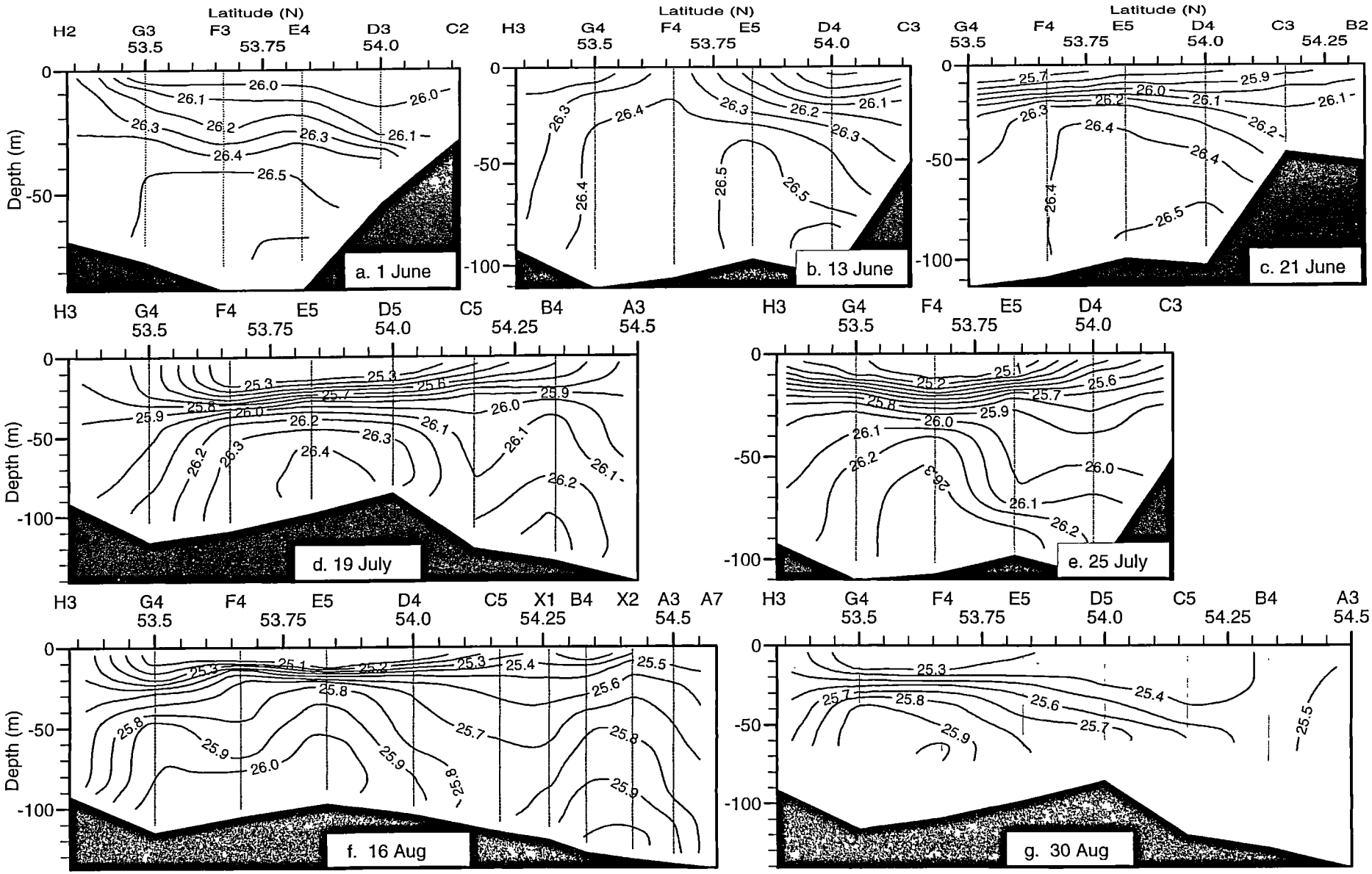

Fig. 3.10 Time sequence of north-south density (σ_t) sections viewed from the east: (a) longitude 5° 40'W; (b) (c) and (e) 5° 30'W; (d) (f) and (g) represent an oblique line through the stratified region (see Fig. 3.1 and text for details). Station numbers are given above the top axes for orientation and the dates of observations are shown.

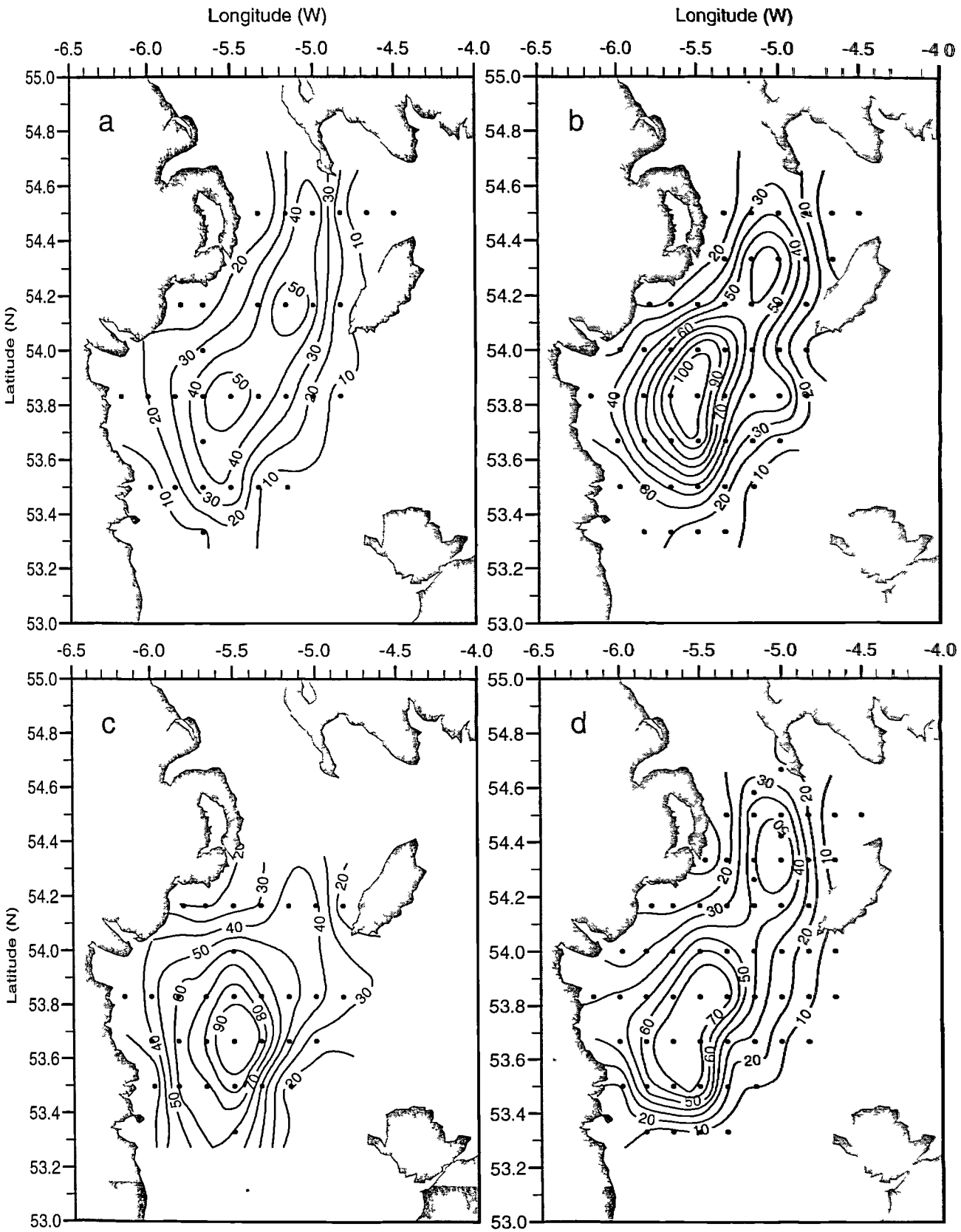

Fig. 3.11 Contours of potential energy anomaly (J m^{-3}) for (a) PM1/95, (b) PM4/95, (c) PM5/95 and (d) PM6/95. Two centres of stratification are apparent in (b) and (d).

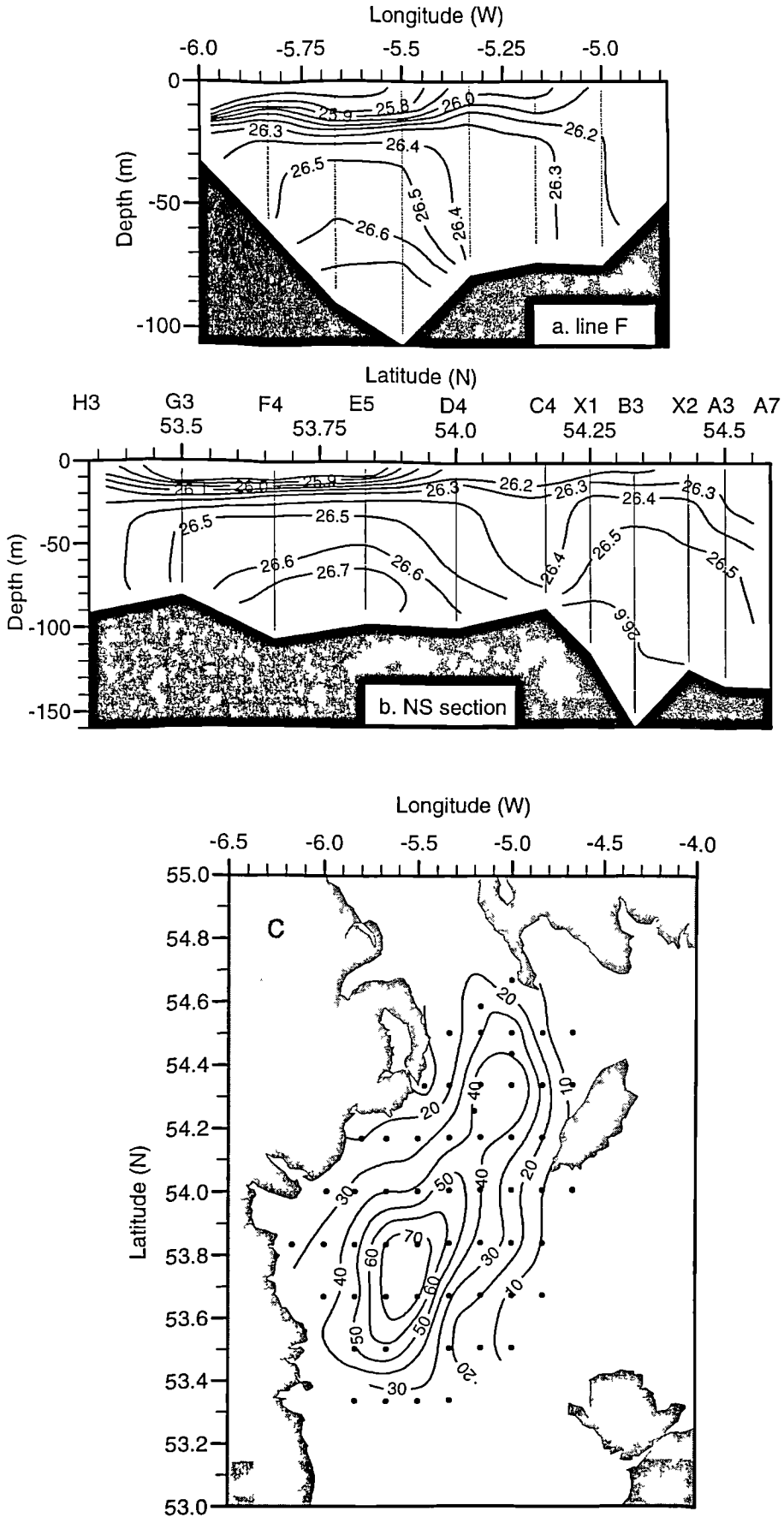

Fig. 3.12 Transverse sections of density (σ_t) for cruise PM1/96 (22-26 July 1996) for (a) latitude 53° 40'N (line F) and (b) a north-south line comprised of the stations indicated. (c) Contours of potential energy anomaly (J m^{-3}) from the cruise.

3.2 Drifter observations

The tracks of Argos drifters active for four or more days in 1995 are shown in Fig. 3.13, in chronological order of release date (see Table 2.4 for details of deployment duration). Each panel shows tracks based on the raw position data obtained from system Argos. Of those drifters that were recovered, two (a3911 and b17823) had lost their drogues and one (b17819) had sustained damage to its tether, effectively reducing the drogue depth to 12 m. Cyclonic motion was evident in 23 of the 34 trajectories and only two (a17818 and a24017) displayed anticyclonic tendencies. Several consistent features are obvious from the individual tracks. Firstly, there was a southward flow along the Irish coast which was particularly noticeable in the earlier deployments (e.g. a24056, a3945 and a17823). Furthermore, drifter a24020 provided evidence of a possible North Channel inflow into the region. Secondly, few drifters escaped the area of interest and those that did leak from the gyre (a24055, a17830 and a17805) did so to the southwest of the Isle of Man indicating a southward flowing counter-current that transports material around the southern tip of the Isle of Man and then eastwards. The only buoy to leave through the North Channel (a3911) had lost its drogue. Finally, there was a coherent northeastward flow shown by the congruence of drifter tracks west of the Isle of Man (e.g. b24055, b17804, b17802 and c17823) where speeds were typically 20 cm s^{-1} (see Fig. 3.18 later). Speeds in the southward flowing arm, along the Irish coast were less, typically 9 cm s^{-1}. A cyclonic turn which appeared in several of the earlier tracks (a24057, a17830 and a3945) occurred close to day 144 in all cases and was probably due to a period of southerly winds between days 141-148 (21-28 May). Drifter b17804 made a complete cyclonic circuit in 55 days: after negligible movement for 13 days it then took 42 days to encircle the gyre at an average speed of 10 cm s^{-1}.

The 1996 drifter tracks (see Table 2.5 for durations) in Fig. 3.14 revealed essentially the same features. One of those released in April (d24058) confirmed the tendency for drifters early in the season to escape the gyre around the southern tip of the Isle

of Man. Two of the July 1996 deployments (f24056 and f24062) were drogued at a depth of 8.5 m and were released as close as possible to drifters drogued at the usual depth of 24m (f24017 and f6373 respectively). Whereas the other three July deployments exhibited cyclonic motion, the two shallow drogued buoys simply moved southeastwards, indicating that the cyclonic flow in the gyre may be confined to a jet-like core (see Fig 3.19 later) and is not necessarily evident in the surface currents.

Fig. 3.15 is a composite 'spaghetti diagram' of all drifter tracks from the two years. For clarity, tidal fluctuations have been removed using the lowpass filter described in §2.5.3. The tracks have been colour coded by the month in which they were released (see figure caption for coding) and the solid circles denote the start positions. It is noticeable that the majority of tracks leaving the study region were from early deployments (April to June). The zone to the south of the Isle of Man is highlighted as the main area where drifters escaped the gyre. The extent of the gyre is shown clearly by the composite picture which also indicates how retentive the system is, only 7 from 43 tracks (16%) escaping the gyre, if drogueless buoys are excluded. Another striking feature of Fig. 3.15 is the similarity between the pattern of drifter trajectories and the spatial distribution of potential energy anomaly as seen in the contours of Fig. 3.11. To examine its usefulness as a contour map for the flow field, Fig. 3.16 presents maps of potential energy anomaly from cruises PM1/95, PM4/95, PM6/95 and PM1/96; overlayed on these are segments of drifter tracks which were contemporaneous to within 5 days before or after the cruise (e.g. Fig. 3.16a shows potential energy anomaly from PM1/95 (days 150-153) along with segments from drifters active between days 145-158). Whilst there is no obvious agreement between contours and drifter tracks in Fig. 3.16a, in the remaining diagrams the drifter segments show a qualitative similarity to the contour directions (it should be remembered that the two segments that left the gyre in Fig. 3.16d belong to drifters which had their drogues centred at 8.5 m). As well as suggesting the centres of high stratification to be stagnation areas for residual flow, the figures reveal several

possibilities for the gyral circulation. Drifters made circuits, or partial circuits, around the southern stratification maximum (e.g. f24017), around the northern centre (e.g. b17802) or a complete circuit of the stratified area as described by drifter b17804.

To illustrate the flow field fully, Fig. 3.17a shows six selected trajectories (a24056, b24055, b17804, b17802, b17817 and f24017) which collectively define the gyre and its possible circulation paths. These tracks are overlaid on contours of ϕ from PM4/95 which is typical of the stratification in July and August (see Fig. 3.11). The qualitative agreement of these trajectories with the contours is clear as is the coherence of trajectories around the different parts of the gyre. The same trajectories are overlaid on bathymetric contours of the region in Fig. 3.17b. Depth might be expected to act as a surrogate for potential energy anomaly, since the latter is a depth integrated parameter. Along the western Irish Sea front, the bathymetry is also important in determining the transition between mixed and stratified water through h/u^3. Although agreement between contours and tracks can still be seen along the two long sides of the gyre, this is not the case at the northern and southern limits of the region where drifters cross isobaths. There is also variability in the circulation patterns seen throughout the year (Fig 3.16) which is consistent with a variation in the spatial pattern of the density field.

Lagrangian residual velocities were obtained from drifter trajectories as described in §2.5.3. Fig. 3.18 presents the along-track speeds of 14 drifters that followed part of any of the recirculation paths suggested by Fig. 3.17. The solid line shows the along-track speed of drifter b17804 for its entire deployment. Following Limeburner and Beardsley (1996), the speeds are given as a function of angular position around an idealised gyre with its centre at station E5 and a major axis directed towards 30°T (the same orientation as the recirculation shown by drifter b17804). Angles are expressed as positive anticlockwise, hence 0° refers to the north-eastern part of the

gyre, 90° defines flow down the Irish coast and 270° relates to flow along the western Irish Sea front. (The speeds of all other drifters were analysed and in no way alter the range of values seen in Fig 3.18, but did not lend themselves so easily to this form of presentation). The maximum speeds of 22 cm s^{-1} are found at angles of 200-300° (i.e. the western Irish Sea front) where the average speed is 18 cm s^{-1}. It should be noted that there are no low values at this range of angles; drifters moving around this part of the gyre did so rapidly. Southward flows along the Irish coast (50°-150°) ranged between 5-15 cm s^{-1} with an average of 8 cm s^{-1}. The overall ensemble average, which represents a mean recirculation speed for the gyre, is 9 cm s^{-1}.

Although the congruence of drifter trajectories with contours of ϕ strongly suggests that the observed residual currents are density-driven, two other mechanisms which must also be considered are tidal residuals and wind-driven flow. Fine resolution barotropic models (e.g. Proctor, 1981; Davies and Aldridge, 1993) do not predict the cyclonic residual circulation and it is unlikely that rectification of the weak tides in this region could produce Eulerian residuals of the magnitude seen in Fig. 3.18. Since the Eulerian tidal residual is known to be small, a good estimate of the Lagrangian tidal residual velocity can be obtained by calculating the Stokes velocity, $U_s = U^2/2c$ where U is the tidal current amplitude and c is the phase speed of the tidal wave (Pingree and Maddock, 1985; Horsburgh *et al.*, 1998). Taking U as 0.3 m s^{-1} and c as 20 m s^{-1} gives a value for U_s of less than 1 cm s^{-1}. To confirm the low Lagrangian tidal residuals, a particle tracking model similar to one used for oil-spill tracking (Elliott, 1991) was constructed using 3 km resolution M_2 and S_2 tidal data obtained from the primitive equation model described in Chapter 5. Particles were released at several locations near 53.6 °N, 5.4 °W which is where several drifters moved rapidly northwards (if Lagrangian residuals were a significant factor in the flow, this is where they would be most noticeable). Particles were released at 30 minute intervals over a tidal cycle and then advected for 15 days with a time step of

30 min. The maximum displacement vector (taken as the Lagrangian residual) was 5 km in 15 days, corresponding to a residual current of less than 0.5 cm s^{-1}.

The basic differences in the shape of the trajectories constitutes the strongest evidence that drifters were not simply responding to local winds. Table 2.4 shows that 10-15 drifters were sometimes active simultaneously. The separation scale of the drifters is two orders of magnitude smaller than the scale of wind field variability, yet the tracks seen in Fig. 3.13 are (with some exceptions) markedly different. For most of the 1995 deployments, winds were less than 8 m s^{-1} (see Fig. 3.7) and variable in direction. It is unlikely that light, variable winds could produce the coherence in drifter tracks seen in Fig. 3.17. Table 3.1 presents results of correlations between the fluctuations of components of daily mean wind and drifter velocity, $<U-\overline{U}, W-\overline{W}>$. Overbars denote averages for the deployment, the durations of which are given in Table 3.1. Correlation coefficients are given for zonal and meridional drifter velocities lagging the mean winds by 24 h (although there were negligible differences for lags of 0 h and 48 h).

Significant correlations for both velocity components were obtained in only three cases where wind forcing was, in any case, expected to be important: a3911 where the drogue was lost and the drifter exited through the North Channel, a6372 which was not entrained into the gyre and a17819 whose damaged drogue line became shortened. It is reasonable to conclude that both component velocities will correlate significantly where local wind dominates the dynamics (such as surface flows or flows outside the gyre region). Since such dual correlations did not occur for the other drifters we can be confident that local wind forcing was not responsible for the drifter trajectories. This reinforces the difference between surface residual flows and those at the thermocline, in this region. In many cases, one velocity component correlates significanly showing that wind stress can affect the motion in a statistically significant way without being the primary dynamical influence. These single component correlations are more frequent amongst the May and June releases.

Table 3.1 Correlation coefficients, ρ_u and ρ_v, between fluctuations of daily mean wind and drifter velocity components. Correlation coefficients relate to zonal and meridional velocity components lagging the wind by 24 h and were determined between the days shown below. n-2 is the degrees of freedom and the 5% and 1% significance points are shown. An asterisk in the final column denotes significant correlations for both components at the 5% level.

Drifter ID	Deployment Duration	ρ_u	ρ_v	n-2	5%	1%	
a24017	125-135	0.17	0.35	9	0.60	0.73	
a24021	127-137	-0.32	0.35	9	0.60	0.73	
a3940	127-143	0.06	0.29	15	0.48	0.61	
a3947	126-150	0.44	0.19	23	0.40	0.50	
a6372	125-150	0.49	0.57	24	0.39	0.50	*
a3911	125-151	0.56	0.62	25	0.38	0.49	*
a3914	126-156	0.21	0.47	29	0.35	0.46	
a24056	127-150	0.27	0.49	22	0.40	0.52	
a24057	127-152	-0.20	0.53	24	0.39	0.50	
a3945	126-163	0.36	-0.03	36	0.33	0.42	
a24055	126-163	0.17	0.69	36	0.33	0.42	
a24020	127-164	-0.23	0.39	36	0.33	0.42	
a17818	137-151	0.19	0.74	13	0.51	0.64	
a17830	137-156	0.14	0.61	18	0.44	0.56	
a17812	137-163	0.37	0.33	25	0.38	0.49	
a17823	140-164	-0.07	0.50	23	0.40	0.50	
a17804	151-171	0.64	-0.41	19	0.43	0.55	
a17805	151-181	0.36	-0.02	29	0.36	0.46	
b6372	151-170	0.13	0.76	18	0.44	0.56	
b24055	173-205	-0.13	-0.40	31	0.35	0.45	
b17823	173-207	0.04	0.26	33	0.33	0.42	
b17804	173-227	0.16	0.37	53	0.27	0.35	
b17812	200-212	0.30	0.42	11	0.55	0.68	
b17829	201-212	0.48	0.27	10	0.58	0.71	
b17830	199-212	0.25	-0.66	12	0.53	0.66	
b17806	200-214	0.14	0.26	13	0.51	0.64	
b17818	200-222	0.41	0.32	21	0.41	0.53	
b24020	200-221	-0.12	-0.24	20	0.42	0.54	
b17807	200-227	0.24	-0.14	26	0.37	0.48	
b17819	201-226	0.59	0.46	24	0.39	0.50	*
b17831	201-227	0.38	-0.36	25	0.38	0.49	
c17814	206-214	0.76	-0.30	7	0.67	0.80	
c17823	207-220	-0.54	-0.11	12	0.53	0.66	
b17817	206-227	-0.07	0.68	20	0.42	0.54	
b17802	207-228	-0.35	-0.21	20	0.42	0.54	

Obviously, this reflects the stronger winds then but it is also possible that the well-developed thermocline in July and August may 'shield' flow at the drogue depth from the direct influence of the wind (i.e. flow at this level is decoupled from the surface layer). Further evidence that the regional circulation is not wind-driven is provided by an analysis of individual tracks: drifters moving northeastwards along the western Irish Sea front (b24055, b17802, b17804 and c17823) did so continuously despite opposing winds and at very different times in the observations whilst drifter b24055 moved to the west, across the North Channel, in the face of an easterly wind component.

The remaining forcing mechanism to account for the observed circulation is the baroclinicity of the density field. It has already been shown (Fig. 3.17) that the spatial pattern of horizontal density gradients agrees well with drifter tracks. Geostrophic calculations were performed to assess whether the magnitude of the observed residual flows is consistent with baroclinic forcing. Horizontal density gradients from observations were used in the thermal wind equation (equation 1.2) which was integrated vertically subject to a condition of zero velocity at the bed. Fig. 3.19 shows the calculated geostrophic velocity component normal to line F for PM5/95 (solid lines denote flow into the page, dotted lines show flow out of the page). The predicted geostrophic flow is concentrated in two narrow (~10 km wide), jet-like cores either side of the dense pool and centred just below the thermocline, consistent with the drogue depth of 24 m. These jets are located immediately above the strongest gradients of density near the bed. The predicted flow speeds are lower than the maximum along-front speeds observed in Fig. 3.18 but it should be remembered that hydrographic sections were not necessarily perpendicular to the maximum density gradients. The solid circles in Fig. 3.19 indicate the site of 'simultaneous' drifter crossings where comparisons were made with the meridional components of their residual velocities. Such comparisons were carried out for all drifters crossing a transverse section where observations were made and

simultaneous is taken to mean during the same cruise period. The results are given in Table 3.2 (positive velocities denote northward flow).

Table 3.2 Comparison of meridional components of residual velocity from drifter trajectories with geostrophic estimates based on contemporaneous cruise hydrography and calculated from the thermal wind equation. Positive velocities denote northward flow.

Drifter ID	Year day 1995	Line Crossed	Longitude of crossing (°W)	Drifter velocity (± 1 cms^{-1})	Geostrophic velocity (± 1 cms^{-1})
PM1/95 (Day 150-153)					
a24057	152	C	5.00	-7	-4
a24020	152	C	5.56	-7	1
a3914	150	E	5.17	8	1
a3945	153	E	5.47	6	2
a17830	150	E	4.87	-4	0
b6372	153	E	5.82	-3	-2
PM3/95 (Day 171-173)					
a17804	171	B	4.70	3	-1
PM4/95 (Day 198-202)					
b24055	200	B	5.37	-4	-4
b17804	198	D	5.15	5	8
PM5/95 (Day 205-208)					
b17806	206	F	5.55	-3	-4
b17807	205	F	5 50	-1	-4
b17819	205	F	5.34	10	8
b24020	205	G	5.80	-7	-4
b17802	208	G	5.47	1	2
PM6/95 (Day 226-231)					
b17802	226	A	5.00	11	11
b17804	226	F	5.78	-10	-9
b17817	226	F	5.32	8	9
b17807	226	G	5.41	16	15
b17819	226	G	5.74	-3	-3

Such comparisons can only be used in a qualitative way because of uncertainties concerning a reference level for geostrophic flow, the fact that hydrographic observations and drifter crossings were not truly simultaneous and that observations

do not represent an average for the density field over the same period that the drifter speeds were calculated. Nevertheless, the results in Table 3.2 serve to convince that the magnitudes of the observed flows are consistent with baroclinic forcing, particularly from cruise PM4/95 onwards (July/August) where agreement with geostrophic estimates is within 11%.

It is possible to manipulate the drifter residual velocities to propose a map of the regional circulation. Velocities obtained from the tidally filtered tracks were grouped into two ensembles according to their time of release. The velocity components were then assigned to a grid of 1/15° of latitude by 1/10° of longitude (equivalent to four cells of the numerical model discussed later) and averaged. In order to obtain sufficient spatial coverage it is necessary that the time period to which the resulting circulations apply be rather broad. Fig. 3.20a shows the residual velocity field (from 3300 values) for May/June, derived from the first 18 drifters shown in Fig. 3.13 and Fig 3.20b shows the velocity field (from 2551 values) based on the July/August drifters in Fig.3.13 and the three deep-drogued drifters from July 1996. It would have been desirable to have had more drifters pass through each cell in order to arrive at these pseudo-Eulerian circulation maps but they nevertheless provide a useful qualitative and quantitative description of the observed residual velocities. The strength of residual flow in different parts of the region can now be visualised, and the observed velocities can be compared with results from the numerical model described in the following chapters.

3.3 Discussion of observations

The observations described here constitute the first comprehensive seasonal spatial coverage of hydrographic properties in the western Irish Sea and chart the development of the three-dimensional density field from spring to autumn. In the spring and early summer (April until early June), freshwater input along the Irish coast has a strong influence on the regional circulation. Wedge-shaped isohalines

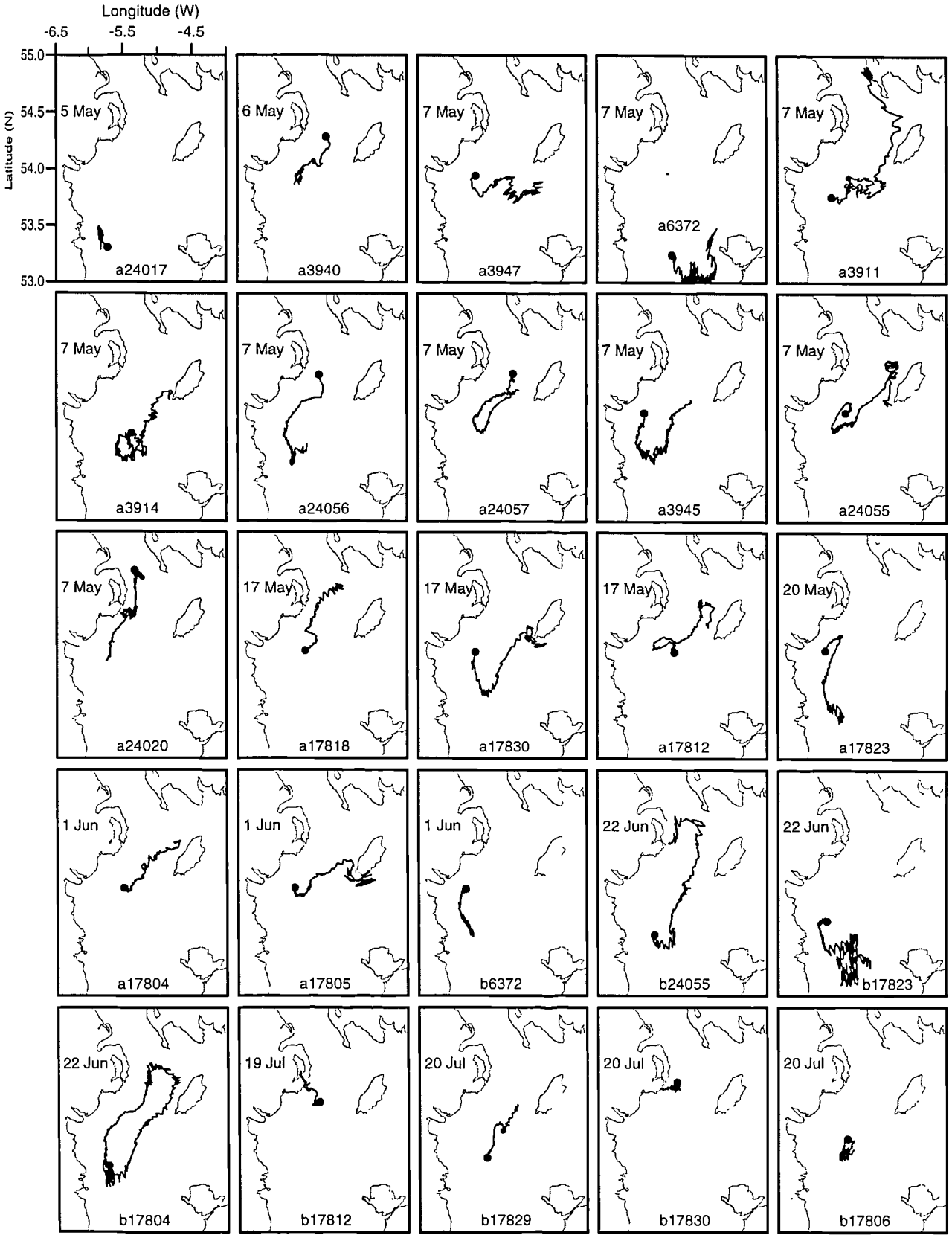

Fig. 3.13 Argos drifter tracks (unfiltered) of more than 3 days duration for 1995. Panels are in chronological order of release date which is shown in the top left corner (see also Table 2.4). Solid circles denote the release positions. Sequence is continued on the next page.

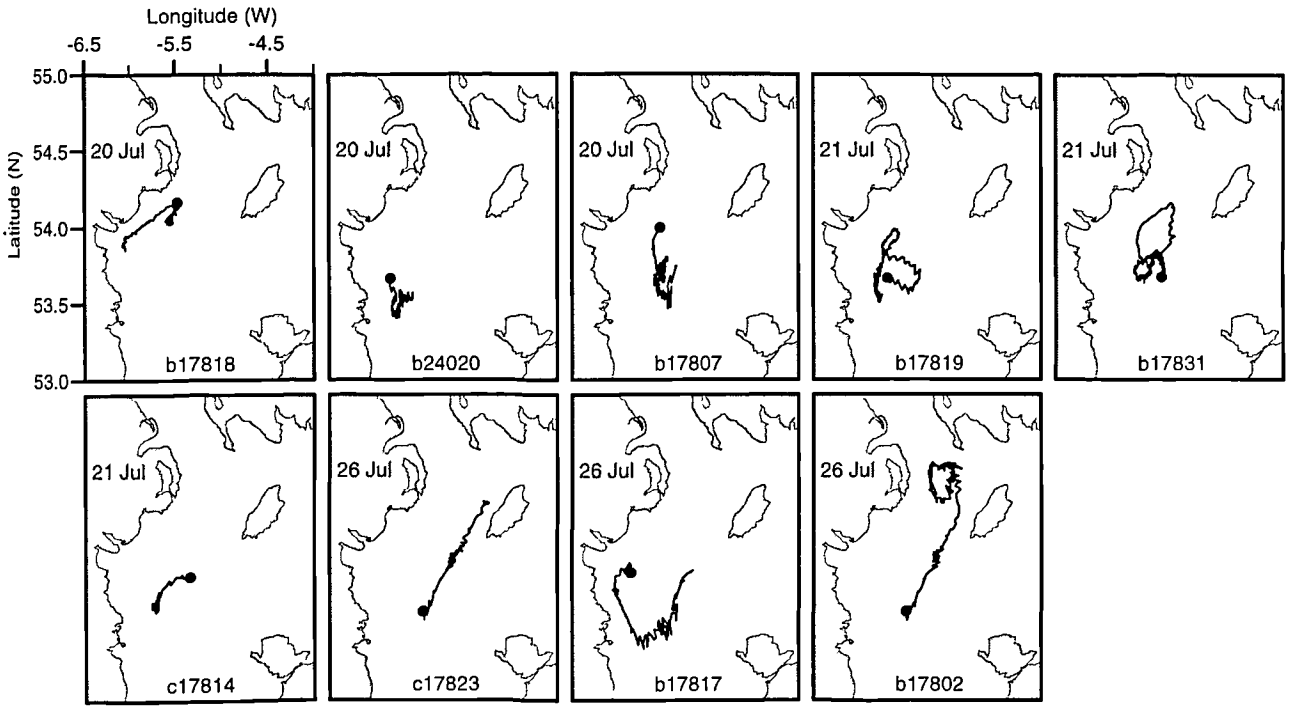

Fig. 3.13 (continued from previous page). Argos drifter tracks from 1995 deployments (see Table 2.4 for deployment details).

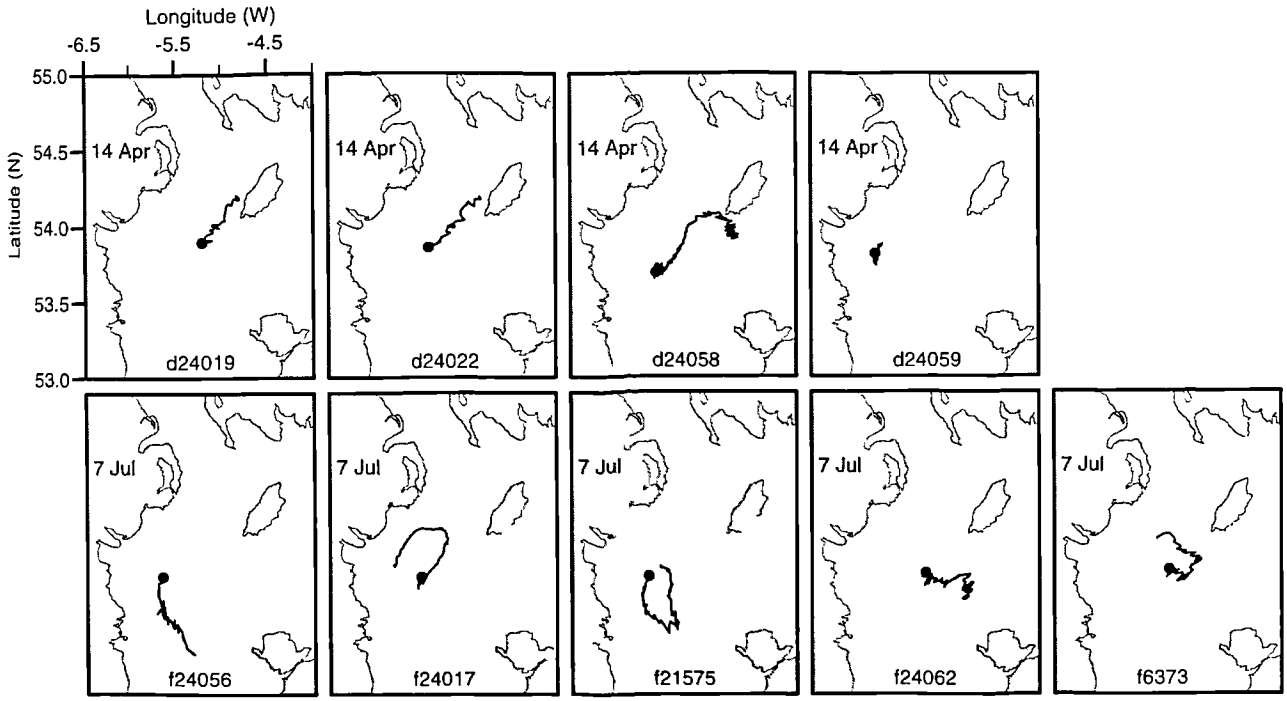

Fig. 3.14 Argos drifter tracks (unfiltered) from 1996 (see Table 2.5 for deployment details). Solid circles denote release positions. Buoys f24056 and f24062 were drogued at 8.5m depth.

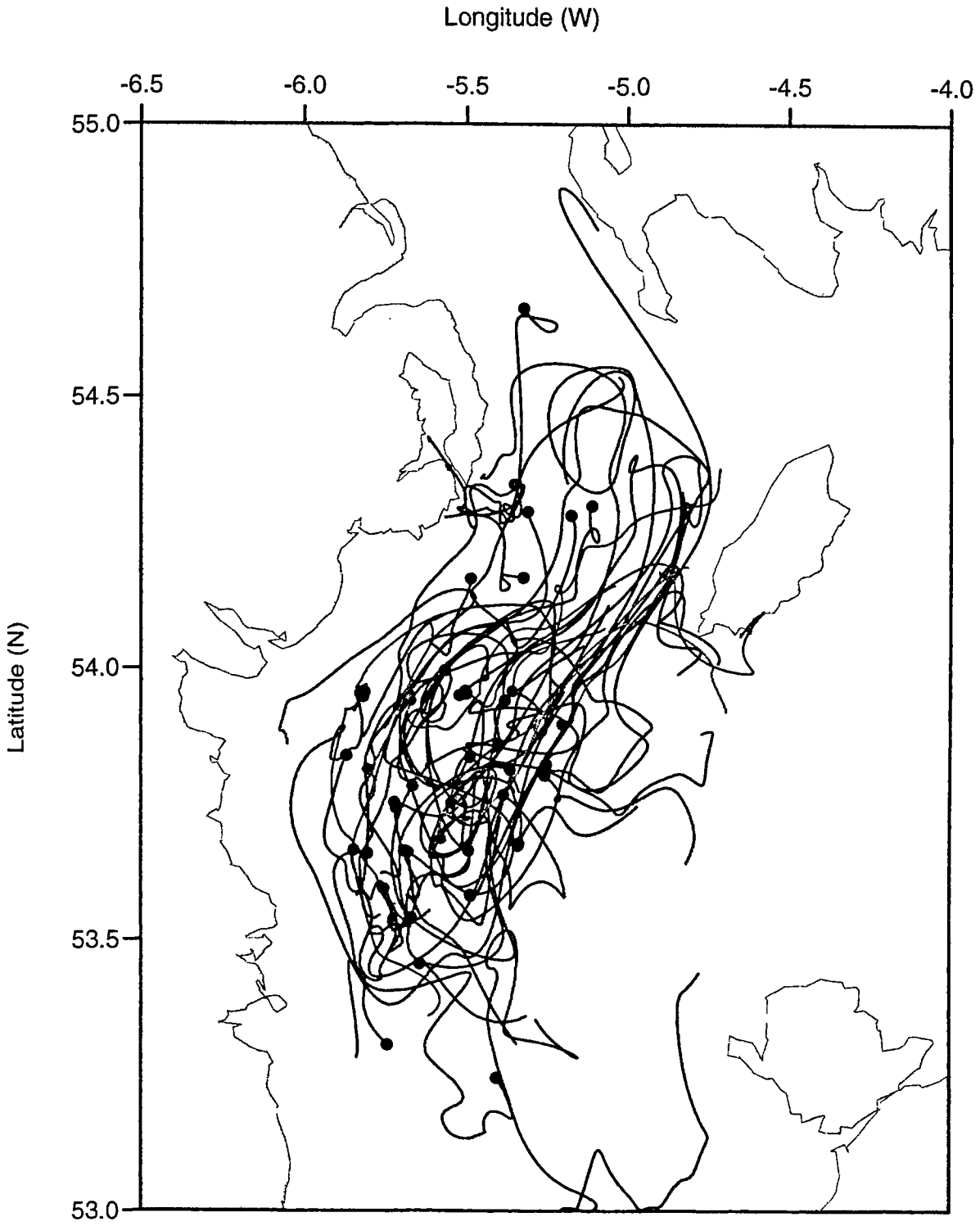

Fig. 3.15 Spaghetti diagram of all Argos drifter trajectories from 1995 and 1996. The tracks have been lowpass filtered to remove tidal fluctuations and are colour coded by month (orange=April, red=May, green=June, blue=July, black=August). Solid circles denote release positions.

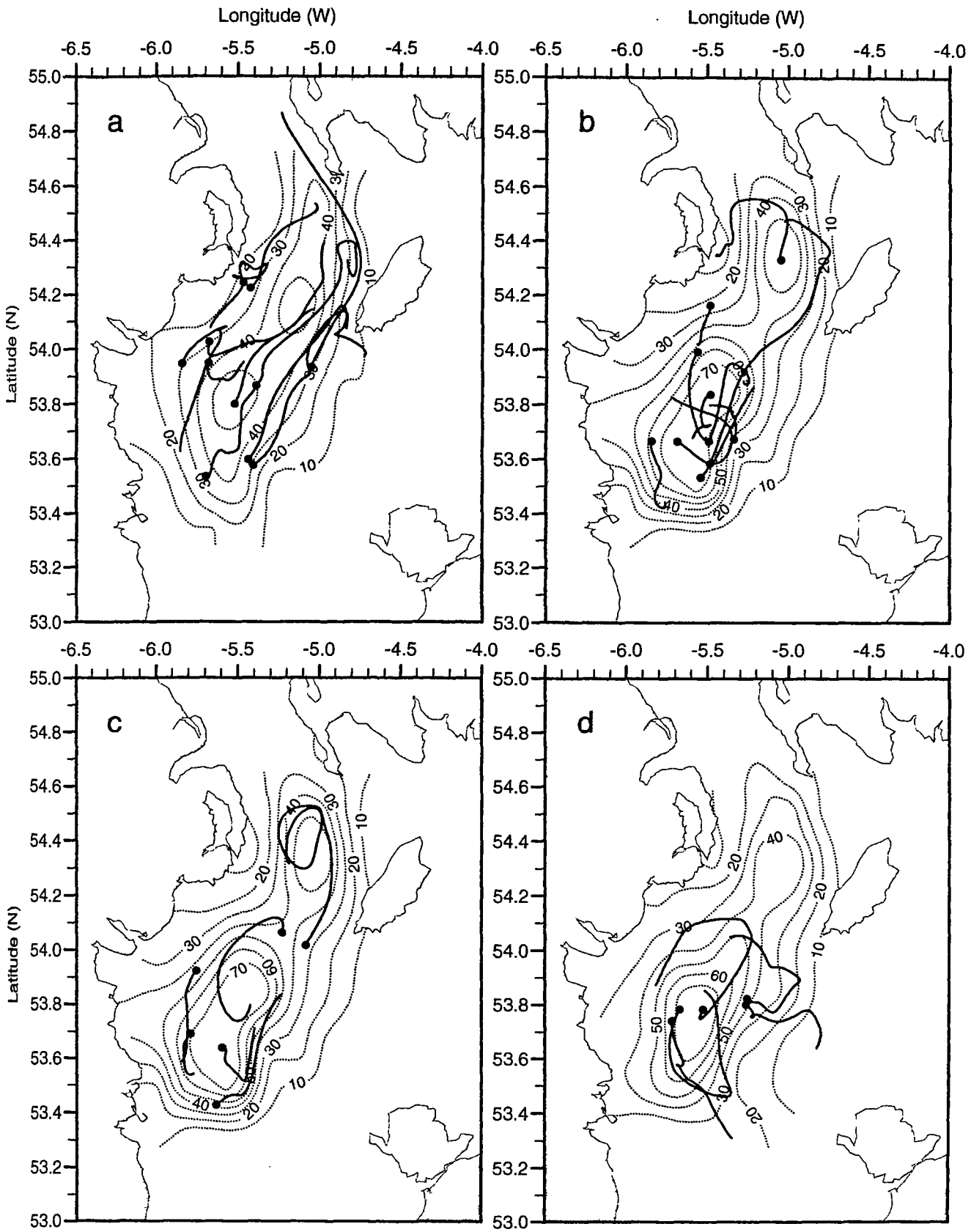

Fig. 3.16 Dotted lines contours of potential energy anomaly (J m^{-3}). Red lines are segments of tidally filtered drifter tracks contemporaneous to within 5 days either side of the cruise: (a) PM1/95 with drifter segments, days 145-158. (b) PM4/95 with segments, days 193-207. (c) PM6/95 with segments, days 220-235. (d) PM1/96 with segments, days 198-212. The red dots shows the beginning of each track segment.

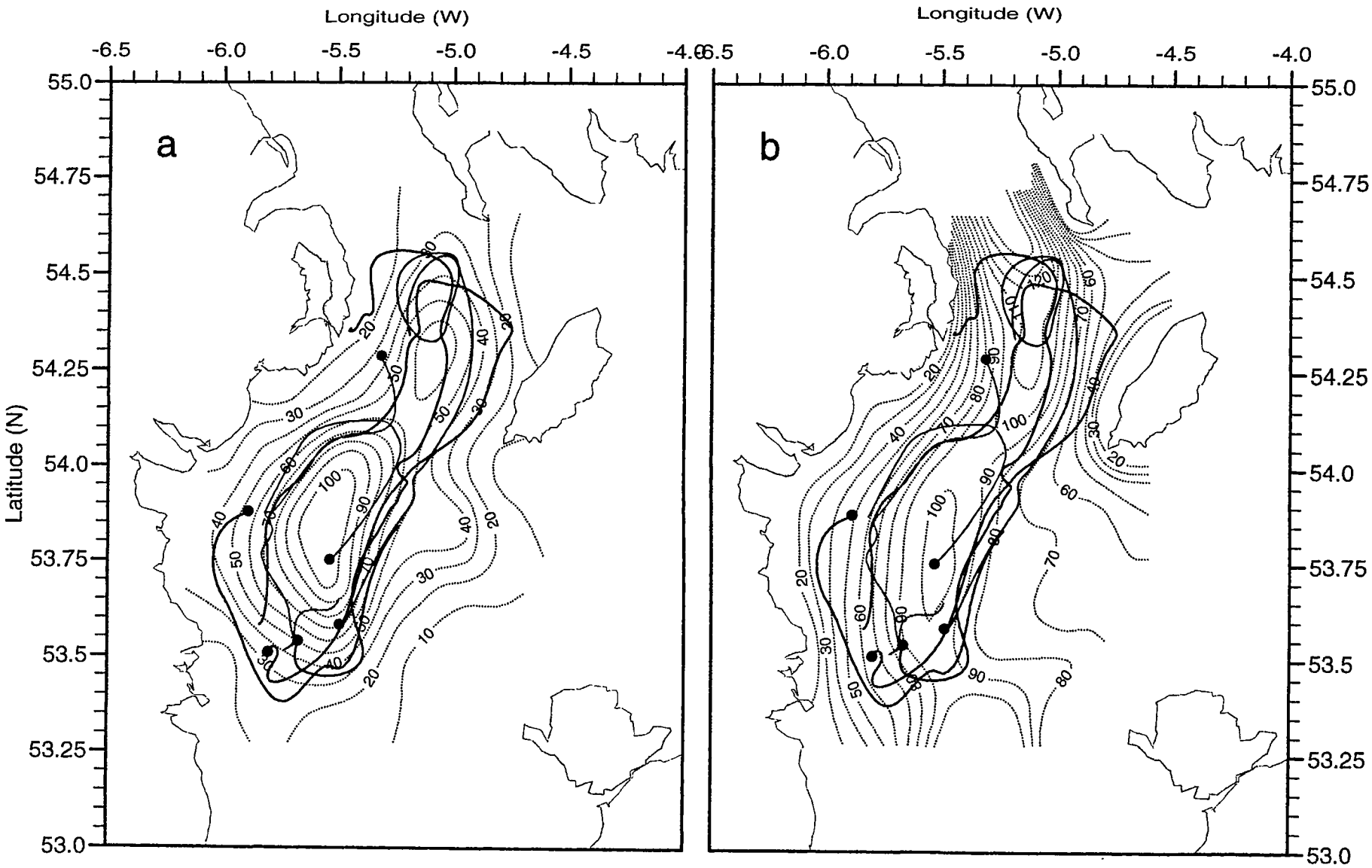

Fig. 3.17 Lowpass filtered tracks of six Argos drifters chosen to define the extent of the gyre and the possible recirculations (see text for drifter numbers and deployment details) overlayed on (a) the spatial distribution of potential energy anomaly (contours in Jm^{-3}) from cruise PM4/95 hydrographic data and (b) regional bathymetry (contours in m).

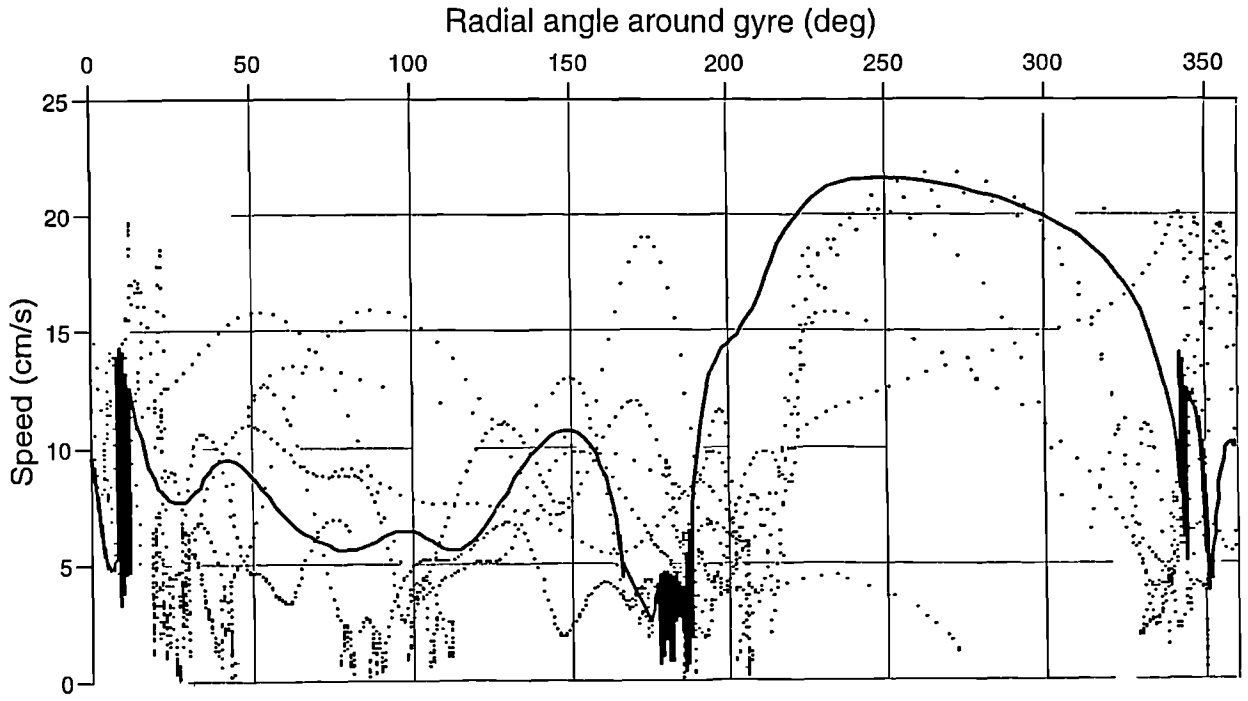

Fig. 3.18 Along-track speeds (cm s^{-1}) expressed as a function of radial angle around an idealised gyre whose axis is directed towards 30°T and whose centre is at station E5. The solid line shows the speed for drifter b17804 during its deployment and the scattered values are speeds from 13 other recirculating drifters.

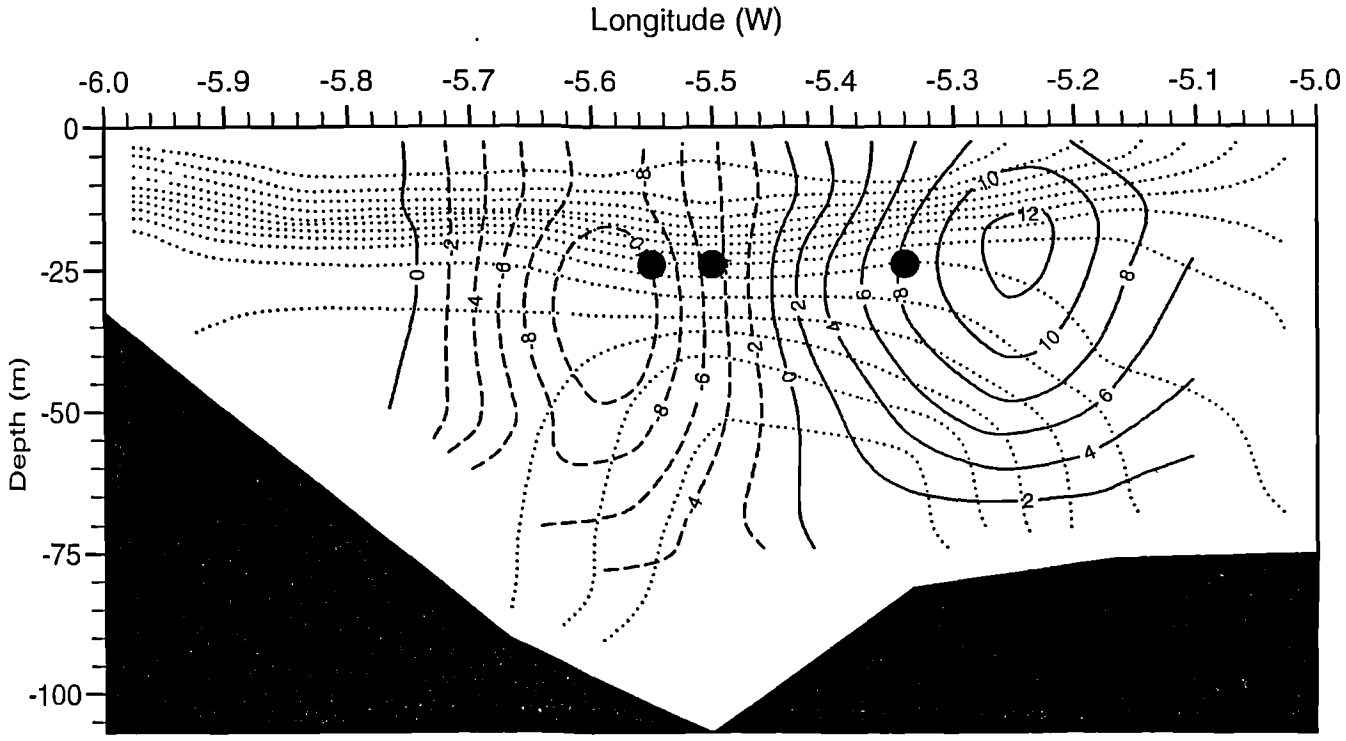

Fig. 3.19 Meridional geostrophic velocity (cm s^{-1}) calculated for line F (latitude 53° 40'N) during cruise PM5/95. Solid isopleths represent flow into the page, dashed contours indicate flow out of the page. The dotted lines shows the density field (σ_t) from which the calculations were made (see Fig. 3.9e). The solid circles indicate positions where drifters cross the transverse section during the cruise.

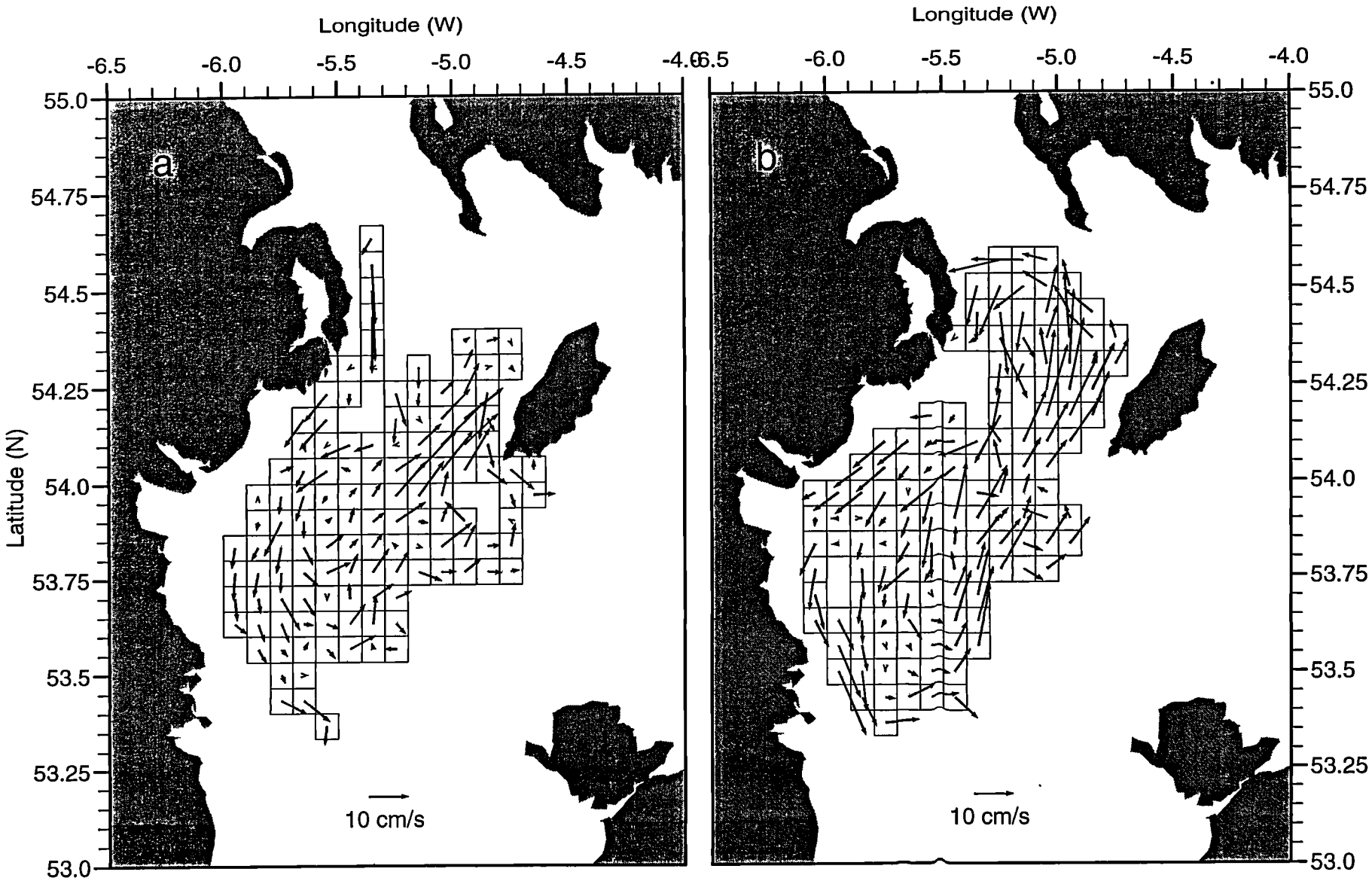

Fig. 3.20 Mean Lagrangian residual velocity vectors obtained from lowpass filtered drifter tracks, gridded on to 1/15° latitude by 1/10° longitude cells for (a) May/June ensemble of 18 drifters and (b) July/August ensemble of 16 drifters.

provide horizontal density gradients consistent with southward geostrophic flow and several of the drifter releases during this period exhibited southward movement along the coast of Ireland. The significant contribution of salinity to the vertical density structure (Fig. 3.4) until late May is consistent with previous findings (Gowen *et al.*, 1995) that salinity in May is responsible for up to 50% of the stratification. An important consequence of this haline stratification is to pre-condition the water column such that thermal input can more readily continue the stratification process. The pre-existing haline stratification suppresses vertical turbulent mixing and therefore heat input is immediately restricted to a surface layer causing accelerated thermal stratification. As the heating season progresses, temperature replaces salinity as the most significant influence on density. In the fully developed summer regime, from late June until September, density is primarily controlled by temperature, as it continues to be (weakly) in the final breakdown phase from late September until stratification is eroded at the end of October.

Observed vertical and horizontal differences of temperature were consistent with previous one- and two-dimensional seasonal studies of the area (Lavin-Peregrina, 1984; Durazo-Arvizu, 1993). The development of thermal stratification at E4 (Fig. 3.8) agrees well with the time series from a similar station in 1981 (Lavin-Peregrina, 1984) where surface temperatures rose from 8 °C in April at 0.045 °C d^{-1} to a maximum of 15 °C in late August, whilst bed temperatures rose at the lower rate of 0.037 °C d^{-1}. In 1995, an isolated pool of cold (~9 °C) bottom water was first seen in the early June observations, prior to which the bottom water in the area was indistinguishable from that of the southern part of the North Channel. By July, vertical stratification extended as far as the North Channel and recirculation was seen as far north as 54° 30'N in a number of drifter trajectories (e.g. b24055, b17804, c6374). Contours of surface temperature from several of the cruises (reinforced by the track of drifter a24020) suggested the possibility of a southward flow of water along the western side of the North Channel. Brown and Gmitrowicz (1995)

described a consistent northwards flow of approximately 10 cm s^{-1} on the eastern side of the North Channel with a weaker flow (~ 2 cm s^{-1}) to the south of Belfast Lough (at 54° 40'N) on the western side of the channel. Three drifters (a24021, c21578 and the drogueless a3911) lend support to the northward flow on the eastern side of the channel and the track of a24020 was consistent with southward flow in the western part of the channel below 54° 40'N. These results do not necessarily imply an exchange through the North Channel from the Malin shelf, rather it is likely they show that the recirculation extends into the southern part of the North Channel.

In the summer regime, drifter speeds of up to 20 cm s^{-1} on the eastern flank of the gyre and of typically 9 cm s^{-1} on the western flank were consistent with more limited drifter measurements from previous years (Hill *et al.*, 1997a). The extent of the gyre is shown clearly by the composite picture of drifter trajectories (Fig. 3.15), which also indicates the level of retention of the system, with only 7 from 43 tracks (16%) escaping the gyre. Drifter speeds showed that the non-tidal currents were in reasonable agreement with geostrophic calculations based on the observed density field, with better agreement in July and August. The drifter releases also provided the first direct observational evidence of an along-front jet in the western Irish Sea with typical speeds of 20 cm s^{-1}. Lagrangian techniques thus overcome many of the difficulties associated with observing such jets (Hill *et al.*, 1993). The jet is concentrated in a narrow (~10 km) core and is located above the strongest near-bed density gradients at a depth consistent with the base of the thermocline. A similar jet-like flow has been recently observed in the Celtic Sea (Horsburgh *et al.*, 1998) where the core of the jet was again located above the strongest density gradients at the bottom of the Celtic Sea tidal mixing front. Hill *et al.* (1997b) have reported the recirculation of part of the Scottish coastal current around an intrusion of dense, saline Atlantic water in the Hebrides and Brown *et al.* (1999) have identified density-driven circulation paths in the North Sea. A feature common to all of these flows is the existence of strong density gradients near the sea bed. The western Irish

Sea gyre thus appears to be a special case of a general class of intense, organised, baroclinic flows around dense pools of bottom water in shelf seas.

A consistently observed feature was the appearance of two distinct maxima in stratification which are linked to the regional bathymetry (Fig. 3.17). Recirculation around either, or both, of these centres was observed in the drifter tracks. It is interesting to note that although several large, gyral circuits are revealed there is no evidence in the individual tracks of smaller scale eddies due to frontal instability. Such eddies and surface frontal meanders have been frequently identified elsewhere in satellite images (e.g. Simpson and Pingree, 1978). Assuming that surface eddies are a feature of the Irish Sea, the most likely explanation is that these disturbances are not felt at the drogue depth (24 m), although limitations in the Argos data means that eddies on the scale of an internal Rossby deformation radius (5-10 km in this region) are not fully resolved.

The drifters demonstrated high levels of retention inside the recirculation region which is also a known retention system for the planktonic larvae of the commercially important crustacean, *Nephrops norvegicus* (Hill *et al.*, 1996). *N. norvegicus* larvae hatch into the water column from late March onwards and spend approximately 50 days in the plankton, during which time they must be retained over a mud substrate if they are to subsequently survive (Nichols *et al.*, 1987). The critical period for larval retention is from March until June (Nichols *et al.*, 1987) and it is the prevailing circulation at that time (see Fig. 3.20a) that is of relevance to the distribution of *N. norvegicus* larvae. Drifter tracks showed the greatest tendency to depart the area to the south of the Isle of Man in May and June thus a better retention strategy for the species would be for larvae to hatch later in the year when recirculation is more pronounced. Presumably the compromise between retention and other factors (e.g. food availability, adult competition for burrows) favours an optimum, earlier larval release. The drifter retention statistics and the stagnant behaviour of drifters in the centre of the western Irish Sea indicate that the spring/early summer circulation is

sufficiently retentive to maintain a breeding population. The region is also an important spawning and nursery ground for several species of commercially important fin-fish (Dickey-Collas *et al.*, 1997). It is thought that juvenile fish are entrained into and then retained within the gyre. Characteristic residual velocities of the drifters were 10 cm s^{-1} which is of the same order as the tidal currents in this area, demonstrating the local importance of density-driven flow. These residual flows greatly exceed the speeds at which the juveniles of many species of pelagic fish are able to swim (Dickey-Collas *et al.*, 1997).

Gradients of temperature were generally stronger at the bed than at the surface and closed contours of bottom temperature existed along the western side of the area (despite the absence of a surface front) providing a density structure consistent with a southward geostrophic flow. The strongest bottom fronts were typically found some 10-20 km towards the cold pool relative to the surface manifestation of the western Irish Sea front. Evidence exists to suggest that bottom fronts are far more stable than their surface counterparts which are prone to baroclinic instabilities (Griffiths and Linden, 1982) and can also be affected significantly by the wind (Simpson and Bowers, 1981; Lavin-Peregrina, 1984; Wang *et al.*, 1990). Bed friction and topography have been found to suppress eddy formation in numerical models (James, 1984; James, 1989) and growth rates of instabilities on a two-layer front are reduced by bottom slopes (Flagg and Beardsley, 1978). Observations in the North Sea (van Aken *et al.*, 1987; Brown *et al.*, 1999) and in the Irish Sea (Allen, 1979; Lavin-Peregrina, 1984; Hill *et al.*, 1994) confirm that surface fronts are usually less pronounced than bottom fronts in shelf seas. The dynamical significance of bottom fronts explains why the gyre was not predicted sooner by maps of h/u^3 (Simpson and Hunter, 1974) which only predicts the transition from vertically mixed to stratified water. As Fig. 3.9 shows, stratification near the Irish coast does not preclude the existence of the near-bed fronts required for baroclinic flow. Furthermore, since it is the relatively stable bottom fronts that are dynamically

important, the cold pool and associated cyclonic circulation is able to persist throughout October.

Two-dimensional models (e.g. Garrett and Loder, 1981) of frontal systems predict weak (< 5 cm s^{-1}) cross-frontal secondary circulations with implications for biota. Cross-frontal advection of relatively nutrient-rich waters from the cold pool would have consequences for the succession of phytoplankton species throughout the summer. Any nutrient reservoir within the dome would also be important to phytoplankton at the pycnocline and may act as a source for a secondary, autumnal bloom when stratification breaks down. Cross-frontal flow causes a relaxation of isopycnals and therefore a decrease in potential energy. In the absence of restorative mechanisms, the dome should simply collapse. However, the potential energy of the system *is* replenished because tidal mixing ensures that the well-mixed water flanking the dense pool warms at a comparable, or greater, rate to the cold relict water. In terms of a particular isopycnal, cross-frontal fluxes act to make it horizontal whilst mixing due to tide and wind (to a lesser extent) tend to make it vertical. The gyre is maintained so long as the density gradients persist near the bed. Previous observations (Lavin-Peregrina, 1984) and model studies (James, 1978) show that density gradients at the bed exceed those near the surface once stratification is well established.

These observations show that horizontal density differences near the bed did not diminish despite a gradual warming of the cold pool and that the gradients were maintained even when surface cooling and stronger winds eroded the surface structure. On the eastern flank of the cold pool, the rapid spatial change in tidal mixing energy is sufficient to maintain these sharp gradients. At the western end of the same sections, however, the tidal streams are at their weakest. The bottom fronts here may be maintained partly by depth variations controlling h/u^3 (Simpson and Hunter, 1974) but another candidate mechanism (Chapman and Lentz, 1994) is the downslope advection of density due to Ekman transport in the bottom boundary layer

beneath a southwards barotropic flow along the Irish coast. By this mechanism isopycnals can be moved downslope and initially weak density anomalies can be intensified into bottom frontal gradients in the absence of any surface front. In early spring, weak southward (barotropic) coastal flows may pre-condition the density field by advecting fresh water downslope to form the observed horizontal density gradients (due to salinity) in April and May. The same mechanism could provide a means of entraining into the gyre larvae and fish fry that are known to be hatched along the coast of Ireland but which are retained in the centre of the western Irish Sea in later months (Dickey-Collas *et al.*, 1997). The existence of such a boundary layer flow obviously requires further investigation, but the geography of the region is amenable to its operation (freshwater input, coastal boundary, weak tides) and the density fields observed are consistent with its outcome.

In the autumnal breakdown of stratification, strong winds are obviously important and breaking internal waves (Lavin-Peregrina and Sherwin, 1985) may also contribute to increased mixing. The observations showed the cold pool to persist until 5 October in 1995 but by 31 October the water column was vertically mixed at all stations sampled. The persistence of the cold pool suggests that its decay is not immediate following the autumnal equinox. The deepest water in the centre of the dense pool is below the maximum depth of wind influence and it is likely that convective cooling and overturning is a necessary ingredient for the complete breakdown of the dense pool. Wind events can actually lead to an increase in the temperature gradient at bottom fronts in some circumstances. It is well known that wind-driven advection of well-mixed waters over warmer stratified water can lead to convective instability and the erosion of surface fronts (e.g. Wang *et al.*, 1990). Conversely, if the wind advects the warmest water above the thermocline in the stratified region into the well-mixed regime then tidal stirring will rapidly distribute the heat vertically throughout the water column; the well-mixed water can warm appreciably whilst the cold pool temperature remains constant and stronger gradients

are obtained near the bed. In the autumn this could cause a final intensification of near-bed density gradients and a short-lived increase in the density-driven flow.

Chapter 4. Numerical Modelling

4.1 Numerical models of the Irish Sea

The Irish Sea has been the focus of considerable modelling effort in recent years although primitive equation, density-advecting numerical models have not been applied in the area until now. Davies and Aldridge (1993) examined the sensitivity of computed M_2 tidal elevation and currents in the Irish Sea and found root mean squared (r.m.s.) accuracies of 7.8 cm for elevation amplitude and 4° for phase, although currents were overestimated (by up to 20 cm s^{-1}). The overprediction of tidal currents could be corrected by careful prescription of frictional parameters (i.e. bed friction and eddy viscosity profile). Davies and Jones (1992) modelled the wind-driven circulation of the Celtic and Irish Seas in response to a major wind event (storm surge) and found surge elevations to be in reasonable agreement with observations from coastal gauges. Wind-induced surface residual currents of 25-50 cm s^{-1} were obtained (Davies and Lawrence, 1994a) in response to a steady, spatially uniform wind-stress of 1 N m^{-2} (with a weaker counterflow near the bed). The imposed wind stress of 1 N m^{-2} (assuming a simple quadratic law for wind stress, $\tau = 0.0018\ W^2$) corresponds to a wind speed, W, of 24 m s^{-1} (or Beaufort Force 9). Winds of this magnitude occur mostly during autumn and winter and it is then that the wind-driven flow fields are probably most significant. None of the imposed wind forcings produced a cyclonic flow pattern in the western Irish Sea. Neither does tidal rectification account for the observed summertime circulation. Davies and Lawrence (1994b) found that non-linear advective terms influenced the local generation of the M_4 tide around Anglesey and in the shallow eastern Irish Sea. The generation of M_4 in the western Irish Sea is negligible. Fine resolution barotropic models (Proctor, 1981; Davies and Aldridge, 1993; Davies and Lawrence, 1994b) do not predict the residual currents that make up the western Irish Sea gyre, a fact which supports a baroclinic interpretation of the feature.

The first attempt to include density-driven flow in a numerical model of the Irish Sea (Heaps and Jones, 1977) predicted currents of only 1-2 cm s^{-1} and did not correctly reproduce density-driven flows in the western Irish Sea. However, the imposed density field was based on limited observations from September and October (i.e. did not contain the sharp temperature gradients that obtain in the summer) and was not permitted to evolve. Furthermore, the coarse model grid used (14 km) would have been unable to maintain the sharp frontal gradients necessary to produce significant currents.

A three-dimensional, diagnostic model (Hill *et al.*,1996; Hill *et al.*, 1997a) was the first to reproduce the gyre. It was based on a series of local, one-dimensional, heating-stirring models (Simpson and Bowers, 1984) which evolved the seasonal density field. A climatic, sinusoidal heating term (James, 1977) determined the surface heat flux. Once the density field was updated, an elliptic equation in surface elevation was solved (Hukuda *et al*, 1989) to give a dynamically consistent flow field. The model showed how the observed density-driven circulation can be accounted for by the density field which results from a local balance between heating and stirring. Surface currents and the distribution of stratification from the model were shown to be in good agreement with previous observations (Hill *et al.*,1996; Hill *et al.*, 1997a).

4.2 Diagnostic models

Diagnostic models use a prescription (usually from observations) of the density field to deduce the baroclinic pressure gradient, from which velocities can be calculated. These models provide a computationally efficient way to infer the long-term shelf circulation from hydrographic measurements. Greatbatch and Goulding (1992) used a diagnostic model, coupled to a prognostic model for temperature and salinity, to examine the variability of circulation on the Newfoundland and Labrador shelf. Tang *et al.* (1996) used a climatic density field to examine aspects of the circulation of the same area, including the three-dimensional current structure and mesoscale

features due to the joint effect of baroclinicity and relief (JEBAR - see, for example, Huthnance, 1984). The present generation of diagnostic models includes vertical mixing, turbulence closure schemes (Ezer and Mellor, 1994), and accomodates a variety of boundary conditions (Dowd, 1998). Finite elements are used by Lynch *et al.* (1992) to resolve complex topography. However, diagnostic models are known to be sensitive to misalignments of gradients of density over steep topography (Sheng and Thompson, 1996) and can produce unphysical noise in the velocities. Sheng and Thomson (1996) found that splitting the bottom density into to a mean and an anomaly produced a method that was robust to errors in the density field and avoided the need for three-dimensional gridding of scattered observations. An alternative approach (e.g. Ezer and Mellor, 1994), which recognises that the real density field contains variability unresolved by the observations, is to allow the adjustment of the density field using an ocean circulation model until a dynamic balance is achieved. Whilst the minimal physics diagnostic models provide computational speed and (often) physical insight, they do not advect or mix momentum and density, conserve angular momentum or evolve the flow field dynamically. Recent investigations (Dowd, 1998) point to the need to include an equation for density advection in coastal problems. These shortcomings are overcome by three-dimensional, primitive equation models which include a prognostic equation for density (or equations for temperature and salinity, where density is subsequently calculated from an equation of state). These models must be able to resolve and maintain sharp frontal gradients and should also resolve the Rossby radius of the first baroclinic mode (James, 1990) which is typically 5 km in the western Irish Sea. Computational efficiency is required since seasonal effects are of interest. A number of such "full physics" models have emerged (many as a result of decades of continual development) which have the numerical skill to model the complex dynamical processes that prevail in coastal regions.

4.3 Coastal ocean models

This section reviews briefly some of the models available for coastal oceanographic modelling. The hydrodynamical framework common to them all is described and major differences between them are highlighted. A more comprehensive review of coastal ocean models is given by Haidvogel and Beckmann (1998) and a description of techniques appropriate to the modelling of density-driven flow can be found in James (1990). The governing equations are the hydrostatic primitive equations (4.1 - 4.3) and the continuity equation where an assumption of incompressibility has been made (4.4). The three simplifying approximations are that the fluid is hydrostatic, incompressible and Boussinesq (i.e. density differences are neglected unless multiplied by gravity). An obvious limitation of all hydrostatic models is their inability to model non-hydrostatic processes (e.g. convective instability).

$$\frac{\partial u}{\partial t} + \mathbf{v}.\nabla u - fv = -\frac{1}{\rho_o}\frac{\partial p}{\partial x} + F_x \qquad (4.1)$$

$$\frac{\partial v}{\partial t} + \mathbf{v}.\nabla v + fu = -\frac{1}{\rho_o}\frac{\partial p}{\partial y} + F_y \qquad (4.2)$$

$$\frac{\partial p}{\partial z} = -\rho g \qquad (4.3)$$

$$\nabla.\mathbf{v} = 0 \qquad (4.4)$$

the equations are presented here in Cartesian form with x increasing eastwards, y increasing northwards and z increasing vertically upwards. Thus:

$(u, v, w) = (x, y, z)$ components of velocity vector $\mathbf{v}$

g = acceleration due to gravity

f = Coriolis parameter, $2\Omega\sin\phi$ where Ω is Earth's rotation rate, 7.29×10^{-5} s^{-1} and ϕ is latitude.

F = frictional and mixing terms

ρ_0 = reference density

Also required is a prognostic (or transport) equation for density,

$$\frac{\partial \rho'}{\partial t} + \mathbf{v}.\nabla\rho' = F_\rho \qquad (4.5)$$

where ρ' is the departure of density from a reference value, ρ_o, so that total density, $\rho = \rho_o\ (z) + \rho'\ (x, y, z, t)$. Alternatively, separate prognostic equations for temperature and salinity can be used (Blumberg and Mellor, 1987) and density is then diagnosed from an equation of state, $\rho = \rho\ (T, S)$.

The models discussed here differ in the way in which the hydrostatic equations (4.1 - 4.4) are discretised in space and time, and in their choice of numerical algorithms and methods for parameterising sub-grid scale processes. Table 4.1 lists some of the better known coastal ocean models along with their key features (for a more complete list see Haidvogel and Beckmann, 1998). Most of the models in Table 4.1 adopt finite difference techniques to solve the discretised form of equations 4.1 - 4.5. The finite element model (QUODDY) of Lynch *et al.* (1996) is the exception to this. Finite element models offer the use of unstructured, non-uniform computational grids which allow high resolution where required (e.g. good resolution of irregular coastlines). Lynch *et al.* (1997) demonstrated the global and local performance of their model with application to the circulation in the Gulf of Maine.

For stability, and second-order spatial accuracy, finite difference models adopt a horizontal staggering of prognostic variables on a grid, the most commonly used being the Arakawa C-grid (Arakawa and Lamb, 1977) which is shown in Fig. 4.1b. The boundary condition of zero flow normal to a solid boundary is easily satisfied on this grid. The C-grid can be applied to rectangular coordinates as in the HAMSOM model (Backhaus, 1985) or curvilinear coordinates as in the Princeton Ocean Model POM (Blumberg and Mellor, 1987) and the SPEM model (Haidvogel *et al.*, 1991). James (1987) used an Arakawa B-grid (see Fig. 4.1a) to avoid averaging four velocity points in the calculation of the Coriolis terms, which was found to seriously

Table 4.1 Numerical features of primitive equation coastal ocean models (adapted from Haidvogel and Beckmann, 1998)

Model	External Mode	Vertical Co-ord.	Hor.[1] Grid	Numerics $(x/z)^2$	Time[3] Stepping	Advection[4]	Reference
DieCAST	Rigid	z	RC	FD/FD	LF	C	Dietrich *et al.* (1987)
GFDLM	Rigid	z	RB	FD/FD	LF	C,U,FCT	Cox (1984)
GHERM	Free	σ	RC	FD/FD	SpE	TVD	Beckers (1991)
HAMSOM	Free	z	RC	FD/FD	SI	U	Backhaus (1985)
MICOM	Free	ρ	RC	FD/FD	SpE/LF	Sm	Bleck *et al.* (1992)
POL	Free	σ	RC RB	FD/FD	SpE	TVD PPM	Xing and Davies (1996) Proctor and James (1996)
POM	Free	σ	CC	FD/FD	SpE/LF	C,U,Sm	Blumberg & Mellor (1987)
QUODDY	Free	σ	UT	FE/FE	SI	G	Lynch *et al.* (1996)
SPEM	Rigid	σ	CC	FD/S	LF	C	Haidvogel *et al.* (1991)

Key: [1]RC/RB, rectangular C-grid/B-grid; CC, curvilinear C-grid; UT, unstructured triangles.
[2]FD, finite differences; FE, finite elements; S, functional spectral expansion.
[3]LF, leapfrog; SpE, split explicit; SI, semi-implicit.
[4]U, upstream; C, centred; FCT, flux corrected transport; Sm, Smolarkiewicz; TVD, total variation diminishing; PPM, piecewise parabolic method; G, Galerkin.

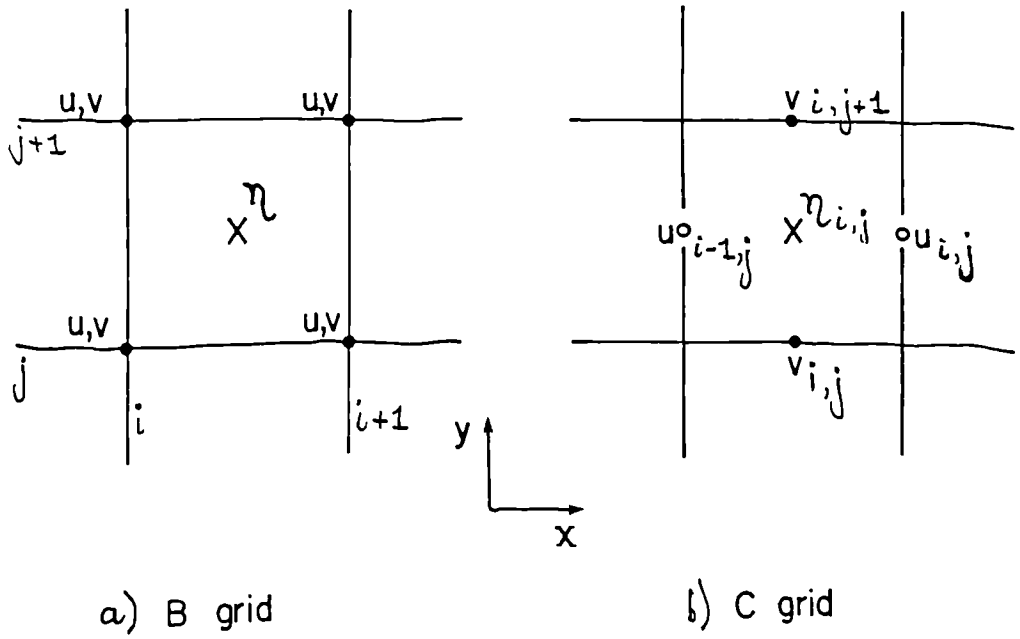

Fig. 4.1 Finite difference grids (a) Arakawa B-grid and (b) Arakawa C-grid (Arakawa and Lamb, 1977)

affect the model's ability to maintain a sharp front in near-geostrophic balance. The B-grid is also used by the well-established Geophysical Fluid Dynamics Laboratory Model GFDLM (Cox, 1984).

The simplest treatment of the vertical coordinate is to use levels of constant geopotential, or z-coordinates. The HAMSOM, DieCAST and GFDLM models (Table 4.1) all use fixed grids of variable layer thickness in the vertical. A difficulty with z-coordinates is that resolution is reduced in shallow regions as the number of grid boxes decreases. This problem can be overcome by the use of sigma-coordinates (Phillips, 1957; Freeman *et al.*, 1972) which convert the physical depth interval , $-h \leq z \leq \eta$, on to a constant domain, $a \leq \sigma \leq b$, through the transformation

$$\sigma = (b-a)\left(\frac{z-\eta}{h+\eta}\right) + b \qquad (4.6)$$

With $b = 0$, $a = 1$, the coordinate, σ, becomes relative depth with the domain zero to one. As Table 4.1 shows, σ-coordinates are widely used in coastal models and they ensure that an equal number of vertical grid boxes are present at each horizontal grid point. Difficulties can occur when topographic variations are of the same order as the water depth and care must be taken when resolving severe bottom topography. The sigma transformation causes horizontal gradients of depth and surface elevation to appear in the transformed differential operators which can result in numerical diffusion in the vertical grid and also errors in the baroclinic pressure gradient terms. Truncation errors in the pressure gradient term can be minimised by the use of high vertical resolution and by using the density anomaly (density minus a reference value) in computations (Haney, 1991). Grid scales must be chosen carefully as hydrostatic consistency (Haney, 1991) places constraints on the horizontal grid size for a given increment of sigma near steep topography. In a model of stratified tidal flow over banks, Chen and Beardsley (1995) estimated numerical errors to be of the order of 1% of the maximum residual current.

The MICOM model (Bleck *et al.*, 1992) aligns coordinate surfaces with isopycnals. Outside boundary layers, mixing largely takes place along isopycnal (isentropic) surfaces. Isopycnal coordinate models reduce spurious diapycnal mixing and they resolve density fronts in fewer layers than other models. However, difficulties arise where isopycnals intersect solid boundaries. An alternative to using a discrete number of vertical layers, or grid boxes, is to use an expansion of continuous functions, or spectral method to represent the vertical coordinate (for a review of spectral methods see Davies, 1987). A continuous current profile is obtained by expanding a set of coefficients (which vary horizontally and with time), and a set of vertical basis functions. In the SPEM model, Haidvogel *et al.* (1991) choose Chebyshev polynomials as the basis set, and use the appropriate vertical domain of, $-1 \leq \sigma \leq 1$. Many coastal problems require the prediction of sea surface elevation and therefore most of the models in Table 4.1 have a free surface. If surface gravity waves are not a necessary part of the simulation then the rigid lid approximation can be made with significant computational savings (in rigid lid models, the effect of sea surface elevation is replaced by pressure at the lid). If a free surface is retained then the size of the time-step for explicit methods is limited by the propagation speed of gravity waves. This leads to the well known CFL (Courant-Friedrichs-Lewy) condition (see, for instance, Roache, 1972):

$$\Delta t \leq \frac{\Delta x}{\sqrt{2gh_{\max}}} \tag{4.7}$$

where Δt is the time-step and Δx is the grid spacing (for a square grid) with $h_{\max}$ the maximum depth. It is possible to overcome the constraint of the CFL condition in two ways. In the first, termed 'mode splitting', the governing equations are split into depth-integrated (external mode) and vertical structure (baroclinic, or internal mode) parts. The external mode equations can be solved using a time step which satisfies the CFL condition and resolves gravity waves at the free surface whilst internal mode calculations are carried out using a much longer time step (which is a multiple of the

external mode time step). This approach is denoted, 'SpE', or 'split explicit' in Table 4.1 and is used by several of the models. The alternative approach (adopted by HAMSOM and also the version of POM used in this study) is to treat surface elevation and the horizontal divergence terms in the continuity equation implicitly in time, but to retain a large, explicit time step for the internal mode (this technique is denoted, 'SI', or 'semi-implicit' in Table 4.1). Implicit methods are unconditionally stable (Roache, 1972) but care must be taken not to choose so large a time step that desirable features of the solution (such as the tide) are unresolved or excessively smoothed. Furthermore, the use of a larger time step does not guarantee improved computational efficiency because implicit methods demand the iterative solution of an elliptical set of equations and, for large time steps, many iterations are often required for convergence.

Implicit schemes are also normally employed for the spatial discretisation of vertical diffusion terms in the internal mode solution, otherwise an explicit time step would be limited to:

$$\Delta t \leq \frac{(\Delta z)^2}{2K_M} \tag{4.8}$$

where Δz is the vertical grid length and K_M is the vertical eddy viscosity. Vertical implicit systems form a tridiagonal set which is solved by Gaussian elimination or the Thomas algorithm. To avoid discretisation errors arising when using the large time steps facilitated by semi-implicit methods, second-order approximation in time is usually achieved with so-called leapfrog schemes (see Roache, 1972; Kowaltik and Murty, 1993). Leapfrog time differencing requires the storage of variables at three time levels and is stable subject to the CFL condition but there is a tendency for solutions at alternate time levels to separate. This can be corrected with a weak time filter (Asselin, 1972) or by applying a first-order method every ten steps or so (Kowaltik and Murty, 1993).

In coastal oceanographic problems it is important to maintain sharp gradients of temperature (e.g. at fronts), salinity (e.g. for buoyant plumes) or passive tracer (e.g. suspended load). The choice of advection scheme is an important part of the numerical method since in shelf seas strong tidal advection can rapidly erode frontal features if excessive numerical diffusion is present. It is well known (see, for example, Kowaltik and Murty, 1993) that upwind advection schemes possess considerable numerical diffusion which can smooth fronts and concentration gradients unrealistically whereas second-order methods (e.g. Lax-Wendroff or centred differences) are not positive-definite and can introduce spurious concentrations as well as unphysical ripples at fronts. The variety of advection schemes listed in Table 4.1 is evidence of recent efforts to produce a monotonic, positive-definite scheme with low implicit diffusion (for a more comprehensive review of advection schemes see James, 1996). Many of the methods involve considerable computational overhead. The flux corrected transport (FCT) scheme (Boris and Book, 1976) and the total variation diminishing (TVD) method (Yang and Przekwas, 1992) are both hybrid schemes in which the advective flux is taken as the sum of contributions from a *first-order upwind and a second-order scheme.* The methods differ in how they determine the proportion contributed from each scheme. The TVD method uses limiter functions (Yang and Przekwas, 1992) of the concentration gradient to guarantee ripple-free behaviour near fronts. James (1996) has applied the TVD scheme and the piecewise parabolic method (PPM) of Colella and Woodward (1984) to oceanographic situations. The PPM approach has been used to model shock-wave discontinuities in gas dynamics (Colella and Woodward, 1984) and calculates volume-integrated fluxes across cell boundaries by constructing a parabolic variation of the advected variable within each grid box. In a model of North Sea stratification (Proctor and James, 1996) the PPM scheme performed better than TVD in terms of maintaining structure but required 30% more computational time. An alternative approach, used by MICOM and the version of POM used in this work (ECOMsi), is a scheme due to Smolarkiewicz (1983) in which an upwind scheme is recursively applied and numerical diffusion is corrected at each step using

an antidiffusion velocity based on the local, first-order truncation error. For large-scale ocean circulation models, Farrow and Stevens (1995) have adapted the quadratic upstream interpolation (QUICK) method of Leonard (1979). A final means of retaining accuracy in tracer fields is a semi-Lagrangian approach where the tracer transport equation is solved in a Lagrangian framework. This technique has been used by Dippner (1993) in a frontal-resolving model of the German Bight.

The remaining difference between the models listed in Table 4.1, and an important consideration in finite resolution models, is the way in which sub-grid-scale processes are parameterised. The parameterisation of mixing processes serves both to capture unresolved scales of motion and also to ensure stable and noise-free numerical solutions. The effect of turbulence on the mean flow gives rise to Reynolds stresses, the gradients of which produce acceleration in the same way as gradients of viscous stress. The friction term in equation (4.1) can be written as below with the primed quantities indicating fluctuating components of velocity and where ν is molecular kinematic viscosity:

$$F_x = \frac{\partial}{\partial x}\left(\nu\frac{\partial u}{\partial x} - \overline{u'u'}\right) + \frac{\partial}{\partial y}\left(\nu\frac{\partial u}{\partial y} - \overline{u'v'}\right) + \frac{\partial}{\partial z}\left(\nu\frac{\partial u}{\partial z} - \overline{u'w'}\right) \qquad (4.9)$$

A simple analogy with viscous stress provides a first gradient approximation involving a kinematic eddy viscosity (see, for example, Tritton, 1988; Pond and Pickard, 1983). Neglecting the molecular viscous terms (which are several orders of magnitude smaller than the Reynolds stresses in turbulent regions of flow) gives:

$$F_x = \frac{\partial}{\partial x}\left(A_x\frac{\partial u}{\partial x}\right) + \frac{\partial}{\partial y}\left(A_y\frac{\partial u}{\partial y}\right) + \frac{\partial}{\partial z}\left(A_z\frac{\partial u}{\partial z}\right) \qquad (4.10)$$

A more general formulation (Fofonoff, 1962) which preserves the symmetry of the Reynolds stresses (as rates of strain are due to symmetrical combinations of velocity gradients) is:

$$F_x = \frac{\partial}{\partial x}\left(2A_M \frac{\partial u}{\partial x}\right) + \frac{\partial}{\partial y}\left(A_M\left[\frac{\partial u}{\partial y} + \frac{\partial v}{\partial x}\right]\right) + \frac{\partial}{\partial z}\left(K_M \frac{\partial u}{\partial z}\right) \quad (4.11a)$$

and the friction term in (4.2) can be similarly written:

$$F_y = \frac{\partial}{\partial y}\left(2A_M \frac{\partial v}{\partial y}\right) + \frac{\partial}{\partial x}\left(A_M\left[\frac{\partial u}{\partial y} + \frac{\partial v}{\partial x}\right]\right) + \frac{\partial}{\partial z}\left(K_M \frac{\partial v}{\partial z}\right) \quad (4.11b)$$

where A_M and K_M denote horizontal and vertical eddy viscosities respectively. The third term on the right hand side of equations (4.11a) and (4.11b) represents the vertical, turbulent diffusion of momentum and is discussed in detail in the following section. The first two terms on the right hand side of (4.11a) and (4.11b) represent horizontal diffusion and parameterise sub-grid-scale horizontal momentum exchange. Horizontal mixing due to eddies on the scale of the internal Rossby radius should, of course, be explicitly resolved in baroclinic models designed to capture these processes. In fine-resolution, eddy-resolving models of the North Sea (James, 1989; Proctor and James, 1996) there is no explicit horizontal diffusion. In practice, small values of horizontal eddy viscosity, A_M, and diffusivity, A_H (for quantities other than momentum), are usually used to damp small-scale computational noise. In fine-resolution model implementations, the Laplacian formulation used in (4.11a) and (4.11b) is sometimes replaced with a biharmonic formulation (O'Brien, 1989) which has greater scale selectivity and thus dissipates small scale motions more rapidly than large scale flows. Another way of ensuring that the parameterisation of horizontal mixing relates to the scales of motion being resolved is to formulate the horizontal eddy viscosity, A_M, in terms of the grid dimensions and the shear in the mean flow. This is particularly relevant for models which incorporate non-uniform grids. POM and QUODDY adopt a parameterisation due to Smagorinsky (1963) in which the horizontal eddy viscosity in (4.11a) and (4.11b) is calculated according to:

$$A_M = \alpha \Delta x \Delta y \left[\left(\frac{\partial u}{\partial x} \right)^2 + \left(\frac{\partial v}{\partial y} \right)^2 + \frac{1}{2} \left(\frac{\partial u}{\partial y} + \frac{\partial v}{\partial x} \right)^2 \right]^{1/2} \quad (4.12)$$

where Δx and Δy are the local grid dimensions and α is a parameter whose value is application dependent.

No systematic comparison of the models listed in Table 4.1 in a realistic coastal environment has yet been performed. However, Haidvogel and Beckmann (1998) examined the performance of several models when applied to idealised baroclinic test problems. The most significant differences between models were observed when dealing with the combined effects of steep bathymetry and stratification. Nevertheless, all of those models described here have achieved useful results in prognostic regional studies. The HAMSOM model was used by Backhaus (1985) to model the major features of the North Sea circulation including the Norwegian coastal current and the anticyclonic residual flow pattern. Dippner (1993) modified the Backhaus (1985) model to solve a prognostic density equation in a Lagrangian framework and used this to simulate the formation, and tidal advection, of a salinity front in the German Bight. Schrum (1997) has recently used an eddy-resolving version of HAMSOM to model thermohaline development and baroclinic instability along a tidal mixing front in the German Bight. The hybrid advection model of James (1989) simulates meanders and eddies at the Flamborough Head tidal mixing front in the North Sea. It was found that eddies in a frictional run were suppressed compared to those in a frictionless run. Proctor and James (1996) modelled the seasonal development of stratification in the southern North Sea and revealed internal waves of tidal period due the the interaction of the barotropic tide with topography in the presence of a strong thermocline. The SPEM model (Haidvogel *et al.*, 1991) has been assessed with a variety of oceanographic problems including the propagation of barotropic shelf waves and baroclinic Kelvin waves (over one wave period). Chapman and Lentz (1994) have used the model to examine the dynamics of a surface-to-bottom freshwater plume on a uniformly sloping continental shelf and

highlight the importance of density advection in the bottom boundary layer. There are, however, difficulties associated with using continuous polynomial basis functions to resolve internal shear in the presence of a strong pycnocline (Davies, 1987). The spectral method in the vertical combined with the rigid lid condition suggest that while SPEM may prove useful for modelling shelf edge processes it is probably unsuitable for use in stratified shelf seas.

There is a considerable literature on regional applications of POM, a representative (but not exhaustive) cross-section of which is provided in Table 4.2. A brief description of some of these is now given to illustrate the range of problems to which POM has been applied, with the emphasis on prior applications of ECOMsi. The interested reader is referred to the papers cited in Table 4.2 for further details. In an early application of POM, Blumberg and Mellor (1983) modelled the climatological circulation of the South Atlantic Bight using the model's diagnostic mode to initialise prognostic runs. In simulations of the Hudson-Raritran estuary (Oey *et al.*, 1985a; Oey *et al.*, 1985b) the model predicted small scale (3 km) eddies and instabilities due to differential advection of the three dimensional density field. The eddies produced intense vertical mixing with the potential to modify estuarine dispersion. Galperin and Mellor (1990) studied the dynamics and thermodynamics of Delaware Bay, River and the adjacent continental shelf. The model showed salinity fluctuations due to tides and runoff events and predicted monthly residual currents and salinity distributions. However, it failed to predict correctly the movement of buoyant plumes (Münchow and Garvine, 1993), probably due to the use of a grid matching algorithm at the estuary mouth. The model also appeared to be insufficiently sensitive to buoyancy forcing and too sensitive to wind forcing. Ezer and Mellor (1992) used a version of the model with curvilinear coordinates to predict Gulf Stream variability and separation that were in good agreement with observations. Heat transfer, wind stress and slope water inflow were seen to be important factors in maintaining the northern recirculation gyre, on which realistic separation depends. Oey and Chen (1992) used a two-way nested grid model with grids of 20 km and 4

Table 4.2 Regional applications of the Princeton Ocean Model (POM)

Reference	Region Modelled	Features	Comments
Blumberg & Mellor (1983)	South Atlantic Bight		Initialised using diagnostic model
Oey *et al.* (1985a,b)	Hudson-Raritran Estuary		Resolved 3 km eddies
Galperin & Mellor (1990)	Delaware Bay		Insensitive to buoyancy forcing
Ezer & Mellor (1992)	Gulf Stream	CC	
Oey & Chen (1992)	Norwegian Coastal Current	NG	Two-way nested grid
Ezer & Mellor (1994)	North Atlantic Basin	CC	Diagnostic comparison
Wang *et al.* (1994)	Hudson Bay	ECOMsi	Density driven circulation
Zavatarelli & Mellor (1995)	Mediterranean Sea	CC	
Allen *et al.* (1995)	Oregon Continental Shelf	2D model	
Chen & Beardsley (1995)	Idealised symmetrical bank	ECOMsi	Tidal rectification study
Chen *et al.* (1995)	Georges Bank	ECOMsi	
Oey (1996)	Gulf of Mexico		Sensitivity study of Smagorinsky coefficient, α.
Jiang & Garwood (1996)	3D overflow simulation		Idealised shelf / process study
Allen & Newberger (1996)	Oregon Continental Shelf		Downwelling study
Kourafalou *et al.* (1996)	River plume process study		Idealised shelf / process study
Matano (1996)	Southern Indian Ocean		Study of Aghulas retroflection
Sheng & Thompson (1996)	Scotian Shelf		Diagnostic model comparison
Xue & Bane (1997)	Gulf Stream		Effect of atmospheric cooling
Ezer & Mellor (1997)	Atlantic Ocean, 80°N-80°S	CC	30 year climatic simulation
Blumberg & Pritchard (1997)	New York, East River	CC	Water quality study
Evans & Middleton (1998)	Bass Strait, Australia		Study of wind-relaxation upwelling mechanism
Holloway & Barnes (1998)	Internal waves process study	CC	61 sigma levels used to resolve bottom boundary layer flows

Key: CC, orthogonal curvilinear coordinates; NG, nested grids; ECOMsi, semi-implicit version.

km to perform a real-time simulation of eddies and meanders in the Norwegian Coastal Current. Uncertainties regarding the imposed surface cooling were thought to explain why the model failed to predict nearshore cool water. Ezer and Mellor (1994) used a curvilinear grid of the North Atlantic which varied from 20 to 100 km to conduct a diagnostic model comparison. Noise in the diagnostic flow field due to misalignment of the climatic density gradients with bathymetry was rapidly removed when the prognostic model allowed the density field to adjust dynamically. Zavatarelli and Mellor (1995) found that the model accurately reproduced inflows, outflows and deep water formation processes in the Mediterranean Sea. Temporal and spatial variability in surface salinity was shown to maintain horizontal density gradients which drive a cyclonic circulation in the northern Balearic basin.

Arguably some of the best uses to which a full physics model can be put are processes studies and comparisons with analytical models. POM has been employed in a number of process studies which utilise simplified geometry and minimal forcing to gain dynamical insight. Examples include the behaviour of buoyant plumes on the inner shelf (Kourafalou *et al.*, 1996), the modelling of three-dimensional instabilities on dense overflows (Jiang and Garwood, 1996) and a high vertical resolution investigation into bottom boundary layer flow (Holloway and Barnes, 1998). POM has also been used recently in large-scale oceanic simulations. Ezer and Mellor (1997) have carried out the first decadal circulation simulations with POM in a model of the entire Atlantic Ocean and achieved good agreement with other ocean models. Mantano (1996) used the model to show that bottom topography, rather than current inertia, is responsible for the Aghulas retroflection. Oey (1996) carried out a sensitivity study for a model of the Gulf of Mexico and found that the shedding period of loop current eddies was most sensitive to the choice of the constant in the Smagorinsky formulation for horizontal eddy viscosity (α in equation 4.12).

Chen and Beardsley (1995) and Chen *et al.* (1995) have used ECOMsi, which incorporates a semi-implicit treatment of the external mode, to investigate stratified tidal rectification over symmetrical banks and over an idealised Georges Bank. The model was forced with the M_2 tide at one open boundary with a gravity wave radiation condition (Orlanski, 1976) at the other. A sponge layer (Lorenzzetti and Wang, 1986) was added to damp internal waves propagating towards the boundary. The results showed an intensified, subsurface, along-isobath residual current due to the modification of friction by stratification, internal waves and the presence of a tidal mixing front in the boundary layer above the top of the bank. A qualitatively correct two-cell circulation pattern was also obtained. Mixed layer thicknesses from the model and from an energy argument were mutually consistent. In the Georges Bank case, the predicted seasonal variability of intensity and location of tidal mixing fronts either side of the Bank agreed well with numerous observations.

Wang *et al.* (1994) used ECOMsi to model the climatological, summer circulation in Hudson Bay. A horizontal resolution of 27.5 km was used with 11 sigma levels and a 10 minute time step. The model reproduced a stable, cyclonic current pattern. Whilst this was attributed primarily to the boundary forcing and the shape of the basin, the authors did note a well-developed dome of saline water (due to freshwater input) which maintained stability of the cyclonic flow. Mesoscale, topographic gyres of diameter 100 - 200 km, thought to be due to the interaction of wind driven and buoyancy driven mean flows with topography, were produced in the simulation. Temperature and salinity sections suggested that baroclinic mechanisms were also present on smaller scales.

4.4 Turbulence Closure

The prescription of the vertical mixing coefficient, K_M, in equations (4.11a) and (4.11b) is important because cross-frontal circulation and the sharpening of density gradients are known to be sensitive to its parameterisation (James, 1984; Garrett and Loder, 1981). The notion of an eddy (or turbulent) viscosity was first proposed by

Boussinesq in 1877; unlike the molecular viscosity, because it represents the effects of turbulent fluctuations, K_M is a property of the flow not the fluid. Consequently, the simplest choice of K_M = *constant* is mostly unrealistic. In tidal models, vertical eddy viscosity is often formulated in terms of the tidal currents. Bowden *et al.* (1959) suggested

$$K_M = 0.0025\,(U^2 + V^2)^{1/2} H \tag{4.13}$$

where U and V are the meridional and zonal components respectively of the depth mean tidal current and H is the total depth. In deep water, Davies and Furnes (1980) used

$$K_M = 2 \times 10^{-5}\,(U^2 + V^2)/\omega \tag{4.14}$$

where ω is the frequency of the long period waves (about 10^{-4} s^{-1}).

Vertical mixing is inhibited by stratification. Simpson and Bowers (1981) incorporated this feedback into their model of frontal movement by the use of a variable mixing efficiency that was controlled by the gradient Richardson Number

$$Ri = \frac{g}{\rho_0}\frac{\partial \rho}{\partial z}\Big/\left(\frac{\partial V}{\partial z}\right)^2 \tag{4.15}$$

where V is the total horizontal velocity. Stability analyses (Turner, 1973) show that turbulence is suppressed when Ri exceeds 0.21-0.25 locally. The Munk-Anderson scheme (Munk and Anderson, 1948) employed the Richardson number in expressions for eddy viscosity, K_M, and diffusivity, K_H, as below:

$$K_M = K_{M0}\,(1+\alpha Ri)^{-\beta} \tag{4.16a}$$

$$K_H = K_{H0}\,(1+\alpha\beta Ri\,(\beta\text{-}1))^{-(\beta-1)} \tag{4.16b}$$

where K_{M0} and K_{H0} are, respectively, prescribed values of eddy viscosity and diffusivity in unstratified conditions. The choice of coefficients α and β is problem

specific. Wang *et al.* (1990) took $\alpha = 3.33$, $\beta = 1.5$ (as originally proposed by Munk and Anderson, 1948) but found that variations in mixed layer depth were not properly simulated. James (1977) also found results of a simple frontal model to be sensitive to the choice of coefficients. Other implementations of the scheme are reviewed by Nunes Vaz and Simpson (1994). Alternative, exponential relationships for viscosity and diffusivity, based on the Richardson number, were put forward by Mamayev (1958), and Leenderdtse and Lui (1975).

The above schemes describe turbulent mixing coefficients solely in terms of properties of the mean velocity field. Since the mixing coefficients reflect the effect of turbulent fluctuations, it seems reasonable that properties of turbulence be employed in their determination. Given sufficient computing power, the turbulent fluctuations can be explicitly modelled and their covariance used to calculate the Reynolds stresses. So-called direct Navier-Stokes (DNS) simulations have been performed on massively parallel computers to investigate the fundamental nature of turbulence itself (e.g. Wang *et al.*, 1996). However, DNS simulations are only possible for idealised problems and the resolution of ocean models makes the direct evaluation of Reynolds stresses unfeasible.

There is an intermediate class of turbulence model in which eddy viscosity and diffusivity are prescribed through the solution of differential equations (sometimes called transport equations) for one or more properties of the turbulence. A fuller description of such models can be found in Launder and Spalding (1972), Rodi (1980) and Mellor and Yamada (1982). The objective here is merely to describe the origins of the turbulence closure scheme employed in ECOMsi and to illustrate the position it occupies in the range of models available. Transport equations for the nine components of the Reynolds stress tensor, $\overline{u'_i u'_j}$, can be obtained (Launder and Spalding, 1972) by multiplying the fluctuating components of the momentum equations and time-averaging. In this section only, tensor notation is used for

conciseness: suffixes can take three values (one for each coordinate direction) and a repeated suffix implies summation over all three values. The full set of differential equations governing Reynolds stress transports can then be written as below, where primes have been dropped from the fluctuating velocities and buoyancy forces have, for now, been neglected:

$$\frac{D\overline{u_i u_j}}{Dt} = -\frac{\partial}{\partial x_k}\left[\overline{u_i u_j u_k} - \nu\frac{\partial \overline{u_i u_j}}{\partial x_k}\right] - \frac{1}{\rho}\left[\frac{\partial \overline{p u_j}}{\partial x_i} + \frac{\partial \overline{p u_i}}{\partial x_j}\right] + \overline{\frac{p}{\rho}\left(\frac{\partial u_i}{\partial x_j} + \frac{\partial u_j}{\partial x_i}\right)} - \left[\overline{u_i u_k}\frac{\partial U_j}{\partial x_k} + \overline{u_j u_k}\frac{\partial U_i}{\partial x_k}\right] - 2\nu\overline{\frac{\partial u_i}{\partial x_k}\frac{\partial u_j}{\partial x_k}} \qquad (4.17)$$

Note the appearance of the triple correlation in the first term of the right hand side of (4.17). Were equations formulated to describe the triple correlations, they would contain fourth order correlations, and so on. This is the closure problem. At some point, the unknown variables must be expressed in terms of lower order quantities. The use of eddy viscosity in the mean momentum equations, (4.11a) and (4.11b), can be avoided if, instead, the right hand side of (4.17) could be parameterised in terms of mean velocities and Reynolds stresses. This is termed, variously, second-order closure, Mean Reynolds Stress (MRS) closure (Mellor and Herring, 1973) or level 4 closure (Mellor and Yamada, 1974). All efforts to parameterise the third term on the right of (4.17) have adopted the *energy redistribution hypothesis* of Rotta (1951), in which the pressure-velocity gradient correlations are assumed proportional to the deviation from isotropy:

$$\overline{\frac{p}{\rho}\left(\frac{\partial u_i}{\partial x_j} + \frac{\partial u_j}{\partial x_i}\right)} \propto \overline{u_i u_j} - \frac{\delta_{ij}}{3}\overline{u^2_k} \qquad (4.18)$$

Physically, the term partitions energy between the turbulent components whilst not contributing to the total and the suggested form promotes a return towards isotropy. MRS closure models have proven successful in the simulation of rapidly changing flows (Launder *et al.*, 1975) and have been applied in the atmosphere (Gibson and

Launder, 1978) and in the oceanic benthic boundary layer (Richards, 1982). However, such models necessitate the solution of 10-20 differential equations at each time step. For most practical shelf-sea applications, a model involving fewer transport equations is required.

Two important physical quantities are the kinetic energy of the velocity fluctuations, or turbulent kinetic energy (TKE), and the characteristic length scale of the turbulence. *Turbulence closure models* retain an eddy viscosity in the mean momentum equations and include a transport equation for TKE and either a prescribed function, or a second differential equation, for length scale. Following Prandtl (1945) and Kolmogorov (1942), on dimensional grounds, kinematic eddy viscosity is taken to be the product of the turbulence length scale, λ, a turbulent velocity, q, where $q^2 = \overline{u^2 + v^2 + w^2}$ = 2TKE and a non-dimensional function, S, which acts both as a proportionality constant and includes the stabilising effects of stratification. Thus

$$K_M = S \lambda q \qquad (4.19)$$

A transport equation for TKE is obtained (see Townsend, 1980, or Tritton, 1988) by multiplying the momentum equation in tensor form (decomposed into its mean and fluctuating parts) by the velocity fluctuation and then averaging. Alternatively, the TKE equation can be derived by setting $i = j$ in (4.17) and dividing by two.

$$\underset{(1)}{\frac{D}{Dt}\left(\frac{q^2}{2}\right) = -\overline{u_i u_j}\frac{\partial U_i}{\partial x_j}} \underset{(2)}{- \frac{\partial}{\partial x_j}\left[\frac{1}{2}\overline{q^2 u_j}\right]} \underset{(3)}{- \frac{\overline{p u_j}}{\rho}} + \underset{(4)}{\nu \frac{\partial}{\partial x_j}\left[\frac{\partial}{\partial x_j}\left(\frac{q^2}{2}\right)\right]} + \underset{(5)}{\frac{\partial \overline{u_i u_j}}{\partial x_i}} - \underset{(6)}{\frac{\nu}{2}\overline{\left(\frac{\partial u_i}{\partial x_j} + \frac{\partial u_j}{\partial x_i}\right)^2}} \qquad (4.20)$$

Each of the numbered terms on the right of (4.20) has a clear physical significance. (1) represents the production of turbulent energy by the Reynolds stresses working against the mean velocity gradient. (2) is the advection of turbulent energy by the fluctuations and (3) is turbulent transport of the pressure gradient. (4) and (5) both contain diffusive terms arising from manipulation of the viscous term (see Townsend, 1980, p.42). Both terms sum to zero when integrated over a bounded flow and are, in any case, relatively small at high turbulence Reynolds numbers ($u_0 L/\nu$, where u_0 is a typical turbulent fluctuation and L a typical length scale). Term (6), the turbulent energy dissipation, represents the work done by viscous stresses against turbulent velocity gradients. Dissipation is usually denoted ε, and can be expressed in several ways (see Townsend, 1980, p.42), which become equivalent at large turbulent Reynolds number. The term is universally modelled according to Kolmogorov's (1941) isotropic dissipation hypothesis which describes the cascade of energy from large eddies to the smallest scales where turbulence is locally isotropic and viscous dissipation occurs. Dimensional arguments suggest that dissipation should be of the form $\varepsilon = c\, q^3/\lambda$, where c is a non-dimensional constant and λ is the length scale. Term (1) contains the Reynolds stresses which appear in the mean momentum equations. Terms (2) to (5) all represent the redistribution of turbulent energy throughout the flow so these terms are usually modelled as a generalised diffusion term involving a mixing coefficient defined similarly (and often put equal to) K_M in (4.19). The parameterisations for the right hand side of (4.20) are then:

Production term (1) $$K_M\left(\frac{\partial U_i}{\partial x_j}\right)^2 \qquad (4.21a)$$

Diffusion terms (2)-(5) $$\frac{\partial}{\partial x_j}\left[K_q \frac{\partial}{\partial x_j}\left(\frac{q^2}{2}\right)\right] \qquad (4.21b)$$

Dissipation term (6) $$\varepsilon = cq^3/\lambda \qquad (4.21c)$$

There now exists a set of equations in entirely known quantities so the problem is closed, save for the selection of the empirical constants and a definition of the

turbulent length scale. The constants are obtained empirically from laboratory measurements of neutral (unstratified) flow near solid boundaries where diffusion is negligible and therefore the production and dissipation of TKE are in local equilibrium (constants for a range of laboratory flows can be found in Launder and Spalding, 1972 or Rodi, 1980).

The determination of length scale is where work in the field of turbulence modelling diverges most. It may be prescribed algebraically, leading to so-called one-equation, or *k-l*, models, (see Rodi, 1980, for a review of this type of model). The length scale would be expected to increase with height above a solid boundary, and to satisfy the logarithmic law of the wall, $\lambda \rightarrow \kappa z_0$ as $z \rightarrow z_0$ (where $\kappa = 0.40$, von Karman's constant, and z_0 is the roughness length at the boundary). This approach has been adopted by many workers (e.g. Prandtl, 1945; Grant and Madsen, 1979; Davies *et al.*, 1988; Zi and Johns, 1998). A popular choice for length scale, first used in the atmospheric boundary layer by Blackadar (1962), relates the mixing length to an integral of the turbulent intensity.

$$\lambda = \frac{\kappa z}{1+\kappa z / l_0} \qquad \text{with} \quad l_0 = \frac{\gamma \int_{z0}^{h} q\, z\, dz}{\int_{z0}^{h} q\, dz} \qquad (4.22)$$

where γ is an empirical constant. In shelf-sea applications, modifications are required so that the length scale is reduced near the surface as well as near the bed (Nunes Vaz and Simpson, 1994; Zi and Johns, 1998). An simple alternative algebraic prescription for λ in shallow seas has been proposed by Xing (1992).

One-equation models take no account of transport effects on the turbulent length scale. This is important in flows with boundary layer separation or where advection of turbulence is significant (Launder and Spalding, 1972) or where buoyancy fluxes are present (e.g. stratified flow). Also, algebraic prescriptions of λ are based largely on theories and laboratory data for near-wall shear flow. Beyond the boundary layer,

the prescription of λ becomes speculative. Two-equation models remedy this by including a second differential equation for the determination of turbulent length scale, as well as the TKE equation (4.20). The dependent variable of the second equation is not normally the length scale itself. The variable most favoured (by mechanical engineers, at least) is the turbulent energy dissipation, ε, which relates to length scale through (4.21c). Models whose second prognostic equation is for ε are referred to as k-ε models (e.g. Hanjalic and Launder, 1972). Alternatively, the q^2-l models of Mellor and Yamada (1974) contain a transport equation for the product of the length scale and the TKE (although this choice of variable was first considered by Rotta, 1951). Mellor and Yamada (1982) themselves acknowledge the purely empirical nature of their master length scale equation (which is related to other process length scales by several proportionality constants, all of which must be determined from neutral flow data). k-ε and q^2-l models are essentially similar since dissipation and length scale are fundamentally related through (4.21c) and, with the constants suitably tuned, they give similar results, as pointed out by Rodi (1987) and Burchard *et al.* (1998). In a comparison of both types of model against energy dissipation data from mixed and stratified sites in the Irish Sea, Burchard *et al.* (1998) found that the stability functions used had more influence on K_M than the choice of length scale equation. In stratified conditions, both models required modification (a minimum K_M) to parameterise the effects of internal waves. The major difference was that the k-ε model predicted a larger phase lag between tidal currents and dissipation in the bottom boundary layer than did the Mellor-Yamada model.

Both POM and ECOMsi employ the level 2½ scheme of Mellor and Yamada (1974). Mellor and Yamada (1974) developed a hierarchy of closure schemes of varying complexity where the 'level' denotes the simplifications made and the number of equations to be solved. The most complex, level 4, involves making closure assumptions for terms on the right of (4.17) and solving transport equations for the nine Reynolds stresses along with equations for TKE, length scale and heat. To

obtain the level 2½ model, the product of the TKE equation and $\delta_{ij}/3$ is subtracted from (4.17), giving the anisotropic part of the Reynolds stresses. Second order anisotropic variations are ignored and the boundary layer approximation is made, in which all components of mean shear are ignored except for $\partial U/\partial z$ and $\partial V/\partial z$. The turbulent energy equation can then be written

$$\frac{D}{Dt}\left(\frac{q^2}{2}\right)=\frac{\partial}{\partial z}\left[K_q\frac{\partial}{\partial z}\left(\frac{q^2}{2}\right)\right]+K_M\left[\left(\frac{\partial U}{\partial z}\right)^2+\left(\frac{\partial V}{\partial z}\right)^2\right]+\frac{g}{\rho_0}K_H\frac{\partial \rho}{\partial z}-\frac{q^3}{B_1\lambda} \qquad (4.23)$$

where the penultimate term on the right introduces the buoyant production of turbulent energy (e.g. Turner, 1973, p.130). Here, U and V represent the mean flow in the x and y directions, respectively. Vertical turbulent exchanges and mixing coefficients are defined as:

$$-\overline{uw} = K_M\frac{\partial U}{\partial z} \qquad (4.24a)$$

$$-\overline{vw} = K_M\frac{\partial V}{\partial z} \qquad (4.24b)$$

$$-\overline{\rho w} = K_H\frac{\partial \rho}{\partial z} \qquad (4.24c)$$

$$K_M = \lambda q S_M \qquad (4.24d)$$

$$K_H = \lambda q S_H \qquad (4.24e)$$

$$K_q = \lambda q S_q \qquad (4.24f)$$

The level 2½ model allows the elimination of the single point moments of velocity and density (see Mellor and Yamada, 1982, p.855), with the result that all empirical constants involved in the closure scheme are related through algebraic functions, S_M and S_H, and the buoyancy production of turbulent energy. S_M and S_H can thus be considered stability functions that modulate the effective mixing coefficients according to stratification (on further simplification, the stability functions relate directly to the Richardson number). The stability functions originally considered by

Mellor and Yamada (1982) had a dependence on the mean velocity shear which led to potential instabilities (Galperin *et al.*, 1988; Deleersnijder and Luyten, 1994) that could only be overcome by imposing arbitrary constraints, or realizability conditions, on the functions (e.g. Hassid and Galperin, 1983). Modifications proposed by Galperin *et al.* (1988) assumed local equilibrium between turbulent energy production and dissipation (in the algebraic equations only) such that the stability functions depended on

$$G_H = \frac{\lambda^2}{q^2}\frac{g}{\rho_0}\frac{\partial \rho}{\partial z} \tag{4.25}$$

in the following manner:

$$S_H = A_2\frac{1-\left(6A_1/B_1\right)}{1-3A_2G_H\left(6A_1+B_2\right)} \tag{4.26}$$

$$S_M = A_1\frac{1-3C_1-\left(6A_1/B_1\right)-3A_2G_H\left[\left(B_2-3A_2\right)\left(1-6A_1/B_1\right)-3C_1\left(6A_1+B_2\right)\right]}{\left[1-3A_2G_H\left(6A_1+B_2\right)\right]\left(1-9A_1A_2G_H\right)} \tag{4.27}$$

These modifications made the scheme more robust and removed the need for all but minor realizability constraints (i.e. G_H is limited in convectively unstable situations so that mixing coefficients become large and rapid mixing can ensue). Deleersnijder and Luyten (1994) showed that the modified stability functions gave improved agreement with laboratory data for the stress-driven deepening of a mixed layer. The constants, derived from laboratory data (Mellor and Yamada, 1982), are (A_1, B_1, C_1, A_2, B_2, S_q) = (0.92, 16.6, 0.08, 0.74, 10.1, 0.2).

Like Rotta (1951), Mellor and Yamada (1982) use the integral of a two-point correlation function (for details, see Mellor and Herring, 1973) to supply an equation for the master turbulent length scale, λ, which is

$$\frac{D}{Dt}(q^2\lambda) = \frac{\partial}{\partial z}\left[K_q \frac{\partial}{\partial z}(q^2\lambda)\right] + \lambda E_1 K_M\left[\left(\frac{\partial U}{\partial z}\right)^2 + \left(\frac{\partial V}{\partial z}\right)^2\right] + \frac{\lambda E_1 g}{\rho_0} K_H \frac{\partial \rho}{\partial z} - \frac{q^3}{B_1}\tilde{W} \quad (4.28)$$

where the wall proximity function,

$$\tilde{W} = 1 + E_2\left(\frac{\lambda}{\kappa L}\right)^2 \quad \text{with} \quad \frac{1}{L} = \frac{1}{\eta - z} + \frac{1}{H + z} \quad (4.29)$$

ensures that λ behaves as κz near surfaces and $(E_1, E_2) = (1.8, 1.33)$ are empirical constants (Mellor and Yamada, 1982).

4.5 ECOMsi model description

ECOMsi is a semi-implicit form of POM (Blumberg and Mellor, 1987) with orthogonal, curvilinear coordinates in the horizontal and sigma coordinates in the vertical. The model includes prognostic equations for temperature and salinity, wetting-drying capability and a passive, conservative tracer. The finite difference equations are second-order accurate and conserve energy, mass and momentum. The model development is described in detail by Blumberg (1994). The governing equations are (4.1) to (4.4) plus transport equations for temperature and salinity. Density is then calculated through an equation of state, $\rho = \rho(T,S)$ (Fofonoff, 1962). The model also includes prognostic equations for turbulent kinetic energy (4.23) and turbulent lengthscale (4.28). Pressure at depth z is obtained by vertically integrating (4.3) from z to the free surface η to give:

$$p(z) = p_{atm} + g\int_z^0 \rho_o \, dz + \rho_o g\eta + g\int_z^\eta \rho' \, dz \quad (4.30)$$

Atmospheric pressure is neglected so that the pressure at depth z is the sum of hydrostatic pressure, surface elevation and baroclinic components. Horizontal derivatives of pressure which appear in the momentum equations (4.1) and (4.2)

contain only horizontal gradients of surface elevation, η, and of the density departure, ρ', from the reference state $\rho_0 = \rho_0(z)$ which is a function only of depth.

The governing equations are transformed into sigma coordinates using the transformation:

$$\sigma = \frac{z-\eta}{h+\eta} \tag{4.31}$$

where $h(x,y)$ is the depth and $\eta(x,y,t)$ is the surface elevation. Therefore σ ranges from σ 0 at z η, to σ -1 at z $-h$. The coordinates x, y and t remain unchanged in the new coordinate system. Full details of the transformations are provided by Blumberg and Mellor (1987) and are not repeated here. A new velocity, ω, normal to sigma surfaces and physically scaled by the total depth, $D = h + \eta$, can now be introduced:

$$\omega = D\frac{d\sigma}{dt} = w - u\left(\sigma\frac{\partial D}{\partial x} + \frac{\partial \eta}{\partial x}\right) - v\left(\sigma\frac{\partial D}{\partial y} + \frac{\partial \eta}{\partial y}\right) - \left(\sigma\frac{\partial D}{\partial t} + \frac{\partial \eta}{\partial t}\right) \tag{4.32}$$

The continuity equation (4.4) then transforms onto:

$$\frac{\partial \eta}{\partial t} + \frac{\partial uD}{\partial x} + \frac{\partial vD}{\partial y} + \frac{\partial \omega}{\partial \sigma} = 0 \tag{4.33}$$

and the transformed versions of the momentum equations (4.1) and (4.2) can be written in flux integrated form (using 4.33) which explicitly conserves volume when the equations are subsequently placed in finite difference form.

$$\begin{aligned} &\frac{\partial uD}{\partial t} + \frac{\partial u^2 D}{\partial x} + \frac{\partial uvD}{\partial y} + \frac{\partial u\omega}{\partial \sigma} - fvD + gD\frac{\partial \eta}{\partial x} = \\ &-\frac{gD^2}{\rho_0}\frac{\partial}{\partial x}\int_\sigma^0 \rho\, d\sigma + \frac{gD}{\rho_0}\frac{\partial D}{\partial x}\int_\sigma^0 \sigma\frac{\partial \rho}{\partial \sigma}d\sigma + \frac{\partial}{\partial \sigma}\left[\frac{K_M}{D}\frac{\partial u}{\partial \sigma}\right] + F_x \end{aligned} \tag{4.34}$$

$$\frac{\partial vD}{\partial t}+\frac{\partial uvD}{\partial x}+\frac{\partial v^2D}{\partial y}+\frac{\partial v\omega}{\partial \sigma}+fuD+gD\frac{\partial \eta}{\partial y} \quad =$$
$$-\frac{gD^2}{\rho_0}\frac{\partial}{\partial y}\int_\sigma^0 \rho d\sigma+\frac{gD}{\rho_0}\frac{\partial D}{\partial y}\int_\sigma^0 \sigma\frac{\partial \rho}{\partial \sigma}d\sigma+\frac{\partial}{\partial \sigma}\left[\frac{K_M}{D}\frac{\partial v}{\partial \sigma}\right]+F_y \tag{4.35}$$

Horizontal diffusion (F_x and F_y) is expressed by the first two terms of the *untransformed* equations (4.11a) and (4.11b):

$$F_x=\frac{\partial}{\partial x}\left(2DA_M\frac{\partial u}{\partial x}\right)+\frac{\partial}{\partial y}\left(DA_M\left(\frac{\partial u}{\partial y}+\frac{\partial v}{\partial x}\right)\right)$$
$$F_y=\frac{\partial}{\partial y}\left(2DA_M\frac{\partial v}{\partial y}\right)+\frac{\partial}{\partial x}\left(DA_M\left(\frac{\partial u}{\partial y}+\frac{\partial v}{\partial x}\right)\right) \tag{4.36}$$

This simpler formulation avoids numerical diffusion and models the bottom boundary layer over steep topography more realistically (Blumberg and Mellor, 1987). The equations for temperature and salinity are:

$$\frac{\partial TD}{\partial t}+\frac{\partial uTD}{\partial x}+\frac{\partial vTD}{\partial y}+\frac{\partial \omega T}{\partial \sigma}=\frac{\partial}{\partial \sigma}\left[\frac{K_H}{D}\frac{\partial T}{\partial \sigma}\right]+F_T \tag{4.37}$$

$$\frac{\partial SD}{\partial t}+\frac{\partial uSD}{\partial x}+\frac{\partial vSD}{\partial y}+\frac{\partial \omega S}{\partial \sigma}=\frac{\partial}{\partial \sigma}\left[\frac{K_H}{D}\frac{\partial S}{\partial \sigma}\right]+F_S \tag{4.38}$$

and the transformed turbulent kinetic energy and turbulence lengthscale equations are respectively:

$$\frac{\partial q^2D}{\partial t}+\frac{\partial uq^2D}{\partial x}+\frac{\partial vq^2D}{\partial y}+\frac{\partial \omega q^2}{\partial \sigma}=\frac{\partial}{\partial \sigma}\left[\frac{K_q}{D}\frac{\partial q^2}{\partial \sigma}\right]$$
$$+\frac{2K_M}{D}\left[\left(\frac{\partial u}{\partial \sigma}\right)^2+\left(\frac{\partial v}{\partial \sigma}\right)^2\right]+\frac{2g}{\rho_0}K_H\frac{\partial \rho}{\partial \sigma}-\frac{2Dq^3}{B_1\lambda}+F_{q^2} \tag{4.39}$$

$$\frac{\partial q^2\lambda D}{\partial t}+\frac{\partial uq^2\lambda D}{\partial x}+\frac{\partial vq^2\lambda D}{\partial y}+\frac{\partial \omega q^2\lambda}{\partial \sigma}=\frac{\partial}{\partial \sigma}\left[\frac{K_q}{D}\frac{\partial q^2\lambda}{\partial \sigma}\right]$$
$$+E_1\lambda\left(\frac{K_M}{D}\left[\left(\frac{\partial u}{\partial \sigma}\right)^2+\left(\frac{\partial v}{\partial \sigma}\right)^2\right]+\frac{qD^3}{\rho_0}K_H\frac{\partial \rho}{\partial \sigma}\right)-\frac{Dq^3}{B_1}\tilde{W}+F_{q^2\lambda} \qquad (4.40)$$

where horizontal diffusion terms in (4.37) to (4.40) are parameterised as:

$$F_\psi=\frac{\partial}{\partial x}\left(DA_H\frac{\partial \psi}{\partial x}\right)+\frac{\partial}{\partial y}\left(DA_H\frac{\partial \psi}{\partial y}\right) \qquad (4.41)$$

and ψ represents T, S, q^2 or $q^2\lambda$. The horizontal eddy viscosity, A_M, and eddy diffusivity, A_H, are calculated through the grid-dependent formulation of Smagorinsky (1963) as given in equation (4.12). The constants B_1 and E_1, and the wall proximity function, W, are as defined in §4.4. Vertical turbulent exchange coefficients are calculated using the level 2½ turbulence closure model of Mellor and Yamada (1982) with modifications to the stability functions due to Galperin *et al.* (1988):

$$K_M - q\lambda S_M \qquad (4.42a)$$

$$K_H - q\lambda S_H \qquad (4.42b)$$

$$K_q = 0.2q\lambda \qquad (4.42c)$$

where q^2 is twice the turbulent kinetic energy, λ is the turbulence lengthscale and the algebraic stability functions, S_M and S_H, are as described in §4.4.

Boundary conditions at the bed (σ = -1) are:

$$\frac{\rho_o K_M}{D}\left(\frac{\partial u}{\partial \sigma},\frac{\partial v}{\partial \sigma}\right) = \left(\tau_{bx},\tau_{by}\right) \qquad (4.43a)$$

$$q^2 \quad B_1^{2/3}\,u_*^2 \qquad (4.43b)$$

$$q^2\lambda = 0 \qquad (4.43c)$$

along with zero fluxes of heat and salt. τ_{bx}, τ_{by} are bottom stresses in the x and y directions respectively and u_* is the friction velocity at the bed. Bottom stress is determined by matching a quadratic stress law at model grid points nearest to the bed to the logarithmic wall profile, as shown below for τ_{bx}:

$$\tau_{bx} = \rho_o C_D u_b^2 = \rho_o u_*^2 \qquad (4.44a)$$

and

$$u_b = \frac{u_*}{\kappa} \ln\left(\frac{z_b}{z_o}\right) \qquad (4.44b)$$

gives

$$C_D = \frac{\kappa^2}{\left[\ln(z_b / z_o)\right]^2} \qquad (4.44c)$$

where C_D is a drag coefficient, z_b is the height of the nearest velocity point above the bed, z_o is a roughness length and $\kappa = 0.40$ is von Karman's constant. The model uses the larger of this value and $C_D = 0.0025$ (in the case of a poorly resolved boundary layer). Tidal amplitude predictions have been found to be very sensitive to the value of z_o (Oey *et al.*, 1985b; Xing and Davies, 1996) and care must be taken when defining it. A reasonable value of z_o for the Irish Sea is 5 mm (Davies and Lawrence, 1994a). At the surface ($\sigma = 0$):

$$\frac{\rho_o K_M}{D}\left(\frac{\partial u}{\partial \sigma}, \frac{\partial v}{\partial \sigma}\right) = \left(\tau_{sx}, \tau_{sy}\right) \qquad (4.45a)$$

$$\frac{\rho_o K_H}{D}\left(\frac{\partial T}{\partial \sigma}, \frac{\partial S}{\partial \sigma}\right) = \left(Q_{T,S}\right) \qquad (4.45b)$$

$$q^2 = B_1^{2/3} u_*^2 \qquad (4.45c)$$

$$q^2 \lambda = 0 \qquad (4.45d)$$

where τ_{sx}, τ_{sy} are the surface wind stresses in the x and y directions respectively, $Q_{T,S}$ is the surface flux of heat or salt and u_* is now the friction velocity at the surface. Velocities at lateral boundaries are set to zero and the boundary conditions on the new velocity, ω, at the surface and bed are:

$$\omega(0) = \omega(-1) = 0 \qquad (4.46)$$

Equations (4.33) to (4.41), subject to boundary conditions (4.43) to (4.46), are put into finite difference form and solved on the Arakawa C-grid shown in Fig. 4.2 using an implicit scheme in the vertical. Details of the finite difference formulations can be found in Blumberg and Mellor (1987).

Unlike POM, which uses different time steps for the external and internal modes, ECOMsi adopts a semi-implicit scheme in the horizontal. Here, the free surface pressure gradient in the momentum equations and the velocity divergence in the vertically averaged continuity equation are treated implicitly. Using an explicit method, interim solutions to (4.34) and (4.35) are found at the new time level, $t+1$, providing values for u^{t+1} and v^{t+1} except for contributions from the elevation terms, whose calculation has been deferred. The horizontal velocity divergences at the new time level, $\frac{\partial}{\partial x}u^{t+1} + \frac{\partial}{\partial y}v^{t+1}$, are summed for all sigma levels and then substituted into the vertically integrated form of the continuity equation (4.33) giving an elliptical equation for free surface elevation at the new time level, η^{t+1}, everywhere in the domain. Elevations at the forward time level are obtained by solving a linear, five diagonal system using a pre-conditioned conjugate gradient method (Casulli and Cheng, 1992). The free surface pressure gradient is then available in order to calculate the barotropic contribution to horizontal velocities which are now updated to provide the true values of u^{t+1} and v^{t+1}. The semi-implicit method allows time steps much larger than those based on the CFL condition to be used. The internal time step used in the explicit part of the solution is limited by a less stringent CFL condition:

$$\Delta T \leq \frac{1}{c}\left(\frac{1}{\Delta x^2} + \frac{1}{\Delta y^2}\right)^{-\frac{1}{2}} \qquad (4.47)$$

where celerity $c = c_i + U_{max}$, with c_i being the maximum internal wave speed (about 2 m s^{-1}) and U_{max} is the maximum advective speed.

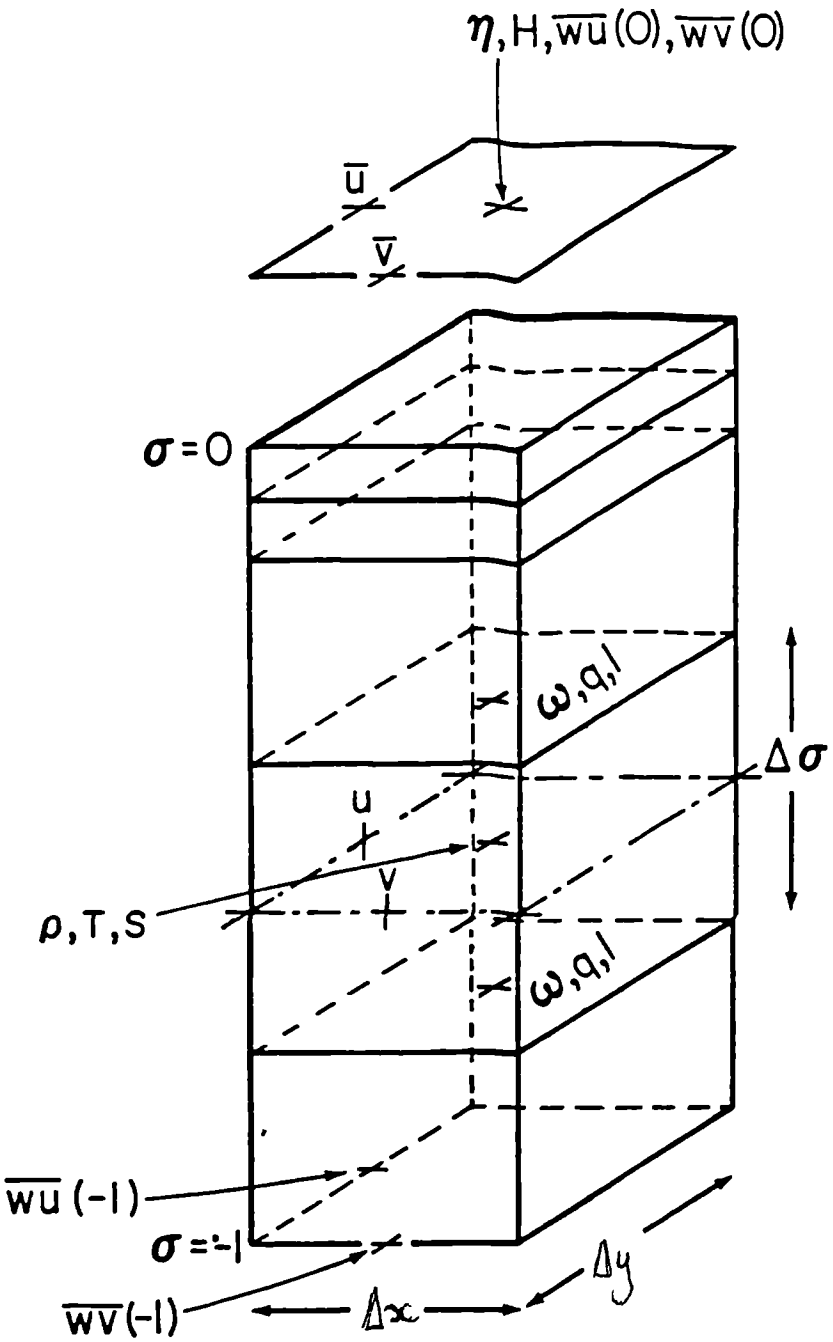

Fig. 4.2 Location of model variables on the vertical grid. Temperature and salinity (thus density) are updated at 'elevation' points on the C-grid. Vertical velocity, ω, is updated at the centre of the corresponding area at a sigma level. The arrangement can be thought of as a cube, with velocity components on each face (adapted from Blumberg, 1994).

ECOMsi provides three algorithms for the advection of scalar fields (temperature, salinity, passive tracer) - centred difference, upwind difference and a positive definite transport algorithm based the successive application of an upwind algorithm such that the numerical diffusion due to first-order truncation error is minimised (Smolarkiewicz, 1983; Smolarkiewicz, 1984). Correction to the first-order error is made by reapplying the upwind algorithm, using an antidiffusion velocity based on the local truncation error. This advection algorithm is second-order accurate and positive definite. Its disadvantage is that the execution time of a typical simulation can be double that of the other advection schemes.

At the open boundaries of the model domain, the surface elevation can be forced by up to six tidal harmonic constituents. Where inflow occurs at a lateral open boundary, temperature and salinity must be specified as a time series (although this feature of the code was altered for the Irish Sea application, as described in the next section). The transport of heat and salt at boundaries where outflow occurs is determined using an upwind advection scheme. Other forcing mechanisms included in the model are surface wind stress (with wind velocity-dependent drag coefficients after Large and Pond, 1981), surface heat flux, salinity flux (evaporation minus precipitation) and freshwater discharge. Solar shortwave radiation is specified using available data whilst longwave radiation is calculated from sea surface temperature, corrected for cloud cover following Reed (1976). Sensible and latent heat losses are predicted using the method of Large and Pond (1982). A further feature of the model is a diagnostic mode where a specified density field is frozen and a dynamically consistent velocity field is spun-up from rest. The diagnostic mode is useful for assessment of the model and can also be used to rapidly initialise a subsequent prognostic run.

Chapter 5. Implementation and validation of ECOMsi

5.1 Implementation of the model in the Irish Sea

The model was configured for the rectilinear grid shown in Fig. 5.1. The grid had 74 rows and 92 columns and cells were 1/30° of latitude by 1/20° of longitude (Δx = 3.3 km, Δy = 3.7 km). The grid and bathymetry were identical to that used in the region by Davies and Lawrence (1994a) and Xing and Davies (1996). Twenty-one sigma levels were used in the vertical, arranged as follows: σ = (0 -0.02, -0.04, -0.07, -0.10, -0.15, -0.20, -0.30, -0.40, -0.50, -0.60, -0.70, -0.80, -0.85, -0.90, -0.93, -0.96, -0.98, -0.99, -0.995, -1.0). The irregular spacing of the vertical coordinate provided enhanced resolution in the high-shear surface and nearbed layers.

To minimise their influence, open boundaries (the solid, bold lines in Fig. 5.1) were placed as far as possible from the region of interest. The model was forced along these boundaries by M_2 and S_2 tidal input, derived from a larger scale shelf model (Flather, 1976). Tidal forcing was ramped up from zero to its full amplitude over one tidal cycle, to avoid generating large transients. A radiation condition was applied at the open boundaries so that the tidal forcing could be prescribed and maintained, yet any disturbances generated within the computational domain could propagate outwards freely. The condition used was a modified form of the Sommerfeld radiation condition (Blumberg and Kantha, 1985; Chapman, 1985) based on linearised, long-wave propagation normal to the boundary, with an additional friction-like term which allows disturbances to relax over a prescribed, characteristic timescale:

$$\frac{\partial \eta}{\partial t} + c\frac{\partial \eta}{\partial x} = -\left(\frac{\eta - \eta_k}{T}\right) \qquad (5.1)$$

where η_k is the prescribed elevation, $c = (gH)^{1/2}$ is the local shallow water wave speed and T is a relaxation timescale for barotropic transients, taken here to be 4 hours (the optimum value found by Blumberg and Kantha, 1985). A zero gradient condition

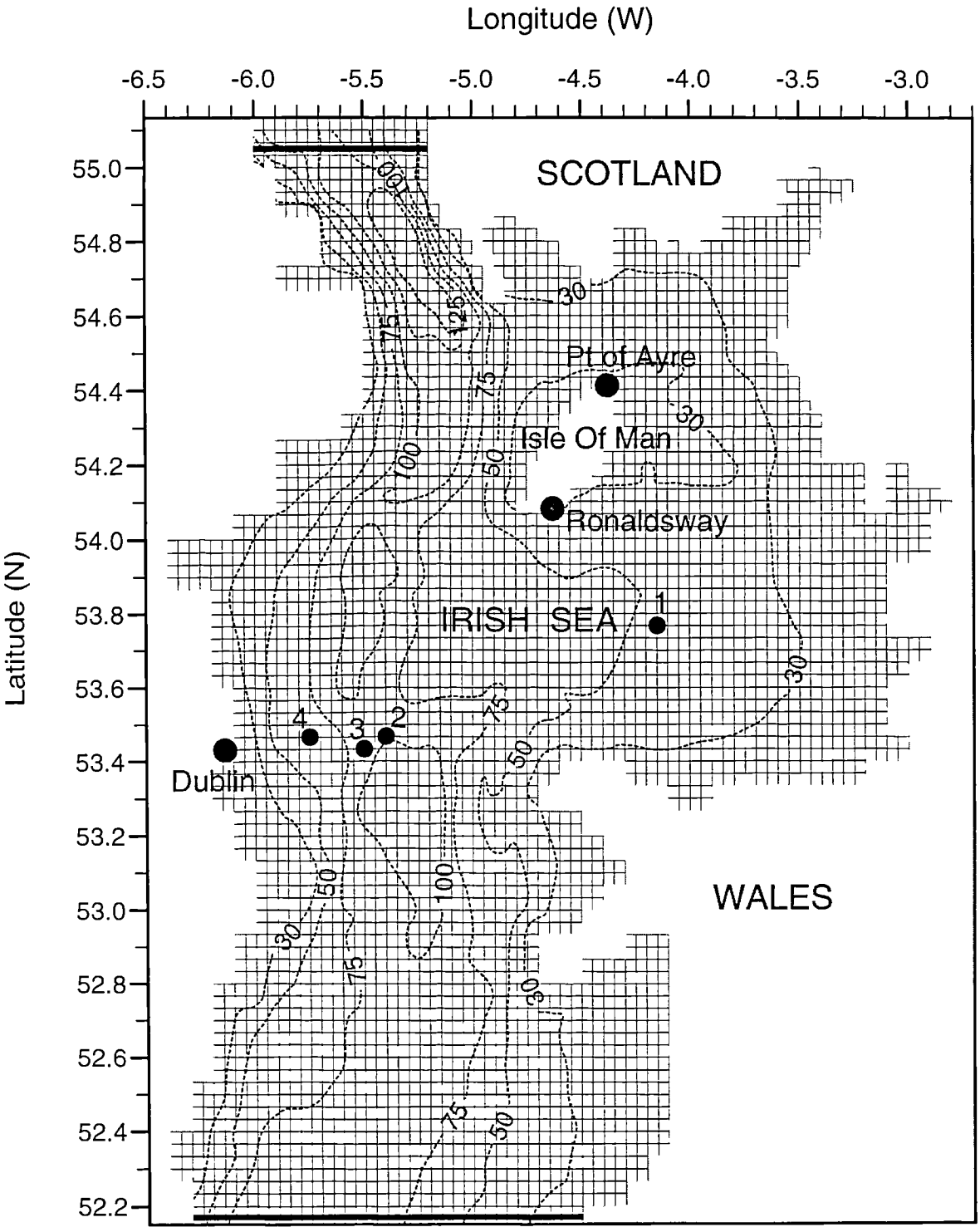

Fig. 5.1 Finite difference grid and model bathymetry (dotted lines) (m) of the Irish Sea model. The solid, bold lines represent open boundaries where M_2 and S_2 input were specified. Also shown are the locations of weather stations where meteorological forcing was obtained and current meter rigs (numbered 1-4) where comparisons were made.

was imposed on tangential velocities at the open boundaries (i.e. $\partial U/\partial y = 0$). To damp internal waves propagating towards the open boundaries, Chen *et al.* (1995) employed a 'sponge layer' (where friction increases to unphysically high values within a few grid cells of the boundary). This was not considered necessary here, since the boundaries were distant from the region of interest and, in the seasonal simulations described in §6, stratification does not extend to the open boundaries (see Fig. 3.11) where internal mode energies were considered to be relatively low.

Open boundary conditions for temperature and salinity were not required for the model validation runs described in this chapter. In the tidal validations, temperature and salinity were held constant throughout the domain and in the frontal simulations, the model was run in a diagnostic mode so that the prescribed density structure did not evolve. In the numerical simulations of a two-layer adjustment problem (see §5.4, later) the model was fully baroclinic, but all four boundaries were closed. Lateral open boundary conditions for temperature and salinity used in the seasonal simulations will be described in detail in the next chapter.

Although all computations were stable with zero explicit horizontal viscosity and diffusivity, a small amount was nevertheless prescribed to reduce computational noise. In the simulations described here and in the next chapter, horizontal eddy viscosity was calculated according to (4.12), with $\alpha = 0.1$ and $A_H = A_M$. The roughness length, z_0, was set at 5mm, consistent with previous applications of turbulence energy models in the Irish Sea (Xing and Davies, 1996).

5.2 Validation of the modelled M_2 and S_2 tides in the Irish Sea

Since tides in the Irish Sea have been extensively modelled, a suitable intitial validation of the model is its tidal predictive performance. Comparisons are made primarily against two recent model studies of tides in the Irish Sea, one of which

(Xing and Davies, 1996) employed turbulence closure physics whilst the other (Davies and Aldridge, 1993) used a spectral approach and prescribed vertical viscosity profiles. In the simulations described here, temperature and salinity were held constant (T = 10 °C, S = 34) and a time-step of 200 s was used. The model was spun-up for six days and then run for 30 days so that harmonic analysis could be performed to obtain amplitudes and phases of elevation and velocity. As found by Davies and Aldridge (1993) and Xing and Davies (1996), computed tides in the Irish Sea are extremely sensitive to input along the open boundaries. Best results were obtained when tidal forcing at the southern boundary was adjusted slightly, towards the interpolated observations of Robinson (1979). The results described here represent an optimisation (over several model runs) of boundary input, vertical resolution and bottom roughness.

The computed M_2 co-tidal chart (Fig. 5.2b) reproduces the general features of this constituent in the region, including the degenerate amphidrome in eastern Ireland and amplification in the eastern Irish Sea. The results are in agreement with observations (Robinson, 1979) and with previous models of the area (Davies and Aldridge, 1993; Xing and Davies, 1996). For comparison, the results of Xing and Davies (1996), who also used two-equation turbulence closure, are shown in Fig. 5.2a. The similarity between the two models is encouraging. Modelled amplitudes and phases of the tidal elevation (Fig. 5.2b) were compared with records from 33 coastal and offshore tide gauges around the Irish Sea (see Appendix 2 for locations and observed values). Root mean squared (rms) errors were 9.4 cm in elevation and 5° of phase. These values compare favourably with other models: Xing and Davies (1996, Calculation 1) obtained rms errors of 11.7 cm for elevation and 5° for phase in their q^2-q^2l run. The same authors (Xing and Davies, 1995, calculation N1) had previously obtained rms errors of 9.7 cm for elevation and 4° for phase with a coarser resolution model. Davies and Aldridge (1993) found rms errors of 9 cm in elevation and 6° of phase using a spectral model. The distribution of signed elevation errors obtained here (see

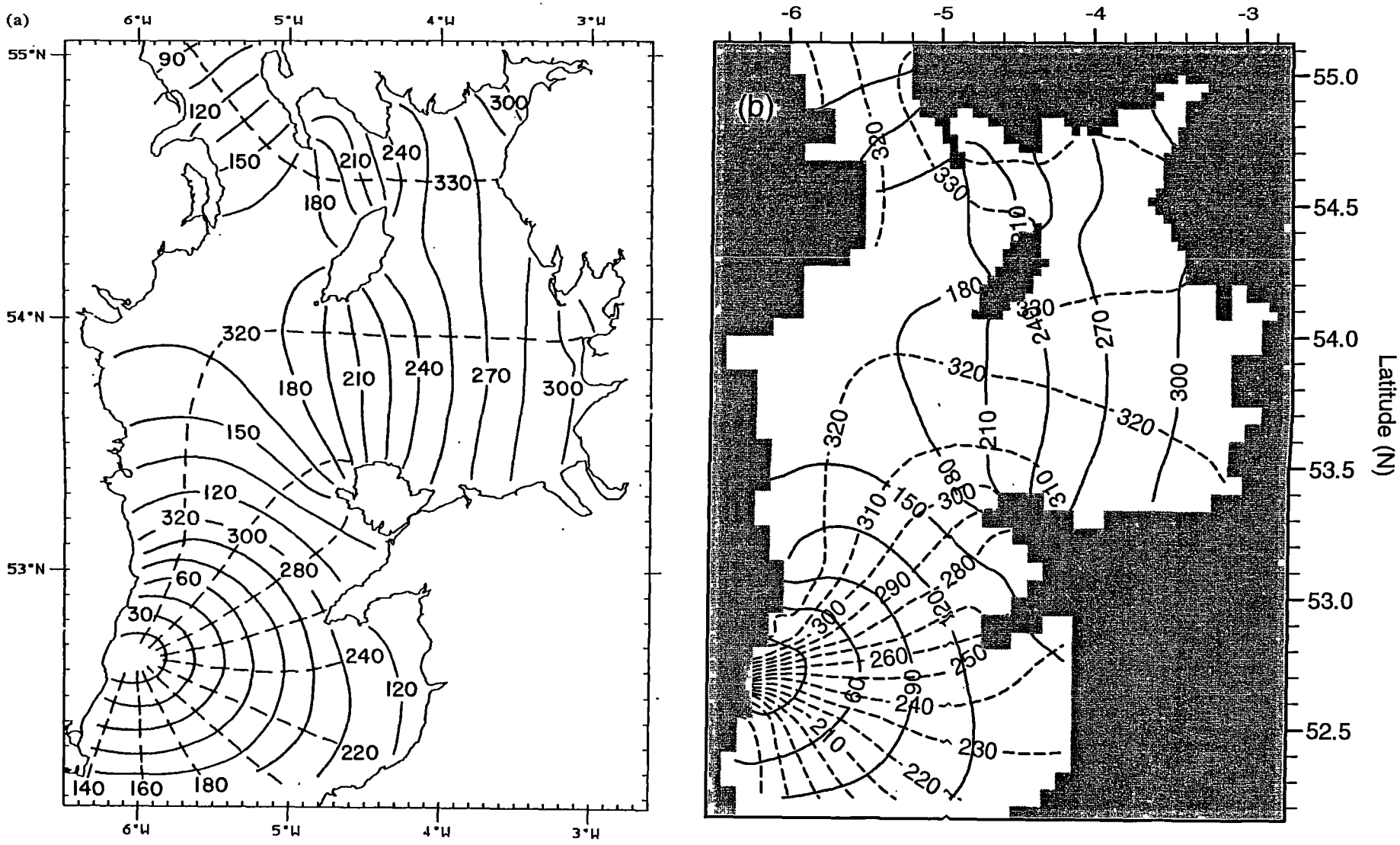

Fig. 5.2 Contours of amplitude (cm, solid lines) and phase (°, dashed lines) of the M_2 tide in the Irish Sea derived from (a) Xing and Davies (1996) and (b) this application of ECOMsi. The two models used identical grids and bathymetry and both used the Mellor and Yamada (1982) q^2-q^2l turbulence closure scheme.

Table 5.1) shows a tendency for underprediction, which is typical of three-dimensional Irish Sea models and is discussed in detail by Davies and Aldridge (1993).

Table 5.1 Distribution of signed elevation errors for M_2 tide from ECOMsi

	Less than						Greater than				
Error (cm)	-25	-20	-15	-10	-5	-5 to +5	+5	+10	+15	+20	+25
Number of values	0	1	0	5	6	13	6	0	1	1	0

Davies and Aldridge (1993) noted that correct prediction of tidal elevation in the Irish Sea can be obtained when computed tidal currents are overpredicted by approximately 20 cm s^{-1}. In this work, it is desirable to model the vertical profile of tidal currents as accurately as possible, since they are largely responsible for the spatial pattern of mixing energy that controls the position of bottom fronts around the western Irish Sea. Modelled elevations are, in any case, considered to be satisfactory and errors can reasonably be attributed to poor resolution of local, coastal features where most of the tide gauges used for comparison are located.

The major and minor axes of computed M_2 surface currents ellipses are presented in Fig. 5.3b. The spatial pattern of surface currents is in close agreement with previous model results (Xing and Davies, 1996), which are shown in Fig. 5.3a for comparison. Current ellipses are predominantly rectilinear with north-south alignment on the western side of the model and east-west alignment in the eastern Irish Sea. The region of weaker tidal currents in the western Irish Sea is predicted by both models. A detailed comparison of the amplitude and phase of computed u and v components of velocity was carried out for a limited number of locations. Xing and Davies (1996) described 17 sites around the Irish Sea where current meter data is available for model validation - most of them in the eastern Irish Sea and Liverpool Bay. Since the focus of this work is the western Irish Sea gyre, comparisons are made here

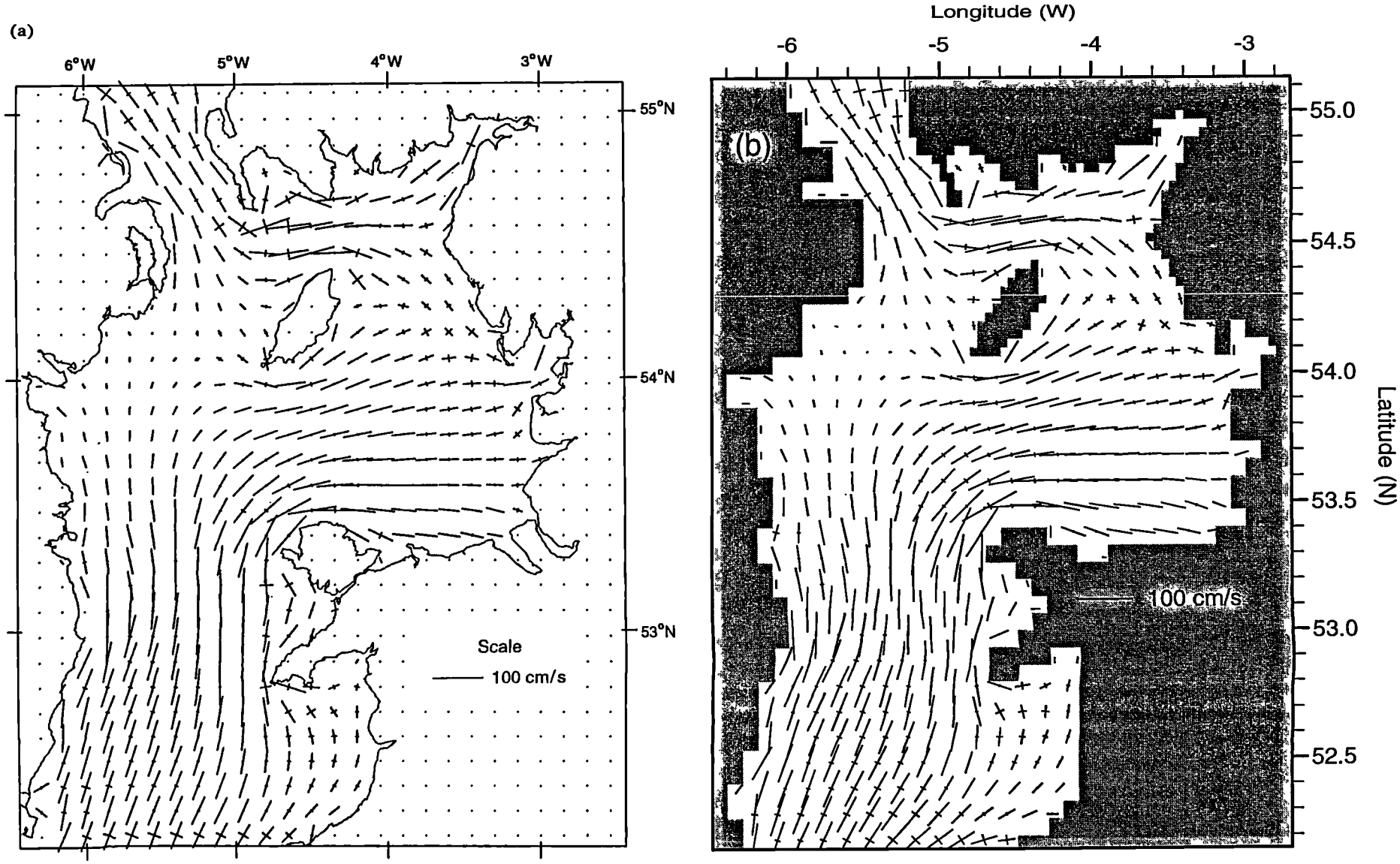

Fig. 5.3 Major and minor axes of the M_2 surface current ellipses in the Irish Sea (at every third row and column) from (a) Xing and Davies (1996) and (b) this application of ECOMsi. The two models used identical grids and bathymetry and both used the Mellor and Yamada (1982) q^2-q^2l turbulence closure scheme.

against current meter data from the three locations in the western Irish Sea (numbered 2-4 in Fig. 5.1) and only one location (site 1, Fig. 5.1) in the shallower eastern part. Amplitudes and phases of the M_2 current components were calculated at those model cells corresponding to each of these current meter rigs, and at σ-levels most closely matching the depths at which observations were made. Table 5.2 shows that, as with previous models of the area (e.g. Xing and Davies, 1996), the computed currents tended to be overestimated. However, the rms amplitude error (Table 5.2) was 5 cm s^{-1} compared with typical values of 11 cm s^{-1} found in previous turbulence closure models of the region (Xing and Davies, 1996). Errors in phase, and in the smaller velocity component, can appear exaggerated when considered in decomposed form. An alternative representation of tidal currents (particularly useful for almost rectilinear currents, as here) is to calculate the tidal ellipse properties (see, for example, Souza and Simpson, 1996). Observed and computed M_2 tidal ellipses are compared in Table 5.3 where M and m are, respectively, the semi-major and semi-minor axes (cm s^{-1}), θ is the orientation of the major axis (° anticlockwise from east) and ϕ is the phase of the semi-major axis (°). Semi-major axes agreed to within 5.5 cm s^{-1} whilst the mean error in the semi-minor axes was 1.3 cm s^{-1}. Modelled current ellipses had a tendency to be slightly more elliptical than those observed. The mean error in orientation was 5° and ellipse phases agreed to within 4°. The model reproduced the expected increase in ellipticity towards the sea bed (Prandle,1982) and showed good predictive skill near the bed (particularly at locations 1 and 2). Davies and Aldridge (1993) considered the accurate prediction of near bed currents to be a critical test of tidal models in the Irish Sea. For the four sites analysed, the modelled and observed semi-major axes, at the level of the deepest measurement, were in agreement to within 6%. The model also predicted vertical current shear consistent with observations at all four locations. This property is a crucial test for three-dimensional models (Xing and Davies, 1996) since shear is determined by the modelled distribution of stresses through the vertical and is not sensitive to input at the open boundary.

Table 5.2 Observed and computed amplitude, h (cm s^{-1}) and phase, g (degrees) of the u and v components of M_2 tidal current at several depths for locations 1-4 in Fig. 5.1. (Bracketed numbers in the first column refer to the corresponding current meter rig designation in Xing and Davies, 1996).

Current Meter	Sigma Level	Relative Depth	Observations (see Xing and Davies, 1996)				Model			
			h_u	g_u	h_v	g_v	h_u	g_u	h_v	g_v
1 (13)	10	0.50	74	237	6	221	78	241	13	251
	11	0.60	72	237	4	218	75	240	13	253
	13	0.80	66	236	7	230	66	238	14	256
	18	0.98	40	234	4	248	38	235	10	256
2 (16)	6	0.15	3	91	76	251	4	90	86	249
	16	0.93	7	151	56	244	9	136	58	241
3 (17)	6	0.15	11	76	75	241	8	45	84	249
	10	0.50	12	107	71	241	10	87	79	246
4 (15)	8	0.30	2	119	55	232	9	74	64	235
	15	0.90	10	137	40	218	12	89	46	226

Table 5.3 Observed and computed M_2 tidal ellipses for locations 1-4 in Fig. 5.1. M and m, are, respectively, the semi-major and semi-minor axes (cm s^{-1}). θ is the orientation (°) anticlockwise from east and ϕ is phase (°) of the semi-major axis.

Location	σ	hH	Observations				Model			
			M	m	θ	ϕ	M	m	θ	ϕ
1 (13)	10	0.50	74	2.0	4	57	79	1.9	9	61
	11	0.60	72	1.2	3	57	76	2.8	10	60
	13	0.80	66	1.2	6	56	67	3.8	11	59
	18	0.98	40	1.0	6	54	39	3.5	14	56
2 (16)	6	0.15	76	1.0	92	71	86	1.4	92	69
	16	0.93	56	7.0	90	64	58	8.7	92	61
3 (17)	6	0.15	76	2.8	98	61	84	3.2	95	69
	10	0.50	71	8.6	97	62	79	3.6	97	66
4 (15)	8	0.30	55	1.8	91	52	64	2.9	98	55
	15	0.90	40	9.9	88	37	47	8.0	101	48

The computed S_2 co-tidal chart (Fig. 5.4b) is also in reasonable agreement with observations (Robinson, 1979 - reproduced in Fig. 5.4a for comparison) and previous regional models (Davies and Jones, 1992). A detailed comparison of S_2 elevations was not performed but current ellipses were compared with (limited) previously reported observations. Davies and Jones (1992) presented S_2 ellipse properties for three of the current meter sites shown in Fig. 5.1. The properties reported were semi-major and semi-minor axes (cm s^{-1}), orientation, θ (°), and the sense of rotation of the current vector. The same properties derived from ECOMsi were compared with these observations in Table 5.4. The modelled values agree well with observations, with mean errors of 1.8 cm s^{-1} for the semi-major axis and 4.5° for orientation. Vertical shear is correctly predicted by the model, as for the M_2 component.

Table 5.4 Observed and computed S_2 tidal ellipses for locations 1-3 in Fig. 5.1. *M* and *m*, are, respectively, the semi-major and semi-minor axes (cm s^{-1}). θ is the orientation (°) anticlockwise from east of the major axis and the sense of rotation is also given. Observed properties are reproduced from Davies and Jones (1992).

Location	σ	*h/H*	Observations				Model			
			M	*m*	θ	+/-	*M*	*m*	θ	+/-
1 (13)	10	0.50	25.2	0.1	4	-	24.4	0.2	11	+
	11	0.60	23.9	0.0	3	+	23.5	0.4	11	+
	13	0.80	21.8	0.0	6	+	21.5	0.7	12	+
	18	0.98	14.8	0.7	5	+	12.4	0.7	15	+
2 (16)	6	0.15	24.0	0.6	92	+	29.0	0.4	92	+
	16	0.93	17.9	2.0	93	+	19.4	2.5	93	+
3 (17)	6	0.15	24.1	2.2	101	+	28.1	0.4	95	+
	10	0.50	22.7	3.5	96	+	27.2	1.2	96	+

The harmonic analysis performed to obtain tidal constituents also provided the Eulerian tidal residual currents predicted by the numerical model. Depth-averaged tidal residual currents are shown in vector form in Fig. 5.5b. For comparison,

residual currents obtained from a previous (5 km grid) model of the Irish Sea (Proctor, 1981) are presented in Fig. 5.5a. In Fig. 5.5b, the arrow lengths are proportional to current magnitude but, to better visualise regions of significant residual flow, currents greater than 5 cm s^{-1} are shown in bold. Residual currents less than 1 cm s^{-1} are designated by open arrowheads with no tails.

Significant Eulerian residuals occur around headlands (where non-linear terms in the momentum equations become significant). The strongest computed non-tidal currents, of up to 18 cm s^{-1}, were obtained around Anglesey. Other areas where significant tidal residual flow was predicted were around the Isle of Man, the North Channel and in the coastal region near the degenerate amphidrome in south east Ireland. The patterns of flow in Fig. 5.5b are consistent with the earlier predictions of Proctor (1981) and both models suggest a clockwise gyre in the north-eastern part of the Irish Sea, between the Isle of Man and the Solway Firth. Although a weak, northward residual flow can be seen to the west of the Isle of Man in both models, it does not exceed 3 cm s^{-1} and there is no evidence in either model of cyclonic flow in the western Irish Sea.

As a final evaluation of barotropic model performance, Fig. 5.6b presents vertical profiles of turbulent energy, q^2 (twice the turbulent kinetic energy), turbulence length scale and vertical eddy viscosity, in 90 m of water in the western Irish Sea 2 (location 2, see Fig. 5.1) throughout an M_2 tidal cycle. Xing and Davies (1996) examine the same properties at this location with their q^2-q^2l run (Rig 16, Calculation 1) and these results are shown in Fig. 5.6a. To facilitate proper comparison, for this run the model was forced with M_2 input only. Obvious qualitative similarities exist between the two sets of results. Turbulent energy is highest near the sea bed (where vertical shear is greatest) and varies more significantly than the other quantities over a tidal cycle. Mixing length varies least over a tidal cycle and has a parabolic profile since (4.29) ensures that it behaves like κz near boundaries, whilst (4.43c) and (4.45d) force it to

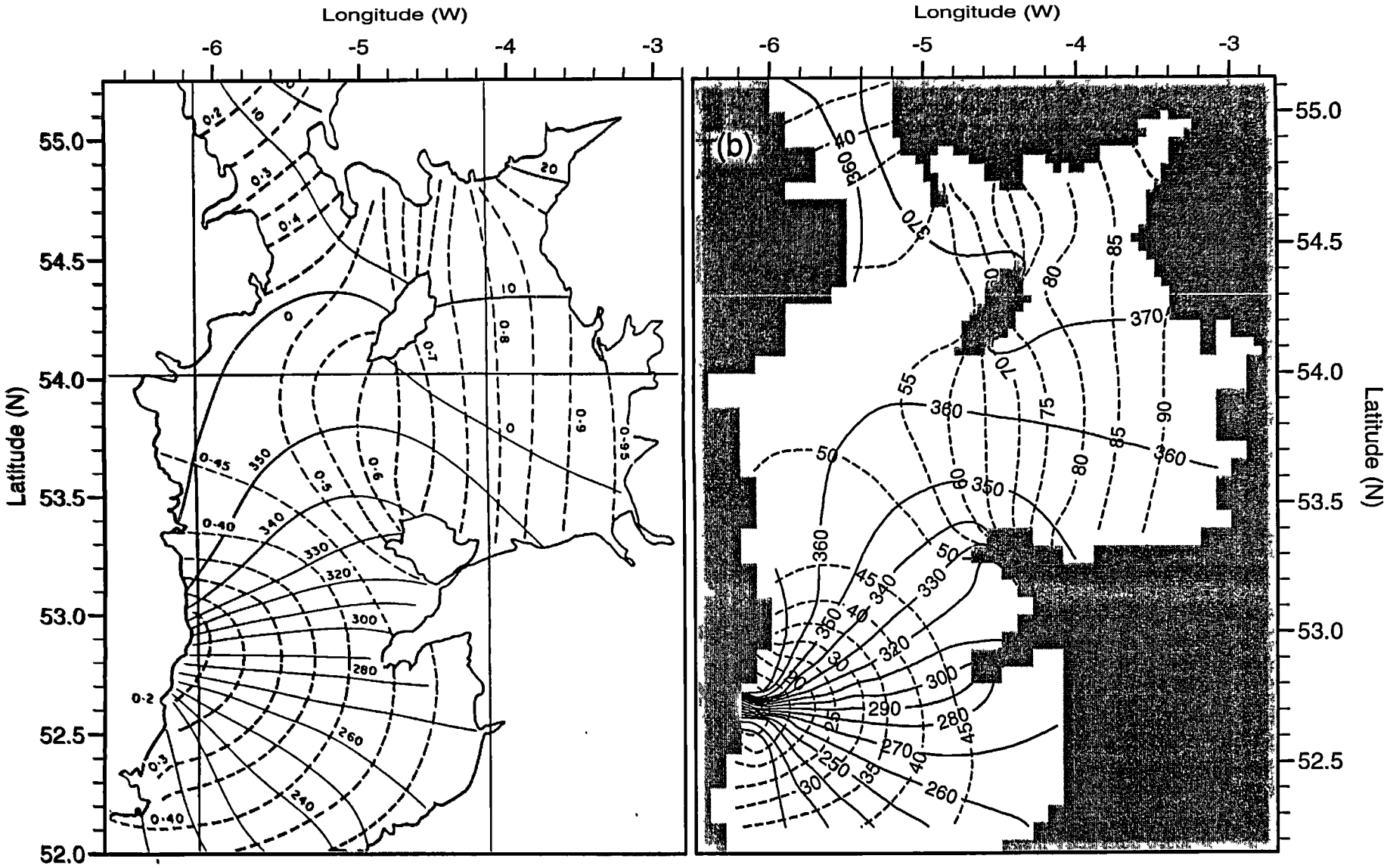

Fig. 5.4 Contours of amplitude (cm, dashed lines) and phase (°, solid lines) of the S_2 tide in the Irish Sea derived from (a) observations (adapted from Robinson, 1979) and (b) ECOMsi.

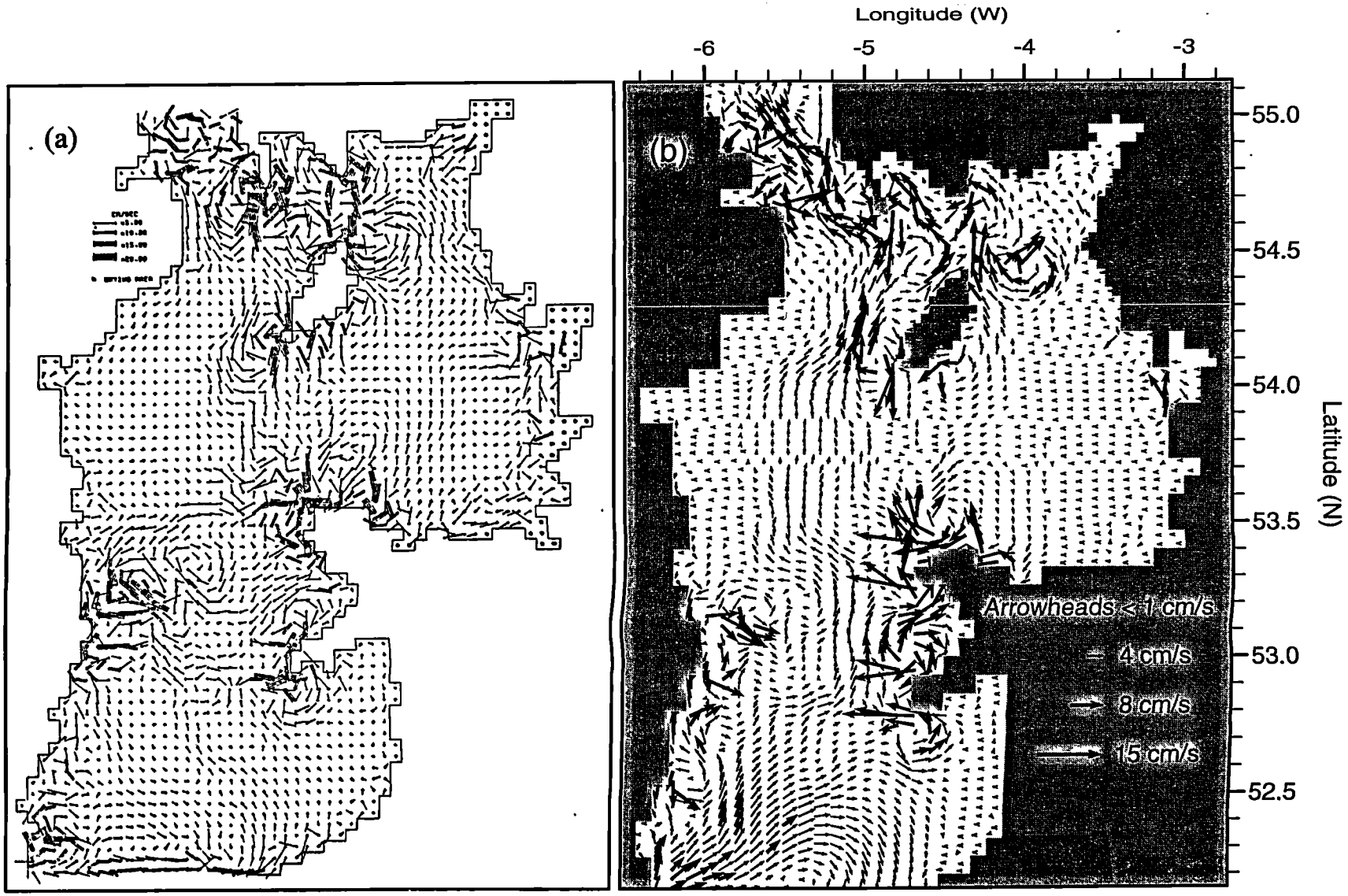

Fig. 5.5 M_2 tidal Eulerian residuals in the Irish Sea (a) from Proctor's (1981) 5 km grid model and (b) ECOMsi. In (b) bold arrows designate residual currents greater than 5 cm s^{-1} and arrowheads only reflect currents less than 1 cm s^{-1}. Note that in the western Irish Sea the tidal residual currents nowhere exceed 3 cm s^{-1} and no gyral pattern is present.

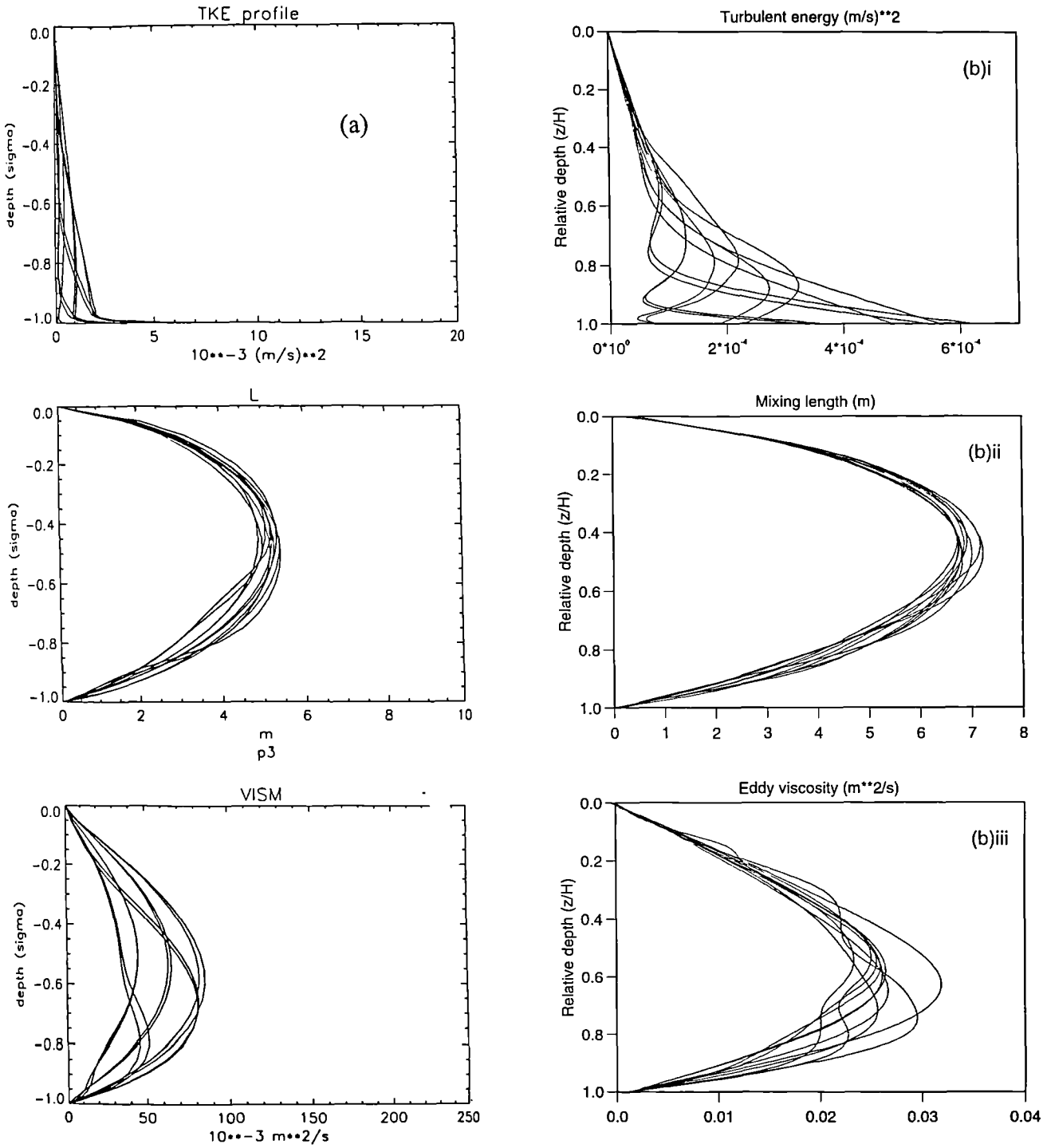

Fig. 5.6 Vertical profiles of turbulent energy, q^2 (m^2 s^{-2}), mixing length (m) and vertical eddy viscosity, K_M (m^2 s^{-1}) at location 2 (Fig. 5.1) in the western Irish Sea from (a) Xing and Davies (1996) and (b) ECOMsi.

become zero there. For this reason, many workers (e.g. Davies *et al.*, 1988; Sharples and Simpson, 1995) prefer simpler, prescribed mixing lengths whose profiles are essentially similar to Fig. 5.6b(ii). The mid-water maximum mixing length predicted by this model was higher than that obtained by Xing and Davies (1996) (7 m as opposed to 6 m). Eddy viscosity also displays a mid-water maximum and falls to zero at surface and bottom boundaries in both models since it is calculated as the product of q, λ and a stability function (see 4.24d). The time variation in eddy viscosity is controlled mainly by the evolution of turbulent energy. Noticeable differences between Fig. 5.6a and Fig. 5.6b are that values of turbulent energy in ECOMsi are lower, by up to an order of magnitude, than those obtained by Xing and Davies (1996). As a consequence, the model predicts maximum eddy viscosities of 0.03 $m^2 s^{-1}$ compared to 0.09 $m^2 s^{-1}$ of Xing and Davies (1996). Turbulent energies obtained here, of 10^{-4} $m^2 s^{-2}$ in mid-water and 4 x 10^{-4} $m^2 s^{-2}$ near the bed, imply velocity fluctuations of 1-2 cm s^{-1} for maximum mean flows of 58-86 cm s^{-1} (see Table 5.3) which seems physically reasonable. Results from a one-dimensional model over a tidal cycle (Sharples and Simpson, 1995) provided contours of turbulent velocity, q (the square root of turbulent energy), between 0.002 and 0.040 m s^{-1}, suggesting a maximum value for q^2 of 1.6 x 10^{-3} $m^2 s^{-2}$, with values of the order 10^{-4} $m^2 s^{-2}$ for much of the cycle. As that model contained several tidal constituents and was applied in shallower water (37 m), the values in Fig. 5.6b(i) seem realistic.

It is possible to deduce the vertical structure of eddy viscosity from a time series of shear stress, calculated from vertical current profiles (Bowden *et al.*, 1959). However, few sets of observations exist where this has been done. Bowden *et al.* (1959) estimated mean eddy viscosities of 0.01-0.03 $m^2 s^{-1}$ from three stations (in 12-20 m of water) near Anglesey. Wolf (1980) statistically analysed current profiles from three stations in the northern Irish Sea and estimated viscosities to be of the order 0.01 $m^2 s^{-1}$. A recent application of a q^2-q^2l model in the East China Sea (Lee and Jung, 1999) also predicted mid-water maxima for K_M of between 0.02 and

0.04 m^2 s^{-1}. In conclusion, the results presented in Fig. 5.6b are considered satisfactory, and are in better agreement with (limited) observations than previous applications of turbulence models in the Irish Sea. Differences between the results shown in Fig. 5.6b and Fig. 5.6a are probably due to the numerical solution of internal modes in the two models and, to a lesser extent, vertical resolution (Xing and Davies (1996) used 25 sigma levels). Xing and Davies (1996) note that reduced viscosity (in their case through an alternative prescription of mixing length) facilitates the prediction of larger vertical shears. As has already been noted, vertical shears predicted by the model used here are in good agreement with observations.

These results demonstrate that this application of ECOMsi makes adequate predictions of all the essential features of tidal processes in the Irish Sea, and performs as well as (and in some respects better than) previous models of the region using similar turbulence closure schemes and grids. To assess the model's ability to correctly predict baroclinic (density-driven) processes, additional validation is required.

5.3 Comparison with diagnostic model studies of shelf-sea fronts

Much of our understanding of frontal dynamics has arisen from semi-analytical and diagnostic models of idealised fronts (e.g. James, 1978; Garrett and Loder, 1981). For this section, ECOMsi was run in a diagnostic mode (equations 4.37 and 4.38 were not evaluated, so the density field remained constant). The model was spun-up until a velocity field consistent with the prescribed density field was obtained. A 2 km square grid was employed with 54 cells in the cross-front direction, 104 cells in the along-front direction and 21 σ-levels. The prescribed density field (see Fig. 5.7a) was uniform in the along-front direction (i.e. into the page). In this way, a pseudo-two-dimensional version of the model was derived where the resulting flow field in the immediate vicinity of the front was forced entirely by the density field. Non-linear terms in the momentum equations were neglected so as to inhibit the formation

of baroclinic instabilities on the three-dimensional front, and a minimal horizontal mixing coefficient (A_M = 10 m^2 s^{-1}) was used to damp computational noise. The results presented here are taken from the mid-point in the along-front dimension (J = 52) in order to minimise any effects due to the solid boundaries (which were assumed to be negligible). Analysis at several other coordinates showed that beyond 10 grid cells from the boundaries there was little variation of the flow field in the along-front direction.

The frontal structure prescribed is shown in Fig. 5.7a. The simulations described here were performed in 100 m of water, in a domain 208 km long by 104 km wide. The strongest density gradients at the front were 0.8 kg m^{-3} over 20 km. These values were chosen to mimic the shelf-sea front described by James (1978) in a rigid-lid, primitive equation model of frontal circulation. The frontal structure is representative of the tidal mixing front in the Celtic Sea, so the density gradient is physically realisitic although somewhat higher than values observed in the western Irish Sea in summertime (e.g. Fig. 3.9e). The model reached a steady state after 6 days of integration, and the resulting velocity field is shown in Fig. 5.7b and Fig. 5.7c. Flow was strongest in the along-front direction (Fig. 5.7b) with peak currents of 24 cm s^{-1} near the surface (at σ-level 5), and at the centre of the front. The small decrease toward the surface was due to the reverse density gradient in the top 20 m of water. The flow in Fig. 5.7b is less than that obtained by a vertical integration of the thermal-wind equation, subject to zero flow at the bed, which predicts maximum flows of approximately 30 cm s^{-1}. However, the model contains friction (responsible for the secondary circulation seen in Fig. 5.7c) and also some horizontal diffusion, so this is not surprising. The modelled along-front flow was geostrophic to leading order which is consistent with our theoretical understanding (Hill *et al.*, 1993). The circulation induced by the unbalanced part of the cross-frontal pressure gradient is shown in Fig. 5.7c, where arrows represent all current vectors whose horizontal component (u) is greater than 0.5 cm s^{-1} *or* whose vertical component (w) exceeds

0.1 mm s^{-1}. To emphasise regions where cross-frontal flow was greatest, bold arrows designate vectors for which $u > 5$ cm s^{-1}. Maximum cross-frontal flow (7 cm s^{-1}) was found in the bottom boundary layer, and there were also strong flows at the level of the pycnocline. The maximum vertical velocity of 0.7 mm s^{-1} was found immediately to the well-mixed side of the front.

James (1978) obtained qualitatively similar results but with slightly reduced magnitudes (peak along-front flows of 12 cm s^{-1} and cross-frontal flows of 3-4 cm s^{-1} which were more evenly distributed throughout the vertical). The different results can be partly explained by the many differences between the two models (e.g. free surface vs. rigid lid, treatment of horizontal eddy viscosity, the exact manner of establishing the density field). Also, James (1978) used a Munk-Anderson (1948) scheme to determine vertical eddy viscosity, in which the Richardson number was calculated from an assumed tidal current profile. This would have resulted in higher current shears, therefore larger values of K_M than obtained in this run where K_M was calculated from turbulence closure physics based on the frontal circulation alone. To investigate the effects of an increase in eddy viscosity, Fig. 5.8 presents results from a further diagnostic run in which eddy viscosity was held at $K_M = 0.05$ m^2 s^{-1}. All other conditions were the same as for the results shown in Fig. 5.7. In Fig. 5.8b, the maximum along-front flow is reduced to 14 cm s^{-1} whilst the cross-frontal circulation is slightly stronger with maximum u of 7.8 cm s^{-1} in the boundary layer, and maximum upwelling of 0.9 mm s^{-1}.

A subtle difference in the transverse circulations is that, whilst in Fig. 5.8c there is relatively strong flow towards the stratified side everywhere above the pycnocline, in Fig. 5.7c the same flow is concentrated at the pycnocline. A consequence of this result is that, apart from in the bottom boundary layer, the advection of density is negligible in frontal dynamics (significant flows occur only on isopycnal surfaces,or put mathematically, $\mathbf{V}.\nabla\rho = 0$). This explains the relative success of heating-stirring

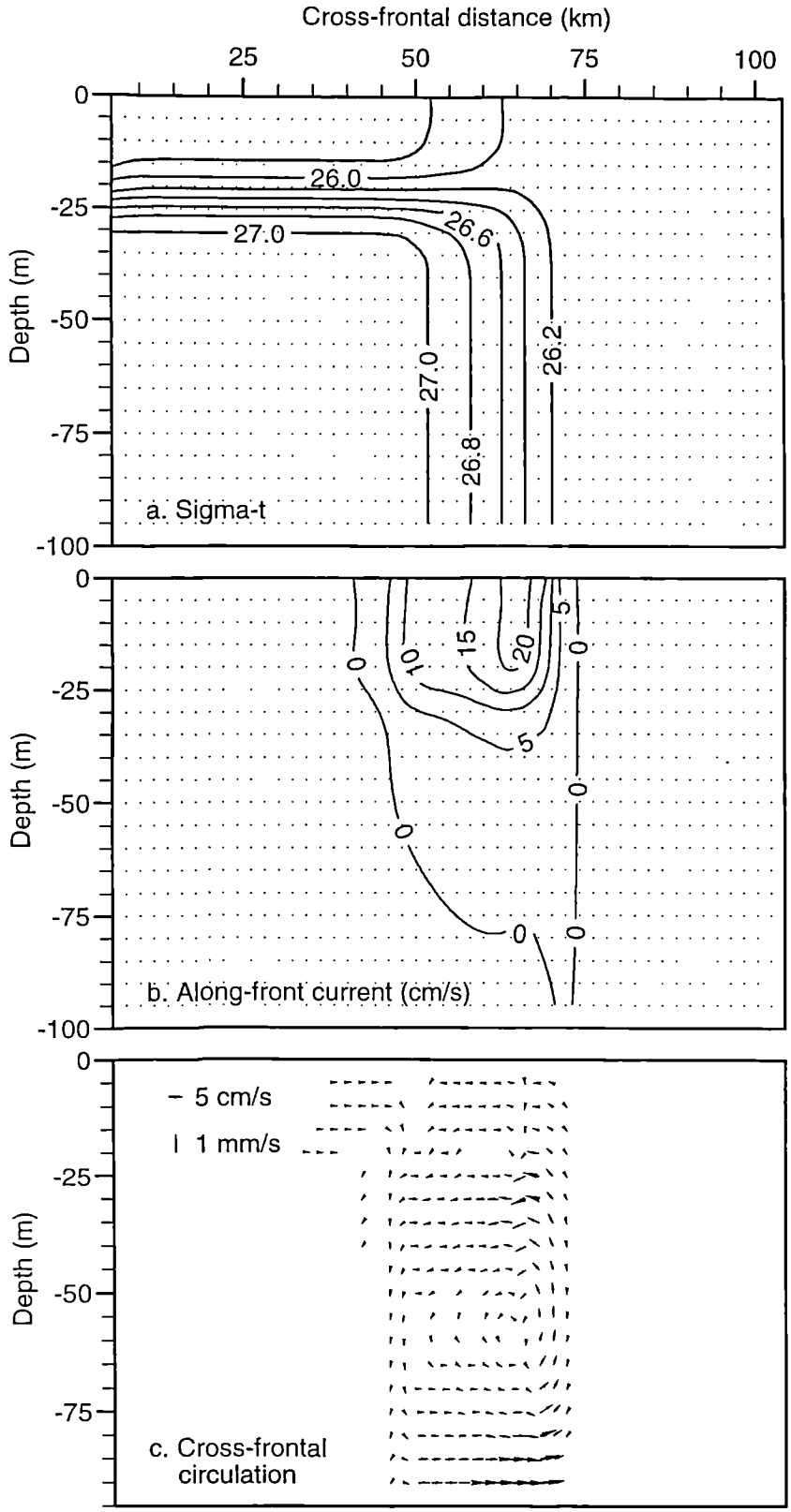

Fig. 5.7 Results from a diagnostic model run for an idealised shelf sea front, showing (a) density field (σ_t) which is uniform in the along-front direction, (b) along-front current (cm s^{-1}) where isopleths denote flow into the page and, (c) cross-frontal circulation in the vertical plane (bold arrows indicate $u > 5$ cm s^{-1}). In this run, vertical mixing was determined from turbulence closure. Note the different vertical and horizontal scales in (c).

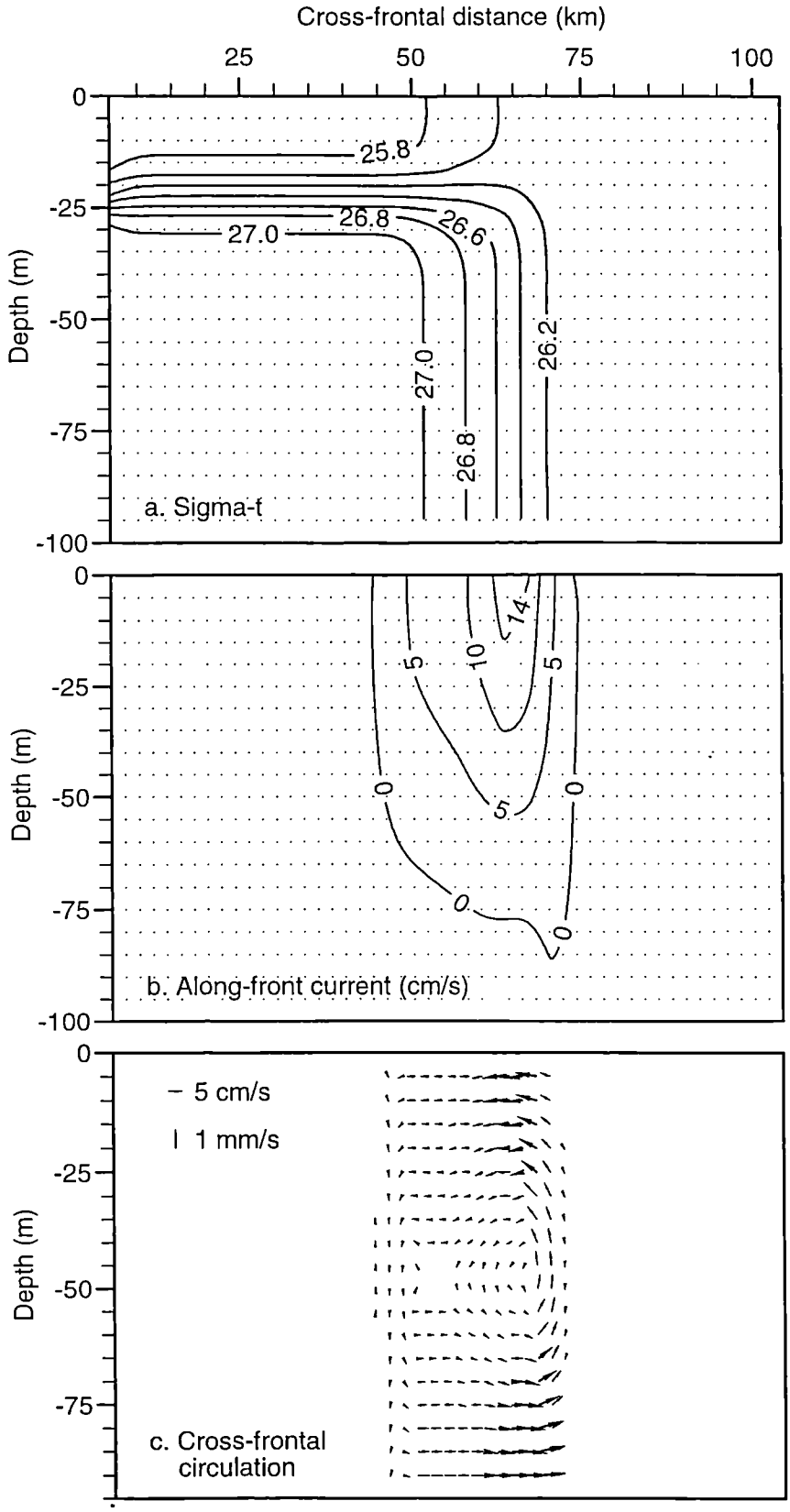

Fig. 5.8 Results from an idealised frontal diagnostic model run (as for Fig. 5.7) only for constant vertical eddy viscosity, $K_M = 0.05$ m^2 s^{-1} . (a) density (σ_t), (b) along-front current (cm s^{-1}) where isopleths denote flow into the page and, (c) cross-frontal circulation in the vertical plane (bold arrows indicate $u > 5$ cm s^{-1}).

models (Simpson and Bowers, 1981; Hill, 1993) in the prediction of frontal evolution, despite the model assumptions precluding density advection (Simpson, 1981). Horizontal flow at the pycnocline may have implications for the recycling of nutrients (from well-mixed waters) to support a standing stock of phytoplankton on the pycnocline. The advection of density in the bottom boundary layer is of great dynamical interest, and is discussed further in the final chapter.

To further assess model performance in the context of frontal dynamics, comparison was made with the two-dimensional, semi-analytical model of Garrett and Loder (1981) which was based on the following steady-state simplifications to the momentum equations:

$$-fv + \frac{1}{\rho}\frac{\partial p}{\partial x} = \frac{\partial}{\partial z}\left(K_M \frac{\partial u}{\partial z}\right) \qquad (5.3)$$

$$fu = \frac{\partial}{\partial z}\left(K_M \frac{\partial v}{\partial z}\right) \qquad (5.4)$$

$$\frac{\partial p}{\partial z} = -\rho g \qquad (5.5)$$

where v is the along-front current, u is the cross-front current and the eddy viscosity, K_M, was calculated from the local Richardson number. Fig. 5.9 reproduces the results of Garrett and Loder's (1981) model for two different, algebraically prescribed density fields. (The type 1 front in Fig. 5.9a corresponds to $s = 1$ in Garrett and Loder's equation 4.8, whilst the type 2 front in Fig. 5.9b corresponds to $s = 0$). For each class of front, Fig. 5.9 shows currents u and v, normalised by the along-front current that would be obtained at the surface by integrating the thermal wind equation (1.2) subject to $v = 0$ at the bed, and for the type 1 isopycnal arrangement. Results are shown for three different Ekman numbers, defined by $E = K_M/(fh^2)$.

The initial density field in ECOMsi cannot be prescribed identically to the algebraic forms used by Garrett and Loder (1981), but essentially similar (and uniform along-

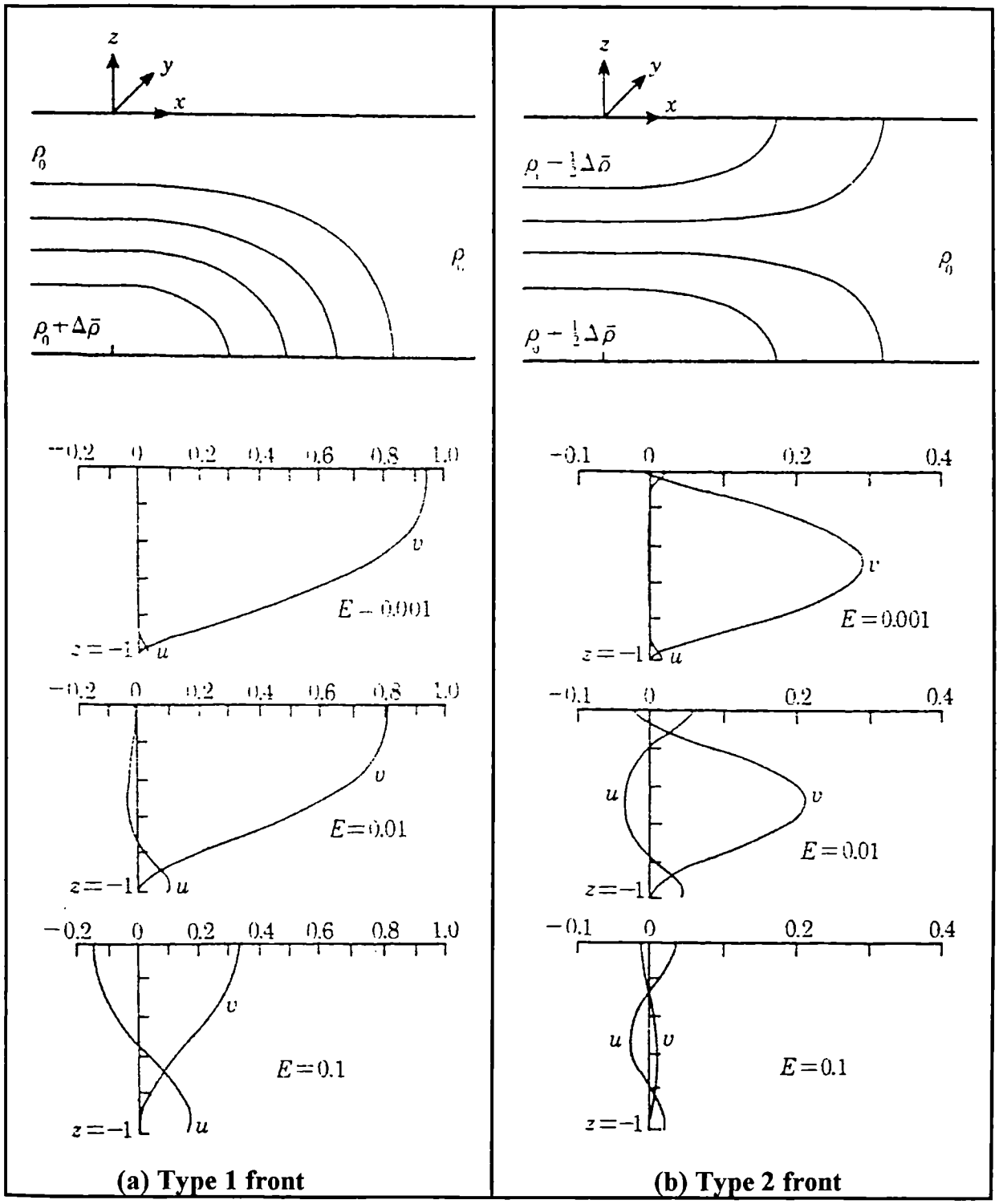

Fig. 5.9 Results from the semi-analytical model of Garrett and Loder (1981) for two different isopycnal arrangements. (a) Type 1 (bottom) front and, (b) Type 2. (surface and bottom) front. The graphs below the respective density structures show the along-front current (v) and cross-front current (u), normalised against the surface current derived from thermal wind calculations, for three different Ekman numbers where $E = K_M/(fh^2)$. Adapted from Garrett and Loder (1981).

front) isopycnal arrangments can be obtained using the idealised 2 km grid described previously. Since the model depth was 100 m and the Coriolis parameter, f, was approximately 10^{-4} s^{-1} then Ekman depth, $E \approx K_M$ (numerically) and model runs analogous to those of Garrett and Loder (1981) were performed by use of a constant vertical eddy viscosity taking the same numerical value as the Ekman numbers shown in Fig. 5.9. The ECOMsi type 1 frontal structure is shown in Fig. 5.10a. For the simulations described here, the model was run in a diagnostic mode for 6 days, then the velocity field at the mid-point of the domain (J=52) was analysed. The vertical profiles presented correspond to the cross-front coordinate where velocity was greatest (X=29) and are normalised against thermal wind calculations based on the density gradient, $\partial\rho/\partial x$, between X=28 and X=30.

The vertical profile of along-front current for the type 1 front with $K_M = 0.001$ m^2 s^{-1} (corresponding to $E = 0.001$) is shown in Fig 5.10b. The striking difference between this plot and the corresponding profile of v in Fig. 5.9a is the existence of negative along-front flow near the bed. No constraints are placed on the velocity field in the primitive equation model (apart from a dependence on the quadratic slip boundary condition, 4.44a). Although the semi-analytical model also uses a (linear) slip bottom boundary condition, the along-front current *is* constrained by adjustment of the sea surface slope to give zero cross-frontal volume flux. As discussed in §1.3 (see equation 1.4), integration over depth of (5.4), subject to the condition $U = 0$ (where U is the depth-averaged cross-frontal current), implies that $v = 0$ at the bed. This provides a reference point for otherwise indeterminate geostrophic calculations. The surface adjustment ensures isostasy at the bed, so it is unsurprising that $v = 0$ at $z = -h$ in Fig. 5.9. Notwithstanding the fact that this analysis requires the existence of some form of slip condition (it is trivial to make bed stress zero if $K_M = 0$ at the bed, as mixing length theory suggests), there is no physical necessity for along-front flow to be zero at the bed. If cross-frontal flow is due to internal friction breaking the

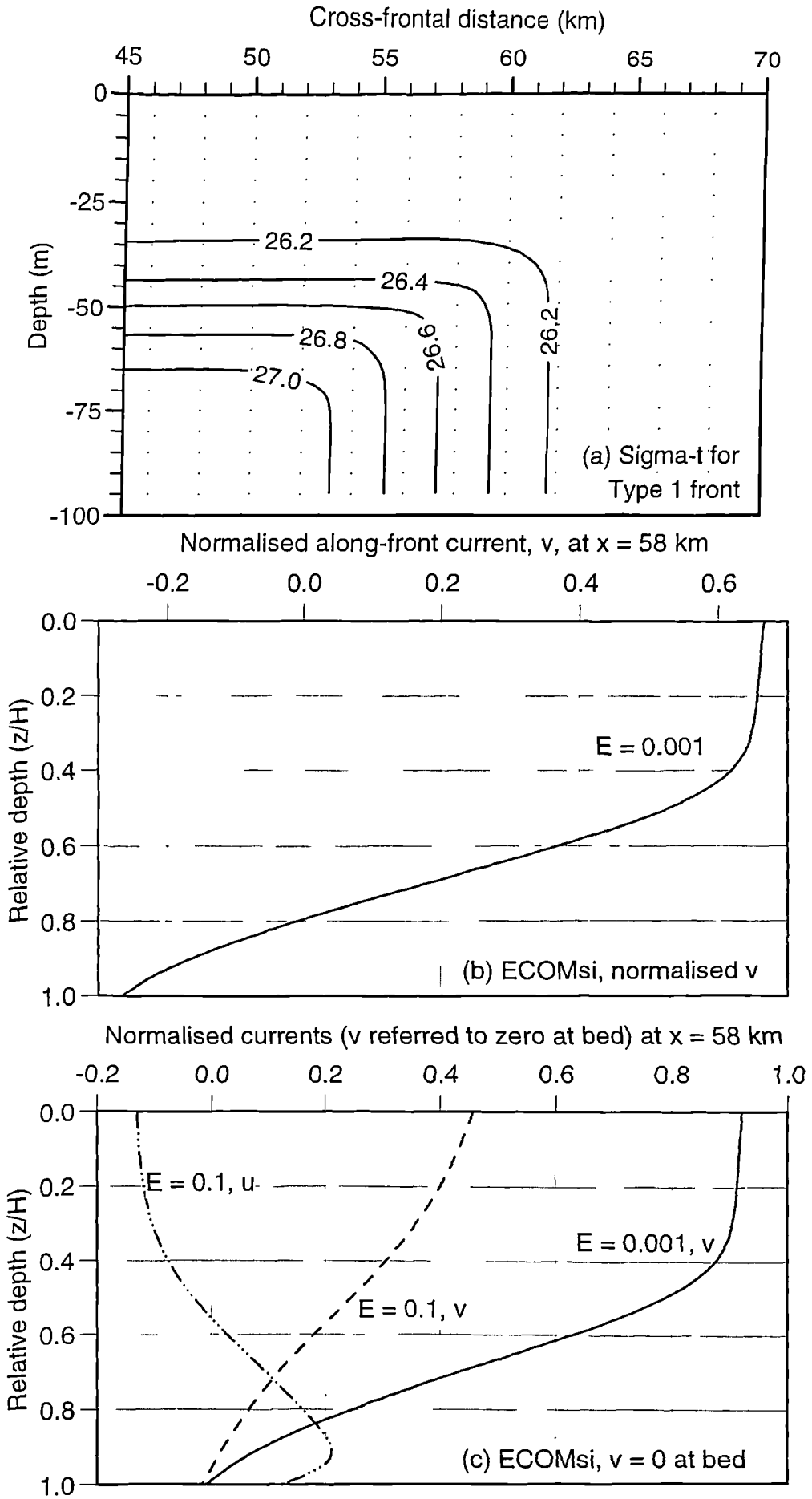

Fig. 5.10 Diagnostic model run for a type 1 front. (a) σ_t for an x-z slice. (b) along-front current, v, at grid cell (29,52) normalised against the surface current obtained from thermal wind calculations (with $v = 0$ at the bed) for $K_M = 0.001$ m^{2}s^{-1}, corresponding to an equivalent Ekman number, $E = 0.001$. (c) along-front normalised current *shear* ($v = 0$ at the bed) for $E = 0.001$, 0.1 and normalised cross-front current, u, for $E = 0.1$.

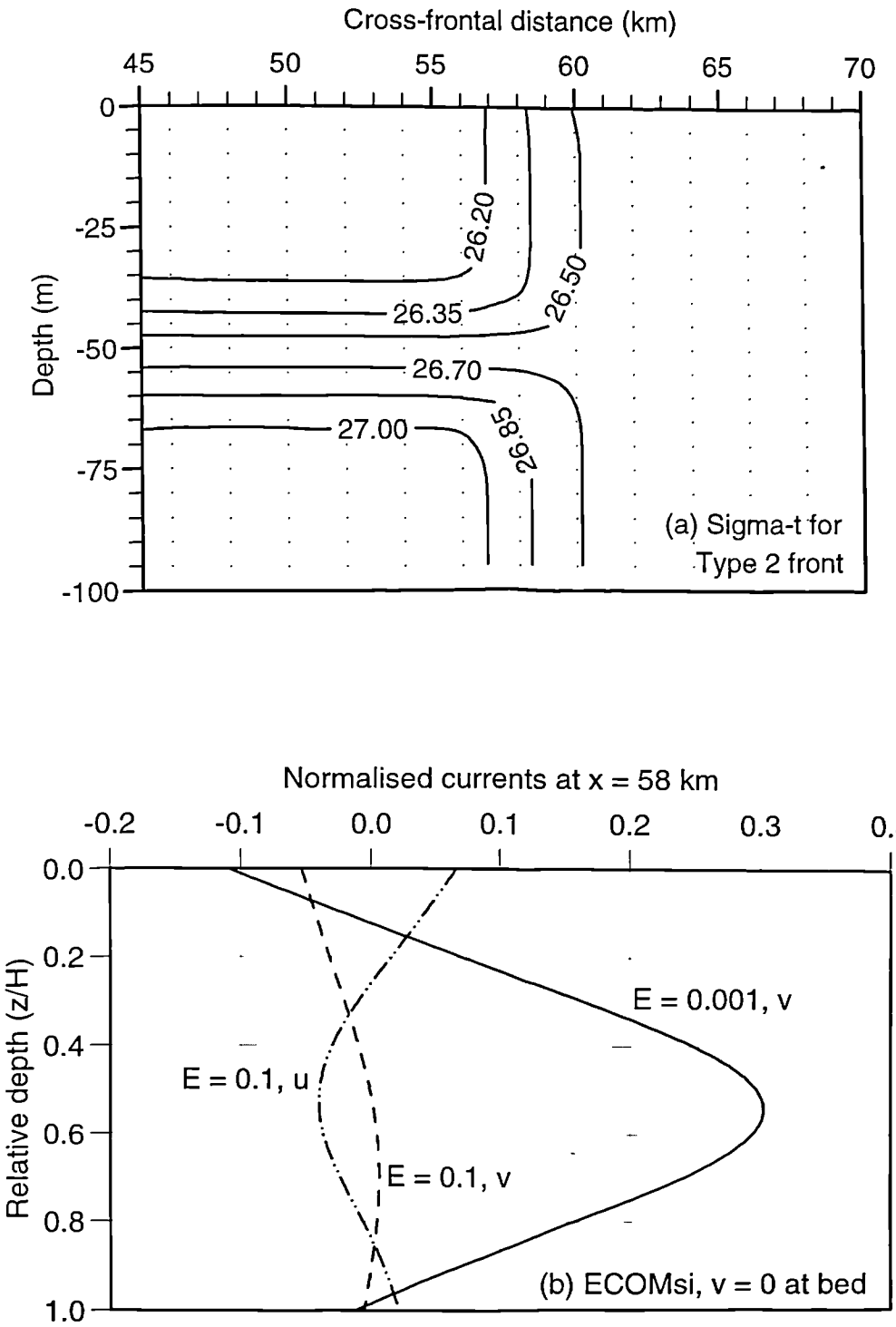

Fig. 5.11 Diagnostic model run for a type 2 front. (a) σ_t for an x-z slice. (b) along-front current shear and cross-front currents at grid cell (29,52) normalised against the surface current obtained from thermal wind calculations (with $v = 0$ at the bed) for $K_M = 0.001$ m^2s^{-1} and 0.1 m^2s^{-1} (corresponding to equivalent Ekman numbers, $E = 0.001, 0.1$).

constraint of geostrophy then (in the coordinate system used here) Ekman dynamics confirms that positive, nearbed cross-frontal flow is due to negative along-front flow.

In terms of model validation, the important result is that the vertical shear in the along-front current is in good agreement with two-dimensional models and geostrophic calculations. For better comparison with Fig. 5.9, the normalised along-front currents in Fig. 5.10c are referenced to $v = 0$ at the bed. Currents are shown for $K_M = 0.001$ m^2s^{-1} and 0.1 m^2s^{-1} (corresponding to $E = 0.001$, 0.1 in Fig 5.9a) and the cross-front current, u, is also shown for $K_M = 0.1$ m^2s^{-1}. (For $K_M = 0.001$ m^2s^{-1} , u is negligible except at the deepest sigma level, so is not shown). Despite the very different modelling approaches, there is reasonable agreement between the profiles shown in Fig. 5.10c and those in Fig. 5.9a. Along-front flow was 0.9 of the geostrophic value for low friction ($E = 0.001$) and cross-front flow was of lower order except when $E \leq 0.1$. Model results for the case of a type 2 front are presented in Fig. 5.11b. For the low friction case ($E = 0.001$), the flow at mid-depth reached 0.3 of the geostrophic value, as found by Garrett and Loder (1981). The negative values at the surface obtained here with the primitive equation model were probably due to an asymmetry in the prescribed density field depicted in Fig. 5.11a. For a type 2 front, high friction ($E = 0.1$) caused significantly diminished flow in both models.

5.4 Comparison with laboratory studies of baroclinic instability

As a further test of baroclinic dynamical performance, the model was used to simulate a rotating, two-layer adjustment problem. The geostrophic adjustment of two-layer systems has been much studied in the laboratory (e.g. Saunders, 1973; Griffiths and Linden, 1981; Griffiths and Linden, 1982). The model runs described here attempted to emulate the experiments of Griffiths and Linden (1981), who created a surface vortex in a rotating tank by filling an inner cylinder with less dense fluid than its surroundings. When the entire system had been brought to solid body rotation, the inner cylinder was carefully withdrawn and the less dense fluid spread

radially at the surface. Conservation of angular momentum imparts anticyclonic motion to the surface vortex, which reached quasi-geostrophic equilibrium over an inertial timescale. Griffiths and Linden (1981) found that anticyclones thus formed were unstable over the parameter range considered. Baroclinic instability caused waves to grow rapidly such that the anticyclonic vortex became asymmetrical and divided into a distinct number of smaller eddies, which finally developed into vortex dipoles. The number of resulting vortices was found to depend on two dimensionless parameters: $\delta = h/H$, the ratio of the depth of buoyant fluid in the inner cylinder to the total depth, and $\theta = (R_D/R_0)^2$, the square of the ratio of the internal Rossby radius of deformation, R_D (see equation 1.5), to the initial radius of the inner cylinder, R_0. Wavenumbers of between 2 and 5 were observed by Griffiths and Linden (1981) and the onset of instability occurred after 2-10 rotation periods.

The model simulations used 21 σ-levels and a 1 km square grid, with 71 cells in both the x and y directions. To match the inviscid assumptions of the laboratory experiments (and because the interface of the two-layer system is at the surface), bed friction in the model was set to zero and vertical eddy viscosity was held at molecular values, $K_M = 10^{-6}$ m^2 s^{-1}. It was necessary to prescribe a small, constant value of horizontal viscosity ($A_M = 1$ m^2 s^{-1}) to maintain computational stability. The simulations were carried out in 20 m depth, using a timestep of 60 s. For the first simulation, a 4 km radius 'cylinder' of less dense fluid was approximated with suitable initial model conditions, where salinities were 33.4 over the full depth of the cylinder and 35.0 in the rest of the model domain, with temperature constant at 15 °C. This gave densities of $\sigma_t = 24.74$ kg m^{-3} inside the cylinder and $\sigma_t = 25.97$ kg m^{-3} elsewhere. The model was run for 6 days and the adjustment of the less dense fluid was observed. This technique has been employed previously by James (1996) to compare different numerical schemes for tracer advection. The adjustment problem is an ideal test for advection schemes since success of the model depends on

maintaining sharp gradients of density at the interface. In the simulations described here, the advection scheme of Smolarkiewicz (1984) was employed.

The initial conditions described above give dimensionless parameters, $\delta = 1$ and $\theta = 1$, which predict a disturbance with wavenumber $n = 2$ (i.e. breakdown into two vortex pairs) (Griffiths and Linden, 1981). The adjustment of the density field can be seen in the sequence of surface salinity contours shown in Fig. 5.12, where time is expressed in inertial periods (16 hours for these simulations). The salinity contour interval is 0.2. The contours in Fig. 5.12 show that although a sharp interface between the two different density fluids was maintained, there was some degradation of the two-layer system due to the artificial diffusivity required for computational stability. The Smolarkiewicz (1984) scheme also appears to give noisier results in two-layer simulations than the PPM scheme described by James (1996) for a similar experiment. Surface currents greater than 5 cm s^{-1} are shown by the arrows in Fig. 5.13, for the same time steps. The vortex begins to become unstable after 4 rotation periods, as the current vectors (Fig. 5.13b) show. Currents near the bed (Fig. 5.14) are cyclonic, as ambient fluid moves radially inwards to replace the buoyant fluid of the inner cylinder, and angular momentum is conserved.

After 6 rotation periods (Fig. 5.12c) there are signs of a possible transition to either a disturbance with wavenumber $n = 3$, or else a vortex dipole, but this development is transient and by 8 rotation periods the vortex has split into 2 distinct eddies (Figs. 5.12e and 5.13e). The surface velocity and salinity fields at T = 8 (8 rotation periods, 133 hours) are shown superimposed in Fig. 5.15. This reveals two anticyclonic eddies, connected by a narrow high velocity stream with flow in opposing directions along its two sides. Identical observations were made by Griffiths and Linden (1981), who noted that the eddies moved radially outwards and the narrow jet eventually broke. Development of the newly-formed eddies into classic vortex dipoles, and the complete separation of vortices, could not be reproduced in these

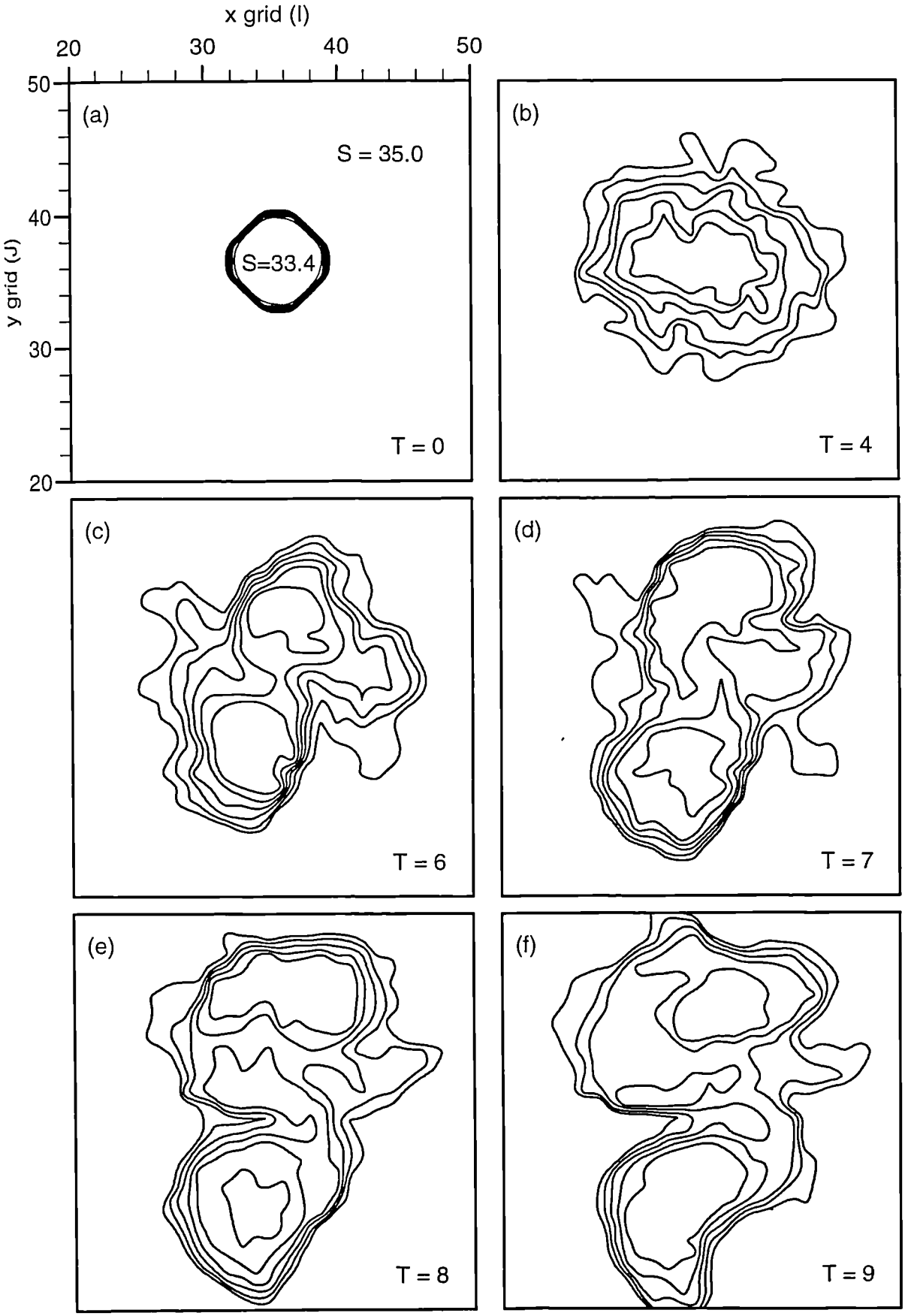

Fig. 5.12 Contours (interval of 0.2) of surface salinity at 0, 4, 6, 7, 8 and 9 rotation periods for a numerical cylinder adjustment experiment with the dimensionless parameters (see text for details) $\theta = 1$, $\delta = 1$, and initial cylinder radius of 4 km. The disturbance has wavenumber $n = 2$.

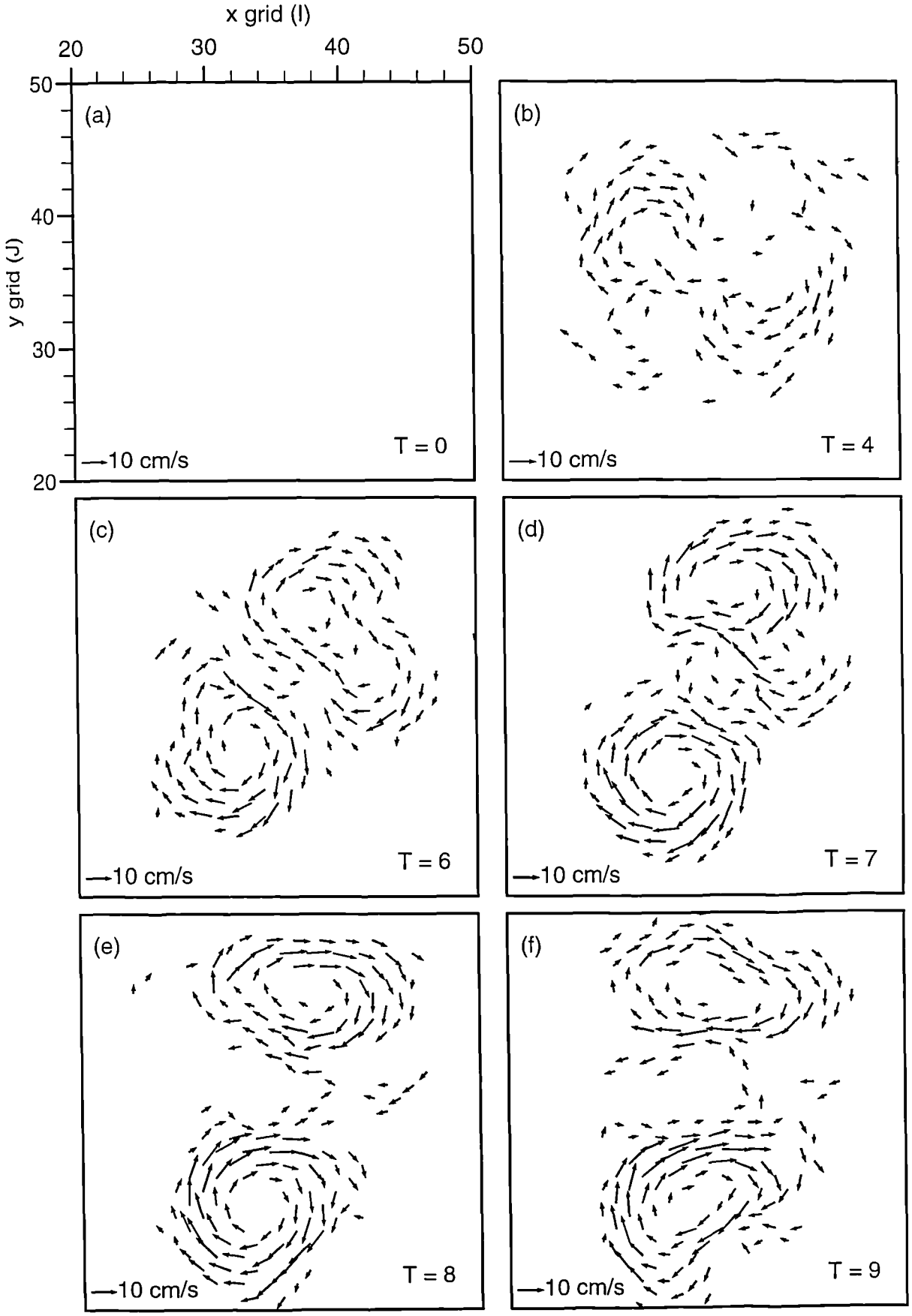

Fig. 5.13 Surface current vectors (for currents > 5 cm s^{-1}) at 0, 4, 6, 7, 8 and 9 rotation periods for a numerical cylinder adjustment experiment with the dimensionless parameters $\theta = 1$, $\delta = 1$, and an initial cylinder radius of 4 km. The disturbance has wavenumber $n = 2$.

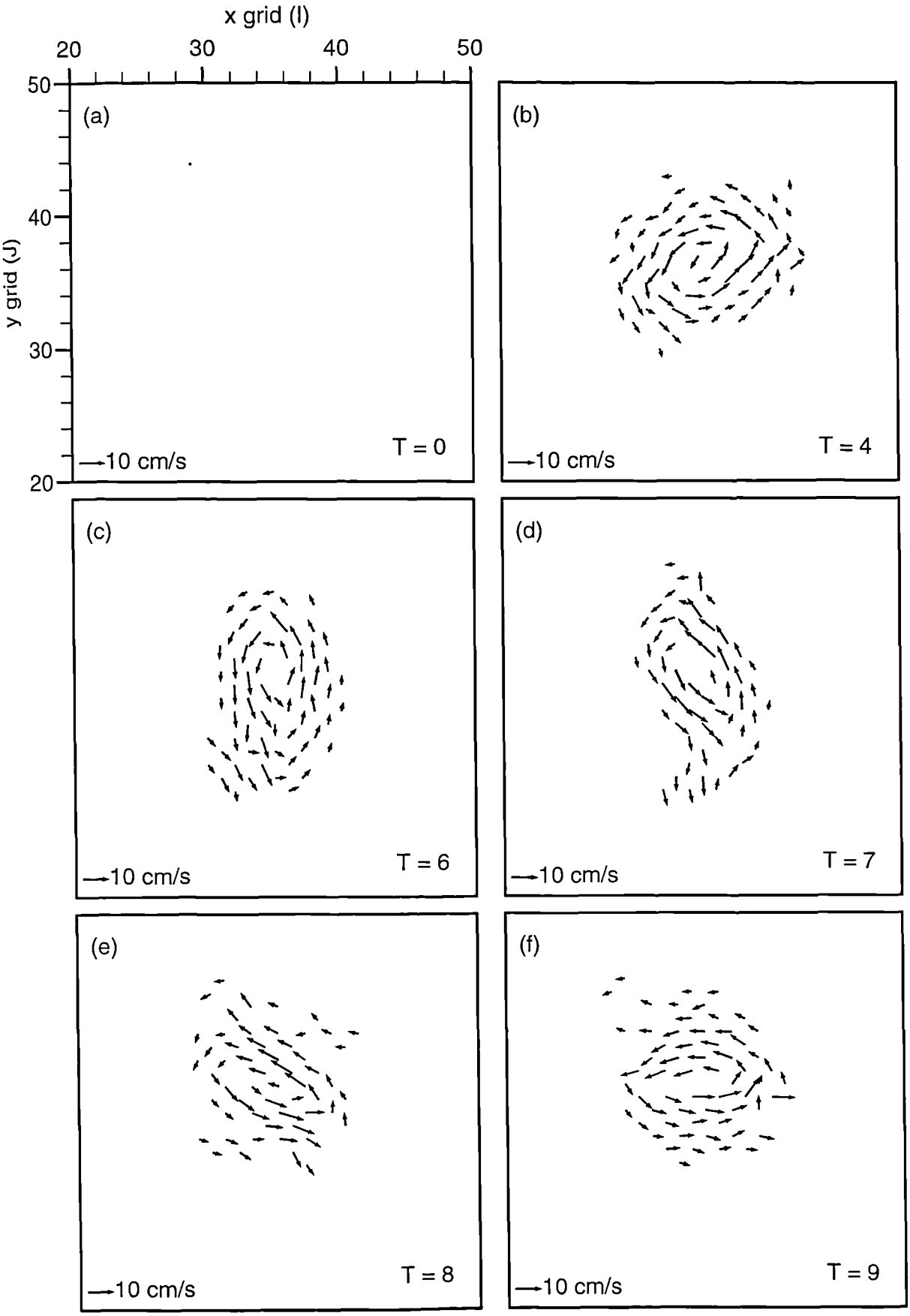

Fig. 5.14 Nearbed ($\sigma = 20$) current vectors (for currents > 5 cm s^{-1}) at 0, 4, 6, 7, 8 and 9 rotation periods for a numerical cylinder adjustment experiment with the dimensionless parameters $\theta = 1$, $\delta = 1$, and an initial cylinder radius of 4 km. Motion is cyclonic at this level.

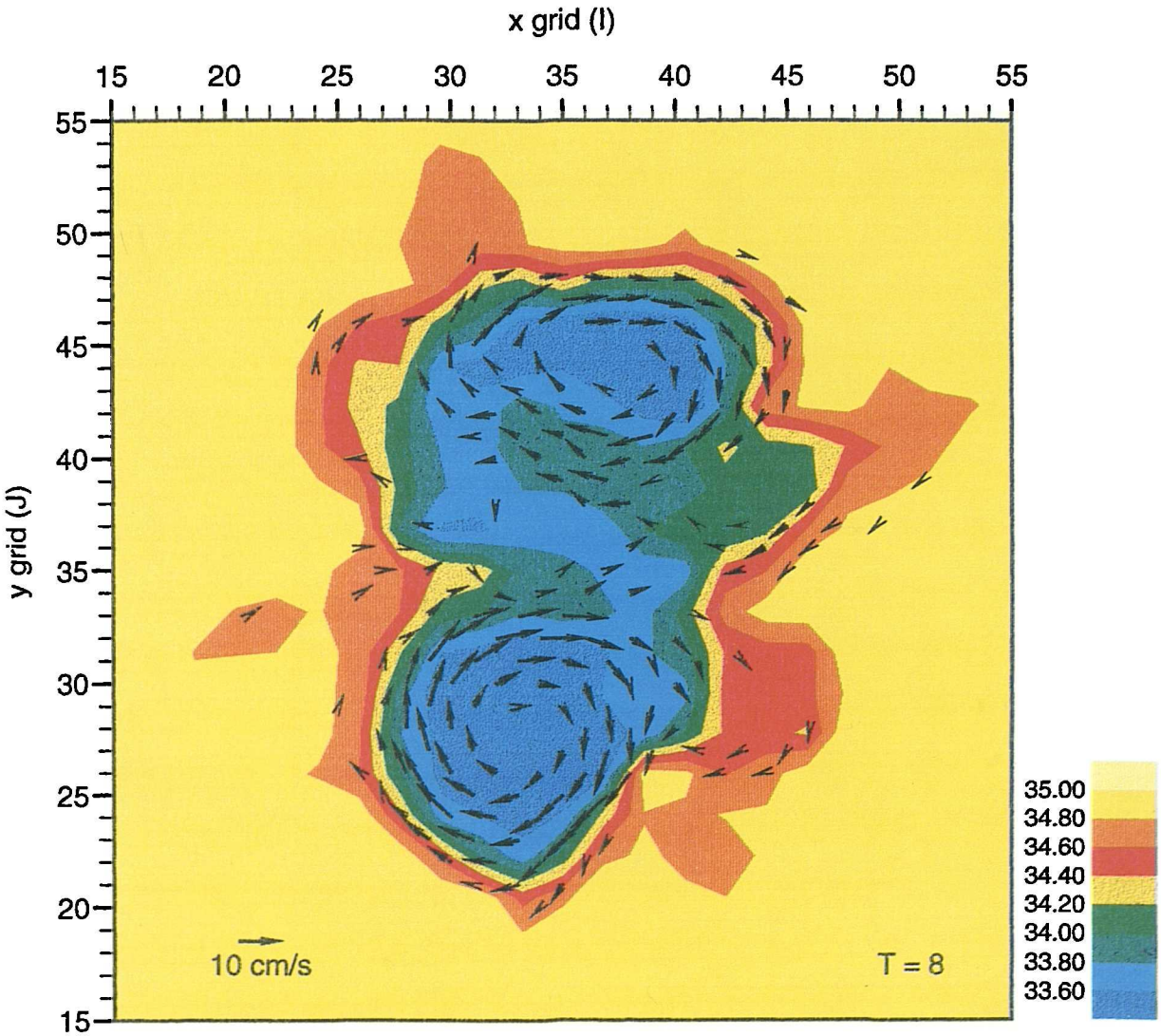

Fig. 5.15 Surface current vectors (> 5 cm s^{-1}) at time T = 8 (8 rotation periods, corresponding to 133 hours of integration) overlaid on the surface salinity distribution at the same time. Note the formation of two distinct vortices, and also the similarity with Fig. 2 of Griffiths and Linden (1981).

model simulations. This may have been due to the prescribed horizontal diffusivity (plus any numerical diffusivity present) damping the growth of instabilities. Another factor is the 1 km resolution of the numerical grid, which is capable of resolving the $n = 2$ disturbance but may not resolve subsequent development into dipoles.

An attempt to reproduce the less easily resolved disturbance with wavenumber $n = 4$ was only partially successful. A central region with salinity 33.4 (σ_t = 24.74 kg m^{-3}) and initial radius 7 km was surrounded by ambient fluid of salinity 34.6 (σ_t = 25.61 kg m^{-3}), giving dimensionless parameters $\theta = 0.1$, $\delta = 1$. Surface currents greater than 5 cm s^{-1} are shown in Fig. 5.16. The velocity field after 1 rotation period (Fig. 5.16b) is presented to demonstrate the initial quasi-geostrophic adjustment of the system. Instabilities begin to develop after 4 rotation periods (Fig. 5.16c). Although four smaller eddies are produced, separation is incomplete and only a fraction of the initial volume of less dense fluid is partitioned amongst these. The central anticyclone persists and is stable to further instability, once volume has been lost to the smaller vortices. This is inconsistent with the laboratory results of Griffiths and Linden (1981) who could not produce a stable surface vortex, although the (temporary) re-establishment of a central vortex was observed in some of their constant flux experiments. Currents near the bed (σ-level 20) show the development of four corresponding cyclones (Fig. 5.17). These are due to vortex stretching of the lower layer beneath the less dense fluid spreading at the surface. Lower layer flows in the laboratory experiments of Griffiths and Linden (1981) were not visualised so no direct comparison can be made, although Saunders (1973) found that an initial cylinder of denser fluid can break into discrete vortices in a similar way to the results described here. It *is* possible to identify vortex dipoles in the layer-averaged currents between σ-levels 2 - 10 inclusive. These depth-averaged currents are shown superimposed on the surface salinity field after 7 rotation periods in Fig. 5.18.

The ability of the numerical model to mimic two-layer adjustment is limited by its discretised nature and both its horizontal and vertical resolution, as well as horizontal diffusivity stabilising baroclinic growth. The incomplete separation of vortices in the $n = 4$ experiment may also have been influenced by the proximity of lateral boundaries and the step-like prescription of initial conditions. Finally, the hydrostatic nature of the numerical model describes buoyancy dynamics imperfectly when vertical motion is important in the development of the instability. Nevertheless, whilst the individual details of these experiments were not identical to their laboratory counterparts, the splitting into vortices on the scale of internal Rossby radii, consistent with theoretical expectations, was observed. It would be interesting to attempt finer resolution numerical simulations of baroclinically unstable laboratory flows in order to better understand their detailed dynamics and also the way in which baroclinic instability is represented in primitive equation models.

These results demonstrate that the model is capable of simulating baroclinic instability and can maintain sharp gradients of density in the presence of strong advective flow fields. This, and the prediction of along-front jets described in the previous section, provide a measure of confidence in the baroclinic performance of the model. This is important if it is to capture all the significant processes that obtain during seasonal simulations in a realistic, shelf sea setting as described in the next chapter.

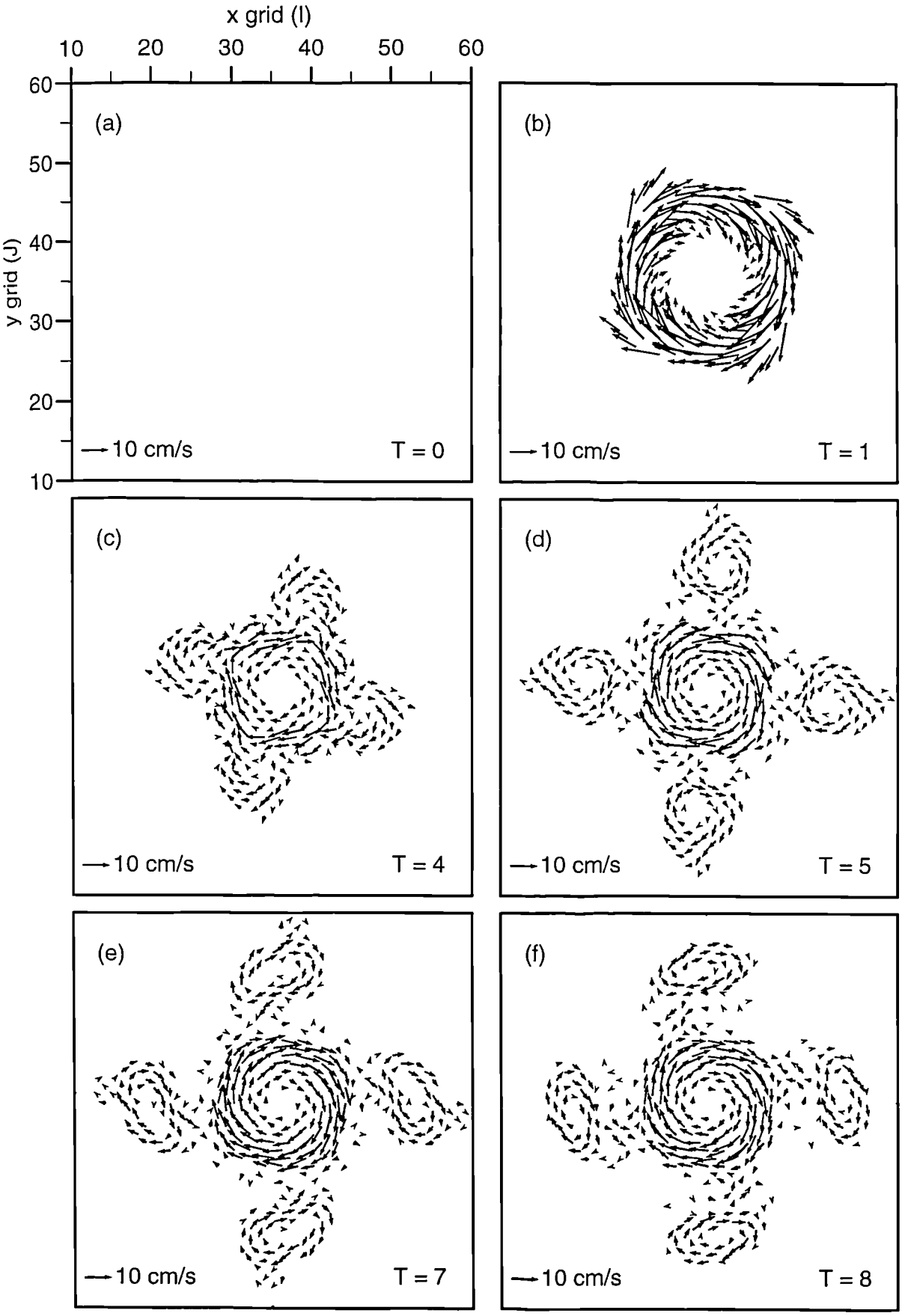

Fig. 5.16 Surface current vectors (> 5 cm s^{-1}) at 0, 1, 4, 5, 7 and 8 rotation periods for a numerical cylinder adjustment experiment with the dimensionless parameters $\theta = 0.1$, $\delta = 1$ ($R_0 = 7$ km). The disturbance of wavenumber, $n = 4$, does not develop completely and the central anticyclone reforms and remains stable to further instability.

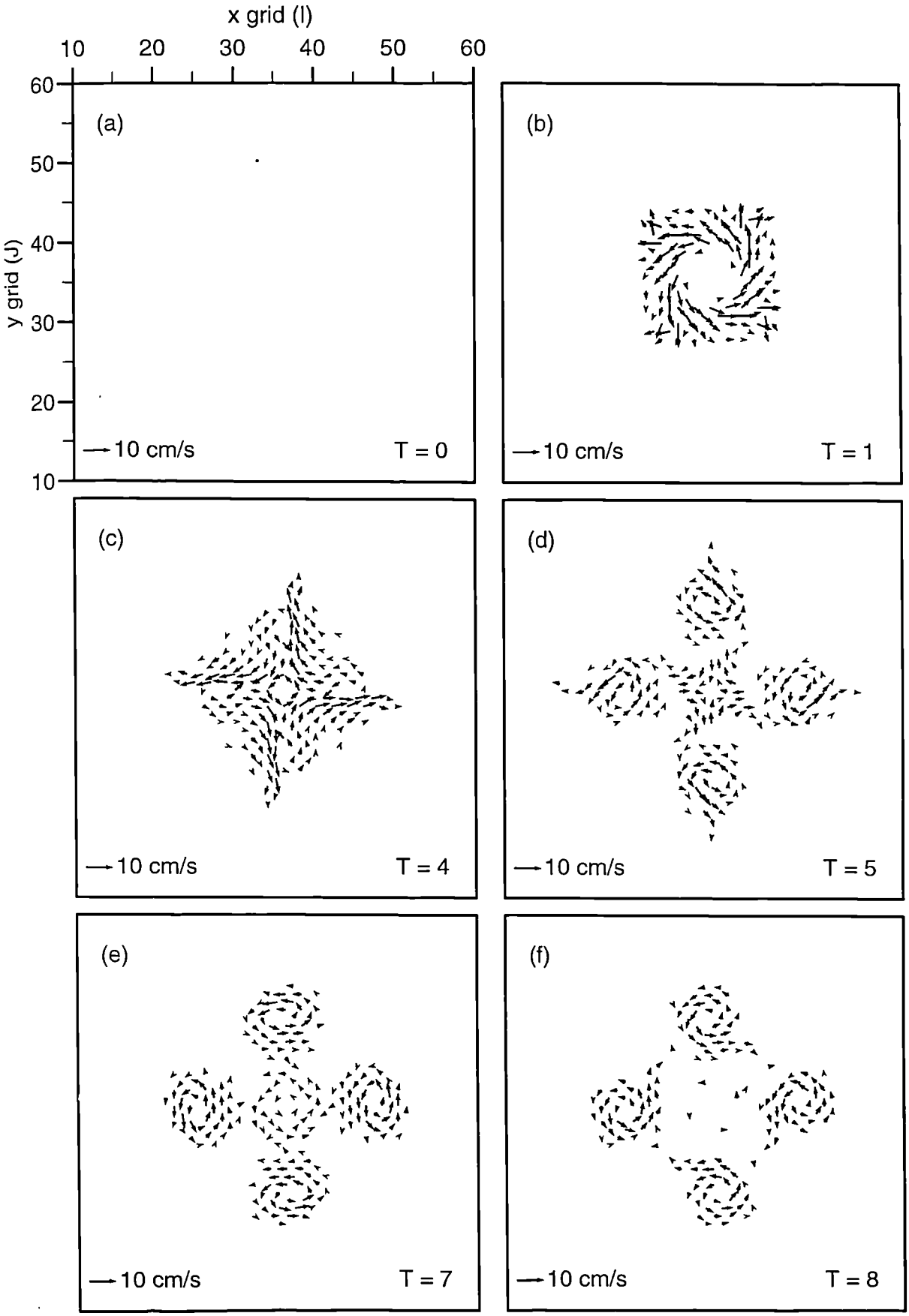

Fig. 5.17 Nearbed ($\sigma = 20$) current vectors (> 5 cm s^{-1}) at 0, 1, 4, 5, 7 and 8 rotation periods for a numerical cylinder adjustment experiment with the dimensionless parameters $\theta = 0.1$, $\delta = 1$, and with an initial cylinder radius of 7 km. Four cyclonic vortices develop at this level.

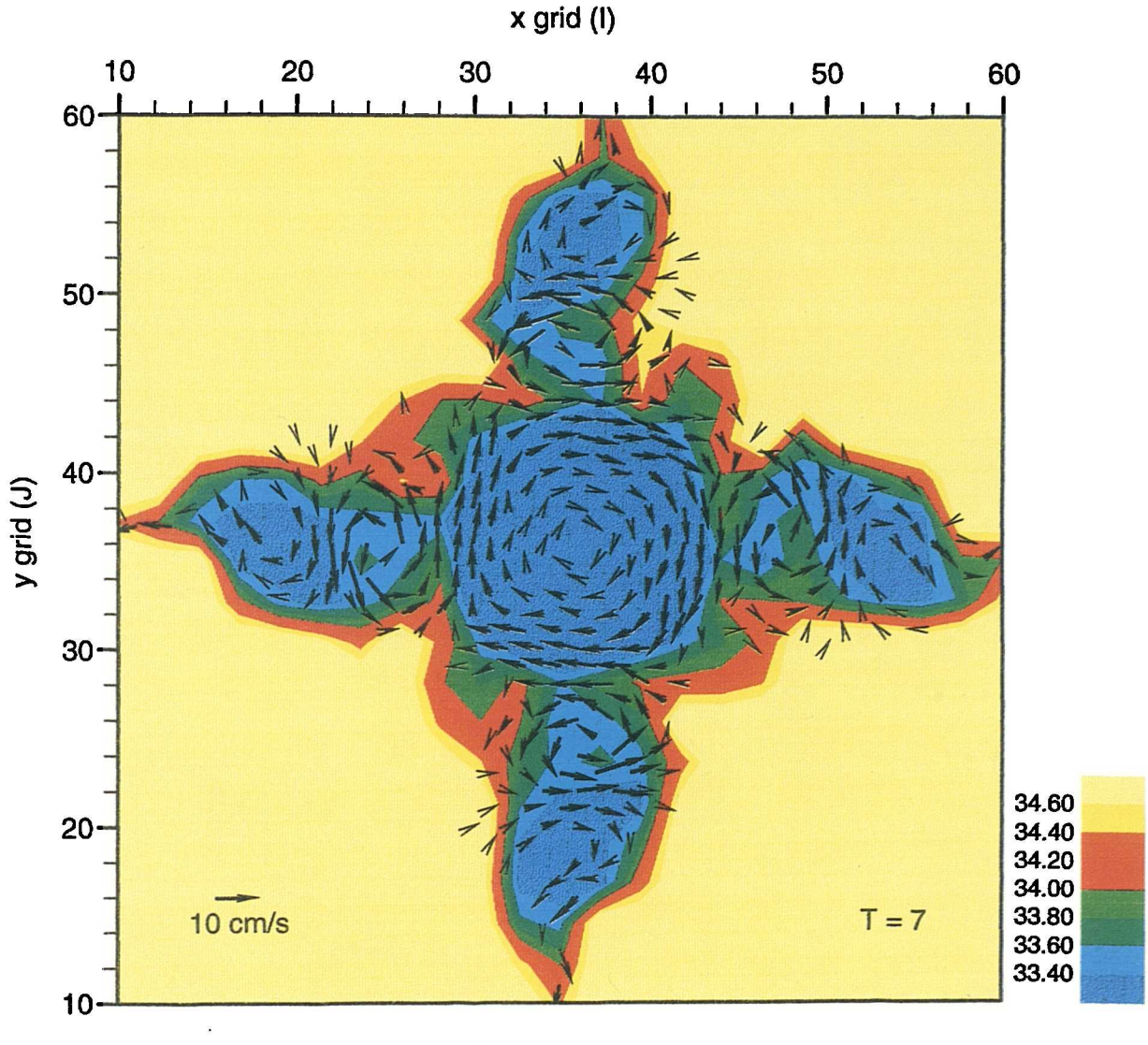

Fig. 5.18 Surface salinity distribution (scale as indicated) for the cylinder adjustment with dimensionless parameters $\theta = 0.1$, $\delta = 1$, at time T = 7 rotation periods. Overlaid are mean current vectors (> 5 cm s^{-1}) from levels $\sigma = 2$ - 10 inclusive. These show the existence in the layer averaged flow of four vortex dipoles which have separated from the central anticyclone.

Chapter 6. Seasonal model simulations.

6.1 Details of seasonal model runs

For the seasonal simulations, the model was forced with observed hourly mean solar insolation from Dublin airport (Fig. 6.1) and vector-averaged hourly mean winds (Fig. 6.2) from 1995. The wind field was synthesised from the higher value from two weather stations on the Isle of Man as described in §3.1 (and see Fig. 3.7). It is known that winds over the sea surface are stronger than those on land because of reduced friction. Galperin and Mellor (1990) used the simple relationship, $W_{sea} = 1.62 + 1.35W_{land}$, to obtain the wind forcing for their model of Delaware Bay. Here, a factor of 1.3 is applied to the winds shown in Fig. 6.2. This is consistent with previous calibrations of marine meteorological buoy data in the Irish Sea against wind speed records from Dublin airport (Lavin-Peregrina, 1984).

The observations described previously show that the density field is controlled primarily by temperature from early summer onwards. For this reason, and because of uncertainty surrounding freshwater inputs, salinity was held constant at 34 in the seasonal model runs. The model was initialised with temperatures of 7.5 °C everywhere, which was a typical observed value during CEFAS spring cruises in 1995 (J. Brown, *pers. comm.*). Simulations began at the vernal equinox (Day 80, 21 March) and were integrated forward in time until Day 304 (31 Oct). A 372 s time-step was used to properly resolve temporal variability in tidal mixing, and for simplicity in any subsequent averaging operations (there being 120 time-steps per M_2 cycle). The value is consistent with previous applications of the model (e.g. Wang *et al.*, 1994 used 600 s). Tidal forcing and boundary conditions have been described in the previous chapter. Ideally, temperature distribution in the model interior will be locally determined. To avoid prescribed external temperature values influencing the solution, a zero gradient open boundary condition for temperature and salinity, $\frac{\partial}{\partial y}(T,S) = 0$, was imposed initially. However, it was found in early model runs

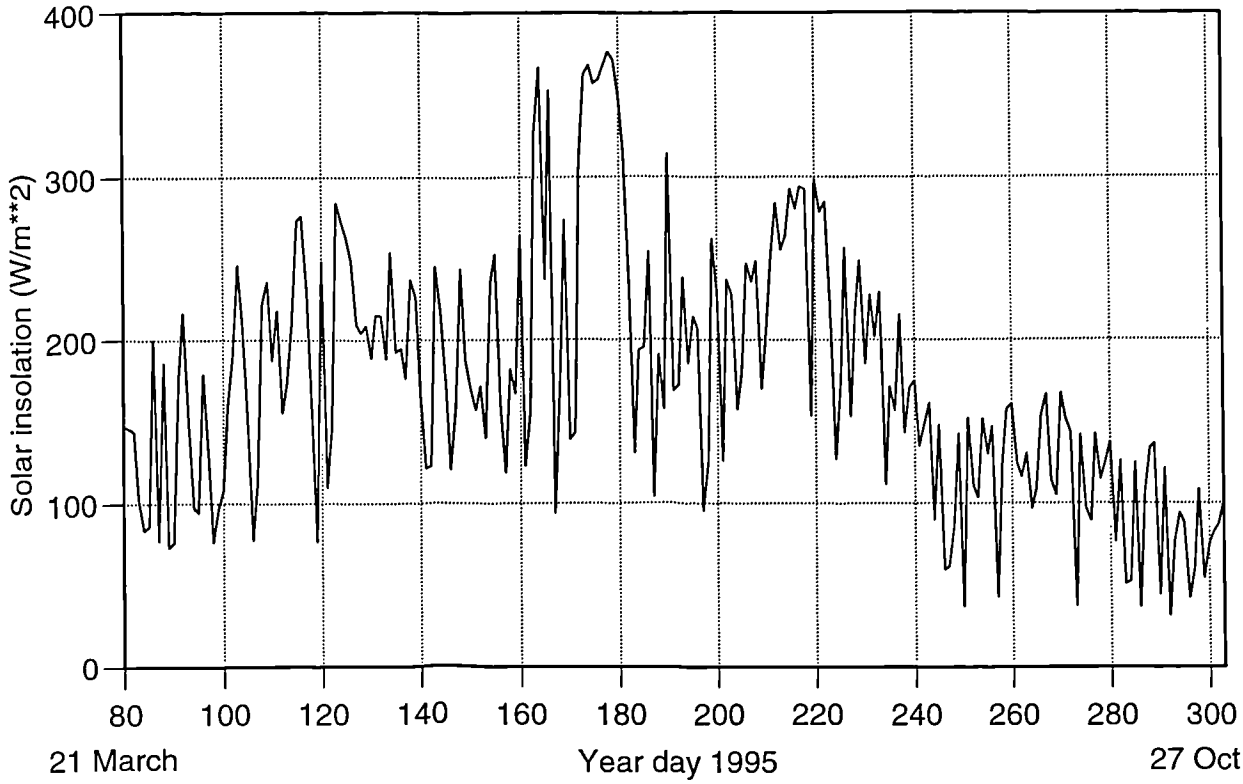

Fig. 6.1 Solar insolation (W m^{-2}) measured at Dublin airport weather station during 1995, for the period of the model runs. For clarity, 24 h averages are shown, although the model was forced with mean hourly values.

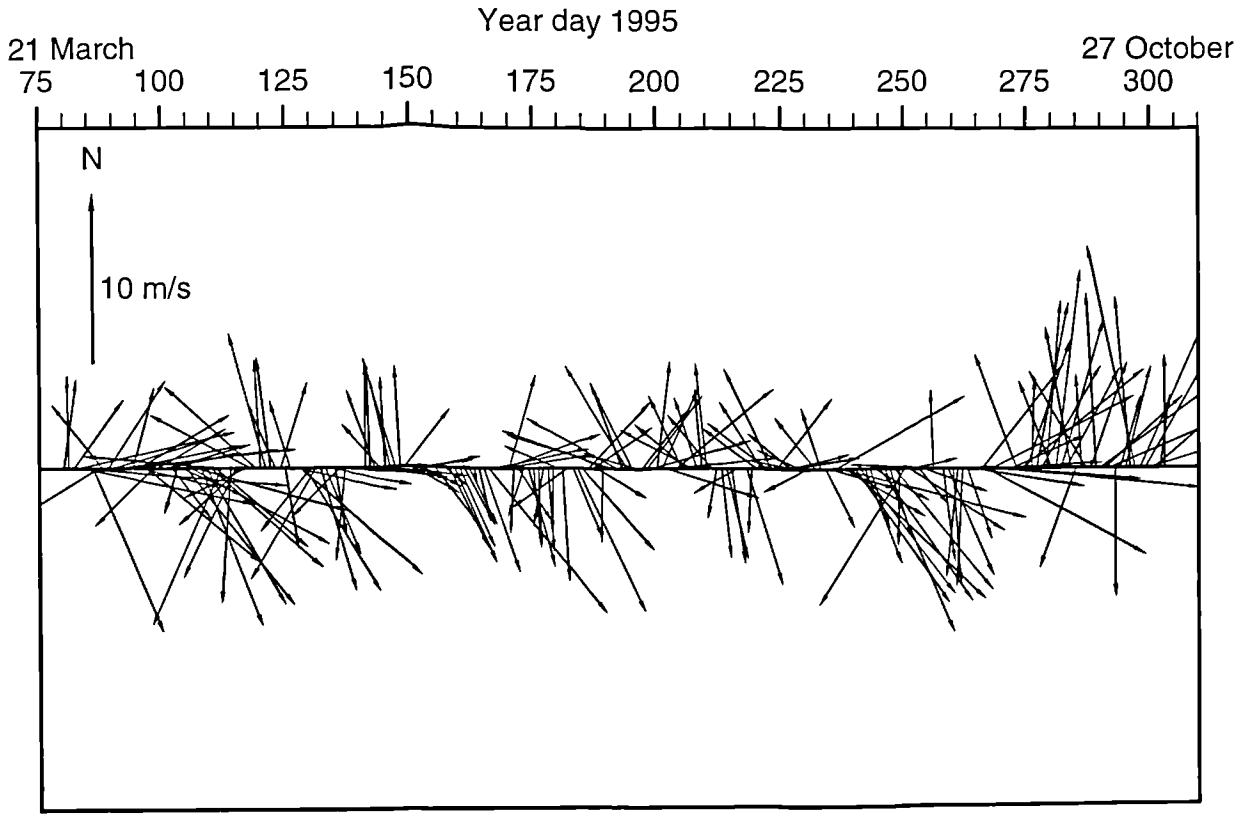

Fig. 6.2 Wind vectors (24 h means) obtained by taking the maximum value from Ronaldsway and Point of Ayre weather stations (see Fig. 2.1 for locations) for the duration of the model runs. The model was forced with hourly values, and a factor of 1.3 was applied to correct for stronger winds over the sea surface due to reduced friction.

that this led to an unrealistic accumulation of heat near the northern boundary. Consequently, the zero gradient condition was retained at the southern boundary and a simple advection scheme (using an upwind algorithm) was introduced at the northern boundary:

$$\frac{\partial}{\partial t}(T,S) + V\frac{\partial}{\partial y}(T,S) = 0 \quad \text{.....at J = 92} \qquad (6.1)$$

A temperature time series for the northern boundary was synthesised from satellite imagery, calibrated against the most northerly, well-mixed CTD station from the 1995 observations. The northern boundary temperature time series is given in Table 6.1. At every time-step, the model interpolates linearly between these prescribed values to obtain the boundary temperature.

Table 6.1 Northern boundary temperature series for the seasonal model runs

Model hour (post equinox)	Equivalent date (1995)	Open boundary temperature (°C)
0	21 March	7.5
1700	1 June	9.0
2200	21 June	11.0
2900	20 July	12.5
3500	14 August	14.0
4400	20 September	15.0
4700	3 October	14.0
5400	1 November	13.5

Parameter settings for the model runs presented here are given in Table 6.2. A small value of horizontal eddy viscosity was prescribed through the grid-dependent Smagorinsky (1963) scheme, with coefficient α = 0.1. To examine whether horizontal eddy diffusivity influenced the results appreciably, Runs B and C were performed using horizontal eddy Prandtl numbers (A_M/A_H) of 2 and 5 respectively. The Mellor-Yamada level 2½ scheme (with a background value of $K_M = 10^{-5}$ m^2s^{-1}) was employed in all computations to parameterise vertical mixing processes. The results focus on Runs A and B, which employed the recursive advection algorithm of

Smolarkiewicz (1984), although runs were also performed using central difference and upwind advection schemes for comparison. Run F was forced with identical winds but no heating, in order to quantify the density-driven contribution to the non-tidal flow. A final model run (Run G) was performed using modified values of air temperature from September onwards, to investigate the sensitivity of the autumnal breakdown phase to this property (which is poorly specified from terrestrial weather stations).

Table 6.2 Parameter settings for the seasonal model runs

Model run	Advection scheme	Horizontal Prandtl number (A_M/A_H)	Heating
A	Smolarkiewicz	1	Yes
B	Smolarkiewicz	2	Yes
C	Smolarkiewicz	5	Yes
D	Central	1	Yes
E	Upwind	1	Yes
F	Smolarkiewicz	1	No
G	Smolarkiewicz	1	Modified T_A

At the spatial resolution employed in this study, when using the Smolarkiewicz (1984) scheme, the model took approximately one hour to run for each day of simulation time on a Sun Microsystems Sparc-10 workstation. This is probably at the limit of acceptability for practical modelling work. Any further numerical refinements, or increases in resolution, would demand greater computational resources.

Temperature and velocity fields were extracted from the model at time-steps corresponding to days in 1995 for which observational data were available. These model output stages are summarised in Table 6.3, along with the cruise designator that references the observations (see Table 2.1). Temperature fields from the model were averaged over two tidal cycles to avoid influencing the comparisons with diurnal variation in the model (which could be a particular source of discrepancy near the surface).

Table 6.3 Model output stages and corresponding cruise designator

Output stage	Year day 1995	Corresponding date 1995	1995 cruise I.D. (see Table 2.1)
1	152	1 June	PM1
2	171	21 June	PM2/Cir5
3	200	20 July	PM4
4	206	25 July	PM5
5	228	16 August	PM6
6	242	30 August	PM7
7	264	21 September	PM8
8	278	5 October	Cor10
9	304	31 October	PM9

In order to present Eulerian residual flow fields that could be systematically compared with the circulation inferred from drifter data described in chapter 3, it was necessary to separate the wind-driven current (direct or indirect) from the density-driven flow. Tidal currents can be removed fairly easily by harmonic analysis (although with both M_2 and S_2 constituents, velocity at every cell must be stored over the synodic period of 15 days, and this is not always practical if several outputs are required and storage is limited). First-order estimates of the modelled, depth-mean, residual circulation due to combined wind and baroclinic forcing were obtained by averaging over two M_2 cycles and subtracting the Eulerian tidal residual shown in Fig. 5.5. However, wind influence can dominate the near surface flow, and the choice of an averaging period for comparison with drifter trajectories is unclear because drifter deployments were of variable duration and staggered in time. The model cannot be run without winds since these are essential to the vertical energy balance and, therefore, to the correct simulation of the thermocline in stratified regions. The technique used here to isolate the density-driven component was to run the model forward until a velocity field was required and then perform a subsequent, short (two day) prognostic run using no wind or heating, and forcing with only the M_2 tidal constituent. This permitted a relaxation of any wind-driven currents whilst maintaining the majority of the tidal energy and facilitating easy removal of the tidal component over the final M_2 period of 12.42 hours. Whilst not without its

limitations, this approach is a more realistic method of separating the baroclinic flow than either a subsequent diagnostic model run, or mere calculation of geostrophic velocity from the modelled density field. Full dynamics are maintained in the presence of tidal straining and realistic spatial gradients of mixing energy. The M_2 Eulerian residual (see Fig. 5.5) was subtracted from the flow field obtained, giving the best available prediction of baroclinic circulation.

6.2 Evolution of the temperature field

6.2.1 Spatial pattern of temperature

In this section, spatial distributions of temperature for the different model runs are presented. Temperature fields from Run A (Smolarkiewicz scheme, eddy Prandtl number = 1, henceforth SM1) are shown in full, and both qualitative and quantitative comparisons with the other advection schemes are carried out (although comprehensive temperature maps from other model runs are not always shown). The results focus on the western Irish Sea, so that comparison can be made with observations, but it is also useful to examine how well the model predicted surface temperature over the full domain. Satellite images of sea surface temperature (SST) in the Irish Sea, such as Fig. 6.3b (from 8 August 1995, 1337 GMT), consistently reveal three areas of relatively warm water - the stratified western Irish Sea, Liverpool Bay and Cardigan Bay. Modelled surface temperatures from stage 5 (16 August) of Run A are shown in Fig. 6.3a. These agree well with the satellite image, predicting the same three main regions of higher SST where temperatures are approximately 18°C, and cooler water (~ 14.5°C) in the central, deep channel of the Irish Sea.

Modelled surface and bottom temperatures from all 9 output stages of Run A are shown in Fig. 6.4a-h. For each stage, the panels show (from left to right) surface temperature, bottom temperature and vertical temperature difference (which is the simplest measure of stratification in the constant salinity model). Direct comparison of these temperature fields can be made with Fig. 3.6. Reasonable agreement with

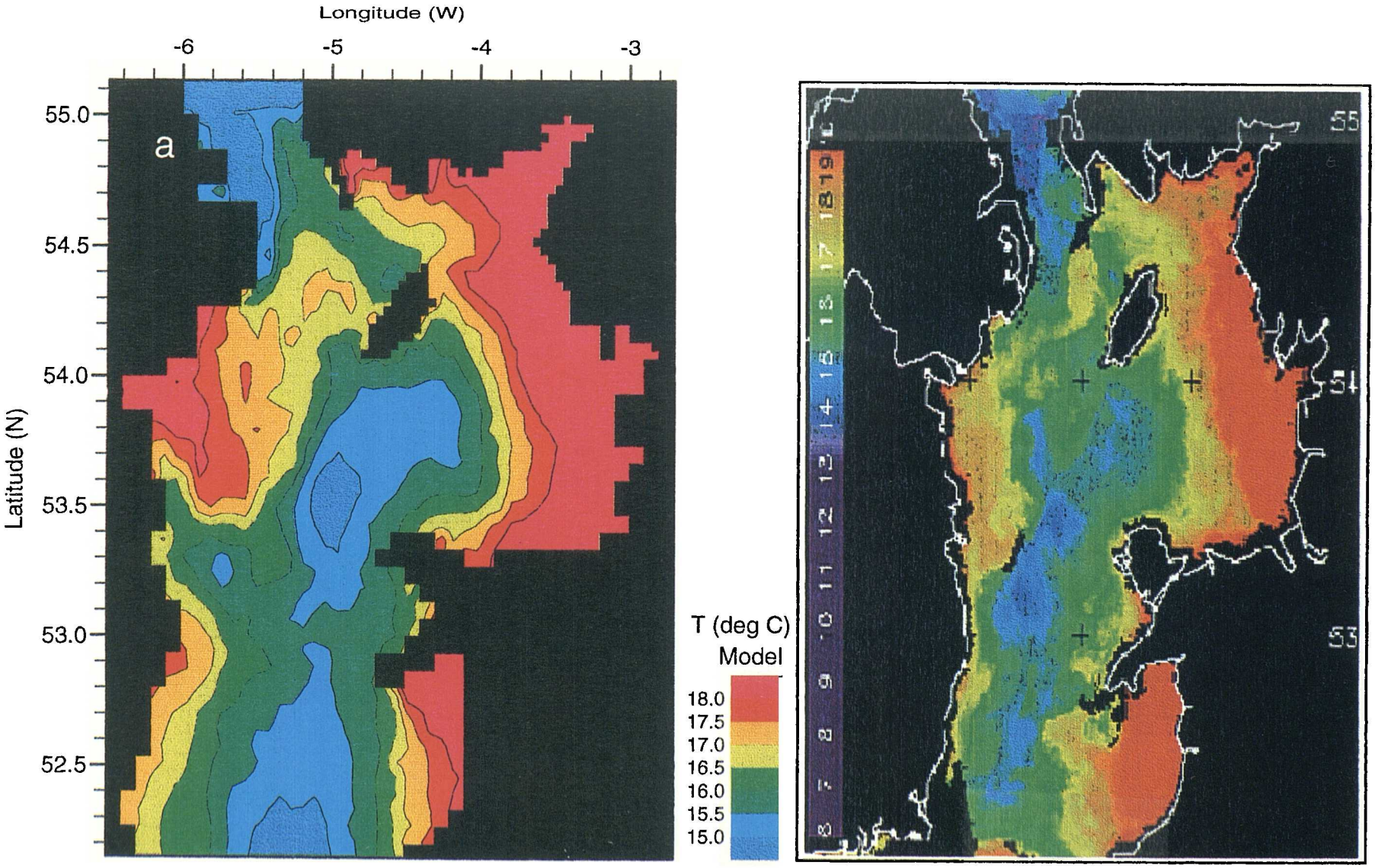

Fig. 6.3 (a) Model surface temperature from Run A, averaged over two M_2 cycles at 16 August. (b) Sea surface temperature (SST) from AVHRR satellite image at 1337 GMT on 8 August 1995, with temperature scale along the left side of the image. The AVHRR image has been cropped to occupy the same geographical region as the model.

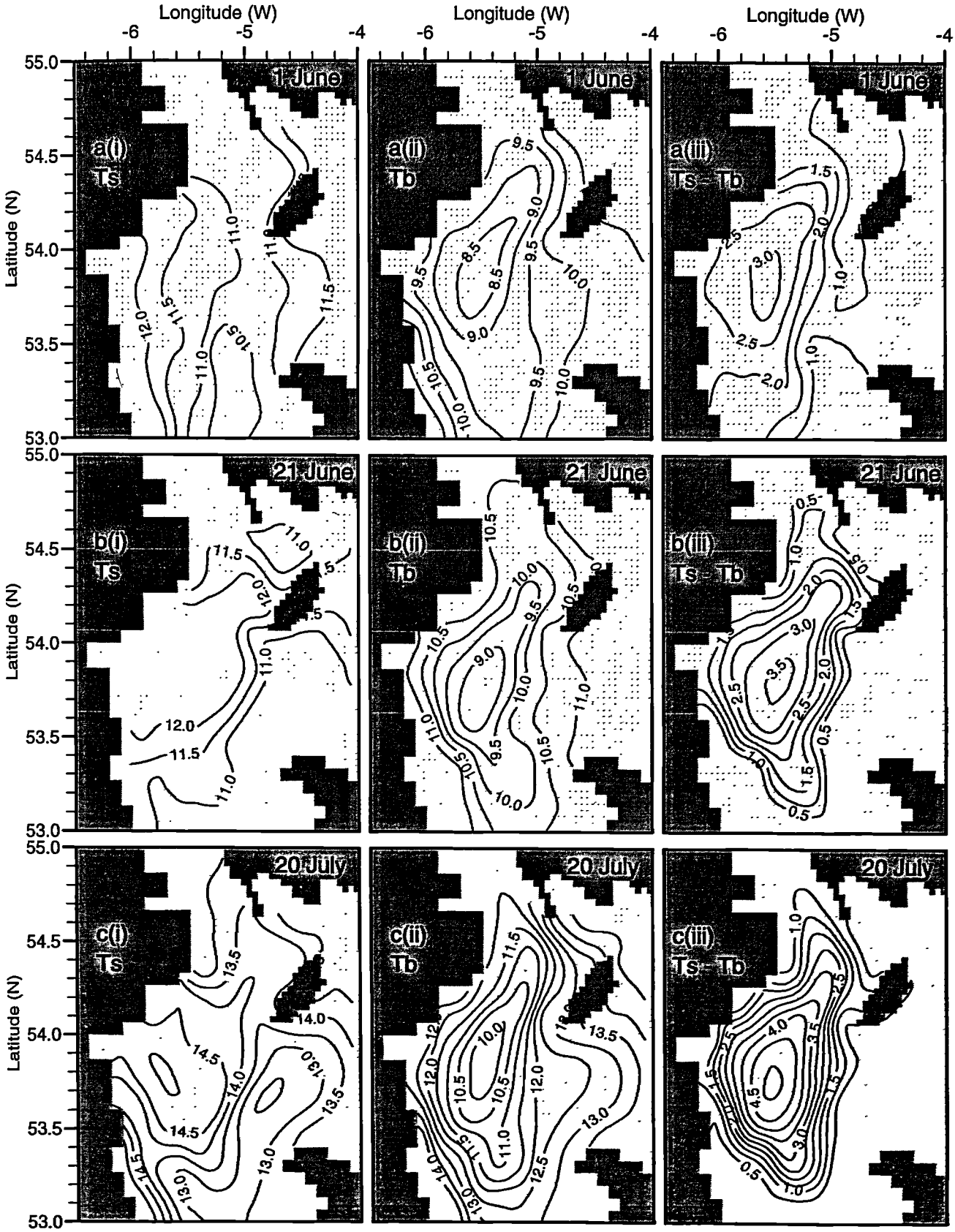

Fig. 6.4 Modelled temperature field from Run A at all output stages (see Table 6.3). Each row of panels corresponds to an output stage and the year day is shown in every diagram. In each case (i) is surface temperature, (ii) is bottom temperature and (iii) is the temperature difference between surface and bed. (continued overleaf.....).

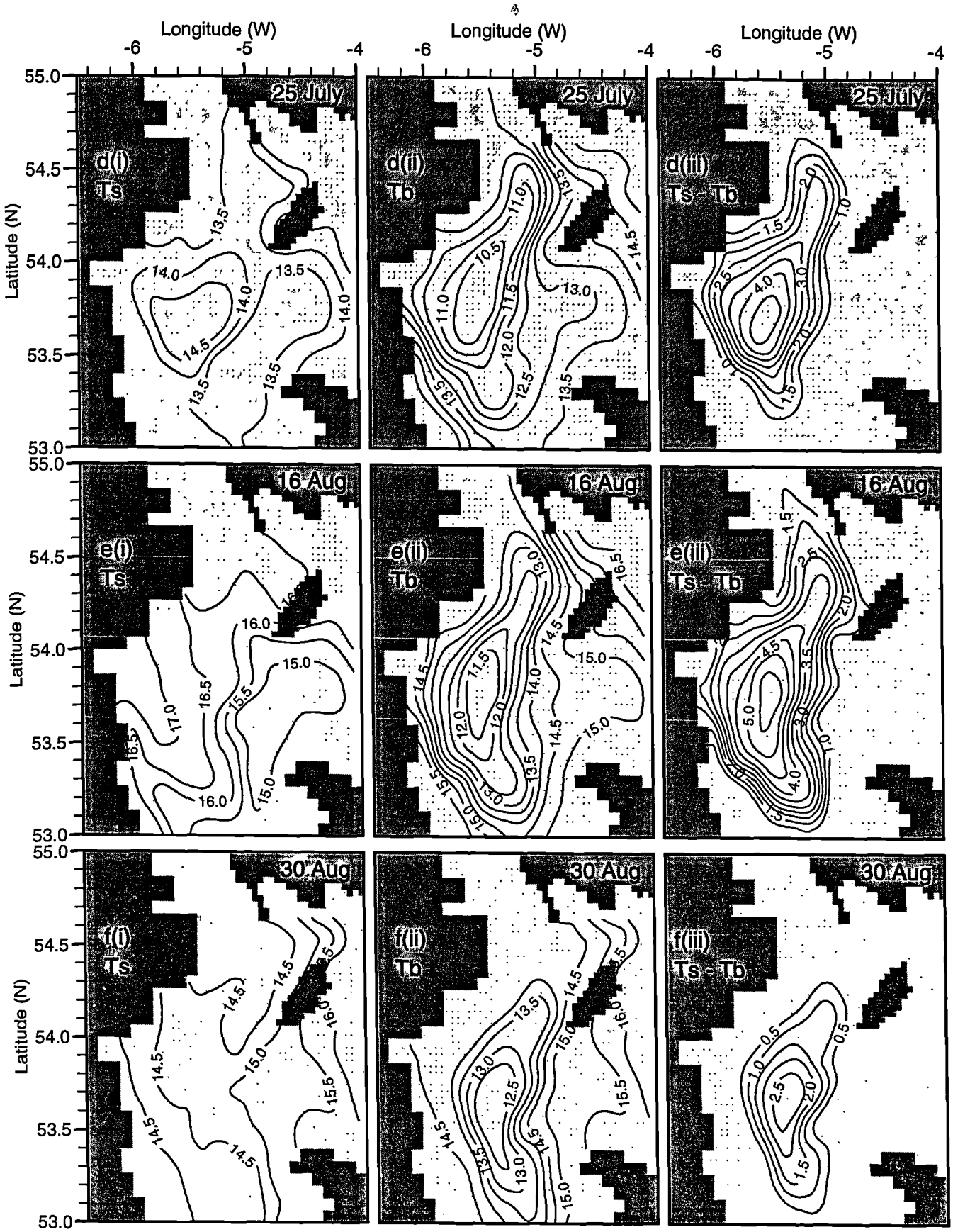

Fig. 6.4 (....continued). Modelled temperature field from Run A. (a) 1 June (c.f. Fig. 3.6a), (b) 21 June (c.f. Fig. 3.6b), (c) 20 July (c.f. Fig. 3.6c), (d) 25 July (c.f. Fig. 3.6d), (e) 16 August (c.f. Fig. 3.6e), (f) 30 August (c.f. Fig. 3.6f), (g) 21 September, (h) 5 October, (i) 31 October. (continued overleaf.....).

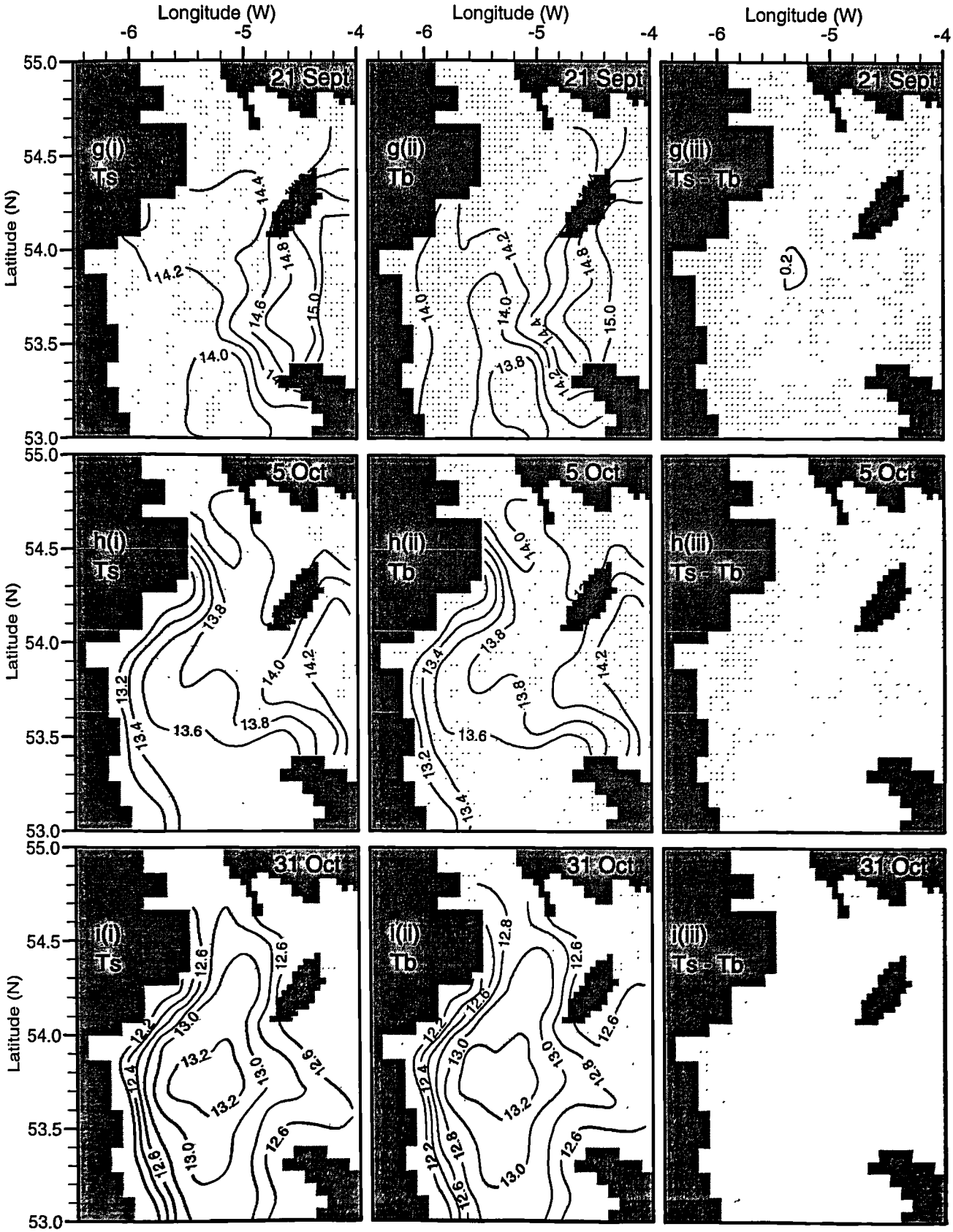

Fig. 6.4 (....continued). Modelled temperature field from Run A. Where direct comparison can be made with the observations presented earlier, the corresponding diagram from Fig. 3.6 is referenced in brackets. The faint dots indicate the centre of each model grid cell.

observed temperature fields was obtained for stages 1-6, but by stage 7 (21 September, Fig. 6.4g) the model predicted only a small region of minimal temperature stratification. By stage 8 (5 Oct) temperature was vertically mixed everywhere, but with a weak horizontal temperature gradient. At the final output stage, corresponding to late October (Fig. 6.4i), the water had cooled differentially showing a relatively warm (but vertically well-mixed) central core in the deepest part of the region.

To compare the performance of the model runs described in Table 6.2, the vertical temperature differences at 20 July and 16 August are presented in Fig. 6.5 and Fig. 6.6 respectively. These dates were selected because the observational data (from cruises PM4 and PM6, see Table 2.1) had the best spatial coverage. It can be seen that Run A (Fig. 6.5b), Run B (Fig. 6.5c) and Run D (Fig. 6.5d) all gave reasonable prediction of the temperature stratification observed during cruise PM4 (Fig. 6.5a). The Smolarkiewicz scheme with an eddy Prandtl number of 2 (Run B, SM2 hereafter) gave the best agreement in the centre of the stratified region where the observed vertical temperature difference was 5.5°C, but the other two runs gave similar predictions of the spatial extent of stratification and of the horizontal gradients of temperature stratification. Run C (Prandtl number = 5, Fig. 6.5e) tended to overpredict the magnitude of stratification throughout the season, and also overestimated the spatial extent of it - stratification extending further south than 53°N during August (not shown). The upwind advection scheme used in Run E (Fig. 6.5f) was highly diffusive, and was incapable of maintaining the cold water pool and hence the stratification. Runs C and E also performed poorly in a statistical sense (as will be shown later) and are therefore not considered here in any further detail. The temperature stratification predicted by Runs A, B and D at August 16 (cruise PM6) is shown in Fig. 6.6. Best agreement with the observations in Fig. 6.6a was achieved by Run A (SM1, Fig. 6.6b). Run B (SM2, Fig. 6.6c) overpredicted the stratification in the centre of the region by approximately 1°C, and the results from Run D (Fig.

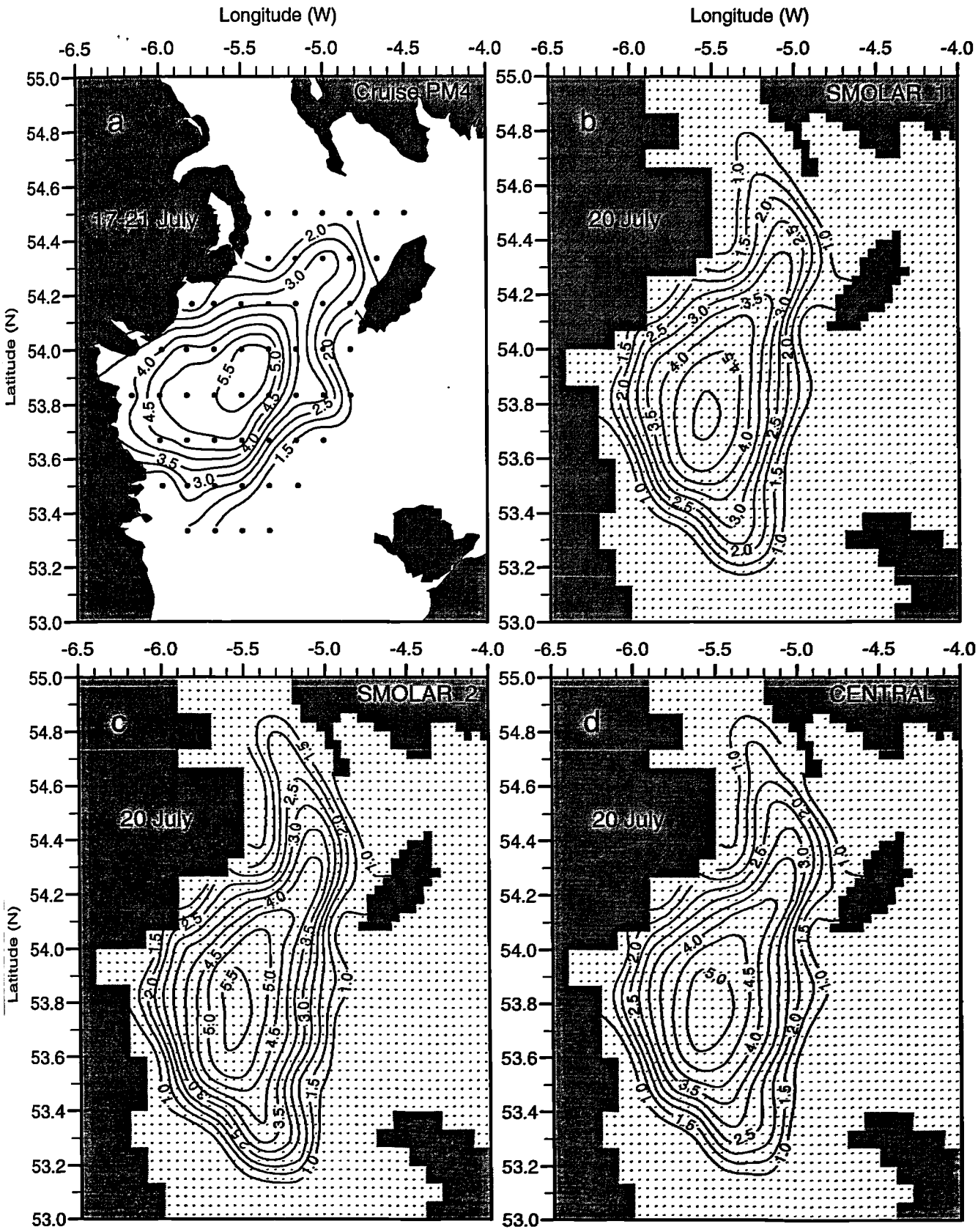

Fig. 6.5 Spatial pattern of vertical temperature differences at 20 July, 1995 from: (a) observations - cruise PM4, (b) Run A, (c) Run B and (d) Run D. See Table 6.2 for details of the parameterisations used in the model runs. Contours are in 0.5 °C intervals. (continued overleaf.....).

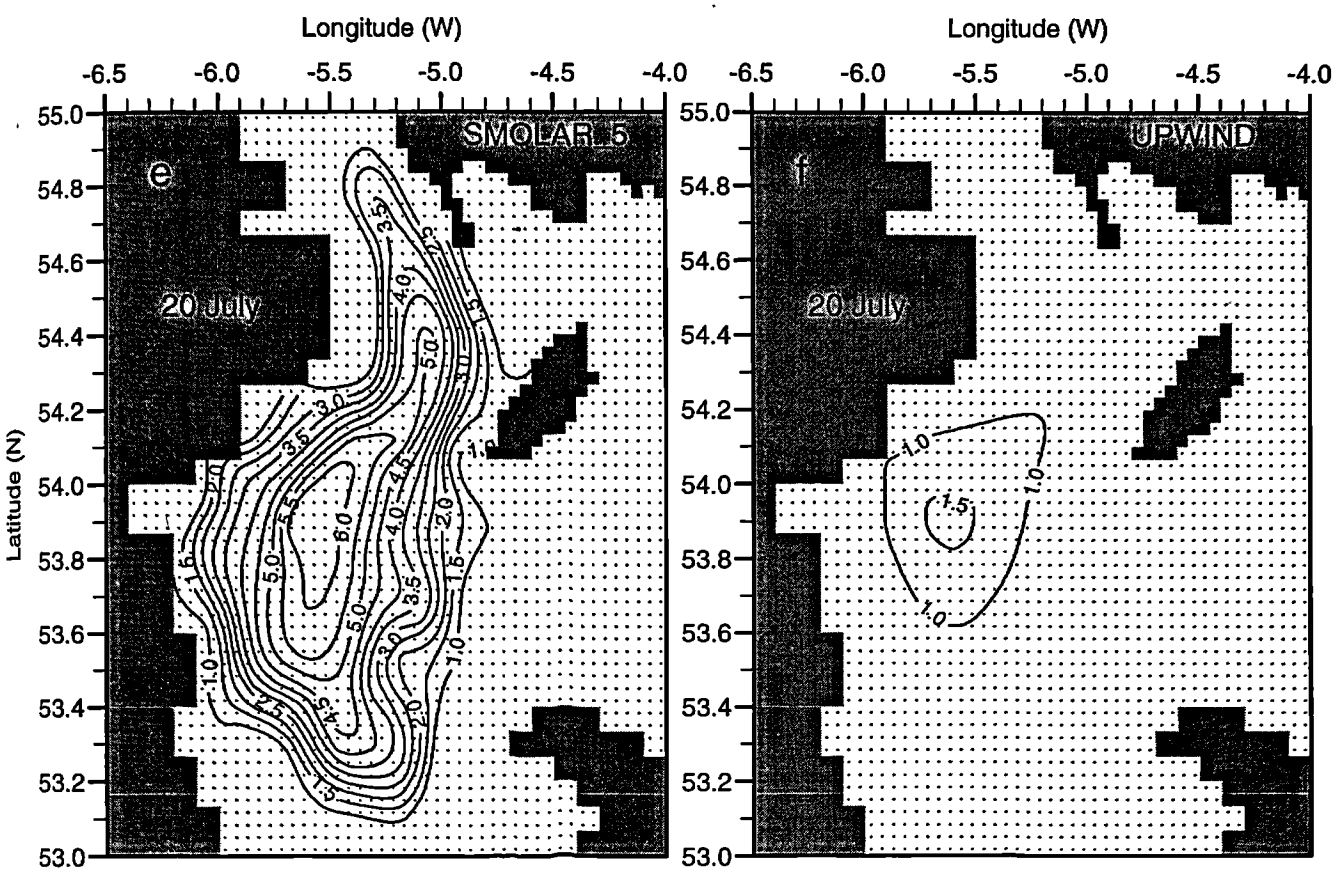

Fig. 6.5 (....continued). Spatial pattern of vertical temperature differences at 20 July, from: (e) Run C and (f) Run E. See Table 6.2 for details of the parameterisations used in the model runs. Contours are in 0.5 °C intervals.

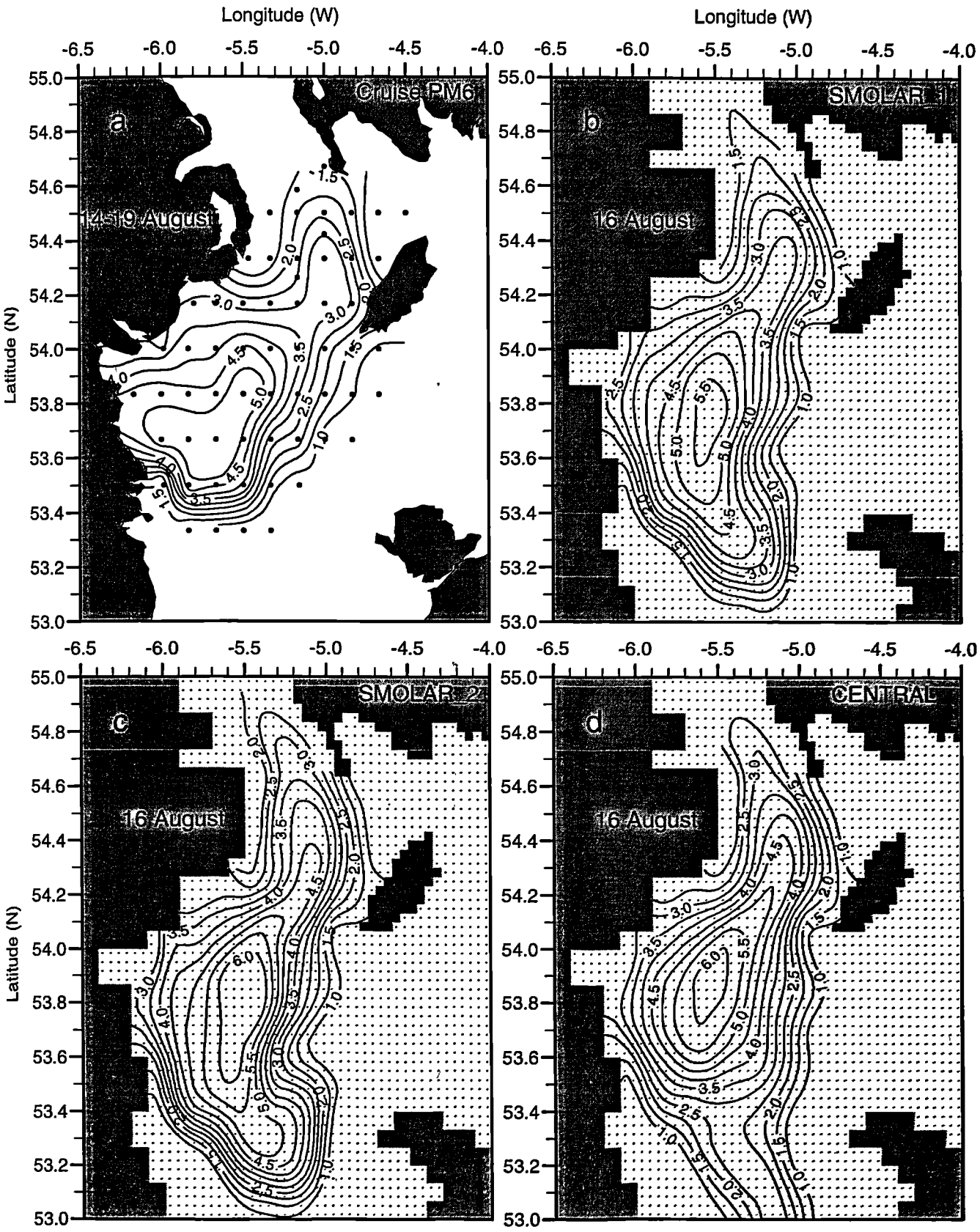

Fig. 6.6 Spatial pattern of vertical temperature differences at 16 August, 1995 from: (a) observations - cruise PM6, (b) Run A, (c) Run B and (d) Run D. See Table 6.2 for details of the parameterisations used in the model runs. Contours are in 0.5 °C intervals.

6.6d) showed spurious stratification towards the southern limit of the region of interest. This resulted from the central difference advection scheme making inaccurate predictions (from August onwards) of the bottom water temperatures, the reasons for which will be discussed later.

6.2.2 Vertical structure of temperature

In order to examine qualitative features of the vertical temperature structure (e.g. position of the thermocline, strength of the thermocline, location of bottom fronts), Fig. 6.7 presents a transverse section from model Run B (SM2) at the first 8 output stages listed in Table 6.3. The *x-z* section is from model row 47, which corresponds to line F of the observations at latitude 53° 40'N. So that comparisons can be made with the observed seasonal evolution of density presented in Fig 3.9, density was calculated here from temperature using a salinity of 34.2 (which was a typically observed value at the centre of line F during June-August 1995). The model successfully reproduced the dome-like density structure for these months, predicting strong horizontal density gradients on both flanks of the cold pool. The depth at which the thermocline was located, and vertical density gradients across the thermocline also agreed well with observations. By August 30, the model run revealed that the surface density structure had been eroded but that a distinct dense pool remained in the bottom 50 m of the water column. Although Run B did exhibit some residual stratification in late September (Fig. 6.7g), it was weak compared to that seen during cruise PM8 (Fig. 3.9h). No stratification remained in the model by 5 Oct (Fig. 6.7h), whereas a small dome-shaped mass of dense water was still visible in the observations at a corresponding time (Fig. 3.9i).

So that comparisons can be made between different model runs and the observed temperatures, Figs. 6.8 to 6.11 present east-west transverse sections of temperature at latitudes of either 53° 40'N (line F) or 53° 50'N (line E), at four stages in the seasonal development. The PM1 cruise data for line E (1 June) is shown in Fig.

6.8a, where it can be compared with the corresponding model output from Runs A, B and D. The model runs all gave similar results with the best predictor of bottom water temperature being Run B (Fig. 6.8c) although this run tended to overpredict the vertical temperature gradient compared to Run A (Fig. 6.8b). In the central difference scheme (Run D, Fig. 6.8d), too much warming of the deep water was predicted. Output from the same three model runs for line F on 25 July is shown in Fig. 6.9. Whilst all three runs correctly reproduced the cold dome and positioned the centre of the thermocline at 20 m depth, only Run B maintained the coldest water at the correct temperature, although it did so at the expense of underpredicting surface temperatures by 1-1.5°C.

Run A (SM1) produced the best agreement with observed temperatures along line F during cruise PM6 (16 August), as shown in Fig. 6.10b. At this time, Run B (SM2, Fig. 6.10c) reproduced the horizontal density gradients equally satisfactorily but tended to underpredict the coldest temperatures in the dome, unlike Run D (central differences, Fig. 6.10d) which overestimated these. None of the model runs presented so far was able to show agreement with temperature observations from line E on 21 September (Fig. 6.11a). Runs A and B destratified too rapidly and although persistent stratification was observed in Run C (Prandtl number = 5, Fig. 6.11d), it has already been mentioned that this scheme agreed poorly with observations for most of the season (e.g. Fig. 6.5e) and exhibited a spurious maintenance of cold, nearbed temperatures.

North-south sections of density from Run B, along the dog-leg section (denoted NS in Fig. 3.1) are presented in Fig. 6.12 for the first 7 output stages. Density has been calculated from the temperature field assuming a salinity of 34.2, as before. The density pattern shown in Fig. 6.12 can be compared directly with the observations of Fig. 3.10, and bottom water densities were seen to be in good agreement with the observations throughout the heating season until 30 August.

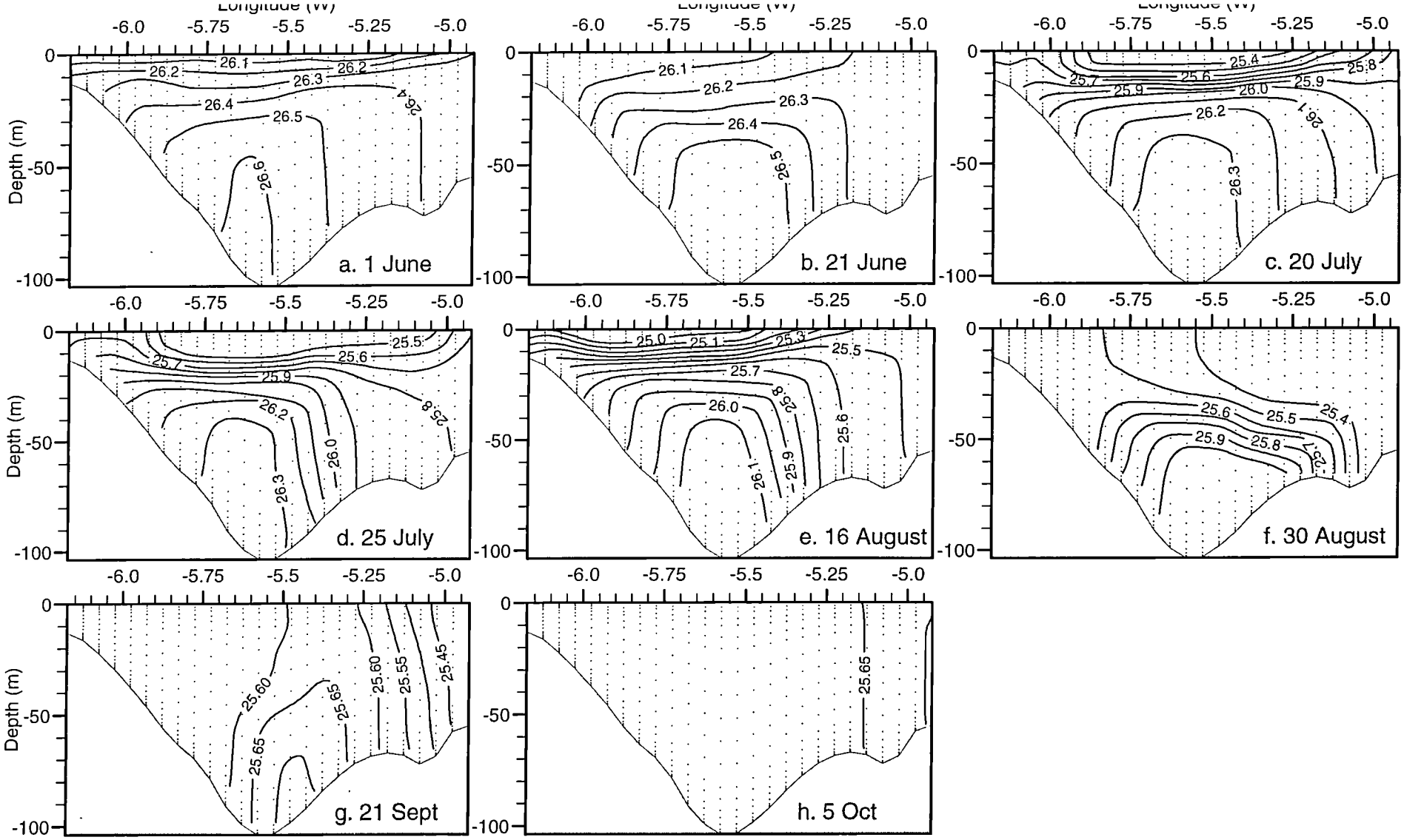

Fig. 6.7 Transverse sections (x-z) of modelled density (σ_t) along row 47 (corresponding to latitude 53° 40' N) from Run B at stages 1-8. (a) 1 June, (b) 21 June, (c) 20 July, (d) 25 July, (e) 16 Aug, (f) 30 Aug, (g) 21 Sept, (h) 5 Oct. To facilitate a qualitative comparison with Fig. 3.9, densities have been calculated from the temperature field based on a salinity of 34.2, which was a typical value for the centre of line F in July. Note the change of contour interval in Fig. 6.7g.

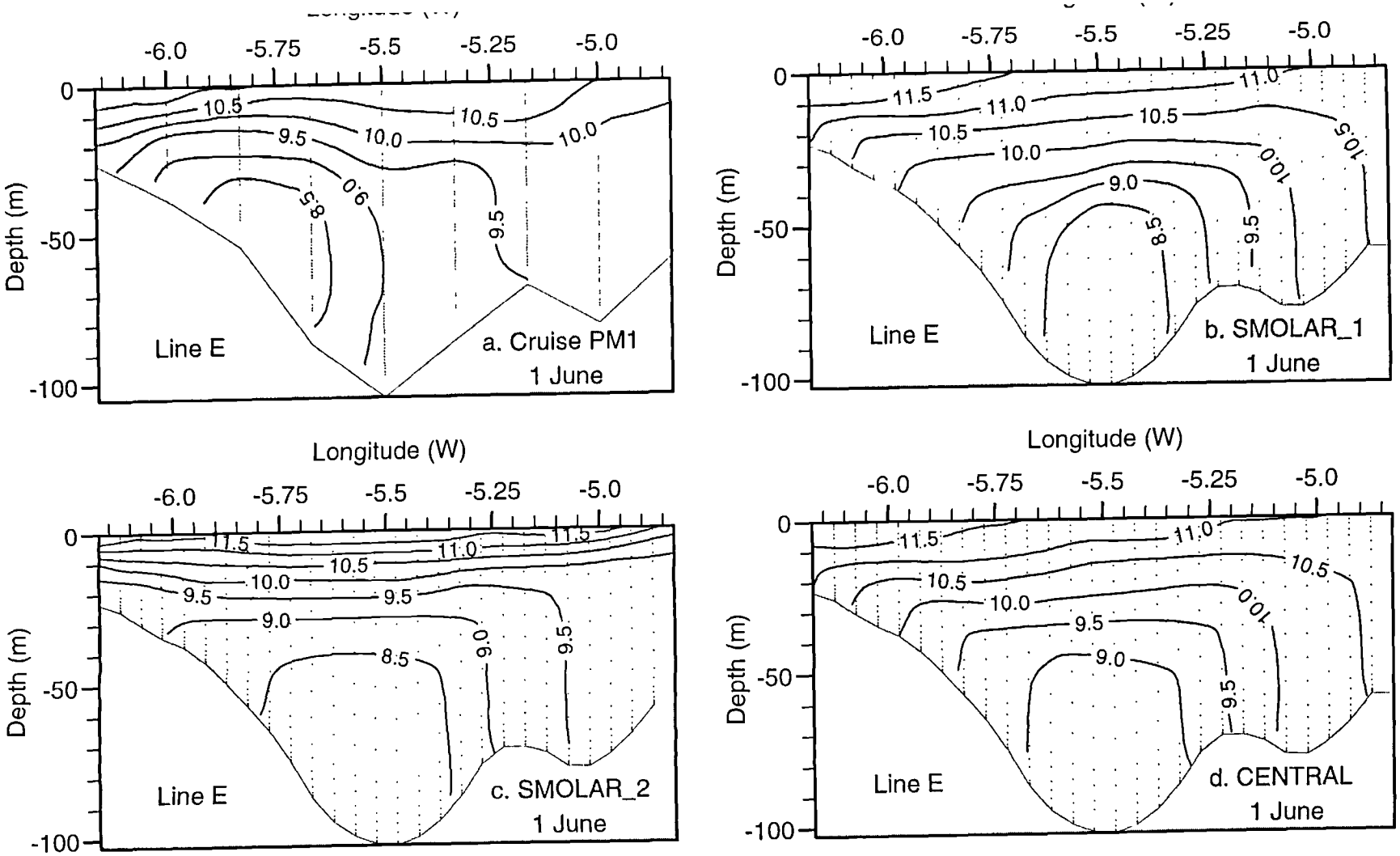

Fig. 6.8 Transverse sections (x-z) of modelled temperature along row 52 (corresponding to latitude 53° 50' N) at 1 June 1995 compared with (a) Observations from line E, cruise PM1. (b) Run A, (c) Run B, (d) Run D. See Table 6.2 for details of the model parameterisations. Contours are in 0.5 °C intervals.

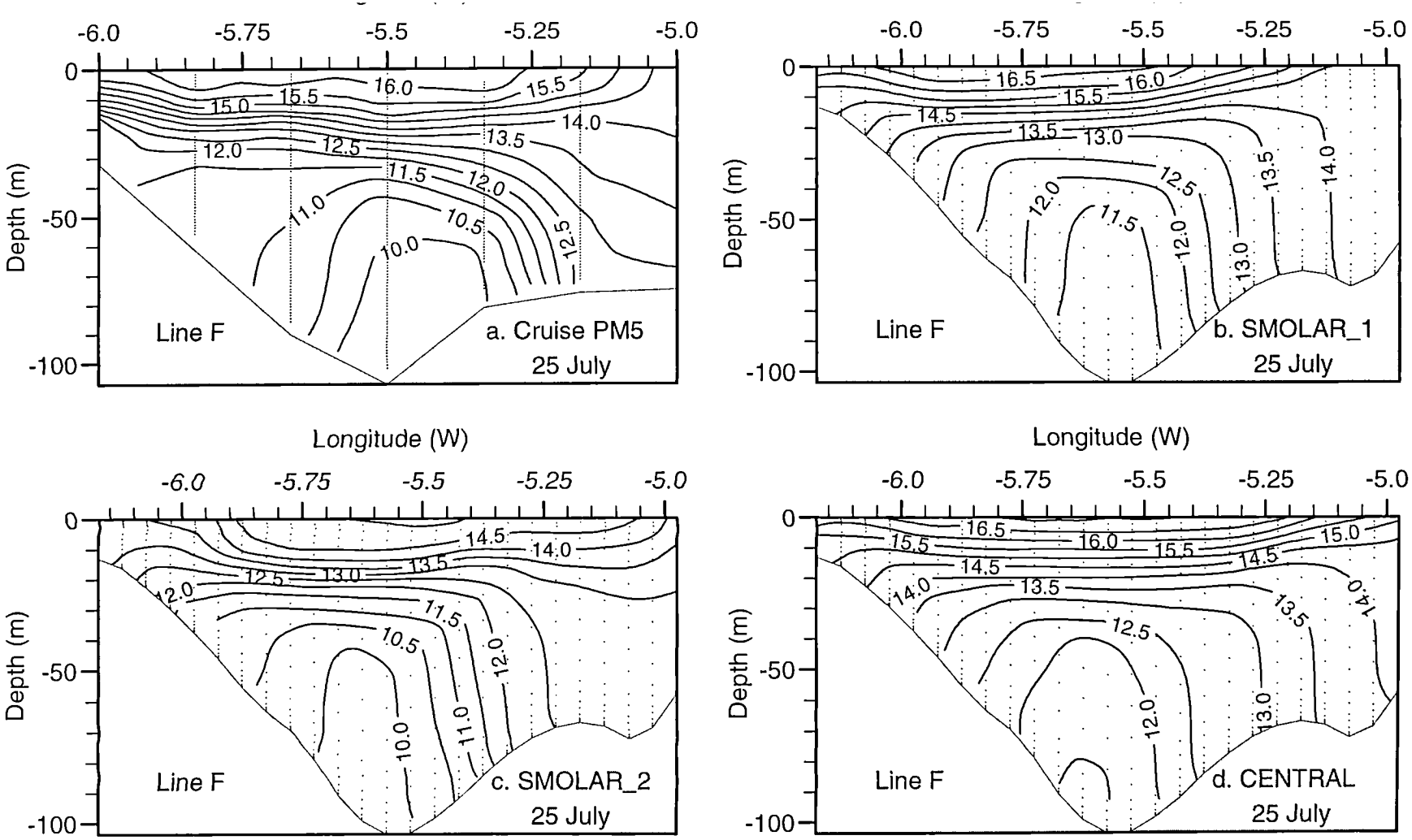

Fig. 6.9 Transverse sections (*x*-*z*) of modelled temperature along row 47 (corresponding to latitude 53° 40' N) at 25 July 1995 compared with (a) Observations from line F, cruise PM5. (b) Run A, (c) Run B, (d) Run D. See Table 6.2 for details of the model parameterisations. Contours are in 0.5 °C intervals.

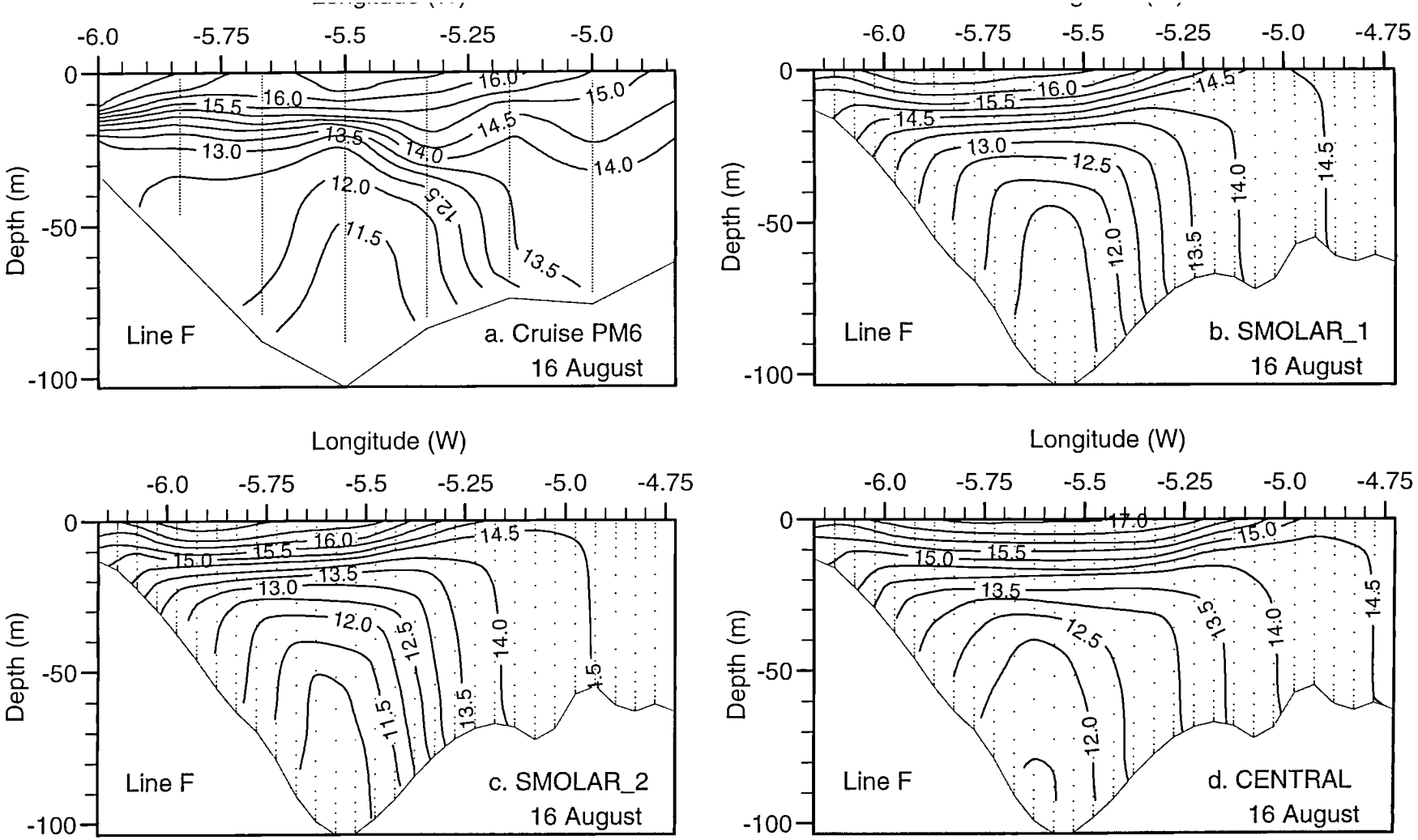

Fig. 6.10 Transverse sections (*x*-*z*) of modelled temperature along row 47 (corresponding to latitude 53° 40' N) at 16 August 1995 compared with (a) Observations from line F, cruise PM6. (b) Run A, (c) Run B, (d) Run D. See Table 6.2 for details of the model parameterisations. Contours are in 0.5 °C intervals.

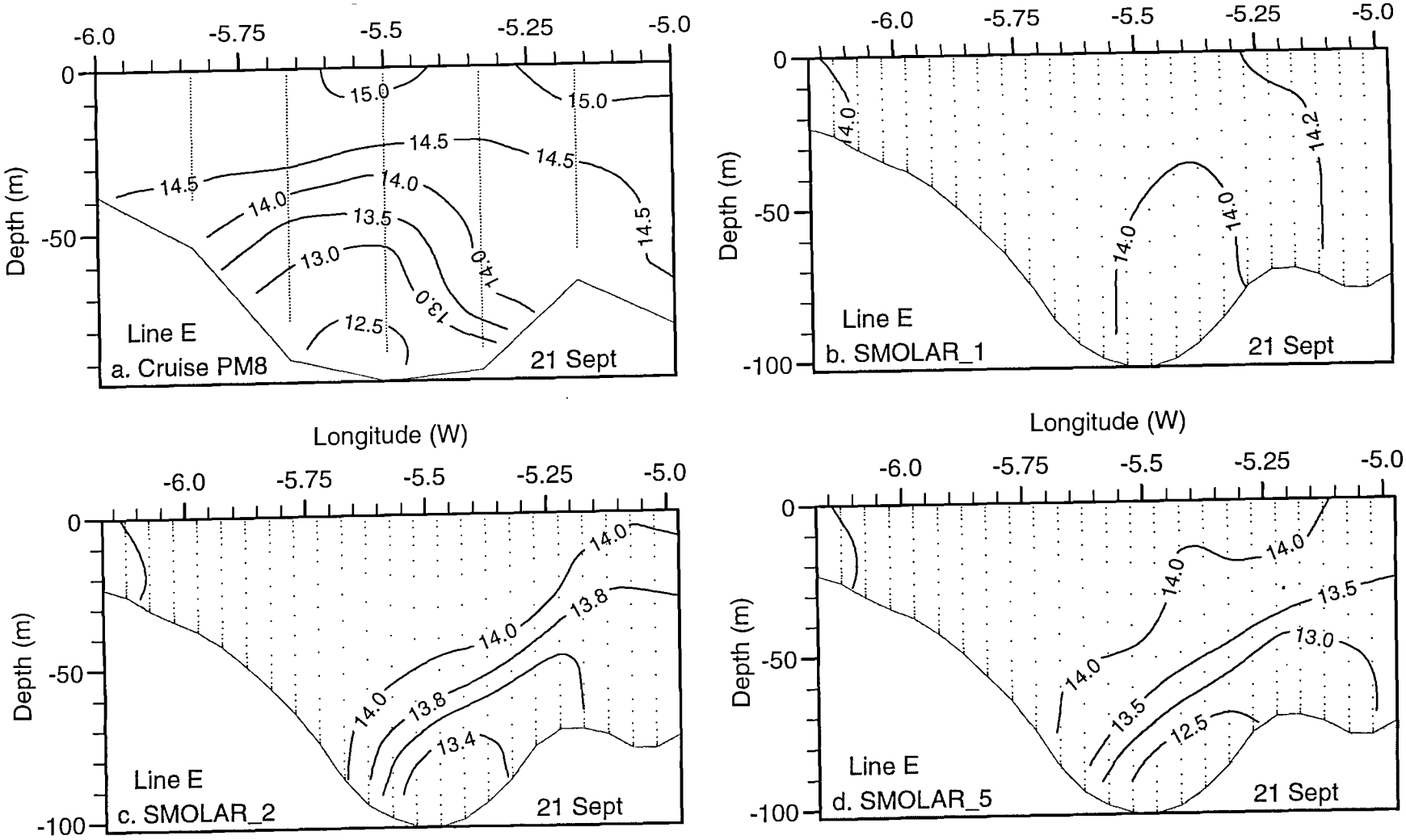

Fig. 6.11 Transverse sections (x-z) of modelled temperature along row 52 (corresponding to latitude 53° 50' N) at 21 September 1995 compared with (a) Observations from line E, cruise PM8. (b) Run A, (c) Run B, (d) Run C. See Table 6.2 for details of the model parameterisations. Contours are in 0.5 °C intervals for (a) and (d), and in 0.2 °C intervals for (b) and (c).

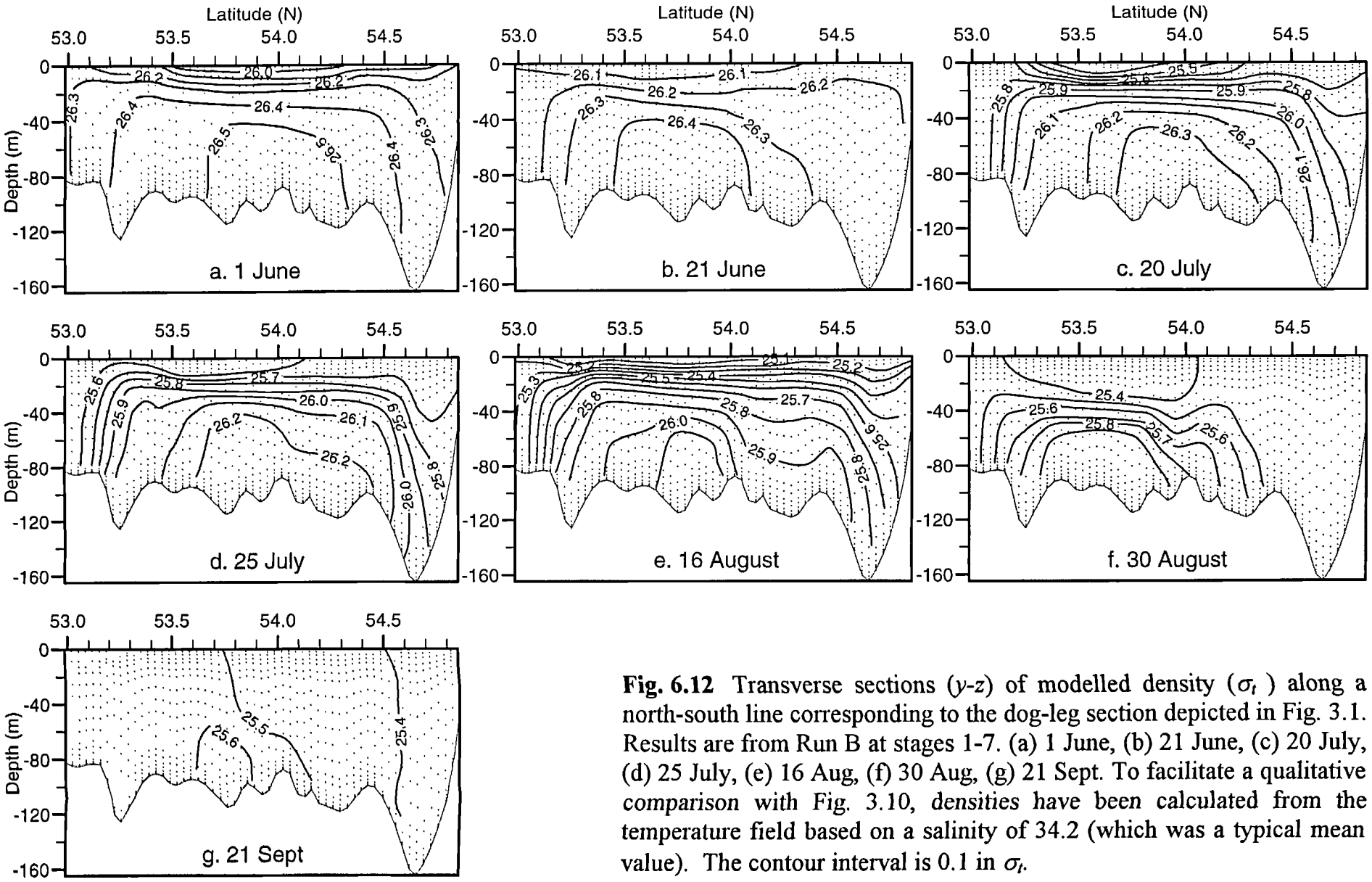

Fig. 6.12 Transverse sections (y-z) of modelled density (σ_t) along a north-south line corresponding to the dog-leg section depicted in Fig. 3.1. Results are from Run B at stages 1-7. (a) 1 June, (b) 21 June, (c) 20 July, (d) 25 July, (e) 16 Aug, (f) 30 Aug, (g) 21 Sept. To facilitate a qualitative comparison with Fig. 3.10, densities have been calculated from the temperature field based on a salinity of 34.2 (which was a typical mean value). The contour interval is 0.1 in σ_t.

6.2.3 Time series of temperatures and model skill assessment

Daily mean surface and bottom temperatures from model cell (21,52) for the full duration of Run A are presented in Fig. 6.13a. This location corresponds to station E4 of the CTD survey grid (Fig. 3.1), and observations over the full cruise program were made either here, or at neighbouring station F4 (see Fig. 3.8). The observed surface and bottom temperatures are depicted in Fig. 6.13a and by solid squares and triangles respectively. Generally, model temperatures agreed well with observations from the beginning of the model run until day 242 (30 August). Thereafter, the breakdown of stratification in the model occurred too rapidly. This was also true of all other model runs described so far. The explanation for this is that air temperature used in the model forcing was obtained from a terrestrial weather station (Dublin airport). The diurnal fluctuation of temperature over land is more extreme than over the sea, and the prescribed air temperatures accelerated the surface heat loss once solar heating had begun to decline. This point was redressed in a subsequent numerical experiment, the results of which will be presented later.

The smooth rise in nearbed temperatures shown in Fig. 6.13a emphasises the isolation of the cold, dense pool. In contrast, surface temperatures from the model showed greater variability whilst remaining physically realistic. The fluctuations in modelled surface temperature were not caused by diurnal effects (being 24 hour averages) but reflected some combination of longer term variability in the solar heat input and advection from nearby areas. The falls in temperature immediately following the sharp peaks seen in Fig. 6.13a occurred at days 105, 126, 158, 181 and 232, and seemed to coincide with the onset of northerly winds (see the wind vector diagram, Fig. 6.2). In Fig. 6.13b, the component of northerly wind is expressed as the cosine of the 48 hour running mean of the meteorological wind angle (i.e. the direction from which it blows). Values of unity mean that the wind was blowing from the north. For all those peaks in surface temperature seen in Fig. 6.13a, the subsequent temperature drop aligns well with the onset of a northerly wind component. (An attempt was made to correlate the time series in Fig. 6.13b with the

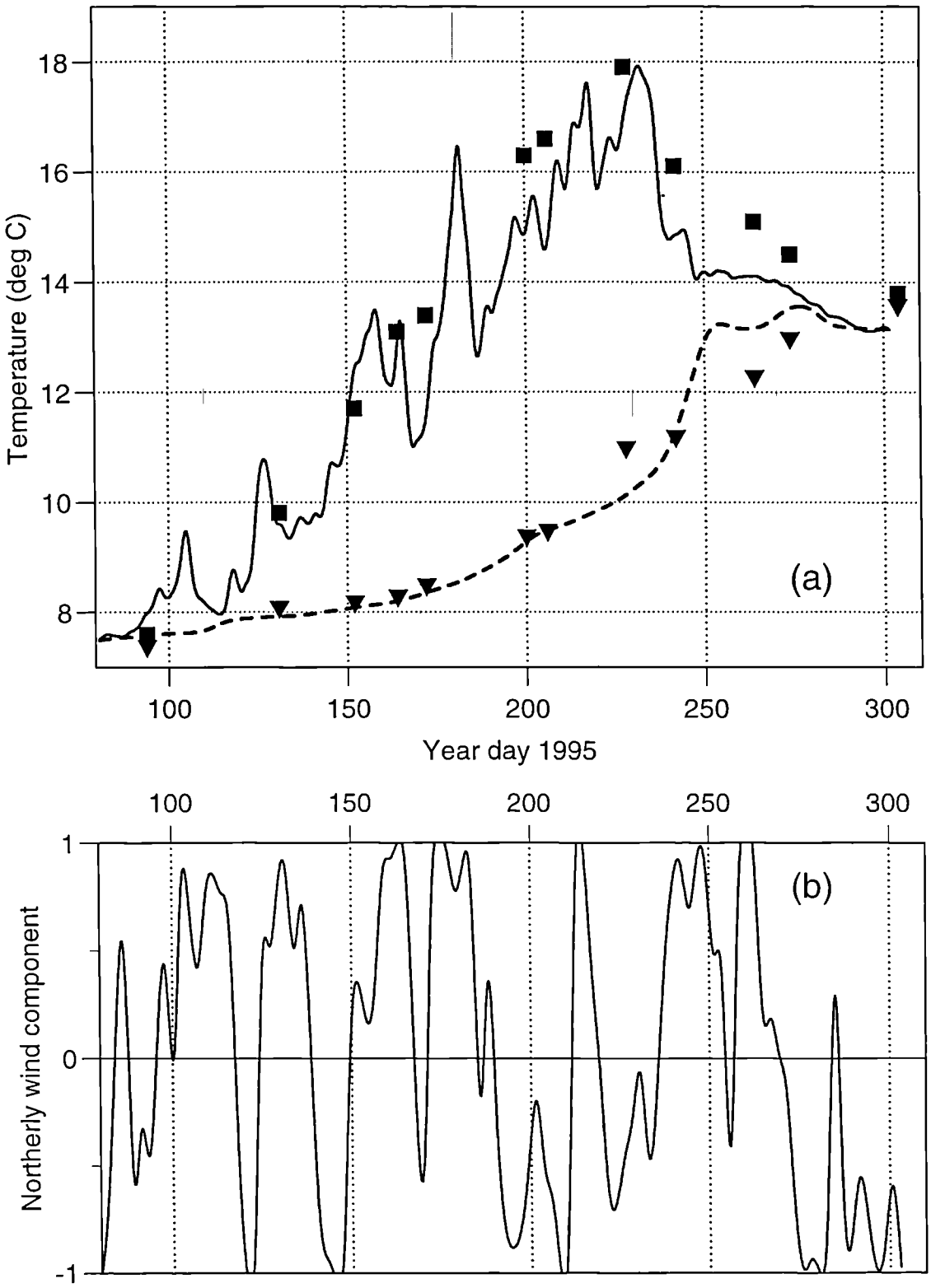

Fig. 6.13 (a) Surface (solid line) and nearbed (dashed line) temperatures (°C, 24 hour means) from model Run A for a cell corresponding to CTD station E4 (see Fig. 2.1) in the centre of the gyre. Also shown are observed surface (solid squares) and nearbed (triangles) temperatures. (b) Index of the northerly component of wind, calculated as the cosine of the 48 hour running mean of meteorological wind direction.

de-trended fluctuations in surface temperature by subtracting a linear trend from the latter, but the results were unrevealing). It is possible that the northern boundary condition on temperature had an influence on this result, with the peaks representing local heating unchecked by any advection of characteristically different water (westerly winds would bring equally warm water from the shallow zone near the Irish coast). Were the modelled surface temperatures in Fig. 6.13a to be smoothed, the resulting curve would still agree well with the observations which suggests that the temperature time series at the northern boundary (Table 6.1) was satisfactorily prescribed.

It was possible to extract surface and bottom temperatures from the various model runs at every location, and at every output stage, where a corresponding observation was made during 1995. In this way, a quantitative measure of performance of the different model runs was obtained. Pairs of modelled temperatures from Run A (stages 1-6) and observed temperatures (cruises PM1-PM7) are plotted in Fig. 6.14. The agreement of both surface and bottom temperatures was good, with slightly better agreement for bottom temperatures. The R^2 values (square of the correlation coefficient) obtained from statistical correlations provide a level of performance, or skill assessment, of the different model runs. The results of this analysis for Runs A-E are given in Table 6.4, where the best performances (by this criterion) were seen to come from Run A (SM1) and Run D (central differences). The central difference run gave better performance with respect to surface temperature prediction, whereas the SM1 scheme scored most highly on bottom temperature simulation.

Table 6.4 Linear regression coefficients, R^2, for the different model runs

Model run	Advection	R^2 values		
		Surface	Bed	Mean
A	SM1	0.743	0.852	0.797
B	SM2	0.721	0.810	0.765
C	SM5	0.676	0.727	0.702
D	Central	0.769	0.827	0.798
E	Upwind	0.489	0.483	0.486

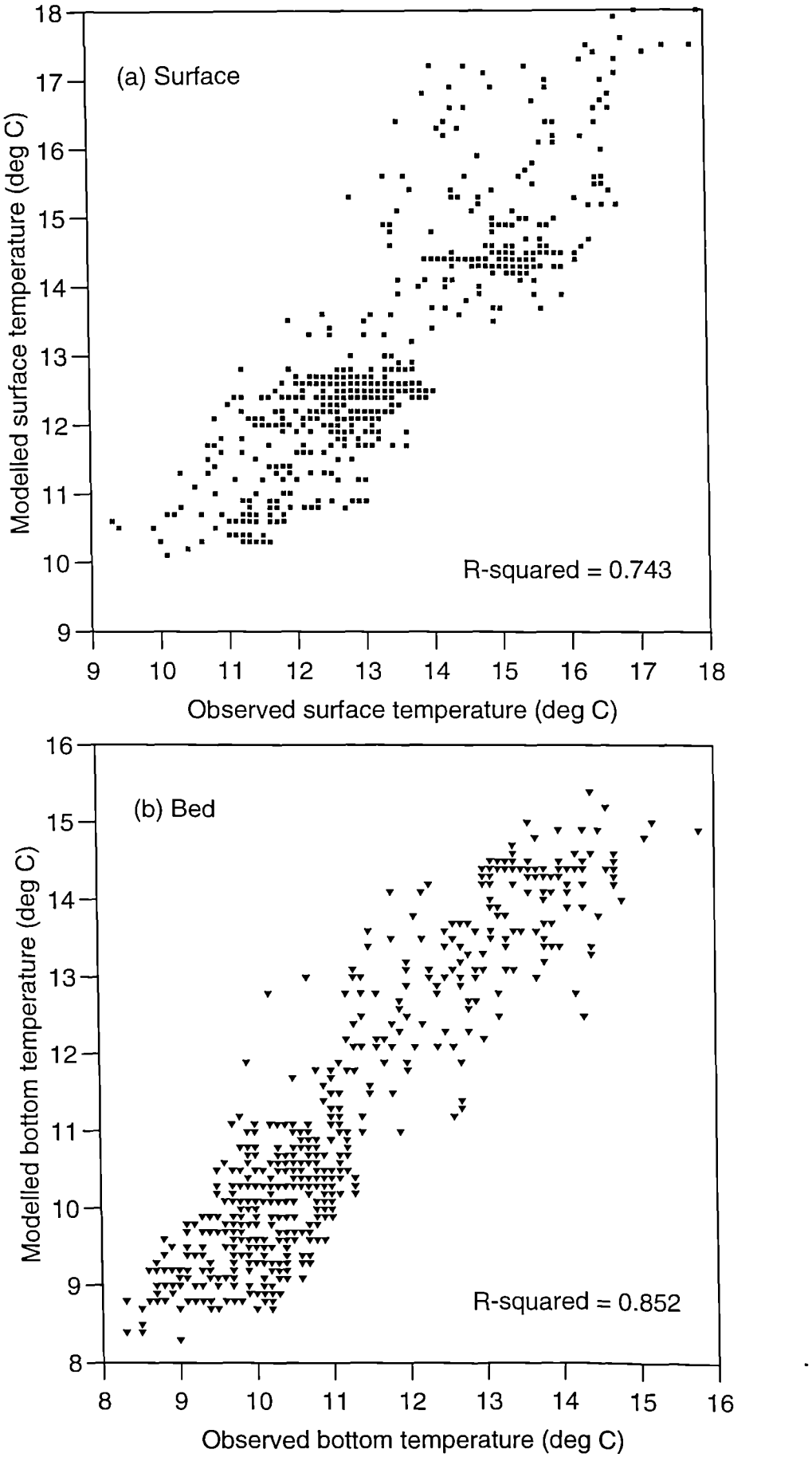

Fig. 6.14 Correlation of observed with modelled temperatures from Run A at each CTD station visited for cruises in 1995 up to and including 30 August (see Table 2.1).(a) Surface and (b) nearbed comparisons. The correlation coefficients, R^2, are shown.

The development of vertical temperature structure with time from Run A, at model 'station' E4, is shown in Fig. 6.15. This provides a more detailed view of the seasonal progression of stratification than does Fig. 6.13. No fixed-mooring time series of temperature exists for comparison, since intense fishing pressure in the region makes thermistor-chain moorings difficult to maintain. Contours of 12 h mean temperature for the duration of the run are shown in Fig. 6.15a. These show that the onset of stratification occurred around day 100 (during April) and that temperature stratification was well-established by day 152, when the first observations were made. Stratification persisted until day 250, after which vertically mixed conditions were predicted. During the stratified period, the bottom temperatures warmed gradually, and smoothly, whereas the surface contours showed considerable variability due to meteorological and advective influences.

During the stratified period, fluctuations of isotherms were seen down to 50 m depth in Fig. 6.15a. To further investigate this temperature variability, Fig. 6.15b presents the vertical structure of temperature (30 min averages) from Run A for a 40 day section of the record between July and August. Oscillations of isotherms throughout the water column, with an apparent semi-diurnal period, can be seen in Fig. 6.15b. This may indicate the existence in the model of internal tides. The 10-15 day scale periodicity implied by the minimum-value isotherms between 60 m and 100 m depth is not physical, but relates merely to the slow warming of the bottom water and the choice of contour interval. The large amplitude oscillation of these nearbed contours is also an artefact, resulting from the small vertical temperature gradients at these depths.

6.2.4 Evidence of internal tides

The wavelike pattern of isotherms in Fig. 6.15b may suggest the presence of internal tides, or may simply indicate the response of the water column temperature structure to the rise and fall of the barotropic tide. Intense packets of coherent waves were visible in the top 40 m on several occasions, punctuated by periods of less coherent

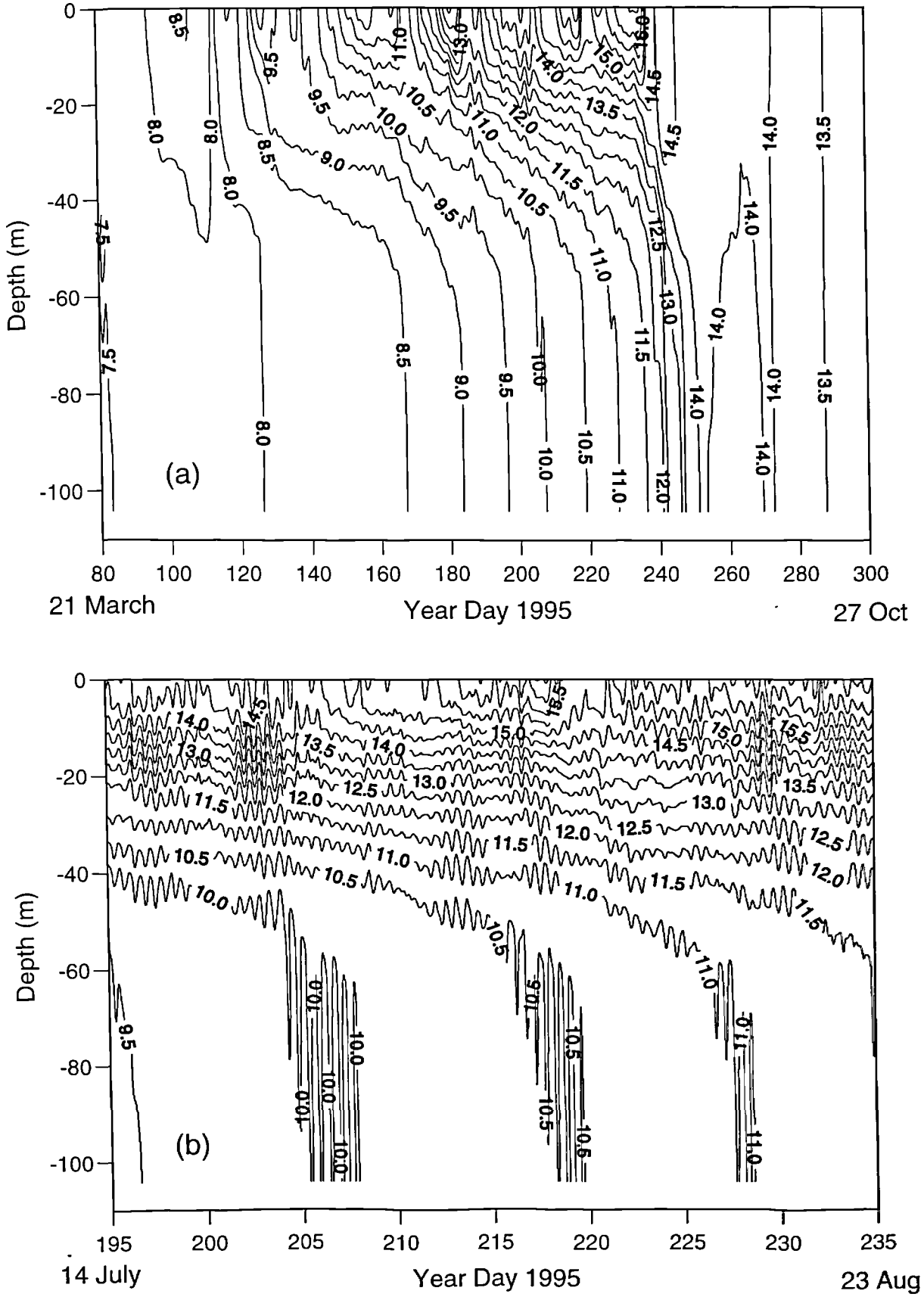

Fig. 6.15 (a) Time series of 12 h temperature means from model Run A at a cell corresponding to CTD station E4 (see Fig. 2.1) for the duration of the model run. (b) Shorter time series of 30 minute mean temperatures from Run A at the same location. Note the occurrence of packets of coherent temperature fluctuations, particularly at around 20 m depth.

oscillation of smaller amplitude. There were two such packets of high amplitude wave activity between days 195 and 210, and these are now examined in more detail. Fig. 6.16b shows again the 30 min average temperature fluctuations at model E4 along with (Fig. 6.16c) the same plot of vertical structure from model C4, to the north (see Fig. 3.1). Fig. 6.16a is the surface elevation at E4 and Fig. 6.16d is the magnitude of the northerly wind component. The coherent wave packets at E4 beginning on days 196 and 202 do not appear to be linked to any particular stage of the spring-neap cycle shown in Fig. 6.16a. Neither can any clear connection be made between the more coherent oscillations and the wind direction as shown by Fig. 6.16d. The fluctuations at the more northerly station (Fig. 6.16c) showed the same two bands of high amplitude activity, but approximately two days sooner. There is a suggestion then of the disturbances propagating from north to south with a lag time of two days.

The relationship between temperature fluctuations at a series of depths (at E4) and the surface elevation of the barotropic tide is shown in Fig. 6.17, for days 200-208. Temperatures from sigma levels 4-8 inclusive are shown in Figs. 6.17b-f. The equivalent depths of these sigma coordinates at zero elevation are shown on the graphs, and these vary by only ± 2% at this location, where the tidal amplitude is 2 m and the depth is 104 m. These levels were chosen to capture the majority of the thermocline yet be below the level of direct wind influence. The strongest fluctuations in temperature (of over 2°C) occurred at 10 m depth (σ-level 5) and a clear semi-diurnal periodicity can be seen, particularly between days 202-205. Although no time series of temperature were available from the 1995 or 1996 cruises, a fixed-mooring at this location during June 1993 provided the temperature time series in Fig. 6.18a from a current meter at 12 m depth. The temperature fluctuations are similar in magnitude, although the record is from June whereas the time series in Fig. 6.17 corresponds to late July. The power spectrum of the observed temperature record, computed using Matlab's fast Fourier transform (FFT)

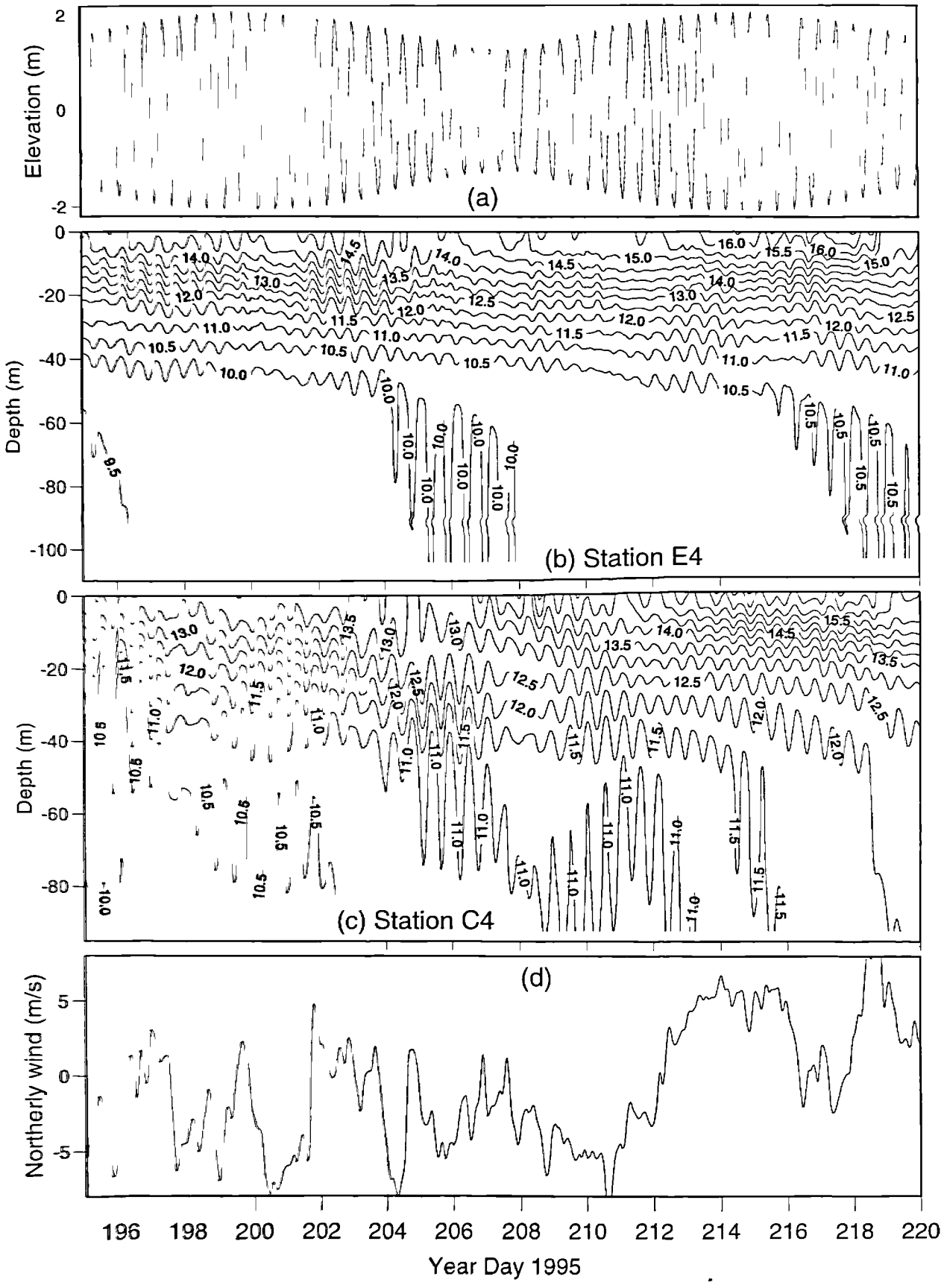

Fig. 6.16 Time series from Run A. (a) Surface elevation at station E4, (b) Temperature fluctuations at station E4 (30 minute mean values), (c) Temperature (30 min. means) at station C4, and (d) Magnitude (m s^{-1}) of the northerly component of the wind for the same period.

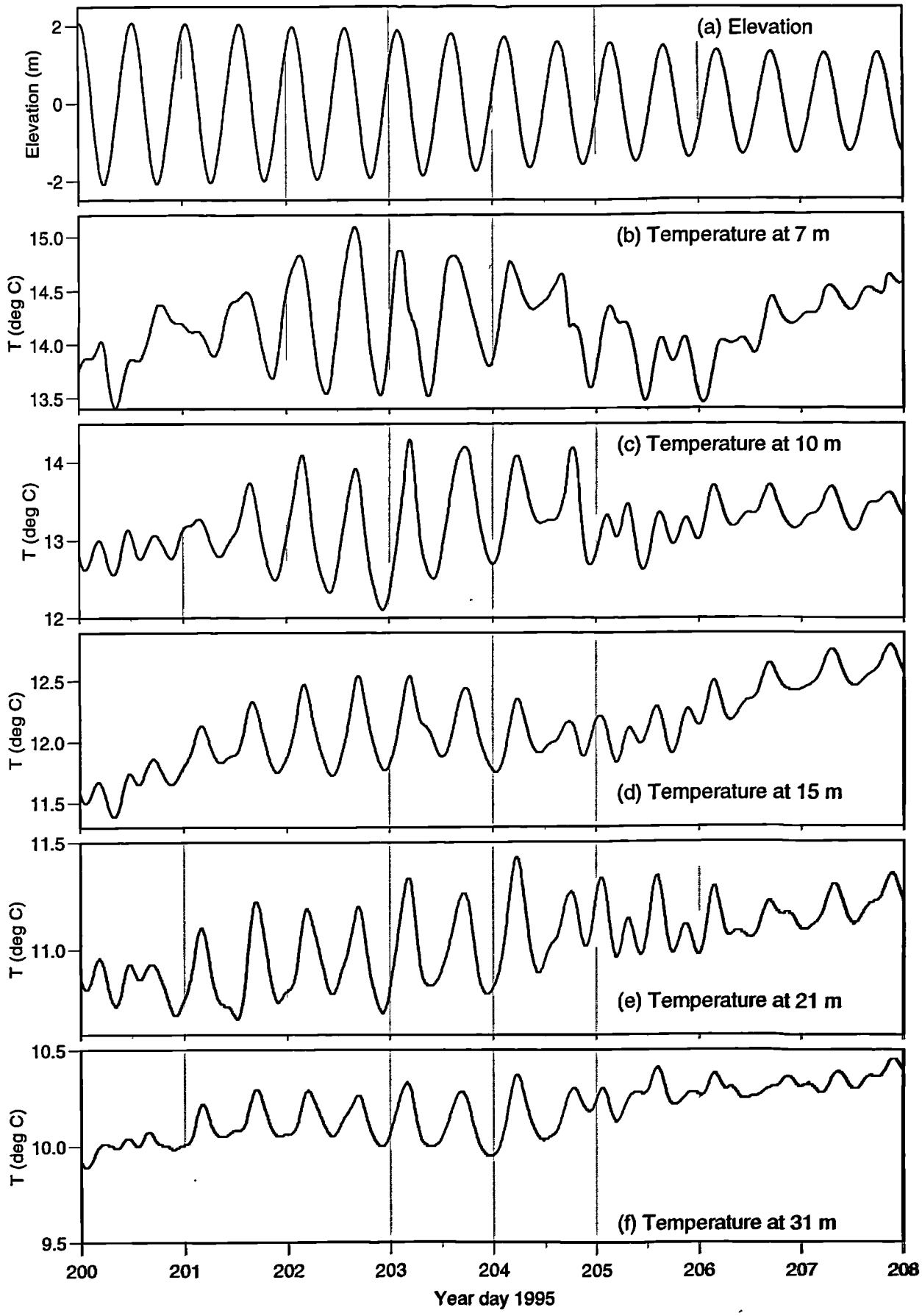

Fig. 6.17 (a) Surface elevation, and then (b-f) variation of temperature at model sigma layers 4-8 (corresponding depths relative to mean sea level are given) for Run A at station E4 (see Fig. 2.1). (b) 7 m, (c) 10 m, (d) 15 m, (e) 21 m, (f) 31 m. Note that the temperature oscillations are not precisely in phase and also that temperature *maxima* coincide with high water between days 201-205 of the sequence.

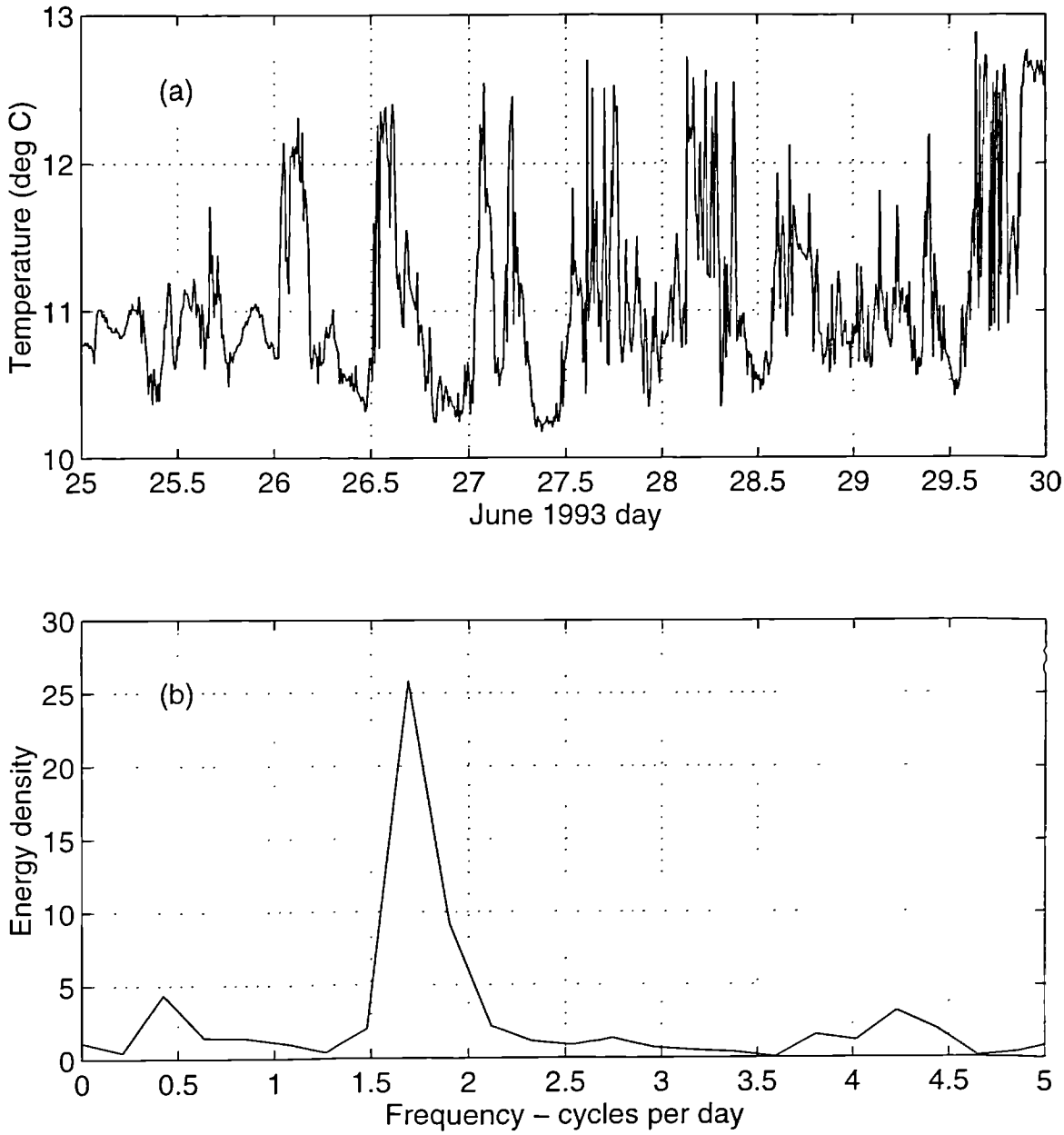

Fig. 6.18 (a) Time series of temperature from 12 m depth at a current meter mooring in the Irish Sea at station E4 (see Fig. 2.1) during June 1993. (b) FFT computed power spectrum (arbitrary units) of the observed temperature record. The spectral peak occurs at a frequency corresponding to a dominant period of 13.5 hours, reflecting semi-diurnal energy with a small inertial contribution.

algorithm, is shown in Fig. 6.18b. This displays a dominant semi-diurnal frequency (the peak is smeared towards inertial frequency slightly, and the minor peak at 2 day period may show atmospheric variability).

The fascinating result in Fig. 6.17 is that the peaks in temperature are almost in phase with local high water for a large part of the sequence. If the temperature structure were rising and falling as the water column stretched in response to the barotropic tide, then one would expect high water to coincide with *minimum* temperatures at any given depth. The phase relationships between surface elevation and temperatures at 7 m,10 m, 15 m and 21 m were calculated from the normalised cross-covariance of the two signals between days 201-205, and are shown in Figs 6.19a-d. The correlation lag at the maximum value of cross-covariance is approximately two hours for all four depths because the temperature series are in phase with each other. For a barotropic tide, the zero lag should occur at the *minimum* value of correlation coefficient. The high values (~0.8) of the normalised correlation coefficient indicate that temperature fluctuations are responding at the same frequency as the surface elevation. Analysis over the full 8 day sequence in Fig. 6.17 gave lower normalised cross-covariance (~0.3) with lags at maximum correlation of 1-2 hours.

A technique commonly used in the analysis of internal tides (e.g. Holloway, 1984, Sherwin, 1988) is to estimate the internal vertical displacements (from temperature time series and vertical temperature gradients) and then compare the amplitudes obtained with theoretical modal structures. It is easy to show (e.g. Apel, 1990 that vertical displacements due to an internal wave of the form $\eta(z)e^{i(kx - \omega t)}$, propagating in a stratified fluid over a flat bottom, can be represented as the sum of a series of normal modes which are eigensolutions of :

$$\frac{\partial^2 \eta}{\partial z^2} + \left(\frac{N^2(z) - \omega^2}{\omega^2 - f^2} \right) k^2 \eta = 0 \qquad (6.2)$$

where N is the buoyancy frequency defined as $N^2 = -g/\rho(\partial\rho/\partial z)$, ω is the internal wave frequency, f is the Coriolis parameter and k is the horizontal wavenumber.

The vertical profile of 24 h mean density (σ_t, based on salinity 34.2) at model station E4 on day 200 (July 20) is shown in Fig. 6.20a, and the calculated profile of N^2 is given in Fig. 6.20b. Numerical solutions of (6.2) based on this N^2 profile with ω taken as the M_2 frequency were found, subject to boundary conditions $\eta = 0$ at $z = 0$ and $z = -h$. Below 50 m depth, N^2 was interpolated onto 5 m intervals to avoid the fine resolution near the bed (small Δz) influencing the numerical solution. The vertical structure of the first three modes (lowest wavenumbers) are shown in Fig. 6.20c, whilst their wavenumbers, wavelengths and phase speeds (from $c = \omega/k$) are given in Table 6.5.

Table 6.5 Wavelength and phase speed of the first three normal modes at M_2 frequency, at cell (21,52), days 201-205. Based on modelled stratification.

Mode	Wavenumber (m^{-1})	Wavelength (km)	Phase Speed c ($m\ s^{-1}$)
1	1.98×10^{-4}	31.7	0.71
2	3.28×10^{-4}	19.2	0.43
3	4.24×10^{-4}	14.8	0.33

With a numerical model, vertical velocities are directly available so estimation based on temperature tendency and $\partial T/\partial z$ can be avoided. Unfortunately, vertical velocity was not selected as an output parameter when these model runs were conceived. However, it was possible to estimate it in the same way as one would from observations. A time series for vertical velocity, w, was calculated from:

$$w = -\frac{\Delta T/\Delta t}{\Delta T/\Delta z} \qquad (6.3)$$

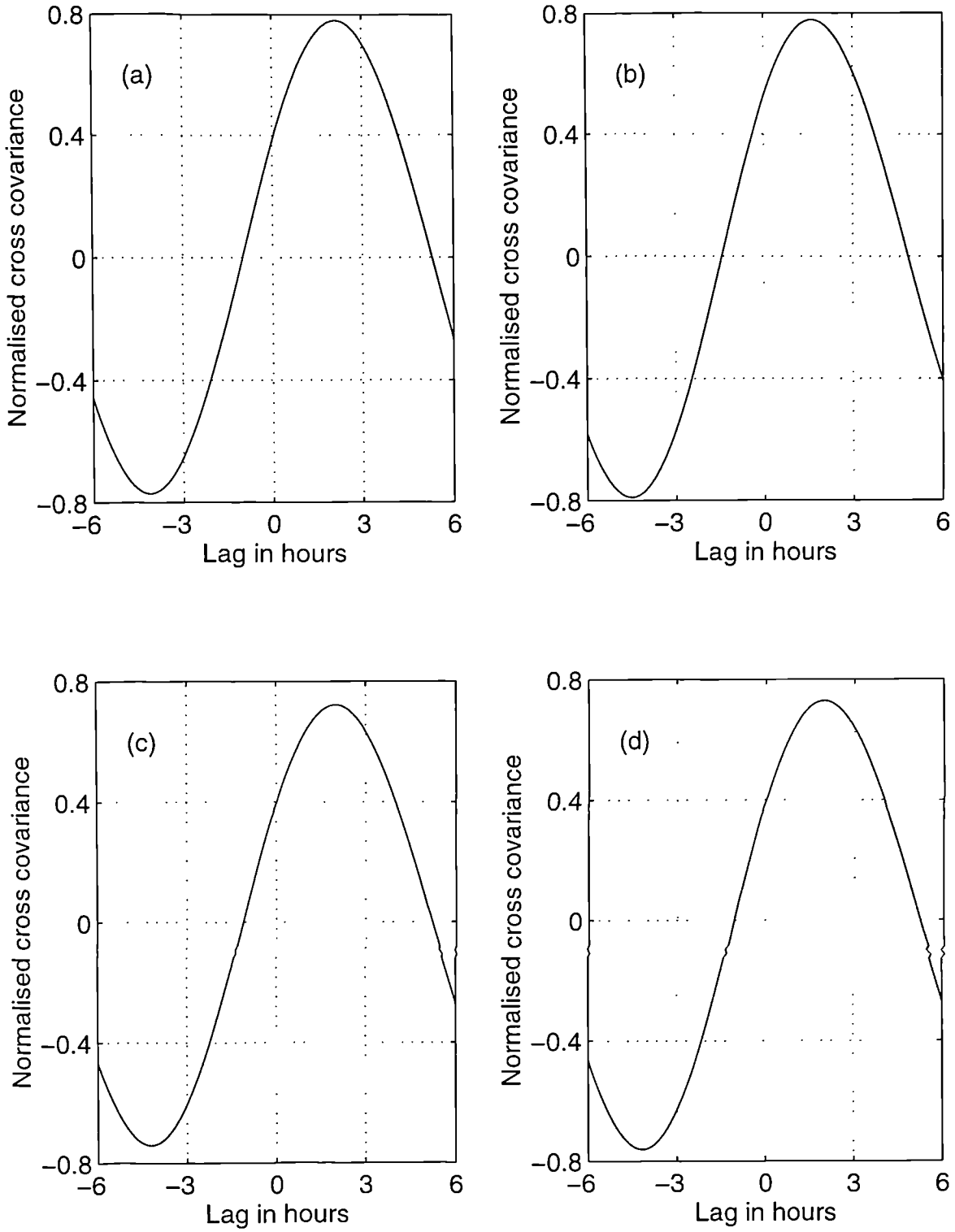

Fig. 6.19 Normalised cross-covariance function of the surface elevation record in Fig. 6.17a between days 201-205 with the temperature signal from (a) 7m, (b) 10 m, (c) 15 m and (d) 21 m. For a barotropic tide, the zero lag should occur at a minimum in the covariance function.

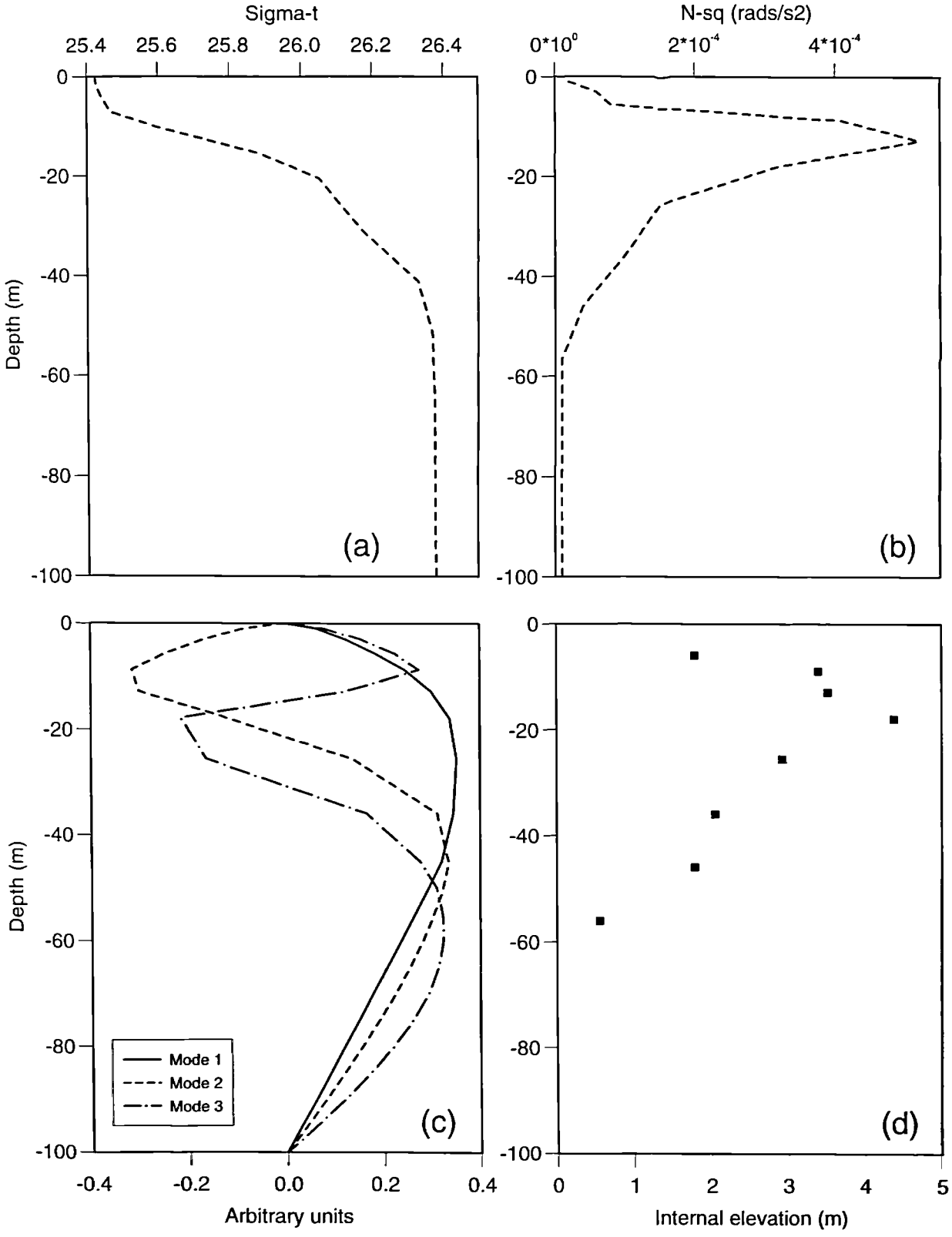

Fig. 6.20 (a) Vertical profile (24 h mean) of density (σ_t) at model cell corresponding to station E4 during day 200, (b) N^2 (rads s^{-1}) calculated from the density profile, (c) amplitudes (arbitrary units) of the first three vertical internal waves modes at the M_2 frequency, and (d) amplitudes of internal elevations at the model cell calculated by integrating the time series of estimated vertical velocity, w, at σ-levels 3-10, between days 201-205.

where horizontal advective terms, $u\partial T/\partial x$ and $v\partial T/\partial y$, in the temperature transport equation have been neglected. This is justified because horizontal temperature gradients are three orders of magnitude smaller than $\partial T/\partial z$ in the centre of the stratified region, so horizontal advection could not affect the temperature tendency, $\partial T/\partial t$, over timescales of the order of a time-step. Surface heating and diffusive terms can be neglected for the same reasons. The resulting time series of vertical velocity, w, from the model was integrated over days 201-205 to obtain internal elevations at σ-levels 3-10 inclusive. (Above this, the water column was strongly influenced by the direct action of the wind and no periodic vertical signal could be derived. Below σ-level 10 in the modelled temperature field, $\partial T/\partial z$ was too small to obtain a reliable estimate of w from 6.3). Internal elevations were then analysed at the M_2 frequency using a least-squares method to give the amplitudes shown by the solid squares in Fig. 6.20d. The internal elevations were in phase, as can be seen in Fig 6.17. It would be possible to go further and least-squares fit amplitudes and phases to the first three modes on the basis of the modelled internal elevations but, considering the small amplitude of the internal tide once the stretching effect of the barotropic tide has been deducted, and the likely poor accuracy of vertical velocities derived in this manner, *this has not been carried out.*

Finally, baroclinic currents, u_{bc}, at σ-levels 1-13 were calculated from $u_{bc}(\sigma, t) = u(\sigma, t) - U(t)$, where $U(t)$ was the depth-averaged current over these levels. Levels below this were neglected to avoid velocity reduction in the tidal boundary layer influencing the results. The instantaneous profile of velocity was uniform throughout the range of levels chosen. The M_2 frequency amplitudes and phases of the depth-averaged components were U (9 cm s^{-1}, 234°), V (24 cm s^{-1}, 223°), which was consistent with results obtained at this location during the tidal validation of the model in the previous chapter. Amplitudes and phases for the calculated baroclinic current components are given in Table 6.6.

Table 6.6 Amplitudes (H) and phases (g) of the M_2 baroclinic current components at cell (21,52), corresponding to station E4, calculated by subtracting the mean velocity over the range σ= 1-13, between days 201-205.

σ Level	Depth (m)	u_{bc} component		v_{bc} component	
		H (cm s^{-1})	g (°)	H (cm s^{-1})	g (°)
1	1	3.7	58	5.3	146
2	3	3.9	61	5.4	147
3	6	4.2	67	5.5	146
4	9	4.9	71	4.5	146
5	13	3.9	76	3.8	164
6	18	3.3	66	4.8	166
7	26	4.4	59	4.2	146
8	36	5.5	88	5.0	180
9	46	6.5	146	6.4	241
10	56	7.0	202	6.6	297
11	67	7.0	225	6.5	316
12	77	6.7	248	6.4	338
13	85	6.5	268	6.5	351

The phase relationships shown in Table 6.6, and the variation in amplitude of the baroclinic currents throughout depth are further evidence that internal tides were present in the model during the period analysed.

6.3 Residual circulation

6.3.1 Horizontal residual flow fields

The residual circulations in the western Irish Sea from model Run A, at four stages throughout the season, are shown in Fig. 6.21. The length of the arrows is proportional to the current vectors and only currents greater than 2 cm s^{-1} are shown. Shown are depth-mean flow fields that were obtained by averaging the model velocities over two M_2 cycles, and then subtracting the depth-mean tidal Eulerian residuals shown in Fig. 5.5. Consequently, contributions from wind-driven and density-driven circulations, as well as a small S_2 contribution, are embedded within the flows seen in Fig. 6.21. Even so, aspects of the familiar gyral pattern described by the drifter observations can be discerned. A weak (3 cm s^{-1}) southward flow near the Irish coast in early June can be seen in Fig. 6.21a, and northward flowing

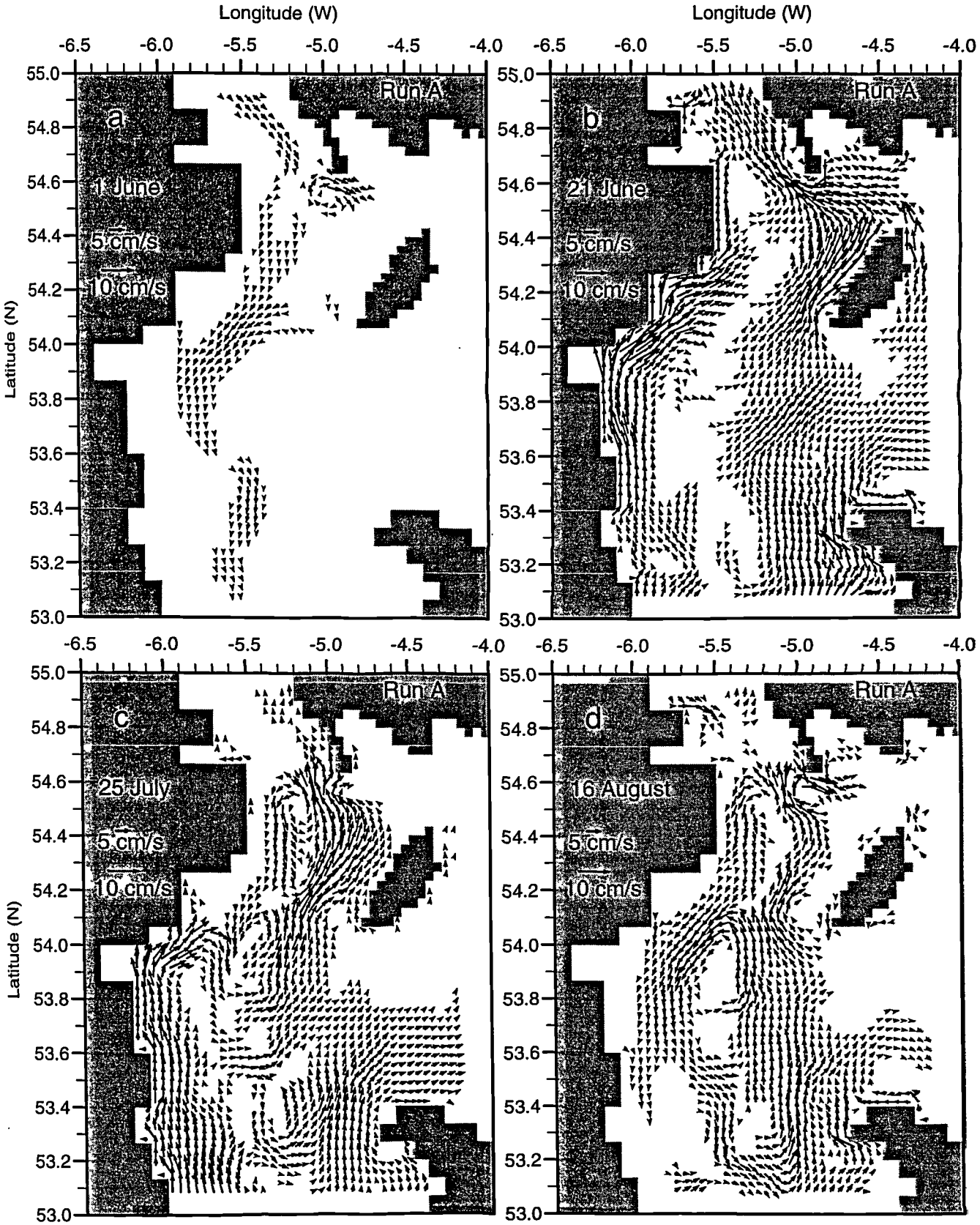

Fig. 6.21 Residual circulation fields from Run A. Depth-mean flows greater than 2 cm s^{-1} are shown and the M_2 Eulerian residual (Fig. 5.5) has been subtracted. (a) 1 June, (b) 21 June, (c) 25 July and (d) 16 August 1995. Note the distinct cyclonic gyre in Fig. 6.21d.

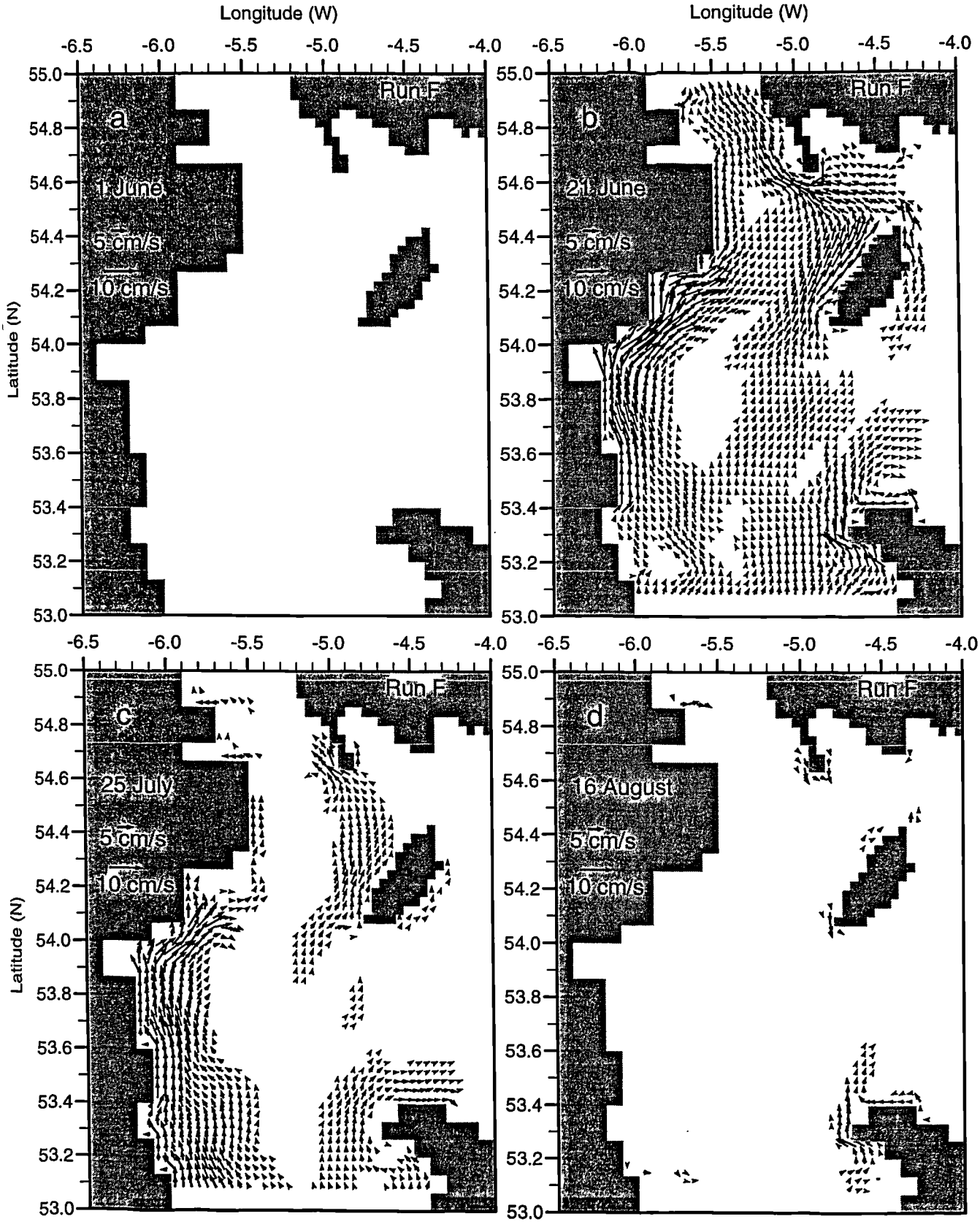

Fig. 6.22 Residual circulation fields from Run F where zero heating was employed. Depth-mean flows greater than 2 cm s^{-1} are shown and the M_2 Eulerian residual (Fig. 5.5) has been subtracted. (a) 1 June, (b) 21 June, (c) 25 July and (d) 16 August 1995. Note now the absence of any cyclonic gyre in Fig. 6.22d.

residuals on the eastern flank of the gyre can be seen in the subsequent three diagrams. By 16 August (Fig. 6.21d), the full cyclonic circulation pattern was apparent with maximum depth-mean speeds of 8 cm s^{-1} in places, on both sides of the gyre. The northward flows of 10 cm s^{-1} along the Irish coast seen on 21 June (Fig. 6.21b) and 25 July (6.21c) were inconsistent with any of the drifter tracks described earlier, but could have resulted from direct wind forcing in the model. Southerly winds prevailed over the period 195-210 and 25 July (Fig. 6.21c) corresponded to day 206. Winds were also southerly on day 171 (21 June) although they immediately gave way to winds from the north.

The simplest way of investigating whether the modelled residual flows were density-driven was to perform a repeat model run with identical wind forcing to Run A, but with zero heating. Run F did precisely this, and the depth-mean residual flow fields at the same four output stages (obtained using the same techniques) are shown in Fig. 6.22a-d. The circulations are clearly different from those in Fig. 6.21. The southward flow present in Fig. 6.21a is absent in Fig. 6.22a, as is the gyre that was so well defined on 16 August in Fig. 6.21d. A comparison of the two runs for July 25 shows that whilst the northward flow near the Irish coast is a feature of both Fig. 6.21c and Fig. 6.22c, the recirculation paths corresponding to the trajectories of drifters in Fig. 3.17 are only visible in Fig. 6.21c. This implies that the former was wind-driven whilst the latter relied on horizontal density gradients for its existence.

To better examine the density-driven component of residual circulation, the wind relaxation run described previously (a two day prognostic run with no wind and M_2 forcing only) was applied to the model, beginning at 21 June. Depth-mean residual currents (averaged over the final M_2 cycle with the Eulerian residual removed) greater than 2 cm s^{-1} are shown in Fig. 6.23a. Speeds of 4 cm s^{-1} were found on the northwestern corner of the circulation at 54.1°N, 5.6°W. Although the shape of the circulation resembled the gyre implied by drifter trajectories, the magnitude of the

residual flow was less than observed, and the segment of the gyre between Anglesey and the Isle of Man (which was repeatedly and reliably observed in drifter motions, see Fig. 3.15) was weak and non-continuous. To obtain an improved comparison with residual flows at a depth corresponding to the drogues of Argos drifters (24 m), the baroclinic flow averaged over σ-levels 4-11 inclusive is presented in Fig. 6.23b. This choice of levels spans a depth range of 3-38 m on the western side of the gyre (Irish coast) and 5-44 m on the eastern side, and ensures that modelled flow at the drogue depth is captured. The shape of the gyre in Fig. 6.23b is now clearer and flows were stronger, reaching a maximum of 5.5 cm s^{-1} on the western flank and 6.5 cm s^{-1} on the eastern limb, to the west of the Isle of Man at latitude 54.1°N.

The same decomposition of baroclinic flow was performed for 16 August (presumably most of the flow was baroclinic at this time, judging from Fig. 6.22d). The depth-mean flow is shown in Fig. 6.24a, and the flow averaged over σ-levels 4-11 is presented in Fig. 6.24b. The pattern agrees well with the drifter composite diagrams (see Fig. 3.15 and Fig. 3.17) and also with the modelled stratification field at this time (Fig. 6.4eiii). Speeds around the modelled gyre in Fig. 6.24b were as high as 13 cm s^{-1} at the two locations described previously (maximum circulation appeared to occur consistently at these places). Flows of 10 cm s^{-1} towards the east were also present at the southern end of the gyre, at latitude 53.2°N. A mean modelled circulation speed was calculated by vector averaging those currents greater than 5 cm s^{-1} in Fig. 6.24b, and was found to be 7.9 cm s^{-1}.

6.3.2 Quantitative comparison with drifter data

Chapter 3 described how data from drifter ensembles were averaged onto a grid of cells, each 1/15° of latitude by 1/10° of longitude, so as to provide a pseudo-Eulerian picture of flow from the collective drifter trajectories. This grid spacing corresponds to four cells of the numerical model. The gridded velocities thus derived, for an ensemble of 16 drifters from July and August (see Fig. 3.20b and text in §3.2), are

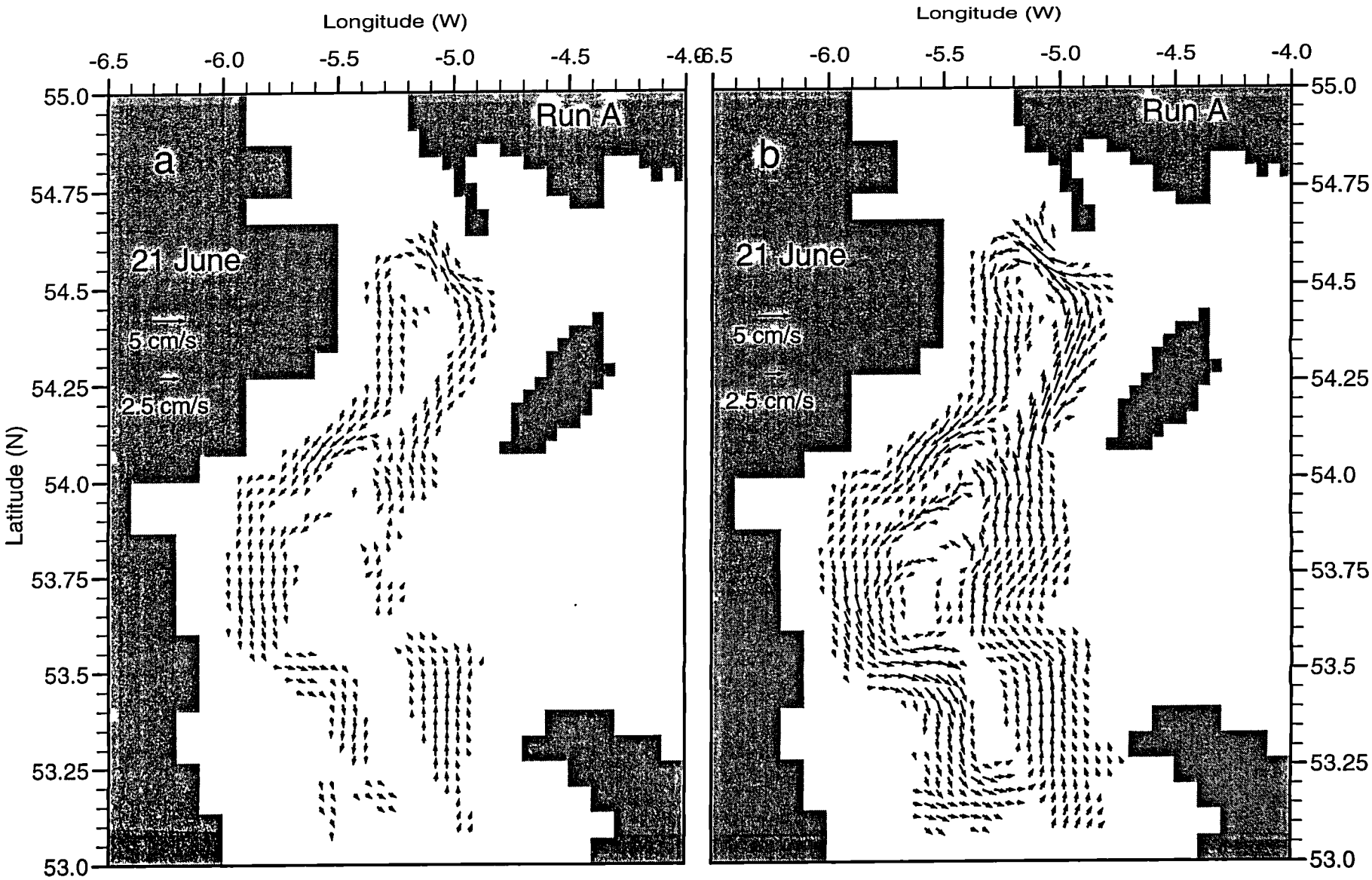

Fig. 6.23 Density-driven circulation (> 2 cm s^{-1}) obtained by integrating the model forward for 2 days from 21 June using only M_2 forcing, and subsequent removal of the Eulerian residual: (a) depth-averaged residual flow, (b) currents averaged over σ-levels 4-11, for consistency with the depth at which the drogues of Argos drifters were placed (24 m).

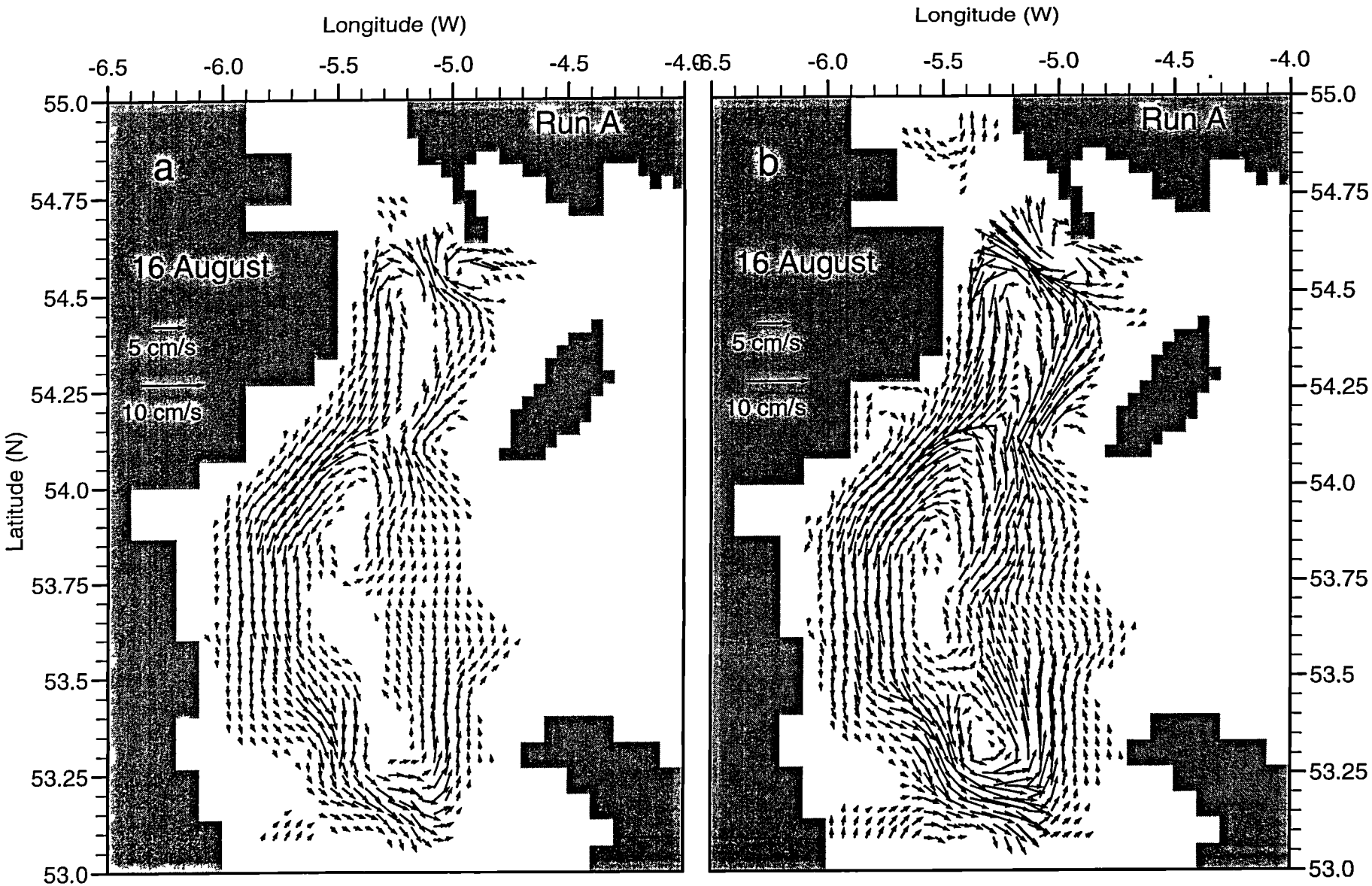

Fig. 6.24 Density-driven circulation (> 2 cm s^{-1}) obtained by integrating the model forward for 2 days from 16 August using only M_2 forcing, and subsequent removal of the Eulerian residual. (a) depth-averaged residual flow, (b) currents averaged over σ-levels 4-11, for consistency with the depth at which the drogues of Argos drifters were placed (24 m).

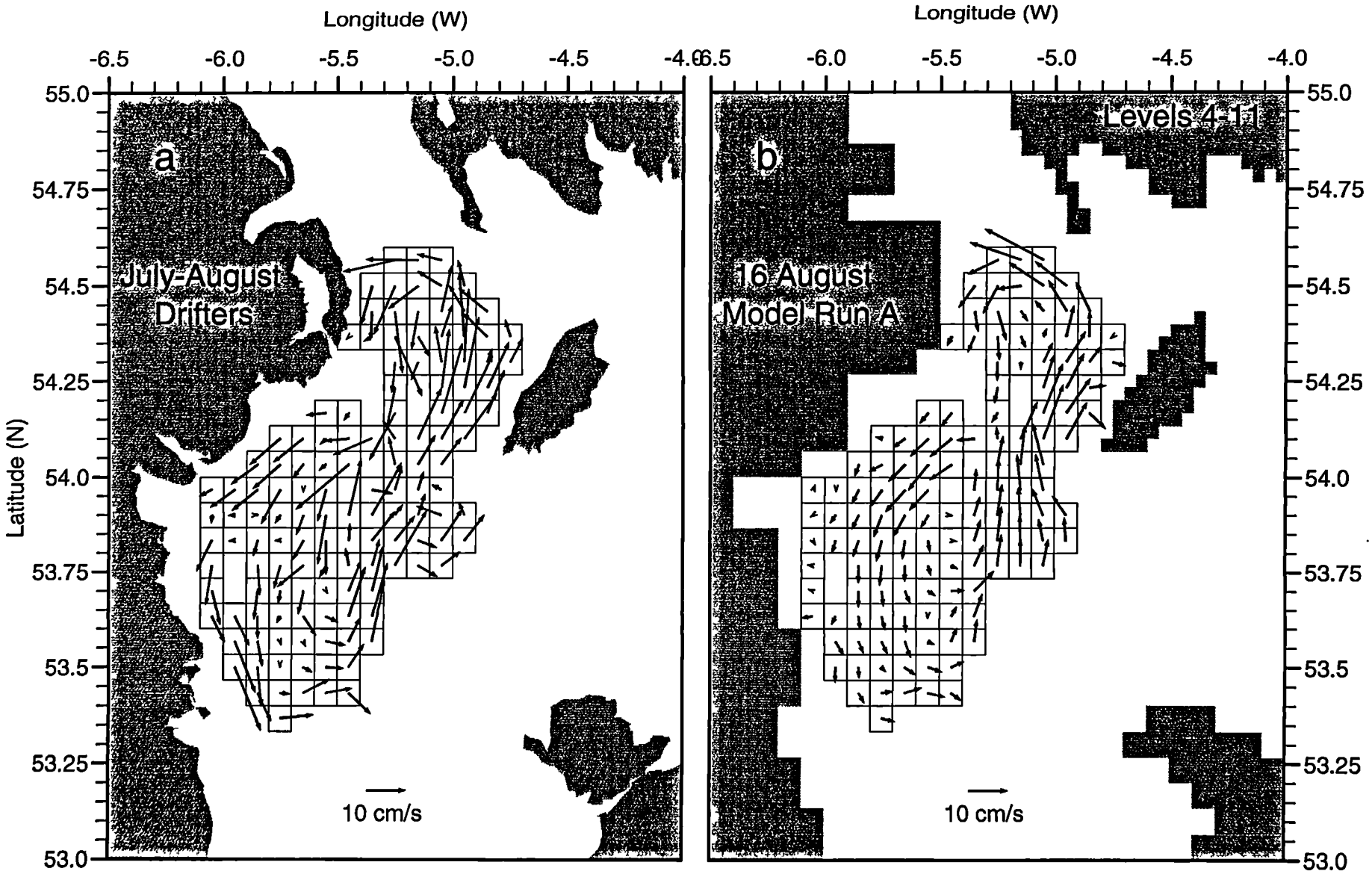

Fig. 6.25 (a) Residual velocity vectors derived from the filtered tracks of 16 Argos drifters deployed in July/August 1995 and (b) residual currents at the same locations (4 cell averages) from σ-levels 4-11 of Run A at 16 August. Apart from averaging over 2 tidal cycles, no other manipulation was performed on the modelled currents in Fig. 6.25b.

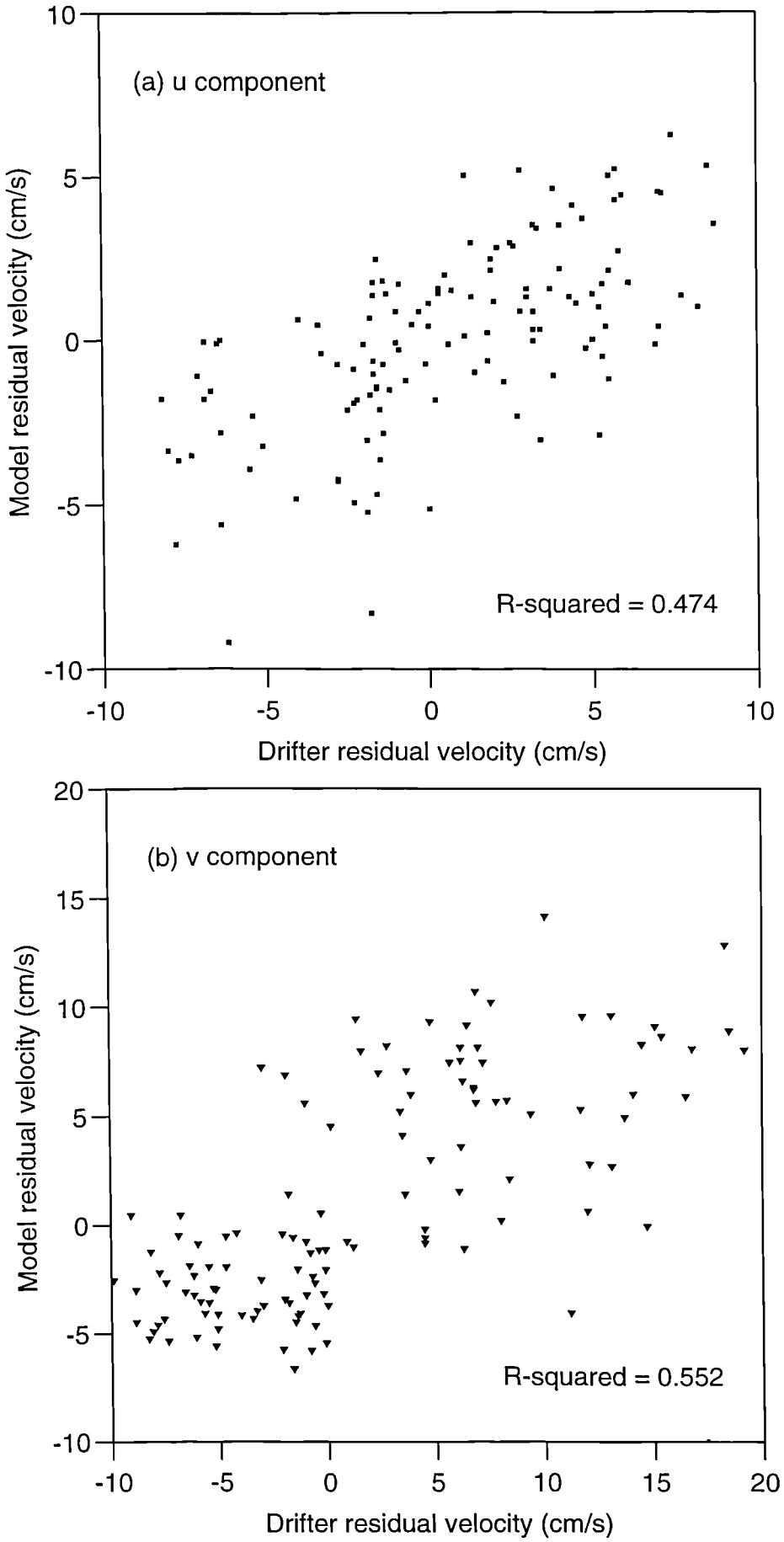

Fig. 6.26 Correlation of both components of modelled residual velocity at 16 August from Run A (σ-levels 4-11) with components of residual velocity from 16 Argos drifters as shown in Fig. 6.25a. (a) u component and (b) v component. Both values of R^2 are significant at the 99% confidence level ($n = 133$).

repeated in Fig. 6.25a where a qualitative comparison can be made with the modelled residual flow (between σ-levels 4-11) shown in Fig. 6.25b. In this instance, the latter has not been relaxed in any way (i.e. no subtraction of wind or tidal residual flow) and was averaged over two M_2 cycles and then grouped into correspondingly sized cells. The gridded model data is only presented for those cells where drifter data existed.

A quantitative comparison was performed by correlating the u and v components of the drifter and modelled velocities at each of these cells. The component pairs are plotted in Fig. 6.26 where the R^2 values (square of the correlation coefficient) are shown. Both components correlate significantly at the 99% confidence level (n = 133 degrees of freedom). Not surprisingly, there was no significant correlation ($R^2 \approx$ 0.1 for both u and v components) of the drifter velocities with the residual velocity components obtained for 16 August in Run F (Fig. 6.22d).

6.3.3. Vertical structure of the residual flow

An east-west vertical section (x-z) through the flow fields seen in Fig. 6.24 (i.e. derived from the wind relaxation run, but with no vertical averaging) is presented in Fig. 6.27a. This section is for the model equivalent of line E, at latitude 53° 50'N. Solid lines indicate the component of flow into the page and reveal a broad current towards the north, with maximum speeds of 10.5 cm s^{-1} in a narrow core at 20 m depth. On the western side of the section (Irish coast) there was a southward flow (dashed lines indicate flow out of the page) of lesser magnitude, with maximum speeds of 7 cm s^{-1} being found slightly deeper, at 30 m depth. The fainter, dotted lines represent the contours of density (σ_t) from the model, at intervals of 0.1 kg m^{-3}. Absolute values are not shown, for clarity, but the densest water in the centre of the dome had σ_t = 26.0 kg m^{-3} and the pattern was similar to that of neighbouring line F, whose density structure at this stage in the model run was shown in Fig. 6.7e. The

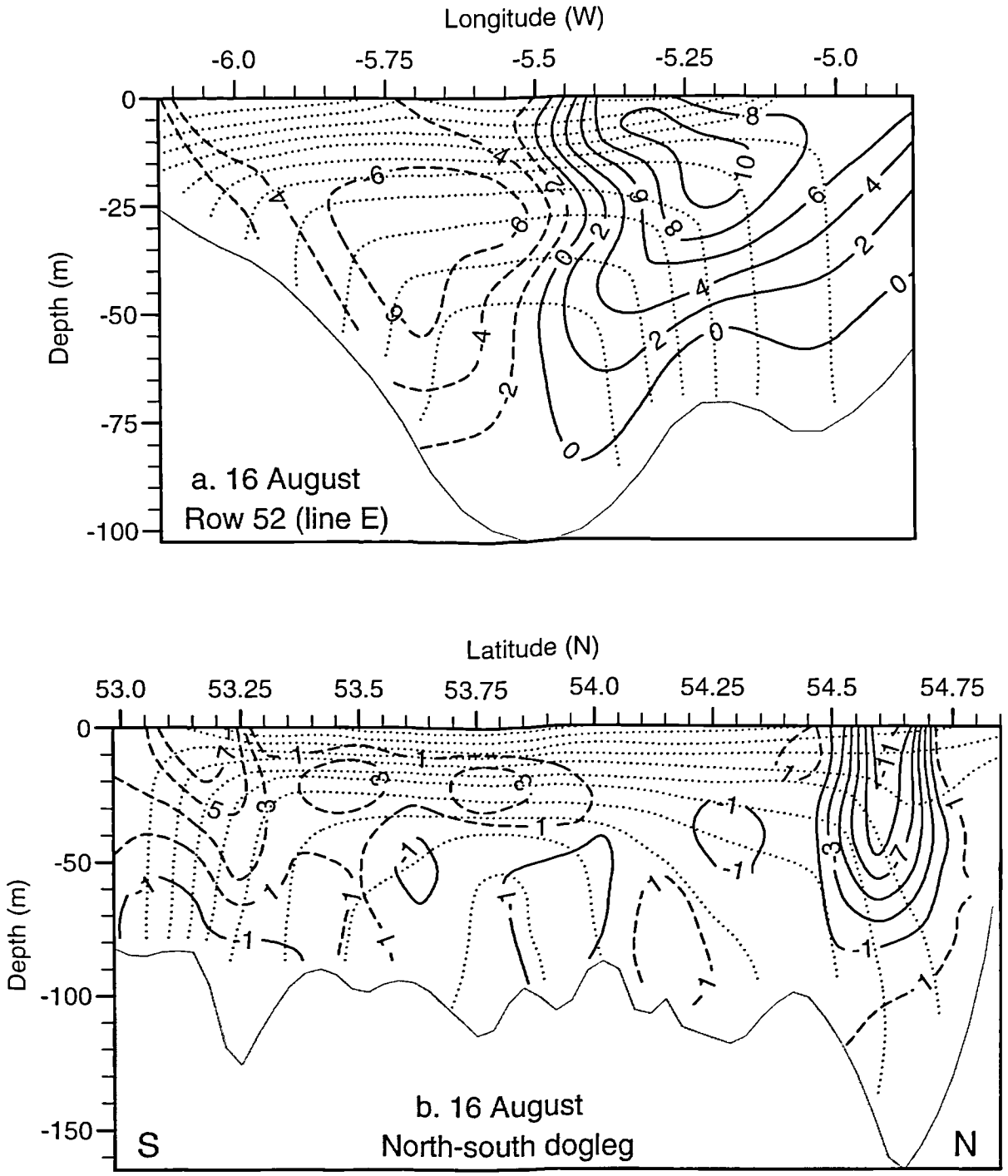

Fig. 6.27 (a) North-south component of residual velocity normal to line E on 16 August. Solid and dashed isopleths indicate flow into and out of the page respectively. The fainter dotted lines show the contours of density at this time. (b) East-west component of residual velocity normal to the NS section described in the text and shown in Fig. 6.12. Isotachs are in cm s^{-1} .

vertical structure of the residual flow field was roughly symmetrical about the density field, with the reversal in direction occurring at longitude 5.5°W.

An oblique section running from the southern to the northern end of the gyre, as shown by the line denoted NS in Fig. 3.1, is shown in Fig. 6.27b. Contours now represent the east-west component of the residual flow from the model at 16 August. Solid and dashed lines represent flows into and out of the page, respectively, as before and the prevailing density field is shown by the dotted, unlabelled lines whose values are as for Fig. 6.12e. The residual component normal to this section was concentrated in surface jets at the northern and southern limits of stratification. Maximum residual flows were 11.5 cm s^{-1} in the north and 7.5 cm s^{-1} in the south. Between these two regions the residual u component was weak (~ 1 cm s^{-1}) and variable in direction, although Fig. 6.27b does suggest that the eastward flow at the southern end of the section was broader than the westward flow at the northern limit.

6.4 Autumnal breakdown of the gyre

6.4.1 Response of the cold pool to strong winds

It is clear from the observations presented previously that the density structure of the western Irish sea cold pool and, therefore possibly the associated cyclonic circulation, persists beyond the autumnal equinox. It was postulated in §3.3 that it may even be possible for strong winds to intensify the nearbed, horizontal density gradients by moving warm water above the thermocline into a regime where it becomes rapidly homogenised by tidal mixing. The now warmer, well-mixed water will create a stronger density contrast with the coldest water beneath the thermocline (which is below the level of wind influence and whose temperatures are unchanged).

Two numerical experiments were performed to test this hypothesis. Both used as their initial conditions the density structure of 16 August. A wind of 17 m s^{-1} was prescribed for 36 hours, in one case from the north and in the other from the south.

This wind speed corresponded to the lower end of Beaufort Force 8 (gale). The response of the model was analysed by reference to the east-west transverse section at 53° 50'N, as shown previously by the dotted lines in Fig. 6.27a (which represent the initial condition for this section). The density field along this section at 12, 24 and 36 hours after the onset of the northerly gale is shown in Fig. 6.28. After 36 hours of this constant wind, the currents in the upper part of the water column were everywhere in excess of 0.5 m s^{-1}. The model was then run prognostically for a further two M_2 cycles, and currents averaged over the last of these to obtain the residual currents due to the new density regime. The v component of these currents normal to the x-z section is superimposed on the density field after 36 hours of wind in Fig. 6.28c. The series of diagrams shows how the surface density structure was rapidly eroded by winds of this magnitude, but the density pattern below 25 m depth was still present. The horizontal gradients of density on the dome's eastern side were not significantly changed, but nearbed density gradients on the western flank of the dome (at 5.75°W) were much stronger after 36 hours. This is consistent with a downwelling of water along the Irish coast advecting isopycnals towards the centre of the cold pool. The warmest surface waters were moved towards the west, as can be seen by the progression near the surface of the 25.4 and 25.5 isopycnals. The residual flow pattern was altered too, with the strongest southward flows increasing to 11 cm s^{-1} in a strong band of currents near the surface. The northward flow was now weaker and more diffuse with maximum flows of 8 cm s^{-1}, offset slightly to the east of the bottom front which marks the eastern flank of the cold pool.

The response of the density field at the same intervals, and the final residual currents, when the gale was blown over the model from the south is shown in Fig. 6.29. It is clear that after 36 hours, the bottom front on the eastern flank of the cold pool had intensified. Associated with this increase in horizontal density gradient was an increase in the northward flowing component of the residual currents. Maximum surface currents of 13 cm s^{-1} marked the centre of an intense band of near surface flow at 5.3°W, concentrated directly above the zone of strongest horizontal density

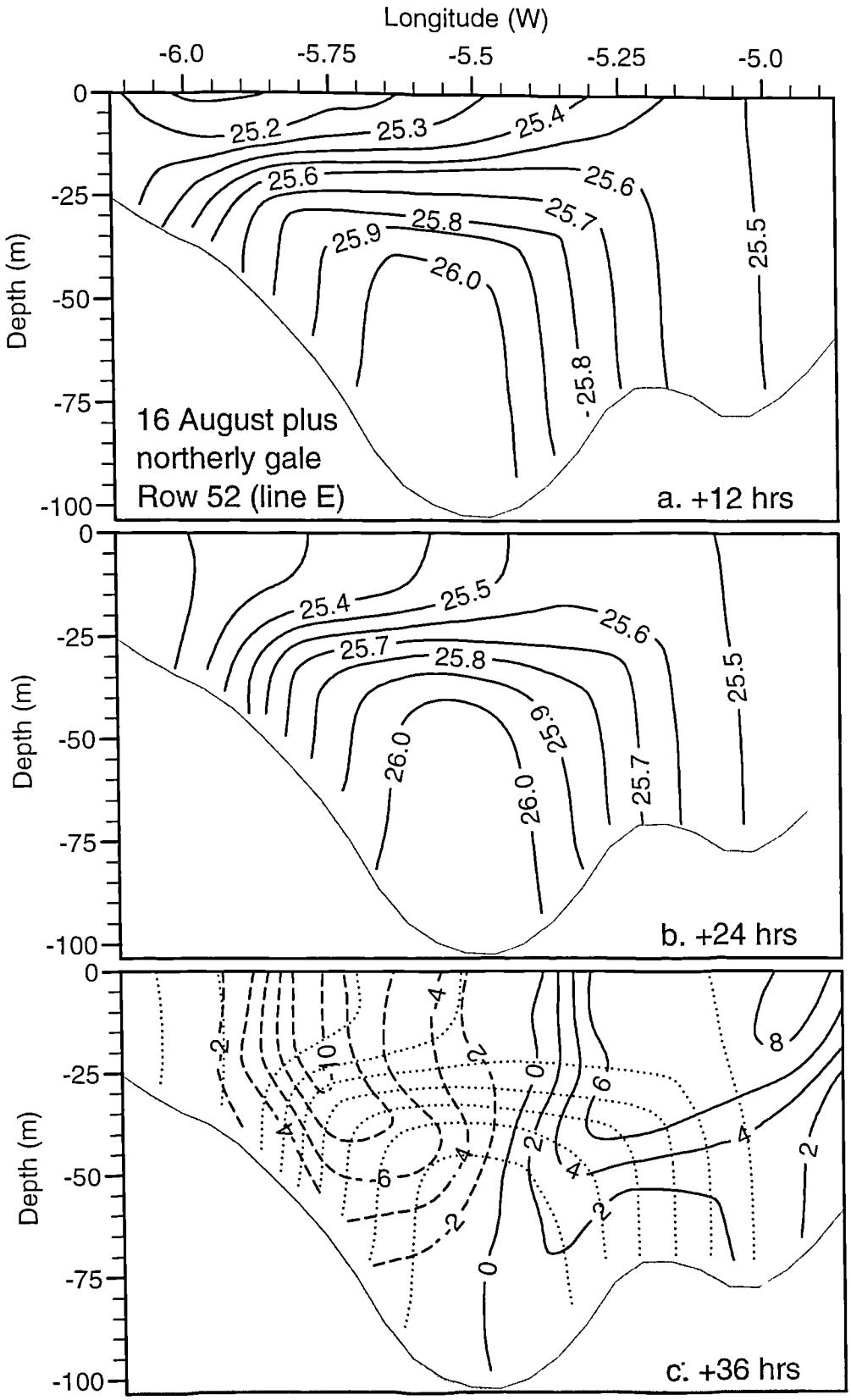

Fig. 6.28 Response of the cold dome at line E on 16 August to a strong (17 m s^{-1}) wind from the north. The initial condition is the density field shown by the dotted lines in Fig. 6.27a. Shown here is the resulting density (σ_t) field at (a) 12, (b) 24 and (c) 36 hours after the onset of the wind. The residual velocity field is also shown in Fig 6.28c. Isotachs are in cm s^{-1} and dashed lines indicate flow out of the page.

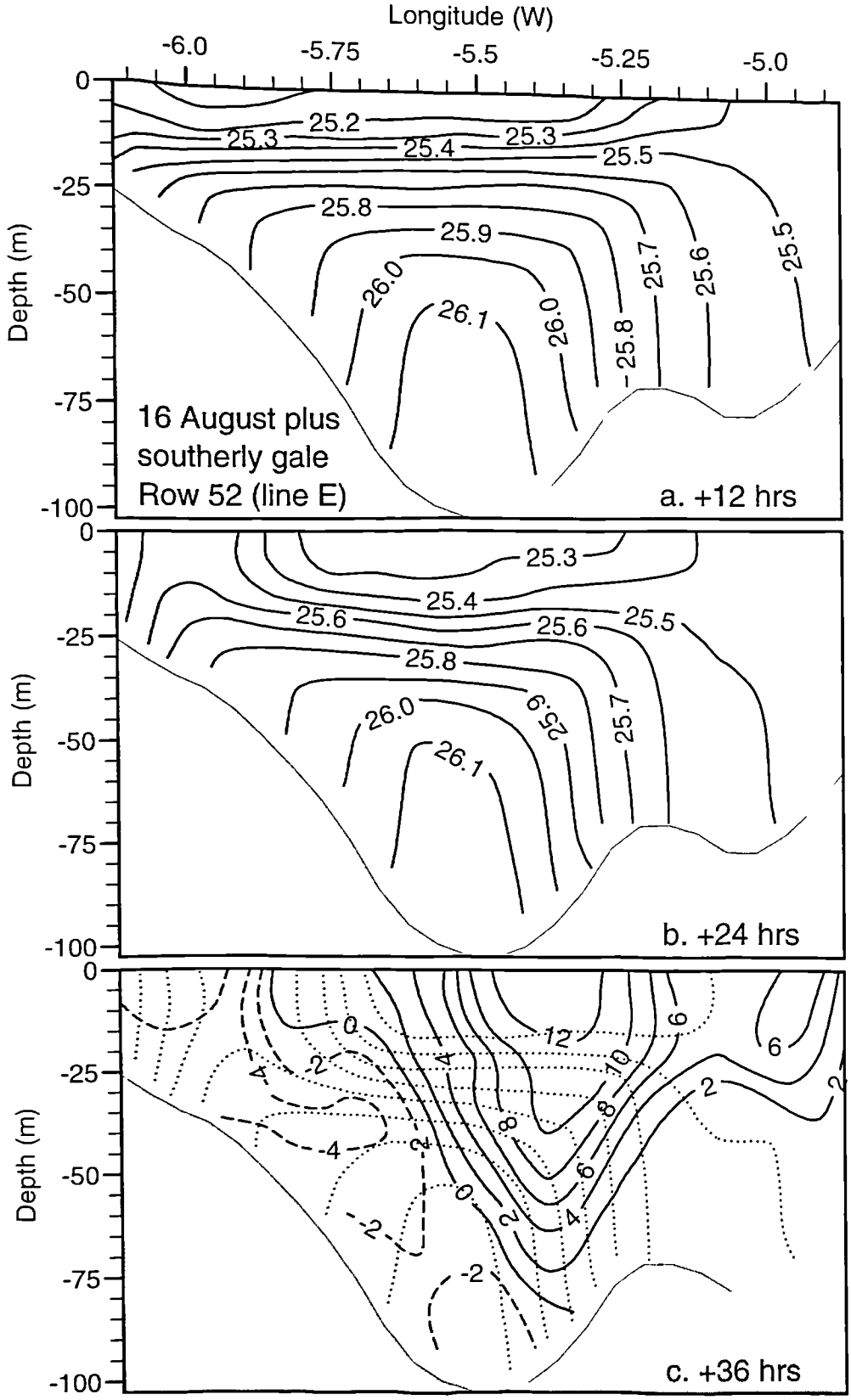

Fig. 6.29 Response of the cold dome at line E on 16 August to a strong (17 m s^{-1}) wind from the south. The initial condition is the density field shown by the dotted lines in Fig. 6.27a. Shown here is the resulting density (σ_t) field at (a) 12, (b) 24 and (c) 36 hours after the onset of the wind. The residual velocity field is also shown in Fig 6.28c. Isotachs are in cm s^{-1} and solid lines indicate flow into the page.

gradients. In contrast, the nearbed density gradients on the western side of the line weakened and the southward flow diminished to 4 cm s^{-1} (from a core with flows > 6 cm s^{-1} shown in Fig. 6.27a). As a result of the southerly winds (and surface Ekman transport to the right) the warmest water above the thermocline was advected towards the east, as can be seen by the 25.3 and 25.4 isopycnals in Fig. 6.29b. A surface density front marking the western limit of the warm water persisted, and advected with it, but as the warm water was advected into the transition zone between stratified and well-mixed areas (at 5.1° W), there was no further trace of a surface front - only the 25.3 isopycnal remained.

6.4.2 Effect of air temperature in the heatflux calculation

The least satisfactory aspect of model performance in the seasonal simulations described here was its failure to maintain agreement with observed temperature stratification beyond August. It can be seen from Fig. 6.11 that none of the (otherwise well-performing) model runs predicted the vertical temperature stratification of 2.5°C that was observed during cruise PM8 (21 Sept). The tendency for stratification in Run A to break down too rapidly can also be seen by the convergence of surface and bottom temperatures (solid and dashed lines respectively) from day 240 onwards in Fig. 6.13a. This discrepancy was not thought to be a result of the prescribed temperatures at the northern open boundary. Table 6.1 shows that the temperature boundary condition varied linearly between 14-15°C from 14 August to 20 September, and the observed surface temperature at station E4 on 21 September (day 264) was 15.1°C (solid black square in Fig. 6.13a), which was in agreement with the boundary condition. However, the modelled surface temperature at this station on day 264 (see Fig. 6.13a) had fallen to 14°C.

Air temperatures for Dublin airport (which were used in the model's calculation of longwave radiation losses from the sea surface) for the period 30 August (day 242) to 21 September (day 264) are shown in Fig. 6.30a. Apart from at the beginning of this period, mean temperatures were approximately 12.5°C with diurnal fluctuations

of up to 7°C. These temperatures were significantly lower than the observed sea surface temperature during the period, and it seems likely that the prescription of air temperature from a terrestrial weather station is the principal reason why modelled stratification decayed too early in the season. Convective overturning and the high specific heat capacity of water ensure that temperature changes at the sea surface, in response to atmospheric cooling, are slow. This, in turn, moderates air temperatures over the sea. Large diurnal fluctuations in air temperature over the sea do not occur, and mean air temperatures over the sea during the autumn and winter are typically higher than those over land.

A record of air temperature from a meteorological buoy was not available for the western Irish Sea, so Dublin airport weather station was selected to supply the heat flux forcing data because of its proximity and the fact that all of the required quantities (solar insolation, air temperature, relative humidity) were available. No calibrated relationship between temperatures at this weather station and the sea region exists for 1995, but during 1981 Lavin-Peregrina (1984) compared properties from Dublin airport and a meteorological buoy situated at a location equivalent to our E5. Lavin-Peregrina (1984) found that daily mean temperature at Dublin airport was greater than that over the western Irish Sea by typically 1°C for much of the summer, but after 10 September 1981 the offshore temperature exceeded that at Dublin airport by 0.5-1.0°C. Model Run G implemented an appropriate adjustment to the prescribed air temperature used to force the model, but was otherwise identical to Run A. In Run G, from 1 September onwards, the model was forced with 24 h mean air temperatures that were calculated from the Dublin airport hourly values, and increased by 0.5°C. This change accounted for both the lack of diurnal fluctuation expected over the sea surface, and the moderating effect of the sea on the daily mean air temperature during autumn. It should be stressed that this run did not attempt to achieve an accurate description of forcing air temperatures in the absence of buoy data, but was merely used as a technique to demonstrate the importance of

prescribing air temperature correctly, in order to obtain an accurate simulation of the breakdown in stratification.

The time series of surface and bottom temperatures at model E4 (cf. Fig. 6.13a) are shown in Fig. 6.30b. Observations from 1995 are shown respectively by solid squares and triangles, as before. In this run, surface temperature was in far better agreement with observations after day 260 than in Run A (Fig. 6.13a). The final breakdown of stratification in Run G took place at day 300 (27 October). Bottom temperatures in Fig. 6.30b (dashed line) remained higher than observations after day 250. The sudden rise in bottom temperatures at day 240 (in both Fig. 6.13a and Fig. 6.30b) lagged the rapid drop in surface temperature (day 235) by a few days. This is thought to represent a major mixing event due to increased winds from day 235 (see Fig. 6.2), where 10 m s^{-1} winds veered from the southwest to the north. The surface temperature drop may also have been overestimated because of diurnal fluctuations in air temperature prior to the applied correction in Run G. The remaining temperature stratification in Run G at day 278 (5 October) was 0.9°C, slightly less than observed during cruise Cor10/95.

A transverse section of temperature from Run G on 21 September along model row 52 (line E) is shown in Fig. 6.31b, along with the observations from cruise PM8 (Fig. 6.31a) The predicted temperature field in this case displays a more dome-like structure than did comparable results from Runs A or B (see Fig. 6.11), although the maximum vertical temperature difference here is only 1.3°C, compared to the observed 2.5°C. This is because bottom temperatures are too high, for the reasons discussed above With further adjustment to the air temperature, better agreement with observed temperatures in three-dimensions could doubtless be contrived, but it is sufficiently clear from Run G that a correct prescription of air temperature over the sea is required if the model is to predict the proper timing of the breakdown in stratification

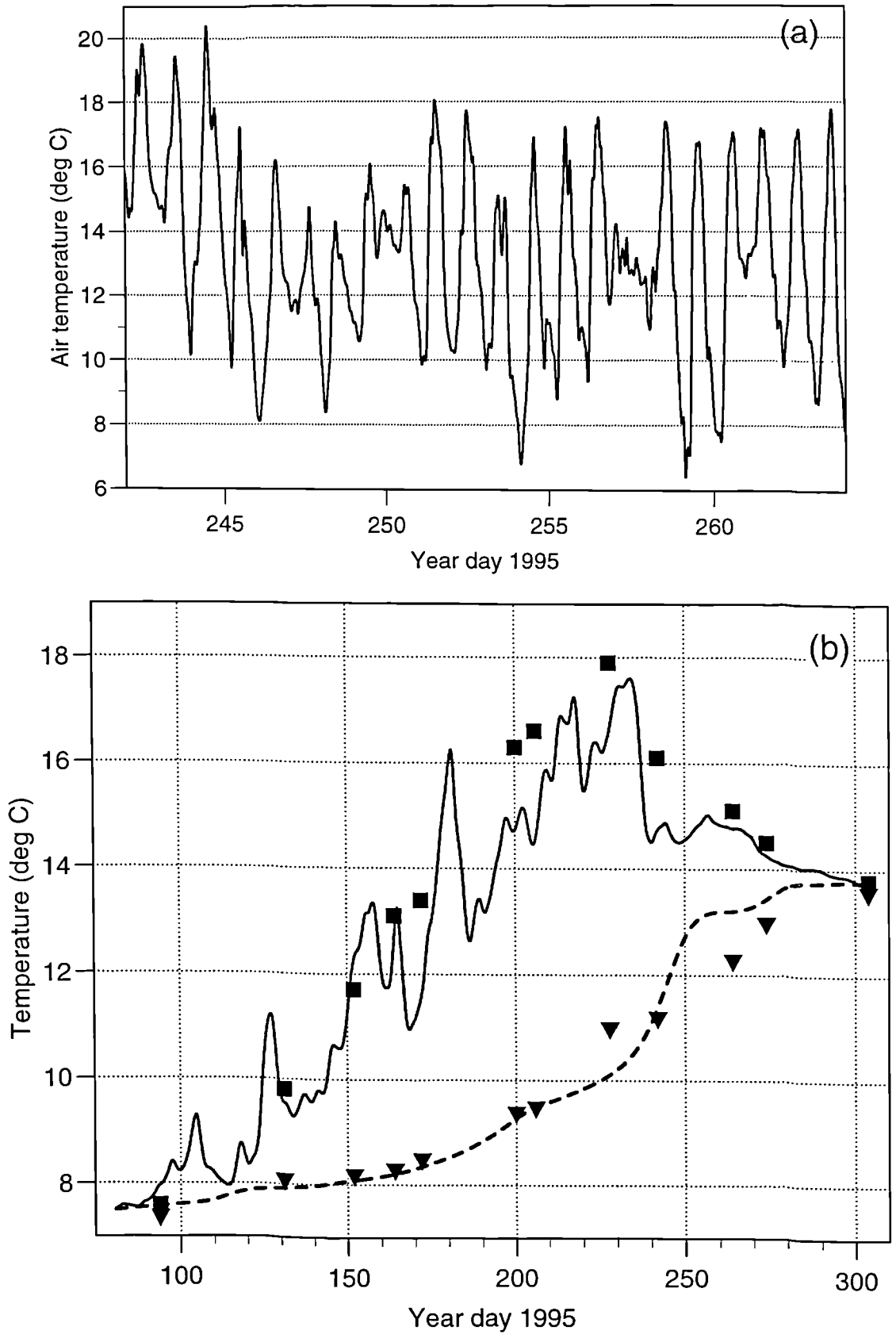

Fig. 6.30 (a) Hourly mean air temperature (°C) at Dublin airport weather station for the period 30/8/95-21/9/95. (b) Surface (solid line) and nearbed (dashed line) temperatures (°C, 24 hour means) from model Run G for a cell corresponding to CTD station E4. Also shown are observed surface (solid squares) and nearbed (solid triangles) temperatures. Note the better agreement with surface temperatures after day 260 than obtained with Run A (Fig. 6.13a).

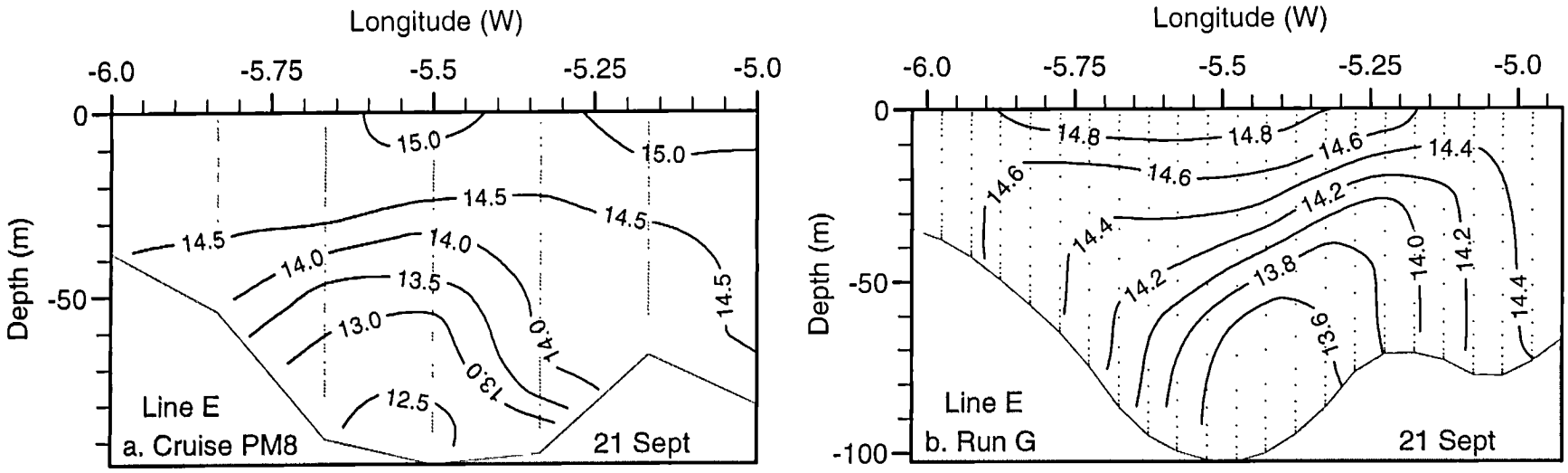

Fig. 6.31 Transverse sections (x-z) of temperature along row 52 (corresponding to latitude 53° 50'N) at 21 September 1995. (a) Observations from line E, cruise PM8. (b) Run G with adjusted air temperature forcing after 1 September. Note the different contour interval between the two diagrams.

Chapter 7. Summary and discussion

7.1 Comparison of model results with observations

This is the first time that a three-dimensional, primitive equation model has been used to simulate the seasonal development of temperature and density-driven circulation in the Irish Sea. Overall, agreement between model predictions and hydrographic and drifter observations during 1995 was extremely good. With appropriate choices of model parameterisations and forcing quantities, all the characteristic features of the western Irish Sea cold pool, and its associated cyclonic near-surface circulation, were reproduced. The model also gave accurate predictions of (at least) surface temperature in the Irish Sea as a whole, as indicated by the comparison with sea surface temperature from satellite imagery in Fig. 6.3. The three areas of relatively warm water (shaded red in both Fig. 6.3a and Fig. 6.3b) were predicted by the model. Only one of these areas (the western Irish Sea) is stratified, the other two (Cardigan Bay and Liverpool Bay) are warmer due to the combination of shallow water and strong mixing. Both images also show a narrow band of coastally confined warmer water along the east coast of the Irish Republic, for the same reasons. This is evidence that the modelled temperature predictions were accurate across the full range of mixing conditions found in the Irish Sea, in stratified and unstratified regions. Interestingly, Fig. 6.3a suggests the presence of isolated patches of warmer water to the west of the Isle of Man which are consistent with the surface eddies seen in Fig. 6.3b, and in other satellite images (e.g. Simpson and Pingree, 1978). Although modelling surface instabilities was not part of the scope of this work, Fig. 6.3a suggests that the model is capable of simulating the baroclinic instabilities which cause frontal meanders and eddies.

The surface and bottom temperatures (and therefore vertical temperature differences) shown in Fig. 6.4 agree well with those in Fig. 3.6 up to and including 30 August. On June 1, both the model and the observations showed an isolated pool of cold water with temperatures of 8.5°C to have formed at the bed. The modelled surface

temperatures at this time were typically 0.5°C warmer than those observed during PM1, leading to vertical temperature stratification of 3.0°C compared to the observed maximum of 2.5°C. Throughout the sequence in Fig. 6.4, surface temperatures disagreed with observations by up to 1.5°C in places, whereas bottom temperatures were more accurately modelled. This is reasonable since cruise data were collected over 2-4 days, providing ample opportunity for temporal variation in surface temperature over the study region. Also, there was no spatial variability in the model's prescription of heat flux at the sea surface and neither did the model incorporate a cloud cover algorithm, so discrepancies of the order 1-2°C in surface temperature would be expected at times. The bottom water temperatures were not influenced by the direct effects of surface heating and cooling, rather they were controlled over longer timescales by advection and diffusion, which explains the better agreement there. Temperatures in the model were also likely to be affected by the prescribed northern boundary condition on temperature. Although it is thought that this condition was prescribed accurately, short-term variability in the North Channel temperature was not accounted for in the model, whereas in reality the North Channel may exert some influence on temperatures in the northern part of the study area.

The spatial extent of modelled temperature stratification matched that shown in the right hand panels of Fig. 3.6 throughout most of the heating season, and was also in agreement with the contours of potential energy anomaly shown in Fig. 3.11. However, modelled stratification extended as far south as 53°N by 16 August (Fig. 6.4eiii), which was inconsistent with the picture shown in Fig. 3.6eiii. It will be shown later that this apparent overprediction of stratification resulted from an anomalously warm (but dynamically insignificant) surface layer at that time. It should be noted that during the two July cruises, PM4 (Fig. 3.6c) and PM5 (Fig. 3.6d), the southern limit of the observations was insufficient to confirm the extinction of stratification, and vertical temperature differences there *did* exceed 1°C.

Spatially complete observations beyond August 1995 were not available for comparison, but the vertical sections from PM8 (21 September) and Cor10/95 (5 October) shown in Fig. 3.9 indicate that stratification broke down too rapidly in Run A because of the incorrect specification of air temperature (as shown by Fig. 6.30). Nevertheless, notwithstanding the timing of events, the results in Fig. 6.4i provide valuable information about the temperature structure of the region following the breakdown of stratification. It was seen that the water cooled differentially, leaving a relatively warm (but vertically well-mixed) central core in the deepest part of the region. This is indicative of convective heat loss, with the most rapid cooling occurring in the shallower areas. The spatial coverage of cruise PM9 was insufficient to make a comparison, since all stations visited lay in the deep channel. However, the differential cooling is physically reasonable and has interesting consequences: the horizontal density gradients along the east coast of Ireland that are predicted by the model could drive a flow northwards, along the Irish coast (the density gradient is the reverse of that observed in the summer), in which case the density-driven circulation in the western Irish Sea may cause a seasonal reversal of the flow along the east coast of Ireland. If so, this could have implications for the dispersal of contaminants and for the biology of the region. However, it should be remembered that in winter months wind-driven currents will be a more dominant contributor to the sub-tidal circulation and the predicted density-driven effect may not be easily discerned. Also, any rainfall would cause lower salinities near the coast which would act to reduce the density there.

The contours of temperature difference in Fig. 6.5 and Fig. 6.6 were used to compare the performance of different model parameters in a qualitative sense. The best results were obtained using the Smolarkiewicz (1984) advection scheme with a horizontal eddy Prandtl number of 1 or 2. Although the central difference scheme gave reasonable results in July (Fig. 6.5d), it made inaccurate predictions of bottom water temperatures (and therefore stratification) from August onwards (Fig. 6.6d). The deficiencies of central difference schemes for advection (i.e. the formation of

numerical ripples and prediction of unphysical values) were described in chapter 4, and were responsible for the false simulation of cold bottom water to the south of the gyre. South of 53.4°N, tidal currents rapidly grow in magnitude (see Fig. 1.2) and are approximately normal to the observed gradient of bottom temperatures there. Strong temperature gradients can experience advective velocities of over 1 m s^{-1} at spring tides. The discrepancy evident in Run D (Fig. 6.6d) was not immediately apparent, since strong gradients of temperature near the bed first have to be formed in the region of strong tidal currents. As Fig. 6.5d shows, the central difference scheme behaved acceptably until late July. However, once the cold pool bottom fronts became established, numerical errors in the central difference scheme resulted in increasing errors in temperature simulation to the south of the region. A similar explanation can be put forward for the poor performance of Run C: the Smolarkiewicz scheme is not completely noise free and a horizontal eddy Prandtl number of 5 generates insufficient diffusion to damp numerical errors.

Once spurious temperature gradients are created in this part of the Irish Sea, there results a runaway feedback mechanism since the tidal currents increase rapidly towards the south and advective errors therefore become larger. Also, as was discussed in the introduction, stratification itself has a feedback effect on mixing so erroneous stratification, once established, is unlikely to be removed. Even the best model run (Run A, Fig. 6.6b) predicted vertical temperature differences of 3°C at 53.2°N. Although observations were not made this far south, Fig. 6.6a suggests that top-to-bottom temperature differences at that latitude were 1°C or less. At the northern limit (in the entrance to the North Channel), stratification was modelled accurately in Run A, but was overpredicted here also by other runs (see Figs. 6.6c&d) These discrepancies could be interpreted as identifying a fundamental limitation of the advection scheme used in the model. However, the north-south vertical section (of temperature converted into σ_t) in Fig. 6.12 shows that south of 53.2°N the water column was vertically mixed below 20 m depth.

In fact the location of the (dynamically important) bottom front agreed well with the observed position on 16 August (see Fig. 3.10f), but there was no surface front in the modelled density field. The vertical temperature difference in Fig. 6.6b was caused by a thin layer of surface water warmer than that observed. It is clear from Fig. 6.4eii that the modelled nearbed temperatures on 16 August were in excellent agreement with observations (cf. Fig. 3.6eii). It seems that the large modelled area of temperature stratification was due to a thin layer of anomalously warm water, caused by incomplete vertical mixing at the southern limit of the gyre. This may have arisen from the use of spatially uniform winds in the model, or surface advection of warm water from the north or west. Another possibility is that mixing was underestimated because only the M_2 and S_2 tidal constituents were used to force the model (the N_2 constituent is of similar magniude to S_2 at this location). Despite arriving at a reasonable explanation for the results in Fig. 6.6b, other model runs do show the advection scheme to be critical in the accurate simulation of the development, and spatial pattern, of stratification. Further work, focused on this particular aspect of the numerical model would be beneficial. Temporal changes in the three-dimensional temperature field over diurnal, spring-neap and seasonal timescales could be analysed in more detail, and comparisons made with alternative (e.g. TVD or PPM) advection schemes (James, 1996).

The vertical structure of density through the cold pool (Fig. 6.7) was in good agreement with the observations in Fig. 3.9 until 30 August. After that, stratification in Runs A and B decayed too rapidly, a deficiency which was remedied somewhat when modified air temperatures were applied from September onwards in Run G. Qualitative differences can be observed: the observed thermocline on 23 June was sharper than that seen in Fig. 6.7b, although observations 9 days previously (Fig. 3.9b) were in excellent agreement with the model at stage 2. The centre of the fully developed model thermocline in Figs. 6.7c-e was found between 15-18 m, which is consistent with observations from line F in July and August 1995 (see Fig. 3.9d-f). It is not unusual for turbulence closure schemes to underpredict mixed layer depths in

oceanic situations (Martin, 1985). This is partly due to the absence of small scale vertical shears (such as from internal waves) and can also result from any smoothing (spatial and temporal) of wind stress in the model. There did not appear to be any substantial underprediction of the thermocline depth in these results, which may be due to the fact that the seasonal thermocline in shelf seas remains shallow. The observations from July and early August 1995 (Fig. 3.9d-f) also show that density increased by approximately 1 kg m^{-3} across the thermocline and the model results in Fig. 6.7c-e are in reasonable agreement, with vertical density differences of typically 0.8 kg m^{-3} across the thermocline. It should be remembered that the model did not contain any effects due to salinity, and that in July 1995 (Fig. 3.4d) a small vertical salinity difference was present.

The strongest gradients of density near the bed (bottom fronts) in the model were consistently located between 5.25° and 5.4°W, as were the observed bottom fronts in Fig. 3.9. The estimated gradients of density near the bed for 25 July and 16 August were ~0.4 kg m^{-3} over a horizontal distance of 10 km. The observed values during July 1995 (Fig. 3.9d&e) were negligibly different, although the observed gradient on 16 August (Fig. 3.9f) was weaker. The model also predicted the (consistently observed) offset of surface to bottom fronts, with the former occurring typically at 5°W, approximately 10 km to the east of the bottom front. This is a curious phenomenon which may simply reflect the spatial increase in tidal mixing strength towards the east, but could also be partially mediated by a flow of dense water from the cold pool, under the bottom front in a bottom boundary layer, as described in §5.3. The advection of dense water in a nearbed layer could act to prevent the tidal stirring from completely mixing the water column near the bottom fronts. The east-west slice corresponding to latitude 53° 40'N on 30 August (Fig. 6.7f) showed how the dense pool of water persisted even when surface density structure was largely eroded. The Searover observations from 30 August (Fig. 3.9g) confirm the absence of density structure above 30 m, and both the modelled and observed north-south sections (Fig. 6.12f and Fig. 3.10g) show that the surface 30 m had become well

mixed, apparently by the northerly winds which blew consistently from day 240 (28 August, see Fig. 6.2).

The vertical sections of temperature shown in Figs. 6.8-6.11 permit a qualitative comparison of the different model runs. The two runs based on the Smolarkiewicz (1984) advection scheme provided the best agreement with observed bottom water temperatures. In a model as complex as this, with several adjustable parameters, a certain degree of trade-off in predictive accuracy between one property and another is inevitable. For instance, on 25 July, Run B (SM2) displayed the best agreement with bottom water temperature but closest agreement with surface temperature was achieved with Run A (SM1). Serious disadvantages of the central difference scheme have already been noted, and these are reinforced by its overprediction of bottom temperatures by 1.5°C on 25 July, and its inability to maintain the bottom front on 16 August (Fig. 6.10d). At this stage, Run A (Fig. 6.10b) provided better agreement with the observations than did Run B (Fig. 6.10c). Excessive cooling during September in Runs A-E, due to the use of terrestrial temperatures in the heatflux calculations, was responsible for poor agreement with observed temperatures on 21 September (Fig. 6.11a). The adjusted forcing that was applied in Run G facilitated better agreement with the 21 September observations (Fig. 6.30b).

The north-south sections presented in Fig. 6.12 show that the bounding front to the south of the cold pool occurred consistently at 53.1°N. Where sufficiently extensive observations were made for the complete north-south section to be compiled (Fig. 3.10d&f), this front appeared to be located further north, at approximately 53.4°. Whilst this can be partly accounted for by the model bathymetry, and horizontal resolution, there is evidence in the observed hydrography of 21 June (Fig. 3.10c) and 25 July (Fig. 3.10e) that stratification may well have extended further to the south at those times. Generally, the hydrographic cruises during 1995 did not sample sufficiently far south to entirely discredit the model results presented in Fig. 6.12. An encouraging feature visible in Fig. 6.12e is the prediction of isopycnals

intersecting the bed in the middle of the section, at around 54°N. This is consistent with the dual dome structure seen in Figs. 3.10d&f. Although two distinct minima were not seen in the modelled fields of vertical temperature difference (e.g. Fig. 6.6b), neither did they appear in the corresponding observations (Fig. 6.6a) although they did appear in calculations of potential energy anomaly (e.g. Fig. 3.11d). This was probably a result of the choice of contouring interval for the two different quantities. The modelled multiple circulation paths (seen in Fig. 6.24b) imply the existence of secondary bottom fronts, and confirm the picture shown in Fig. 6.12e.

The model time series of surface and bottom temperature in the centre of the region (Figs. 6.13a) predicted the onset of stratification at day 90 (31 March). A slight difference in temperature was apparent in the corresponding observations (which were from a CEFAS fisheries cruise, not presented here, and were not 100% reliable). Previous studies in the western Irish Sea confirm that stratification does indeed become established by the end of March: Lavin-Peregrina (1984) found that stratification existed in the region on 7/4/81; Colour Zone Coastal Scanner (CZCS) satellite images show stratification in the western Irish Sea as early as 25/3/82 (Mitchelson, 1984); a series of cruises investigating the relationship between physical conditions and copepod abundance (Gowen *et al.*, 1998) found established stratification in the area by late March in 1993. The breakdown of stratification predicted by Run G (with adjusted air temperatures) agreed with the observations from 1995, shown by the solid squares and triangles in Fig. 6.30b. Previous observations (Lavin-Peregrina, 1984) confirmed the decay of stratification during September and no remaining stratification on 6/10/81. Stratification at a site equivalent to E5 was also absent on 9/10/95 (Gowen *et al.*, 1998).

Similar patterns of isotherm oscillations to those seen in Fig. 6.15b, from a station at the same location as E5 in this study, were presented by Lavin and Sherwin (1985) who noted the implied existence of a variable internal tide. The location is sufficiently far from any significant horizontal temperature gradients for advection to

be responsible for the semi-diurnal oscillations seen in Fig. 6.17 (the same is true for the observations presented in Fig. 6.18). The covariance lags seen in Fig. 6.19 show that whilst the strong temperature oscillations *were* responding to the tidal frequency, they were not a result of the barotropic tide since high water and minimum temperature were not in phase. The calculated internal elevation amplitudes (Fig. 6.20d), whilst not as large as those commonly associated with internal tides (of the order 10 m; see Sherwin, 1988; New, 1988), do suggest that a small internal tide was present. The largest value of 4.4 m at σ-level 6 (~18 m depth) was more than twice the surface elevation amplitude (1.75 m) over the period.

The phase change over depth of the baroclinic current components (Table 6.6) is characteristic of a mode 1 internal tide (in which surface and bottom currents are 180° out of phase). For mode 1, internal elevations should be in phase and Figs.6.17&6.19 make it clear that this was the case. These properties were utilised by Holloway (1984) to identify a mode 1 internal tide at the northwest Australian shelf-break, and also by Petrie (1984) who noted a 180° phase shift between baroclinic currents at two vertical levels on the Scotian slope. Table 6.6 also shows that the v component of baroclinic velocity leads the u component by approximately 90°, which is consistent with the predictions of two-dimensional internal tide generation models (Baines, 1974). It must be stressed that the amplitudes here were small - the baroclinic velocity component was only 20% of the barotropic current - but the balance of evidence is that variable internal tides of mode 1 were present in the model, and therefore quite possibly in the observations of Fig. 6.18, and of Lavin and Sherwin (1985). The modelled internal tide can, in fact, only be mode 1 since the horizontal resolution employed here (~3.3 x 3.7 km) was not capable of resolving the shorter wavelength, higher modes shown in Table 6.5. It is difficult to put forward a generation mechanism for internal tides in this region, where currents are weak and predominantly horizontal. Disturbances may originate at the sharp horizontal frontal zones and then propagate along the strong thermocline into the

central region. Weak internal seiching is another possibility - the stratified region between the Isle of Man and Ireland has steep bathymetry on both sides and is about 60 km across, and could be resonant with the mode 1 wavelength. Propagation of the wave packets from north to south is suggested by Fig. 6.16. What is more important though, is the simple fact that the results show the model able to support internal wave activity. This suggests the model could be used, under controlled conditions, to study internal tides in shelf seas - an idea which is taken up in the next section.

One of the key objectives of this work was to show that the model could reproduce the observed cyclonic circulation pattern in the western Irish Sea, and to demonstrate that this residual circulation is density-driven. Aspects of the cyclonic gyre were visible in the residual circulation even before the wind and baroclinic flows were separated, as can be seen in Fig. 6.21. All of these features, recognisable from the composite drifter diagrams (Fig. 3.15 & Fig. 3.17), were absent in Run F (Fig. 6.22) where no seasonal heating was applied. This is the simplest and most positive proof that the cyclonic circulation is indeed a density-driven flow.

In Fig. 6.21a, the weak (3 cm s^{-1}) southward flow was less than typically observed in southward moving drifters at that time and earlier (e.g. a24056, a24020 and a17823 in Fig. 3.13). It must be remembered that salinity was held constant in the model, and inaccuracies in the modelled residual flow fields are due, in part, to the resulting incomplete prediction of density. Salinity was found to be most important near the Irish coast, particularly in the early spring (see Fig. 3.2). The northward flowing arm of the gyre was not predicted by the model at 1 June (Fig. 6.21a), and it was at this time in the observations that wind influence on the drifters was greatest (as noted by the increased incidence of significant correlation of one velocity component - see Table 3.1 and discussion thereof).

From 21 June onwards, the cyclonic pattern of circulation and the speeds obtained from the model were in reasonable agreement with the drifter data, which lends support to the assumption that salinity has only a second order influence on the density field at that time. Temperature has the primary influence on density from late June onwards as was discussed in chapter 3, and the successful modelling of the gyral circulation confirms this dynamically. The northward arm of the gyre was present in the model from (at least) 21 June (Fig. 6.21b), which is consistent with the track of drifter b24055 deployed on 22 June (see Fig. 3.13). By 25 July (Fig. 6.21c) the northward flowing residual current was confined to the west of the Isle of Man, implying that Lagrangian followers would be taken north along this path and would not, therefore, become entrapped in the tidal residual current at the southern tip of the Isle of Man (see Fig. 5.5) which was responsible for the poor retention in the gyre of drifters during May and early June. The modelled circulation on 25 July also revealed the closed circuit at the northern end of the gyre, at latitude 54.5°N, that was encircled by drifter b17802 (Fig. 3.13).

The best picture of modelled residual circulation comes from the separated baroclinic flows shown in Figs. 6.23&6.24. The multiple possible recirculation paths, seen in Fig. 3.17, were shown to exist in the predicted flow field. The spatial extent of the modelled cyclonic gyre also agreed well with the drifter composite (Fig. 3.15). Modelled maximum speeds along the northward flowing arm of the gyre, to the west of the Isle of Man, were 13 cm s^{-1} - lower than the mean value (18 cm s^{-1}) obtained from drifters over this segment. Mainly, this was due to the subtraction of the tidal Eulerian residual (see Fig. 5.5) which is in the same direction at this location, and has magnitudes of 5-8 cm s^{-1}. The spatial resolution of the model is also likely to affect the accuracy of modelled density-driven flow: the horizontal resolution (and choice of advection scheme) determines those density-gradients which can be maintained, and the vertical resolution affects the level at which maximum flows will be found. Diffusion of momentum in the model (prescribed and numerical) will also tend to result in broader, weaker flows than observed. Consequently, if all currents

shown in Fig. 6.24b were vector averaged then a mean modelled circulation speed around the gyre (on 16 August) of 5.8 cm s^{-1} was obtained. If only those currents greater than 5 cm s^{-1} were considered, then the mean speed (at the range of σ-levels shown in Fig. 6.24b) was 7.9 cm s^{-1} , which is closer to the mean circulation speed calculated from drifters previously (9 cm s^{-1}).

The extent of the residual circulation in Fig. 6.24b corresponds to the spatial pattern of vertical temperature difference in Fig. 6.6b (in the same way that drifter tracks in Fig. 3.17 were congruent with contours of potential energy anomaly) which is further confirmation of the density-driven nature of the flow. The significant correlation between the gridded drifter ensembles and corresponding four cell averages from the model (Fig. 6.26) is proof that the model results are physically realistic. The R^2 values obtained were lower than in the corresponding analysis of temperature (Fig. 6.14) because of the greater variability in both the modelled and observed velocity fields, and the fact that comparisons were limited to those cells through which drifters had passed (and, even then, not as many as one might like to obtain a reliable average). Even so, the technique represents a quantitative approach to model flow field validation which is of value in its own right. The lack of correlation for the zero heating Run G is final confirmation that the cyclonic gyre is density-driven.

The vertical structure of residual circulation (Fig. 6.27) shows that a thermal wind based theory of the density-driven currents can be accepted. The strongest currents were confined in cores at approximately the depth of the thermocline and the isotachs were symmetrical about the cold pool density field. Maximum flows (10.5 cm s^{-1} in Fig. 6.27a) were consistent with the vertical integration of (1.2), subject to a zero along-front flow at the bed (which was not strictly the case, as the zero contour in Fig. 6.27a shows!). The core-like nature of the strongest flow (due to reverse baroclinicity above the thermocline) was consistent with geostrophic calculations presented from observations (Fig. 3.19) and also with detided ADCP sections such as

that shown in Fig. 1.6b. The northward flow in Fig. 6.27a was broader than that implied by the ADCP section (Fig. 1.6b), but the narrow jet in which any drifters might find maximum flows is not easily reproduced by the model because of both horizontal and vertical resolution. The north-south transect in Fig. 6.27b also shows jet-like residual currents normal to the section, this time concentrated at the surface, at the northern and southern limits of stratification. It should be noted that the strongest flows normal to both the east-west and north-south sections were associated with the strongest horizontal density gradients in the bottom part of the water column. This reinforces the dynamical significance of bottom fronts and is strong evidence for a thermal wind based account of the residual flows.

The stability and persistence of bottom fronts to strong winds was demonstrated by the numerical experiment whose results are shown in Fig. 6.28 and Fig. 6.29. The rapid erosion of surface structure was seen in both cases. When the wind was from the north (Fig. 6.28) water from the east of the section was advected over the warmer water. This creates convective instability in the upper 20 m as was found by Wang *et al.* (1990). When the wind was from the south, a lens of water with the highest temperatures moved towards the east where it encountered progressively stronger tidal mixing. In both cases, the dome of cold water near the bed remained intact and the horizontal density gradients intensified, on the western and eastern sides respectively. These increases in density gradients caused corresponding increases in the density-driven residual flow. When the wind was from the north, the density gradients near Ireland strengthened and the southward flow along the Irish coast increased. When the wind was from the south, the density gradient sharpened at the western Irish Sea (bottom) front and northward flow intensified. The flows were now maximum at the surface, unlike the sub-surface jets seen in Fig. 6.27, because there was no reverse baroclinicity above the thermocline. In this extreme example, the resultant density-driven flows were only 20% of the magnitude of the direct wind-driven currents caused by the preceding wind, and the strongest flows were in the same direction as the wind-driven currents. Even so, the simulations identify an

important interaction between the wind and the density field that could modulate the cyclonic flow around the gyre during the heating season. As long as the wind regime does not completely dominate the non-tidal flow, the wind direction determines where the strongest horizontal density gradients will be located, and therefore at which point around the gyre the fastest density-driven currents will be found. Thus the potential energy in the density field is directed by the wind (and possibly other factors) into releasing differing amounts of kinetic energy at varying locations.

7.2 Dynamical and modelling aspects

It was seen in the temperature comparisons that different choices of parameterisations and numerical schemes can confer both advantages and disadvantages. One has to arrive at a quantitative optimisation of those free parameters in the model that give (empirically) the best overall results. This was achieved here with Run A which gave the best agreement with temperature in a statistical sense (Table 6.4) and maintained physically realistic stratification throughout the simulation. Although statistically the central difference scheme provided comparable performance, it also displayed unphysical behaviour in its prediction of the cold pool. This highlights the necessity for an advection scheme such as the one used here when attempting to preserve sharp gradients of properties in regions of strong tidal current. The Smolarkiewicz (1984) scheme was found to perform well when small values of horizontal diffusivity were also prescribed, but to suffer similar deficiencies to the central difference scheme if the damping effect of horizontal diffusivity was too small. An alternative advection scheme, the piecewise parabolic method (PPM) described previously, was used with no prescribed horizontal diffusivity by Proctor and James (1996), and was found to maintain realistic frontal gradients of temperature in the North Sea.

One might think that in a region where the spatial gradient of tidal mixing energy was strong, any advection scheme (however numerically diffusive) would work, since tidal stirring could continuously re-establish the front. The dismal results

obtained from the upwind scheme (Fig. 6.5f) show this rationale to be false. Numerical diffusion produced by the upwind scheme is present at every time step and the error is cumulative, whereas tidal mixing is only sufficient to vertically mix the water column during a fraction of each tidal cycle. With upwind advection, the thermal front cannot form in the first place. It may be possible for sharp gradients of properties to be maintained with non-specialist advection schemes if a strong source term is present to re-establish the gradients (e.g. a fresh water flux from a large estuary, emptying into a strongly tidal basin, and forming a salinity front). This was the case with the German Bight model of Schrum (1997) which used an upwind algorithm but managed to create baroclinic instabilities due to salinity gradients. However, the model was initialised with three-dimensional climatic fields of temperature and salinity and then run prognostically for only five days.

The foregoing highlights the fact that in every model application, careful thought must be given to the critical (and non-critical) parameterisations and forcing variables relevant to the problem. In the case of the western Irish Sea, the numerical advection scheme is an important consideration whereas the turbulence closure scheme, although efficient at reducing vertical mixing in stratified conditions, does not improve demonstrably on the simpler Richardson number based scheme used by Proctor and James (1996) in the North Sea. Similarly, whilst it was shown that the correct specification of air temperature was crucial from September onwards, the model was less sensitive to prescribed air temperature during the spring and summer, when solar inputs were dominant in the calculation of heatflux. The fact that air temperature was critical during the autumnal phase is further evidence that convective cooling is as important as wind mixing for the extinction of stratification in the western Irish Sea. The use of spatially invariant wind forcing does not appeared to have confounded the numerical simulations performed here, but if a more detailed study of the interaction between wind and density field were required, then spatial detail in the wind forcing would be essential.

The correct choice of value for horizontal diffusivity appears to be the key to the accurate simulation of the temperature field everywhere within the model, but particularly in the cold pool. A small amount of horizontal eddy viscosity was required for optimal tidal validation, and some prescribed diffusivity was also necessary to avoid excessive temperature gradients developing in shallow parts of the domain elsewhere in the Irish Sea. Also, physical processes on smaller horizontal scales than 3.5 km (the model resolution) are important and demand parameterisation. In a sensitivity study of the coefficient in the Smagorinsky (1963) formulation (Oey, 1996), only at horizontal grid scales of 0.5 km was the coefficient successfully put at zero. The best results in the present study (Run A) were obtained with the Smagorinsky (1963) coefficient, $\alpha = 0.1$, and an eddy Prandtl number of 1, which on this grid scale gave values of horizontal eddy diffusivity along model row 52 ranging between 50-130 $m^2\ s^{-1}$ over a tidal cycle. These values are consistent with the estimate of 100 $m^2\ s^{-1}$ made by Lavin-Peregrina (1984), based on a two-dimensional set of observations. Durazo-Arvizu (1993) made estimates of lateral diffusivity based on single particle statistics from drifters released along the Irish Sea front, and arrived at values of 100 $m^2\ s^{-1}$ in the zonal (cross-front) direction and 300 $m^2\ s^{-1}$ for the meridional (along-front) direction.

It would be useful to find a way of eradicating the instabilities elsewhere in the domain (possibly by artificially relaxing temperatures in very shallow water) so that the model could run with zero prescribed diffusivity. Since the evolution of bottom water temperature was, in any case, modelled with reasonable accuracy by Run A, a zero K_H run could presumably only do better by replacing the artificial diffusivity with small scale instabilities not present in these runs. It may also be the case that diffusive processes (in reality, small scale eddies) are different in the surface and nearbed layers. In Fig. 6.9 for instance, Run A predicted the surface temperature at line F best (Fig. 6.9b) whereas bottom temperature was better represented in Run B (Fig. 6.9c). Bottom fronts are known to be more stable to baroclinic instability than

surface fronts (Flagg and Beardsley, 1978; James, 1989; Hill *et al.* ,1994) and it may be possible to improve on the correlation coefficients in Table 6.4 if horizontal diffusivity could be related to some combination of horizontal density gradient and proximity to the bed. The different correlation coefficients obtained for the surface and bottom temperature comparisons (Table 6.4) may reflect this stability, but probably also reflect the influence of wind effects on the surface temperature field. The fact that bottom temperatures in the cold pool were reliably predicted by the numerical model, and showed sensitivity to the prescribed amount of horizontal diffusivity, suggests that the slow warming of the relict water (in both the model and in reality) is mediated by lateral, rather than vertical processes.

It is interesting to consider why a far simpler diagnostic model (Hill *et al.*, 1996; Hill *et al.*, 1997a) was able to predict the cyclonic flow field, with broadly the same characteristics as parts of Fig. 6.24b. This model was based on a series of one-dimensional heating stirring models (Simpson and Bowers, 1984), linked to a diagnostic model for velocity (Hukuda *et al.*, 1989). Although the diagnostic model did not predict the full southern extent of the gyre, or the distinct recirculation loops in Fig. 6.24b and Fig. 6.17, it did show the northward and southward flowing arms of the cyclonic circulation with maximum surface flows of 20 cm s^{-1}. These speeds were more consistent with maximum drifter flows than with the mean, and result from the lack of momentum diffusion in the diagnostic model, and the fact that the heating-stirring models can predict unrealistically sharp horizontal density gradients between adjacent vertical cells. The relative success of the diagnostic model (which neglects density advection) highlights the vital balance between tidal and wind stirring and solar input to the energetics of the western Irish Sea gyre. Heating-stirring models should give poor predictions of the density field if significant advective flows (> 2 cm s^{-1}), normal to isopycnals, are present (Simpson, 1981). Although the residual flows around the gyre are greater than 10 cm s^{-1} in places, they are predominantly parallel to isopycnals. Indeed, maps of vertical temperature

difference or ϕ act as reasonable contour maps for the flow field. Outside the bottom boundary layer, only the small, ageostrophic part of the residual flow is normal to the density gradient. Tidal currents can have a significant component normal to the density gradient, such as at the southern limit of stratification, and they can modify the density gradient through tidal straining (e.g. Souza and Simpson, 1996) and by introducing numerical diffusion in advective algorithms, but their physical advective influence is periodic and does not affect the longer-term heating stirring balance. The results obtained with this primitive equation model (which contains all of the physics excluded from the diagnostic model) lends credibility to the results obtained with the latter.

Finally, on a technical note, numerical instabilities due to the free surface (external mode) were eliminated in this model by the use of a semi-implicit scheme, and no internal mode instabilities were observed throughout the seasonal simulations when using the 372 s time-step. Although stability would not have been compromised by the use of a longer time-step, tidal simulations showed that the detail of tidal properties over a cycle became excessively smoothed if time-steps longer than 600 s were employed. Also, the pre-conditioned gradient matrix solver is an iterative procedure, and increasing the time-step requires more iterations to achieve convergence. For tidal applications, whilst in no way unsatisfactory, the semi-implicit scheme does not offer any significant savings in computational time over the more standard mode-splitting version of POM.

7.3 Future work

The model developed here probably represents the best description of the three-dimensional circulation in the Irish Sea to date. Sufficient confidence can be had in the flow fields to now include chemical and biological tracers, or to use the model to provide a database of regional circulation maps for use with biological transport models. The significance of the western Irish Sea gyre for the retention and survival

of the crustacean *Nephrops norvegicus* (Hill *et al.*, 1996) has been discussed. With the inclusion of spatially variable wind forcing, accurate maps of residual currents could be forecast at weekly intervals over the period of larval release and retention, and the consequent predictions of larval transport and dispersion could be compared with seasonal observations of *Nephrops* distribution (Angelico, 1999). Another valuable use of such forecasts would be to connect the advective transports with a series of one-dimensional, coupled physical-biological models of spring blooms in the Irish Sea (e.g. Mills *et al.*, 1997) to increase the dimensionality of the latter. The seasonal patterns of stratification and residual flow in the western Irish Sea and in the North Channel affect the relationship between phytoplankton production and copepod abundance (Gowen *et al.*, 1998). It would be useful to compare this model's predictions of advective transport from the western Irish Sea, with the observed appearance of copepods in the North Channel prior to the summer peak in primary production (Gowen *et al.*, 1998).

The apparent ability of the model to support internal tides in stratification typical of shelf seas suggests that, with better horizontal and vertical resolution, it could be used for idealised studies of internal waves on the pycnocline. Holloway and Barnes (1998) have used a version of POM to study the vertical structure of internal tides on a continental slope, and in particular the currents in the bottom boundary layer and their role in vertical momentum exchange. Observations of turbulence dissipation in stratified shelf seas (Simpson *et al.*, 1998) suggest higher values of dissipation in the pycnocline than can be predicted by one-dimensional turbulence closure models. The mid-water source of turbulent kinetic energy is thought to result from the breaking of internal waves. Although a hydrostatic model could not simulate the breaking of internal waves, it could predict the shear associated with internal waves of varying frequency (so long as the frequency remains significantly lower than the buoyancy frequency). An idealised pycnocline could be established in a model with periodic, or radiation, open boundary conditions and then forced with internal oscillations at a range of frequencies. The local equilibrium assumption (production

equals dissipation) could then be employed to see if the internal wave shears generated were sufficient to account for the turbulence dissipation deficit in one-dimensional models.

Other avenues of future modelling work were suggested by the baroclinic validations carried out in chapter 5. In an experiment not shown here, the model was spun-up to a state consistent with the idealised frontal circulation shown in Fig. 5.7, and was then run forward prognostically. Dense water near the bed initially spread in a thin Ekman layer towards the well-mixed side of the front, but after approximately 10 days a new dynamical balance was reached and the spreading ceased. At shelf sea fronts such a flow would interact in a complex manner with tidal mixing over a spring-neap cycle. Presumably a leading order balance would be reached between horizontal advection in the bottom boundary layer and vertical mixing, as shown in the schematic Fig. 7.1. The advection of density in boundary layers beneath fronts offers intriguing possibilities for study that have wider relevance than to just shelf sea dynamics. Connections can be made with boundary layer shut-down in the deep ocean (MacCready and Rhines, 1993) and with the bathymetric trapping of fronts on slopes (Chapman and Lentz, 1994). In the immediate vicinity of a tidal mixing front, the nearbed layer of dense water could shield the overlying flow from bed stress in the more energetic well-mixed regime. Boundary layer advection may therefore provide a dynamical explanation for the lack of movement of tidal mixing fronts in response to spring-neap cycles (Simspon, 1981; Wang *et al.*, 1990).

The role of cross-frontal, ageostrophic flows in maintaining and restoring frontal density gradients is also worthy of further investigation. As was seen in Fig. 5.10, along-front flow near the bed can be in the opposite direction to the overlying geostrophic jet. In terms of Ekman dynamics, this is consistent with a boundary layer flow in the cross-front direction. There is no formal requirement that the vertically integrated, cross-frontal flux, $U = 0$ in a three-dimensional model, unlike in the two-dimensional model of Garrett and Loder (1981). If negative v is inserted

into the parameterisation of equation (1.4) then cross-frontal flux, U, is positive beneath the jet (i.e. towards the well-mixed side). Assuming that (mean) surface elevation assumes a steady value, then the requirement is for zero divergence of horizontal transport, $\partial U/\partial x + \partial V/\partial y = 0$. Positive U at the strongest part of the front may be matched by non-zero $\partial U/\partial x$ either side to satisfy lateral boundary conditions, and continuity is maintained through non-zero $\partial V/\partial y$. Regions of confluence and diffluence at the entrance and exit regions of mid-latitude jets are well known in meteorology (e.g. Eliassen, 1962) and warrant further investigation in the context of oceanic frontal systems.

The suggestion from the frontal simulations that cross-frontal flow from the mixed to the stratified side may be concentrated at the level of the pycnocline has ramifications for the supply of nutrients to phytoplankton. This circulation would act as a nutrient conveyor belt throughout the stratified period and would have consequences for the succession of species at the thermocline, similar to the 'tidally-fed pump' proposed by Pedersen (1994) but arising for more plausible dynamical reasons. Modelling studies targetted on processes such as those described above (and illustrated schematically in Fig. 7.1) are arguably one of the best uses of primitive equation models. All aspects of frontal flow described here could be investigated using an idealised configuration of the model having periodic boundary conditions in the along-front direction (creating effectively an infinite length front), and open lateral boundary conditions to prevent unphysical continuity constraints affecting the solutions.

One measure of numerical models (according to observationalists) is whether or not they prompt new observations. This work suggest a number of lines of observation worth pursuing. The cross-frontal flow focused at the thermocline, and the boundary layer flow beneath shelf-sea fronts, are both amenable to observation using dye release techniques. Houghton (1997) has used such methods to identify boundary

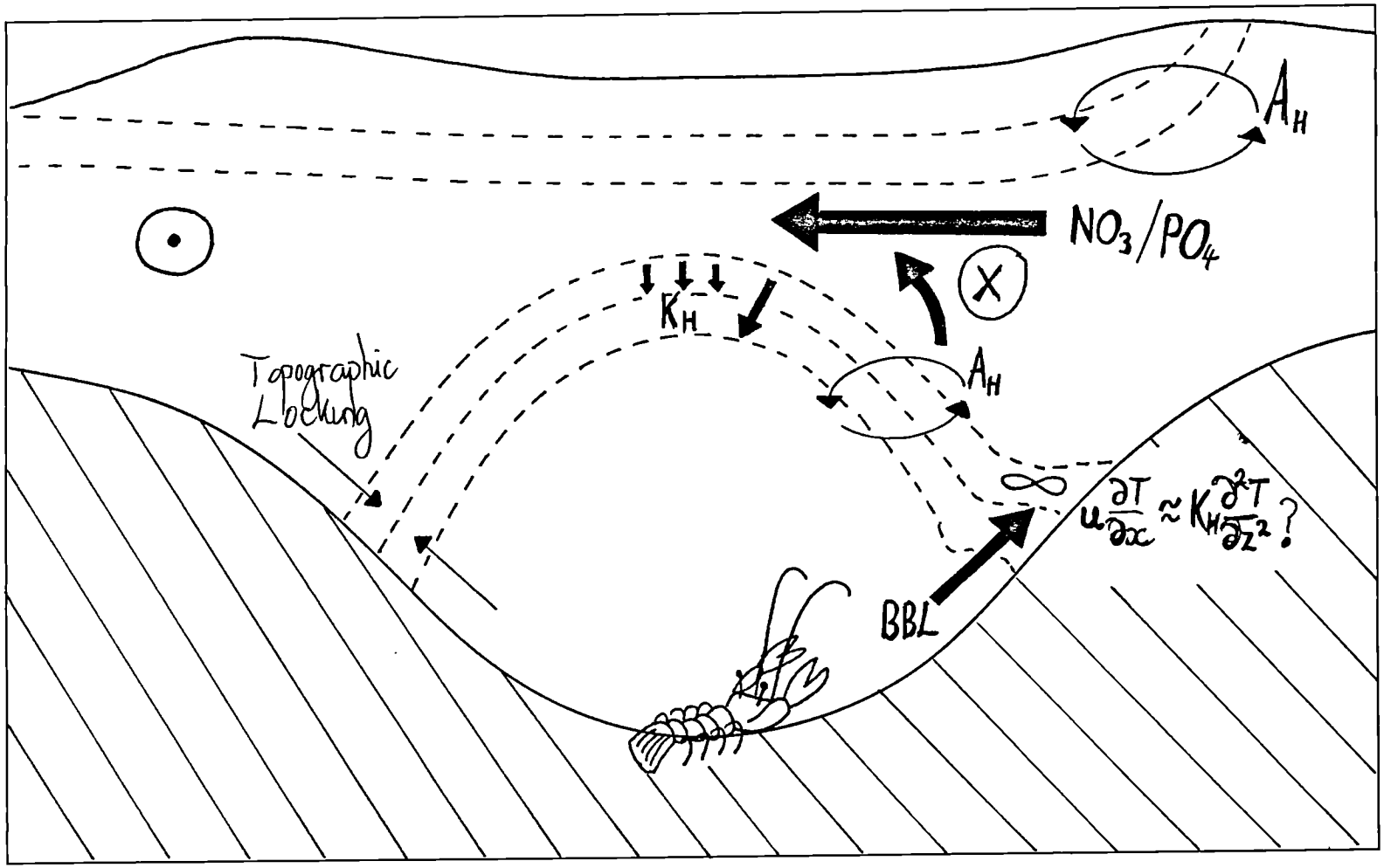

Fig. 7.1 Schematic diagram showing the sub-frontal boundary layer flow, and other aspects of frontal dynamics amenable to further investigation in numerical process studies.

layer flows at shelf-break fronts. The possibility of a seasonal reversal in the density-driven circulation along the east coast of Ireland could be simply tested with some winter drifter deployments. The spatial modulation by strong winds of the isotherms making up the dome-like structure of the cold pool could be confirmed by opportunistic surveys across the western Irish Sea using undulating CTD and ADCP.

7.4 Concluding remarks

The existence of organised, baroclinic flows in shelf seas (of which the western Irish Sea gyre is a special case) and their implications for environmental management now demand that numerical models are able to correctly reproduce their dynamics. Modelling density-driven flows requires computationally efficient, primitive equation models which can maintain sharp frontal gradients and resolve the structure of intense, narrow currents such as those observed here.

This is the first time that the cyclonic circulation in the western Irish Sea has been modelled using a primitive equation model. The model has conclusively shown the cyclonic gyre to be density-driven. Model results, drifter velocities and calculations from the hydrographic data show that the residual circulation is geostrophic to leading order. Quantitative techniques for model validation were developed, and extensive comparisons were made with observational data in order to gain an understanding of those model settings, configurations and parameterisations that are most important in the modelling of density-driven flow in this region of the Irish Sea. The model described here is now sufficiently well-developed and tested that, with minimal future refinements, it could be confidently applied to a range of chemical, biological or water quality management problems.

The utility of three-dimensional, primitive equation models in furthering our knowledge of shelf seas and the deep oceans is indisputable. Only by modellers adopting a more rigorous approach to the testing of models can the credibility of numerical modelling be improved within the interdisciplinary community of

oceanography. Ultimately, this will result in the more confident use of numerical models and more powerful collaborations between hydrodynamicists and oceanographers from other disciplines. Critical tests against observations must be carried out, and these observations must have the best possible spatial and temporal coverage. Clearly, such observations can be made most efficiently, and economically, in shelf sea regions that are easily reached by research vessels. It is in shelf seas - where buoyancy effects, winds and tides interact over a wide range of scales (Hill, 1998) - that some of the most complex and demanding tests of numerical models can be found. Thus shelf seas represent the ideal 'laboratory' for carrying out the necessary testing to prove, and to improve, numerical models.

REFERENCES

Allen, C. M. (1979) The structure and variability of shelf sea fronts. PhD thesis, University of Wales, Bangor.

Allen, J. S. and P. A. Newberger (1996) Downwelling circulation on the Oregon Continental Shelf. Part 1. Response to idealised forcing. *Journal of Physical Oceanography*, **26**, 2011-2035.

Allen, J. S. , P. A. Newberger and J. Federiuk (1995) Upwelling circulation on the Oregon continental shelf: Part 1, Response to idealised forcing. *Journal of Physical Oceanography*, **25**, 1843-1866.

Angelico, M.M.P. (1999) Distribution of *Neprhops novergicus* larvae in the western Irish Sea and its relation to physical structure. PhD thesis, University of Wales, Bangor.

Apel, J.R. (1990) *Principles of Ocean Physics*, International Geophysics Series Volume 38, Academic Press, London, 634pp.

Arakawa, A. and V. R. Lamb (1977) Computational design of the UCLA general circulation model. *Methods in Computational Physics*, **17**, 173-265.

Asselin, R. (1972) Frequency filters for time integrations. *Monthly Weather Review*, **100**, 487-490.

Backhaus, J. O. (1985) A three-dimensional model for the simulation of shelf sea dynamics. *Deustche Hydrographische Zeitschrift*, **38**, 165-187.

Baines, P.G. (1974) The generation of internal tides over steep continental slopes. *Philosophical Transactions of the Royal Society of London*, A227, 27-58.

Bartsch, J. (1993) Application of a circulation and transport model system to the dispersal of herring larvae in the North Sea. *Continental Shelf Research*, **13**, 1335-1361.

Bauer, J., J. Fischer, H. Leach and J. D. Woods (1985) SEAROVER Data Report 1-North Atlantic Summer 1981 NOA'81. Berichte aus dem Institut für Meereskunde an der Christian-Albrechts-Universitat Kiel 143, 155 pp.

Beckers, J. M. (1991) Application of a 3D model to the western Mediterranean. *Journal of Marine Systems*, **1**, 315-332.

Blackadar, A.K. (1962) The vertical distribution of wind and turbulent exchange in a neutral atmosphere. *Journal of Geophysical Research*, **67**, 3095-3120.

Bleck, R., C. Rooth, D. Hu and L. Smith (1992) Salinity-driven thermocline transients in a wind and thermohaline-forced isopycnic coordinate model of the North Atlantic. *Journal of Physical Oceanography*, **22**, 1486-1505.

Blumberg, A. F. (1994) *A primer for ECOM-si*, Tech. Rep., Hydroqual Inc., Manwah, New Jersey, 80 pp.

Blumberg, A. F. and L.H. Kantha (1985) Open boundary condition for circulation models. *Journal of Hydraulic Engineering*, **111**, 237-253.

Blumberg, A. F. and G. L. Mellor (1983) Diagnostic and prognostic numerical circulation studies of the South Atlantic Bight. *Journal of Geophysical Research*, **88**, 4579-4592.

Blumberg, A. F. and G. L. Mellor (1987) A description of a three dimensional coastal ocean circulation model. In: *Three dimensional coastal ocean models*, N.S. Heaps, editor, Coastal and Estuarine Sciences No. 4, American Geophysical Union, Washington, 208 pp.

Blumberg, A. F. and D. W. Pritchard (1997) Estimates of the transport through the East River, New York. *Journal of Geophysical Research*, **102**, 5685-5703.

Boelens, R. G. V. (1995) An integrated science programme for the Irish Sea: Synthesis and recommendations. *Third report of the Irish Sea science coordinator, Department of the Environment, Dublin and Department of the Environment, London*, 36 pp.

Bomback, A. J. (1974) The seasonal development of the western Irish Sea front. MSc thesis, University of Wales, Bangor.

Booth, D. A. (1988) Eddies in the Rockall Trough. *Oceanologica Acta*, **11**, 213-218.

Booth, D. A. and D. Ritchie (1983) *SMBA satellite tracked buoy and drogue*. Oban: Scottish Marine Biological Association, Marine Physics Group Report Number 22, 15 pp.

Boris, J. P. and D. L. Book (1976) Flux-corrected transport: III minimal-error FCT algorithms. *Journal of Computational Physics*, **20**, 397-431.

Bowden, K. F. (1950) Processes affecting the salinity of the Irish Sea. *Monthly Notices of the Royal Astronomical Society Geophysical Supplement*, **6**, 63-90.

Bowden, K.F., L.A. Fairbairn and P.Hughes (1959) The distribution of shearing stresses in a tidal current. *Geophysical Journal of the Royal Astronomical Society*, **2**, 288-305.

Brown, J. and E. M. Gmitrowicz (1995) Observation of the transverse structure and dynamics of the low frequency flow through the North Channel of the Irish Sea. *Continental Shelf Research*, **15**, 1133-1156.

Brown, J., A. E. Hill, L. Fernand, D. B. Bennett and J. H. Nichols (1995) A physical retention mechanism for *Nephrops norvegicus* larvae. *ICES C.M. 1995 K:31 Ref. C* (mimeo).

Brown, J., K.M. Brander, L. Fernand and A.E.Hill (1996) Scanfish: a high performance towed undulator. *Sea Technology*, **37**, 23-27.

Brown, J., A. E. Hill, L. Fernand, and K.J. Horsburgh (1999) Observations of a seasonal jet-like circulation at the central North Sea cold pool margin. *Estuarine Coastal and Shelf Science*, **48**, 343-355.

Brügge, B. (1995) Near-surface mean circulation and kinetic energy in the central North Atlantic from drifter data. *Journal of Geophysical Research*, **100**, 20543-20554.

Burchard, H., O. Petersen and T.P Rippeth (1998) Comparing the performance of the Mellor-Yamada and the k-ε two-equation turbulence models. *Journal of Geophysical Research*, 103, 10543-10554.

Burrows, M. and S.A. Thorpe (1998) Drifter observations of the Hebrides slope current and nearby circulation patterns. *Annales Geophysicae* (submitted).

Casulli, V. and R.T. Cheng (1992) Semi-implicit finite difference methods for three-dimensional shallow water flows. *International Journal of Numerical Methods in Fluids*, **15**, 15629-15648.

Chapman, D.C. (1985) Numerical treatment of cross-shelf open boundaries in a barotropic coastal ocean model. *Journal of Physical Oceanography*, **15**, 1060-1075.

Chapman, D.C. and S.J. Lentz (1994) Trapping of a coastal density front by the bottom boundary layer. *Journal of Physical Oceanography*, **24**, 1464-1479.

Chen, C. and R. C. Beardsley (1995) A numerical study of stratified tidal rectification over finite-amplitude banks. Part I Symmetric banks. *Journal of Physical Oceanography*, **25**, 2090-2110.

Chen, C., R. C. Beardsley and R. Limeburner (1995) A numerical study of stratified tidal rectification over finite-amplitude banks. Part II Georges Banks. *Journal of Physical Oceanography,* **25**, 2111-2128.

Colella, P. and P. R. Woodward (1984) The piecewise parabolic method (PPM) for gas-dynamical simulations. *Journal of Computational Physics*, **54**, 174-201.

Cox, M.D. (1984) A primitive equation three-dimensional model of the ocean. *Technical Report 1.* GFDL Ocean Group, Princeton University, Princeton, New Jersey.

Cushman-Roisin, B. (1986) Frontal geostrophic dynamics. *Journal of Physical Oceanography*, **16**, 132-143.

Davies, A.G. (1972) Aspects of the circulation of the western Irish Sea. MSc thesis, University of Wales, Bangor

Davies, A.G., R.L. Soulsby and H.L. King (1988) A numerical model of the combined wave and current bottom boundary layer. *Journal of Geophysical Research*, **93**, 491-508.

Davies, A.M. (1987) Spectral models in continental shelf sea oceanography. In: *Three-dimensional coastal ocean models* (N.S. Heaps, ed.), Coastal and Estuarine Sciences No.4, American Geophysical Union, Washington, 208pp.

Davies, A.M. and G.K. Furnes (1980) Observed and computed M_2 tidal currents in the North Sea. *Journal of Physical Oceanography*, **10**, 237-257.

Davies, A.M. and J.E. Jones (1992) A three-dimensional wind driven circulation model of the Celtic and Irish Seas. *Continental Shelf Research*, **12**, 159-188.

Davies, A.M. and J.N. Aldridge (1993) A numerical model study of parameters influencing tidal currents in the Irish Sea. *Journal of Geophysical Research*, **98**, 7049-7067.

Davies, A.M. and J. Lawrence (1994a) The response of the Irish Sea to boundary and wind forcing: results from a three-dimensional hydrodynamic model. *Journal of Geophysical Research*, **99**, 22,665-22,687.

Davies, A.M. and J. Lawrence (1994b) A three-dimensional model of the M_4 tide in the Irish Sea: The importance of open boundary conditions and influence of wind. *Journal of Geophysical Research*, **99**, 16,197-16,227.

Davies, A.M., J.E. Jones and J. Xing (1996) A review of recent developments in tidal hydrodynamic modelling. Part 1:spectral models. Special edition of *Journal of Hydraulic Engineering* on Tidal Modelling (in press).

Davis, R.E., J.E. Dufour, G.P Parks and M.R. Perkins (1982) Two inexpensive current-following drifters. Scripps Institution of Oceanography Reference Number 82/28.

Deleersnijder, E. and P. Luyten (1994) On the practical advantages of the quasi-equilibrium version of the Mellor and Yamada level 2.5 turbulence closure applied to marine modelling. *Applied Mathematical Modelling*, **18**, 281-287.

Dickey-Collas, M., J. Brown, L. Fernand, A.E. Hill, K.J. Horsburgh and R.W. Garvine (1997) Does the western Irish Sea gyre influence the distribution of juvenile fish? *Journal of Fish Biology*, **51** (Supplement A), 206-229.

Dietrich, D. E., M.G. Marietta and P.J. Roache (1987) An ocean modelling system with turbulent boundary layers and topography: model description. *International Journal of Numerical Methods in Fluids*, **7**, 833-855.

Dippner, J.W. (1993) A frontal resolving model of the German Bight. *Continental Shelf Research*, **13**, 49-69.

Dowd, M. (1998) On the estimation of circulation from density observations in coastal and shelf regions. *Continental Shelf Research*, **18**, 991-1014.

Duffy, D.G. (1976) The application of the semigeostrophic equations to the frontal instability problem. *Journal of the Atmospheric Sciences*, **33**, 2322-2337.

Durazo-Arvizu, R. (1993) Horizontal circulation and diffusion at tidal fronts. PhD thesis, University of Wales, Bangor.

Eady, E.T. (1949) Long waves and cyclone waves. *Tellus*, **1**, 33-52.

Eliassen, A. (1962) On the vertical circulation in frontal zones. *Geofys. Publ.*, **24**, 147-160.

Elliott, A.J. (1991) EUROSPILL: Oceanographic processes and NW European shelf databases. *Marine Pollution Bulletin*, **22**, 548-553.

Evans, S. R. and J. F. Middleton (1998) A regional model of shelf circulation near Bass Strait: a new upwelling mechanism. *Journal of Physical Oceanography*, **28**, 1439-1457.

Ezer, T. and G. L. Mellor (1992) A numerical study of the variability and the separation of the Gulf Stream, induced by surface atmospheric forcing and lateral boundary flows. *Journal of Physical Oceanography*, **22**, 660-682..

Ezer, T. and G. L. Mellor (1994) Diagnostic and prognostic calculations of the North Atlantic circulation and sea level using a sigma coordinate ocean model. *Journal of Geophysical Research*, **99**, 14,159-14,171.

Ezer, T. and G. L. Mellor (1997) Simulation of the Atlantic Ocean with a free surface sigma coordinate ocean model. *Journal of Geophysical Research*, **102**, 15647-15657.

Farrow, D.E. and D.P. Stevens (1995) A new tracer advection scheme for Bryan and Cox type ocean general circulation models. *Journal of Physical Oceanography*, **25**, 1731-1741.

Fernand, L. (1999) High resolution measurements of the velocity and thermohaline structure of the western Irish Sea gyre. PhD thesis, University of Wales, Bangor (in preparation)

Flagg, C.N. and R.C. Beardsley (1978) On the stability of the shelf water/slope water front south of New England. *Journal of Geophysical Research*, **83**, 4623-4631.

Flather, R.A. (1976) A tidal model of the north west European continental shelf. *Memoires de la Societe Royale des Science de Liege*, **10**, 141-164.

Fofonoff, N. P. (1962) Dynamics of ocean currents. In: *The Sea, Volume 1* (M. N. Hill, ed.), Interscience, New York, pp.323-395.

Freeman, N. G., A. M. Hale and M. B. Danard (1972) A modified sigma equation approach to the numerical modelling of great lakes. *Journal of Geophysical Research*, **77**, 1050-1060.

Galperin, B. and G. L. Mellor (1990) A time-dependent, three-dimensional model of the Delaware Bay and river system. *Estuarine Coastal and Shelf Science*, **31**, 231-281.

Galperin, B., L.H. Kantha, S. Hassid and A. Rosati (1988) A quasi-equilibrium turbulent energy model for geophysical flows. *Journal of Atmospheric Science*, **45**, 55-62.

Garrett, C.J.R. and J.W. Loder (1981) Dynamical aspects of shallow sea fronts. *Philosophical Transactions of the Royal Society of London*, **A302**, 563-581.

Gibson, M.M. and B.E. Launder (1978) Ground effects on pressure fluctuations in the atmospheric boundary layer. *Journal of Fluid Mechanics*, **86**, 491-511.

Gowen, R.J., G. McCullough, M. Dickey-Collas and G.S. Kleppel (1998) Copepod abundance in the western Irish Sea: relationship to physical regime, phytoplankton distribution and standing stock, *Journal of Plankton Research*, **20**, 315-330.

Grant, W.D. and O.S. Madsen (1979) Combined wave and current interaction with a rough bottom. *Journal of Geophysical Research*, **84**, 1797-1808.

Greatbatch, R. J. and A. Goulding (1992) A long-time-scale density stratified shelf circulation model. *Continental Shelf Research*, **12**, 115-141.

Griffiths, R.W. and P.F. Linden (1981) The stability of vortices in a rotating stratified fluid. *Journal of Fluid Mechanics*, **105**, 283-316.

Griffiths, R.W. and P.F. Linden (1982) Laboratory experiments on fronts I. *Geophysical and Astrophysical Fluid Dynamics*, **19**, 159-187

Haidvogel, D.B. and A. Beckmann (1998) Numerical models of the coastal ocean. In: *The Sea, Volume 10* (K.H. Brink and A.R. Robinson, eds.). John Wiley & Sons Inc., New York, pp.457-482.

Haidvogel, D. B, J. L. Wilkin and R. E. Young (1991) A semi-spectral primitive equation ocean circulation model using vertical sigma and orthogonal curvilinear horizontal coordinates. *Journal of Computational Physics*, **94**, 151-185.

Haney, R. L. (1991) On the pressure gradient force over steep topography in sigma coordinate ocean models. *Journal of Physical Oceanography*, **21**, 610-619.

Hanjalic, K. and B.E. Launder (1972) Fully developed asymmetric flow in a plane channel. *Journal of Fluid Mechanics*, **52**, 689-704.

Hassid, S. and B. Galperin (1983) A turbulent energy model for geophysical flows. *Boundary-Layer Meteorology*, **26**, 397-412.

Heaps, N.S. (1979) Three-dimensional modelling of the Irish Sea. In: *Proceedings of the 16th Coastal Engineering Conference1978*, Hamburg, pp.2671-2686.

Heaps, N.S. and J.E. Jones (1977) Density currents in the Irish Sea. *Geophysical Journal of the Royal Astronomical Society*, **51**, 393-429.

Henderschott, M.C. and M.P. Rizzoli (1976) The winter circulation of the Adriatic Sea. *Deep-Sea Research*, **23**, 353-370.

Hernandez, F., P.Y. Le Traon and N.H. Barth (1995) Optimizing a drifter cast strategy with a genetic algorithm. *Journal of Atmospheric and Oceanic Technology*, **12**, 330-345.

Hill, A.E. (1993) Seasonal gyres in shelf seas. *Annales Geophysicae*, **11**,1130-1137.

Hill, A.E. (1996) Spin-down and the dynamics of dense pool gyres in shallow seas. *Journal of Marine Research*, **54**, 471-486.

Hill, A.E. (1998) Buoyancy effects in coastal and shelf seas. In: *The Sea, Volume 10,* (K.H. Brink and A.R. Robinson, eds). John Wiley & Sons Inc., New York, pp.21-62.

Hill, A.E., I.D. James, P.F. Linden, J.P. Matthews, D. Prandle, J.H. Simpson, E.M. Gmitrowicz, D.A. Smeed, K.M.M. Lwiza, R. Durazo, A. Fox and D.G. Bowers (1993) Dynamics of tidal mixing fronts in the North Sea. *Philosophical Transactions of the Royal Society of London*, **A343**, 431-446.

Hill, A.E., R. Durazo and D.A. Smeed (1994) Observations of a cyclonic gyre in the western Irish Sea. *Continental Shelf Research*, **14**, 479-490.

Hill, A.E., J. Brown and L.Fernand (1996) The western Irish Sea gyre: a retention system for Norway Lobster (*Nephrops norvegicus*). *Oceanologica Acta*, **19**, 357-368.

Hill, A.E., J.Brown and L.Fernand (1997a) The summer gyre in the western Irish Sea: Shelf sea paradigms and management implications. *Estuarine Coastal and Shelf Science*, **44** (Supplement A), 83-95.

Hill, A.E., K.J. Horsburgh, R.W. Garvine, P.A. Gillibrand, G. Slesser, W.R. Turrell and R.D. Adams (1997b) Observations of a density-driven recirculation of the Scottish Coastal Current in the Minch. *Estuarine Coastal and Shelf Science*, **45**, 473-484.

Holloway, P. E. (1984) On the semidiurnal internal tide at a shelf-break region on the Australian north west shelf, *Journal of Physical Oceanography*, **14**, 1787-1799.

Holloway, P. E. and B. Barnes (1998) A numerical investigation into the bottom boundary layer flow and vertical structure of internal waves on a continental slope. *Continental Shelf Research*, **18**, 31-65.

Horsburgh, K.J., A.E. Hill and J. Brown (1998) A summer jet in the St George's Channel of the Irish Sea. *Estuarine Coastal and Shelf Science*, **47**, 285-294.

Hoskins, B.J. (1975) The geostrophic momentum approximation and semigeostrophic equations. *Journal of the Atmospheric Sciences*, **32**, 233-242.

Houghton, R.W. (1997) Lagrangian flow at the foot of a shelfbreak front using a dye tracer injected into the bottom boundary layer. *Geophysical Research Letters*, **24**, 2035-2038.

Houghton, R.W., R. Schlitz, R.C. Beardsley, B.Butman and J.L. Chamberlin (1982) The Middle Atlantic Bight : evolution of the temperature structure during summer 1979. *Journal of Physical Oceanography*, **12**, 1019-1029.

Hu, D., M. Cui, Y. Li and T. Qu (1991) On the Yellow Sea cold water mass related circulation. *Yellow Sea Research*, **4**, 79-88.

Hukuda, H., R.J. Greatbatch and A.E. Hay (1989) A simple three-dimensional model of the circulation off Newfoundland. *Journal of Geophysical Research*, **94**, 12607-12618.

Hunter, J.R. (1972) An investigation into the circulation of the Irish Sea. PhD thesis, University of Wales, Bangor.

Huthnance, J.M. (1973) Tidal current asymmetries over the Norfolk sandbanks. *Estuarine Coastal and Marine Science*, **1**, 89-99.

Huthnance, J.M. (1984) Slope currents and JEBAR. *Journal of Physical Oceanography*, **14**, 795-810.

Huthnance, J.M. (1995) Circulation, exchange and water masses at the ocean margin: the role of physical processes at the shelf edge. *Progress in Oceanography*, **35**, 353 - 431.

James, I.D. (1977) A model of the annual cycle of temperature in a frontal region of the Celtic Sea. *Estuarine Coastal and Marine Science*, **5**, 339-353.

James, I.D. (1978) A note on the circulation induced by a shallow-sea front. *Estuarine Coastal and Marine Science*, **7**, 197-202.

James, I.D. (1981) Fronts and shelf circulation models. *Philosophical Transactions of the Royal Society of London*, **A302**, 597-604.

James, I.D. (1984) A three-dimensional numerical shelf-sea model with variable viscosity and diffusivity. *Continental Shelf Research*, **3**, 69-98.

James, I.D. (1987) A general three-dimensional eddy-resolving model for stratified seas. In: *Three-dimensional models of marine and estuarine hydrodynamics*, (J.C.J. Nihoul and B.M. Jamart, eds.), Elsevier, Amsterdam.

James, I.D. (1989) A three-dimensional model of circulation in a frontal region in the North Sea. *Deutsche Hydrographische Zeitschift*, **42**, 231-247.

James, I.D. (1990) Numerical modelling of density-driven circulation in shelf seas. In: *Modelling Marine Systems Vol II*, (A.M. Davies, ed.), CRC Press, Florida, pp.345-372.

James, I. D. (1996) Advection schemes for shelf sea models. *Journal of Marine Systems*, **8**, 237-254.

Jeffries, D.F., A. Preston and A.K. Steele (1973) Distribution of caesium-137 in British coastal waters. *Marine Pollution Bulletin*, **4**, 118-122.

Jiang, L. and R. W. Garwood Jr. (1996) Three-dimensional simulations of overflows on continental slopes. *Journal of Physical Oceanography*, **26**, 1214-1233.

Killworth, P.D., N. Paldor and M.E. Stern (1984) Wave propagation and growth on a surface front in a two-layer geostrophic current. *Journal of Marine Research*, **42**, 761-785.

Kolmogorov, A. N. (1941) The local structure of turbulence in incompressible viscous fluid for very large Reynolds number (in Russian), *Dokl. Akad. Nauk SSSR*, **30**, p.301.

Kolmogorov, A. N. (1942) The equations of turbulent motion in an incompressible fluid. *Izvestiya Academy of Sciences, USSR: Physics*, **Vol. 6**, 56-58.

Kourafalou, V. H., L. Y. Oey, J. D. Wang and T. N. Lee (1996) The fate of river discharge on the continental shelf. 1. Modeling the river plume and the inner shelf coastal current. *Journal of Geophysical Research*, **101**, 3415-3434.

Kowalik, Z. and T. S. Murty (1993) *Numerical modelling of ocean dynamics*. Advanced Series on Ocean Engineering, Volume 5, World Scientific, Singapore, 481pp.

Large, W.G. and S. Pond (1981) Open ocean momentum flux measurements in moderate to strong winds. *Journal of Physical Oceanography*, **11**, 324-336.

Large, W.G. and S. Pond (1982) Sensible and latent heat flux measurements over the ocean. *Journal of Physical Oceanography*, **12**, 464-482.

Launder, B.E. and D.B. Spalding (1972) *Mathematical models of turbulence.* Academic Press, London, 169pp.

Launder, B.E., G.J. Reece and W. Rodi (1975) Progress in the development of a Reynolds-stress turbulence closure. *Journal of Fluid Mechanics*, **68**, 537-566.

Lavin-Peregrina, M.F. (1984) The seasonal cycle of variability of stratification in the western Irish Sea. PhD thesis, University of Wales, Bangor.

Lavin, M.F. and T.J. Sherwin (1985) Stratification and internal waves in the western Irish Sea. In: *Turbulence and diffusion in stable environments*, J.C.R. Hunt, ed., Proc. Conf. of IMA (March 1983).

Leach, H., N. Didden, V. Fiekas, J. Fischer, A. Horch and J.D. Woods (1987) SEAROVER Data Report II - North Atlantic Summer 1983 NOA'83. Berichte aus dem Institut für Meereskunde an der Christian-Albrechts-Universitat Kiel 175, 91 pp.

Lee, J.C. and K.T. Jung (1999) Application of eddy viscosity closure models for the M_2 tide and tidal currents in the Yellow Sea and the East China Sea. *Continental Shelf Research*, **19**, 445-475.

Leenderdtse, J.J. and S.K. Lui (1975) A three-dimensional model for the estuaries and coastal seas: Volume II. *Aspects of computation.* RAND Corporation. R-1764-OWRT.

Leonard, B.P. (1979) A stable and accurate convective modelling procedure based on quadratic upstream interpolation. *Computer Methods in Applied Mechanics and Engineering*, **19**, 59-98.

Li, Z. and B. Johns (1998) A three-dimensional numerical model of surface waves in the surf zone and longshore current generation over a plane beach. *Estuarine Coastal and Shelf Science*, **47**, 395-413.

Limeburner, R. and R.C. Beardsley (1996) Near-surface recirculation over Georges Bank. *Deep-Sea Research II*, **43**, 1547-1574.

Linden, P.F. and G.J.F. van Heist (1984) Two-layer spin-up and frontogenesis. *Journal of Fluid Mechanics*, **143**, 69-94.

Linden, P.F. and J.E. Simpson (1988) Modulated mixing and frontogenesis in shallow seas and estuaries. *Continental Shelf Research*, **8**, 1107-1127.

Loder, J.W. (1980) Topographic rectification of tidal currents on the sides of Georges Bank. *Journal of Physical Oceanography*, **10**, 1399-1416.

Loder, J.W. and D.G. Wright (1985) Tidal rectification and frontal circulation on the sides of Georges Bank. *Journal of Marine Research*, **43**, 581-604.

Longuet-Higgins, M.S. (1969) On the transport of mass by time-varying current. *Deep Sea Research*, **16**, 431-447.

Lorenzzetti, J.A. and J.D. Wang (1986) On the use of wave-absorbing layers in the treatment of open boundaries in numerical coastal circulation models. *Applied Mathematical Modelling*, **10**, 339-345.

Lynch, D. R., F. E. Werner, D. A. Greenberg and J. W. Loder (1992) Diagnostic model for baroclinic wind-driven and tidal circulation in shallow seas. *Continental Shelf Research*, **12**, 37-64.

Lynch, D. R., J. T. C. Ip, C.E. Naimie and F.E. Werner (1996) Comprehensive coastal circulation model with application to the Gulf of Maine. *Continental Shelf Research*, **16**, 875-906.

Lynch, D. R., M.J. Holboke and C.E. Naimie (1997) The Maine coastal current: spring climatological circulation. *Continental Shelf Research*, **17**, 605-634.

MacCready, P. and P.B. Rhines (1993) Slippery bottom boundary layers on a slope. *Journal of Physical Oceanography*, **23**, 5-22.

Mamayev, O.I. (1958) The influence of stratification on vertical turbulent mixing in the sea. *Izvestia Geophysical Series*, 870-875.

Martin, P.J. (1985) Simulation of the mixed layer at OWS November and Papa with several models, *Journal of Geophysical Research*, **90**, 903-916.

Matano, R. P. (1996) A numerical study of the Agulhas retroflection: the role of bottom topography. *Journal of Physical Oceanography*, **26**, 2267-2279.

Mellor, G.L. and H.J. Herring (1973) A survey of the mean turbulent field closure models. *AIAA Journal*, **11**, 590-599.

Mellor, G.L. and T. Yamada (1974) A hierarchy of turbulence closure models for planetary boundary layers. *Journal of Atmospheric Science*, **31**, 1791-1806.

Mellor, G.L. and T. Yamada (1982) Development of a turbulence closure model for geophysical fluid problems. *Review of Geophysics and Space Physics*, **20**, 851-875.

Mills, D.K., R.J. Gowen and E.A. Woods (1997) Observation and simulation of the spring bloom in the north-western Irish Sea. *Journal of Plankton Research*, **19**, 63-77.

Mitchelson, E.G. (1984) Phyto-plankton and suspended sediment distributions in relation to physical structure and water-leaving colour signals. PhD thesis, University of Wales, Bangor.

Mory, M., M.E. Stern and R.W. Griffiths (1987) Coherent baroclinic eddies on a sloping bottom. *Journal of Fluid Mechanics*, **183**, 45-62.

Münchow, A. and R.W. Garvine (1993) Dynamical properties of a buoyancy-driven coastal current. *Journal of Geophysical Research*, **98**, 20063-20077.

Munk, W.H. and E.R. Anderson (1948) Notes on a theory of the thermocline. *Journal of Marine Research*, **7**, 276-295.

New, A. L. (1988) Internal tidal mixing in the Bay of Biscay, *Deep-Sea Research*, **35**, 691-709.

Nihoul, J.C.J., P. Adam, P. Brasseur, E. Deleersnijder, S. Djenidi and J. Haus (1993) Three-dimensional general circulation model of the northern Bering Sea's summer ecohydrodynamics. *Continental Shelf Research*, **13**, 509-542.

Niiler, P.P., A.S. Sybrandy, K. Bi, P.M. Poulain and D. Bitterman (1995) Measurement of the water-following capability of holey sock and tristar drifters. *Deep Sea Research*, **42**, 1951-1964.

Nof, D. (1983) The translation of isolated cold eddies on a sloping bottom. *Deep-Sea Research*, **30**, 171-182.

Nunes Vaz, R.A. and J.H. Simpson (1994) Turbulence closure modeling of estuarine stratification. *Journal of Geophysical Research*, **99**, 16143-16160.

O'Brien, J. J. (1989) The diffusive problem. In: *Advanced Physical Oceanographic Numerical Modelling* (J. J. O'Brien, ed.), D. Reidel Publishing

Oey, L. Y. (1996) Simulation of mesoscale variability in the Gulf of Mexico: sensitivity studies, comparison with observations and trapped wave propagation. *Journal of Physical Oceanography*, **26**, 145-175.

Oey, L. Y. and P. Chen (1992) A nested-grid ocean model with application to the simulation of meanders and eddies in the Norwegian coastal current. *Journal of Geophysical Research*, **97**, 20063-20086.

Oey, L. Y., G. L. Mellor and R. I. Hires (1985a) A three-dimensional simulation of the Hudson-Raritran estuary. Part I Description of the model and model simulation. *Journal of Physical Oceanography*, **15**, 1676-1692.

Oey, L. Y., G. L. Mellor and R. I. Hires (1985b) A three-dimensional simulation of the Hudson-Raritran estuary. Part II Comparison with observations. *Journal of Physical Oceanography*, **15**, 1693-1709.

Orlanski, I. (1976) A simple boundary condition for unbounded hyperbolic flows. *Journal of Computational Physics*, **21**, 251-269.

Pedersen, F.B. (1994) The oceanographic and biological tidal cycle succession in shallow sea fronts in the North Sea and the English Channel. *Estuarine Coastal and Shelf Science*, **38**, 249-269.

Pedlosky, J. (1979) *Geophysical Fluid Dynamics*. Springer-Verlag, New York, 710pp.

Petrie, B. (1984) M2 surface and internal tides on the Scotian shelf and slope, *Journal of Marine Research*, **33**, 303-322.

Phillips, N. A. (1957) A coordinate system having some special advantages for numerical forecasting. *The Journal of Meteorology*, **14**, 184-186.

Pingree, R.D. (1994) Winter warming in the southern Bay of Biscay and Lagrangian eddy kinematics from a deep-drogued buoy. *Journal of the Marine Biological Association of the U.K.*, **74**, 107-128.

Pingree, R.D. and L. Maddock (1977) Tidal eddies and coastal discharge. *Journal of the Marine Biological Association of the U.K.*, **57**, 869-875.

Pingree, R.D. and D.K. Griffiths (1978) Tidal fronts on the shelf seas around the British Isles. *Journal of Geophysical Research*, **83**, 4615-4622.

Pingree, R.D. and L. Maddock (1985) Stokes, Euler and Lagrange aspects of residual tidal transports in the English Channel and the Southern Bight of the North Sea. *Journal of the Marine Biological Association of the U.K.*, **65**, 969-982.

Pingree, R.D., G.R. Foster and G.K. Morrison (1974) Turbulent convergent tidal fronts. *Journal of the Marine Biological Association of the U.K.*, **54**, 469-479.

Pollard, D., S. Long, E. Hayden, V.Smith, T.P. Ryan, A. Dowdall, A. McGarry and J.D. Cunnigham (1996) *Radioactivity monitoring of the Irish marine environment 1993 to 1995*. Radiological Protection Institute of Ireland report RPII 96/5, Dublin, 41pp.

Pond, S. and G. L. Pickard (1983) *Introductory Dynamical Oceanography*. Pergamon Press, Oxford, 329pp.

Prandle, D. (1982) The vertical structure of tidal currents. *Geophysical and Astrophysical Fluid Dynamics*, **22**, 29-49.

Prandle, D. (1984) A modelling study of the mixing of caesium-137 in the seas of the European continental shelf. *Philosophical Transactions of the Royal Societyof London*, **A310**, 407-436.

Proakis, J.G. and D.G. Manolakis (1992) *Digital signal processing: Principles, Algorithms and Applications, Second edition.* Macmillan Publishing Company, New York, 969 pp.

Proctor, R. (1981) Tides and residual circulation in the Irish Sea. PhD thesis, University of Liverpool.

Proctor, R and I.D. James (1996) A fine resolution three dimensional model of the southern North Sea. *Journal of Marine Systems*, **8**, 285-295.

Ramster, J.W. and H.W. Hill (1969) Current systems in the northern Irish Sea. *Nature*, **244**, 59-61.

Reed, R.K. (1976) On estimations of net long-wave radiation from the ocean. *Journal of Geophysical Research*, **81**, 5793-5794.

Richards, K.J. (1982) Modeling the benthic boundary layer. *Journal of Physical Oceanography*, **12**, 428-439.

Rizzoli, M.P. and A. Bergamasco (1983) The dynamics of the coastal region of the northern Adriatic Sea. *Journal of Physical Oceanography*, **13**, 1105-1130.

Roache, P. J. (1972) *Computational Fluid Dynamics*. Hermosa, Albuquerque.

Roberts, G., J.D. Last, E.W. Roberts and A.E. Hill (1991) Position-logging drifting buoys using Decca navigator and Argos for high resolution spatial sampling. *Journal of Atmospheric and Oceanic Technology*, **8**, 718-728.

Robinson, I. S. (1979) The tidal dynamics of the Irish and Celtic Seas. *Geophysical Journal of the Royal Astronomical Society*, **56**, 159-197.

Rodi, W. (1980) *Turbulence models and their application in hydraulics*. International Association for Hydraulic Research, Delft, Netherlands.

Rodi, W. (1987) Examples of calculation methods for flow and mixing in stratified flows. *Journal of Geophysical Research*, **92**, 5305-5328.

Rotta, J.C. (1951) Statistische Theorie nichthomogener Turbulenz, *Zeitschrift für Physik*, **129**, 547-572; also, **131**, 51-77.

Saunders, P. M. (1973) The instability of a baroclinic vortex. *Journal of Physical Oceanography*, **3**, 61-65.

Savidge, G. (1976) A preliminary study of the distribution of chlorophyll *a* in the vicinity of fronts in the Celtic and western Irish Seas. *Estuarine Coastal and Marine Science*, **4**, 617-625.

Schrum, C. (1997) Thermohaline stratification and instabilities at tidal mixing fronts: results of an eddy resolving model for the German Bight. *Continental Shelf Research*, **17**, 689-716.

Sharples, J. and J.H. Simpson (1995) Semi-diurnal and longer period stability cycles in the Liverpool Bay region of freshwater influence. *Continental Shelf Research*, **15**, 295-313.

Sheng, J. and K. R. Thompson (1996) A robust method for diagnosing regional shelf circulation from scattered density profiles. *Journal of Geophysical Research*, **101**, 25,647-25,659.

Sherwin, T. J. (1987) Inertial oscillations in the Irish Sea. *Continental Shelf Research*, **7**, 191-211.

Sherwin, T. J. (1988) Analysis of an internal tide observed on the Malin Shelf, north of Ireland. *Journal of Physical Oceanography*, **18**, 1035-1050.

Simpson, J. H. (1971) Density stratification and microstructure in the western Irish Sea. *Deep-Sea Research*, **18**, 309-319.

Simpson, J. H. (1981) The shelf sea fronts: implications of their existence and behaviour. *Philosophical Transactions of the Royal Society of London*, **A302**, 531-546.

Simpson, J.H. and J.R. Hunter (1974) Fronts in the Irish Sea. *Nature*, **250**, 404-406.

Simpson J.H. and R.D. Pingree (1978) Shallow sea fronts produced by tidal stirring. In: *Oceanic Fronts in Coastal Processes*, M.J. Bowman and W.E. Esaias, editors, Springer-Verlag, Berlin, pp. 29-42.

Simpson, J.H. and D. Bowers (1981) Models of stratification and frontal movement in shelf seas. *Deep-Sea Research*, **28A**, 727-738.

Simpson, J.H. and D. Bowers (1984) The role of tidal stirring in controlling the seasonal heat cycle in shelf seas. *Annales Geophysicae*, **2**, 411-416.

Simpson, J.H. and I.D. James (1986) Coastal and estuarine fronts. In: *Baroclinic Processes on Continental Shelves,* C.N.K.Mooers,editor, Coastal and Estuarine Sciences No. 3, American Geophysical Union, Washington, pp.63-93.

Simpson, J.H., C.M. Allen and N.C.G. Morris (1978) Fronts on the continental shelf. *Journal of Geophysical Research*, **83**, 4607-4614.

Simpson, J.H., W.R. Crawford, T.P. Rippeth, A.R. Campbell and J.V.S. Cheok (1996) The vertical structure of turbulent dissipation in shelf seas. *Journal of Physical Oceanography*, **26**, 1579-1590.

Skogen, M.D., E. Svendsen, J. Bernsten, D. Aksnes and K.B. Ulvestad (1995) Modelling the primary production in the North Sea using a coupled three-dimensional physical-chemical-biological ocean model. *Estuarine Coastal and Shelf Science*, **41**, 545-565.

Slinn, D.J. (1974) Water circulation and nutrients in the north-west Irish Sea. *Estuarine Coastal and Marine Science*, **2**, 1-25.

Smagorinsky, J. (1963) General circulation experiments with the primitive equations: 1. the basic experiment. *Monthly Weather Review*, **91**, 99-164.

Smolarkiewicz, P. K. (1983) A simple positive definite advection scheme with small implicit diffusion. *Monthly Weather Review*, **111**, 479-486.

Smolarkiewicz, P. K. (1984) A fully multidimensional positive definite advection transport algorithm with small implicit diffusion. *Journal of Computational Physics*, **54**, 325-362.

Sombardier, L. and P.P Niiler (1994) Global surface circulation measured by Lagrangian drifters. *Sea Technology*, **35**, 21-24.

Souza, A.J. and J.H. Simpson (1996) The modification of tidal ellipses by stratification in the Rhine ROFI. *Continental Shelf Research*, **16**, 997-1007.

Sybrandy, A.L. and P.P. Niiler (1991) *WOCE TOGA Lagrangian drifter construction manual.* Scripps Institute of Oceanography Reference 91/6, WOCE Report Number 63.

Tang, C. C. L., Q. Gui and I. K. Peterson (1996) Modeling the mean circulation of the Labrador Sea and the adjacent shelves. *Journal of Physical Oceanography*, **26**, 1989-2010.

Townsend, A.A. (1976) *The structure of turbulent shear flow*. Cambridge University Press, 429pp.

Tritton, D. J. (1988) *Physical Fluid Dynamics*. Oxford University Press, Oxford, 519pp.

Turner, J.S. (1973) *Buoyancy effects in fluids*. Cambridge University Press, 367pp.

UNESCO (1978) Eighth report of the joint panel on oceanographic tables and standards. *UNESCO Technical Papers in Marine Science* No. 28.

UNESCO (1981) Tenth report of the joint panel on oceanographic tables and standards. *UNESCO Technical Papers in Marine Science* No. 36.

van Aken, H.M., G.J.F. van Heist, L.R.M. Maas (1987) Observations of fronts in the North Sea. *Journal of Marine Research*, **45**, 579-600.

van Heist, G.J.F. (1986) On the dynamics of a tidal mixing front. In : *Marine Interfaces Ecohydrodynamics*, J.C.J. Nihoul, editor, Elsevier Oceanography Series No. 42, Amsterdam, pp. 165-194.

Wang, D.P. (1984) Mutual intrusion of a gravity current and density front formation. *Journal of Physical Oceanography*, **14**, 1191-1199.

Wang, D. P., D. Chen and T. J. Sherwin (1990) Coupling between mixing and advection in a shallow sea front. *Continental Shelf Research*, **10**, 123-136.

Wang, J., L. A. Mysak and R. G. Ingram (1994) A three-dimensional numerical simulation of Hudson Bay summer ocean circulation: Topographic gyres, separations and coastal jets. *Journal of Physical Oceanography*, **24**, 2496-2514.

Wang, L-P., S. Chen, J.G. Brasseur and J.C. Wyngaard (1996) Examination of hypotheses in the Kolmogorov refined turbulence theory through high-resolution simulations. Part 1. Velocity field. *Journal of Fluid Mechanics*, **309**, 113-156.

Whitehead, J. A., M .E. Stern, G. R. Flierl and B. A. Klinger (1990) Experimental observations of baroclinic eddies on a sloping bottom. *Journal of Geophysical Research*, **95**, 9585-9610.

Wilson, T. R. S. (1974) Caesium-137 as a water movement tracer in St George's Channel. *Nature*, **248**, 125-127.

Wolf, J. (1980) Estimation of shearing stresses in a tidal current with application to the Irish Sea. In: *Marine Turbulence*, J.C.J. Nihoul, editor, Proceedings of the 11th International Liege Colloquium on Ocean Hydrodynamics, Amsterdam 1979. (Elsevier Oceanographic Series No. 28).

Xing, J. (1992) The numerical modelling of shallow water flow and sediment transport over bedforms in the coastal ocean. PhD thesis, University of Reading.

Xing, J. and A. M. Davies (1995) Application of three dimensional turbulence energy models to the determination of tidal mixing and currents in a shallow sea. *Progress in Oceanography*, **35**, 153-205.

Xing, J. and A. M. Davies (1996) Application of a range of turbulence energy models to the determination of M_4 tidal current profiles. *Continental Shelf Research*, **16**, 517-547.

Xue, H. and J. M. Bane Jr. (1997) A numerical investigation of the Gulf Stream and its meanders in response to cold air outbreaks. *Journal of Physical Oceanography*, **27**, 2606-2629.

Yang, H. Q. and A. J. Przekwas (1992) A comparative study of advanced shock capturing schemes applied to Burgers' equation. *Journal of Computational Physics*, **102**, 139-159.

Zavatarelli, M. and G. L. Mellor (1995) A numerical study of the Mediterranean Sea circulation. *Journal of Physical Oceanography*, **25**, 1384-1414.

Appendix 1. CTD station positions

Station	Latitude (North)	Longitude (West)	Approx Depth (m)
A1	54° 30.0'	5° 20.0'	120
A2	54° 30.0'	5° 10.0'	140
A3	54° 30.0'	5° 00.0'	135
A4	54° 30.0'	4° 50.0'	62
A5	54° 30.0'	4° 40.0'	50
A6	54° 30.0'	4° 30.0'	46
A7	54° 35.0'	5° 10.0'	136
A8	54° 40.0'	5° 00.0'	46
B1	54° 20.0'	5° 28.0'	28
B2	54° 20.0'	5° 20.0'	53
B3	54° 20.0'	5° 10.0'	160
B4	54° 20.0'	5° 00.0'	130
B5	54° 20.0'	4° 50.0'	45
B6	54° 20.0'	4° 40.0'	30
C1	54° 10.0'	5° 48.0'	23
C2	54° 10.0'	5° 40.0'	30
C3	54° 10.0'	5° 30.0'	50
C4	54° 10.0'	5° 20.0'	90
C5	54° 10.0'	5° 10.0'	120
C6	54° 10.0'	5° 00.0'	88
C7	54° 10.0'	4° 50.0'	38
D1	54° 00.0'	5° 59.0'	24
D2	54° 00.0'	5° 50.0'	40
D3	54° 00.0'	5° 40.0'	57
D4	54° 00.0'	5° 30.0'	102
D5	54° 00.0'	5° 20.0'	85
D6	54° 00.0'	5° 10.0'	65
D7	54° 00.0'	5° 00.0'	53
D8	54° 00.0'	4° 50.0'	60
D9	54° 00.0'	4° 40.0'	42

Station	Latitude (North)	Longitude (West)	Approx Depth (m)
E1	53° 50.0'	6° 10.0'	20
E2	53° 50.0'	6° 00.0'	33
E3	53° 50.0'	5° 50.0'	50
E4	53° 50.0'	5° 40.0'	88
E5	53° 50.0'	5° 30.0'	97
E6	53° 50.0'	5° 20.0'	94
E7	53° 50.0'	5° 10.0'	67
E8	53° 50.0'	5° 00.0'	83
E9	53° 50.0'	4° 50.0'	60
F1	53° 40.0'	6° 00.0'	33
F2	53° 40.0'	5° 50.0'	60
F3	53° 40.0'	5° 40.0'	87
F4	53° 40.0'	5° 30.0'	105
F5	53° 40.0'	5° 20.0'	77
F6	53° 40.0'	5° 10.0'	71
F7	53° 40.0'	5° 00.0'	73
F8	53° 40.0'	4° 50.0'	47
G1	53° 30.0'	5° 59.0'	36
G2	53° 30.0'	5° 50.0'	55
G3	53° 30.0'	5° 40.0'	81
G4	53° 30.0'	5° 30.0'	115
G5	53° 30.0'	5° 20.0'	77
G6	53° 30.0'	5° 10.0'	70
H1	53° 20.0'	5° 50.0'	43
H2	53° 20.0'	5° 40.0'	74
H3	53° 20.0'	5° 30.0'	92
H4	53° 20.0'	5° 20.0'	130
X1	54° 15.0'	5° 10.0'	115
X2	54° 25.0'	5° 00.0'	130

Appendix 2. Locations of coastal and offshore tide gauges used in tidal performance comparisons (from Xing and Davies, 1996). Corresponding model cells and the observed amplitude and phase of the M_2 tide are given in the table.

Symbol	Gauge	Equivalent model cell		Observed M_2 tide	
		I	J	Amp. (cm)	Phase (°)
LA	Larne	15	84	97	317
PP	Port Patrick	27	83	135	333
BH	Belfast	13	78	120	315
PO	Portavogie	21	71	156	316
PE	Peel	37	65	175	319
PR	Port Erin	35	61	176	321
PS	Port St. Mary	39	60	195	325
WL	Wylfa	40	40	207	300
AM	Amlwch	43	40	235	305
DU	Dublin	7	38	134	326
HO	Holyhead	36	37	179	292
FB	Fort Belan	44	31	143	285
NE	Nefyn	40	28	140	270
AB	Aberystwyth	48	10	151	230
RO	Rosslare	3	6	56	157
AP	Aberporth	43	4	141	218
CR	Creetown	44	82	233	343
HI	Heston Isle	53	81	276	339
35	OSTG35	50	77	257	333
WO	Workington	59	77	273	332
RA	Ramsey	44	67	262	328
DO	Douglas	42	62	231	327
34	OSTG34	57	63	265	325
BRD	Barrow (RD)	66	62	308	331
MO	Morecambe	72	58	308	326
HE	Heysham	72	57	315	326
FE	Fleetwood	70	56	305	326
12	OSTG12	49	50	238	317
10	OSTG10	56	49	262	318
FO	Formby	68	44	313	316
QC	OSTGQC	64	43	290	316
HB	Hillbre Isle	65	40	292	318

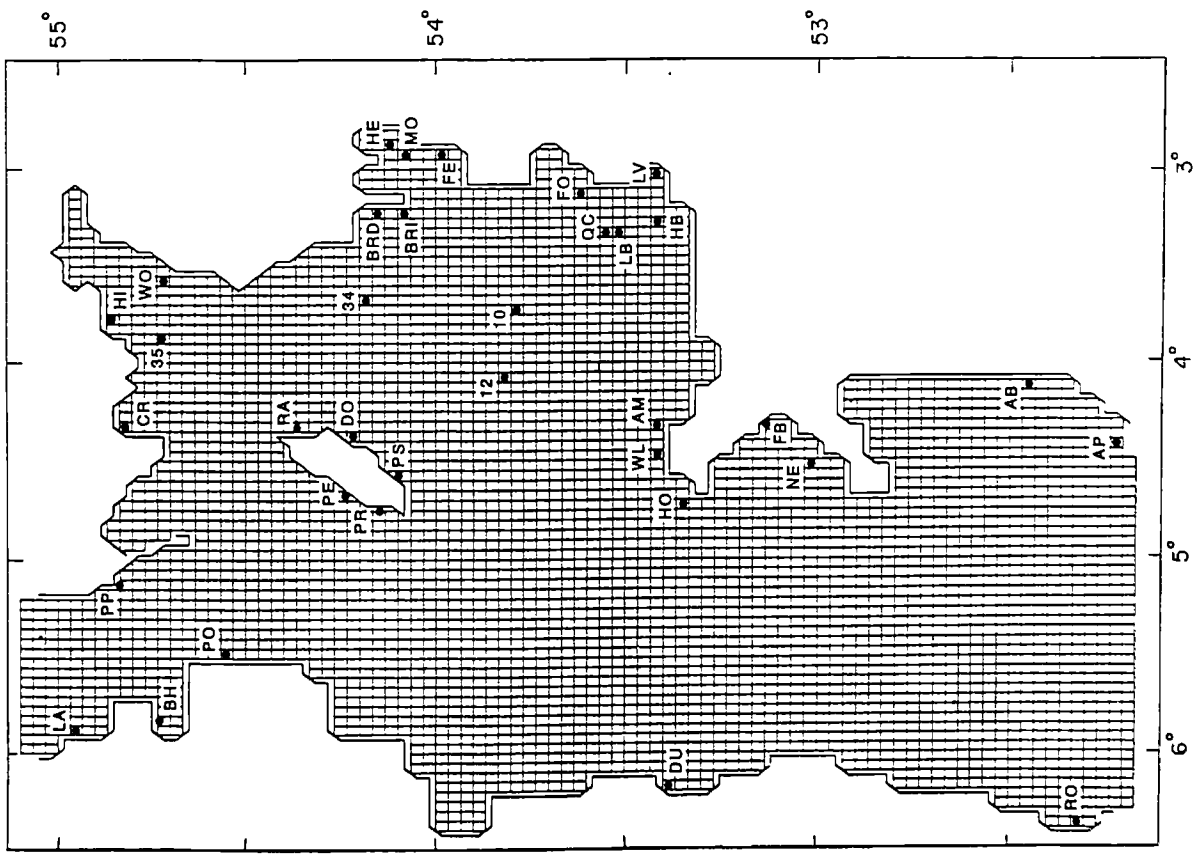

APPENDIX 3

Reprint of :

Hill, A.E., **K.J. Horsburgh**, R.W. Garvine, P.A. Gillibrand, G. Slesser, W.R. Turrell and R.D. Adams (1997b) Observations of a density-driven recirculation of the Scottish Coastal Current in the Minch. *Estuarine Coastal and Shelf Science,* **45**, 473-484.

Estuarine, Coastal and Shelf Science (1997) 45, 473 484

Observations of a Density-driven Recirculation of the Scottish Coastal Current in the Minch

A. E. Hill[a], K. J. Horsburgh[a], R. W. Garvine[b], P. A. Gillibrand[c], G. Slesser[c], W. R. Turrell[c] and R. D. Adams[c]

[a]*School of Ocean Sciences, University of Wales, Bangor, Marine Science Laboratories, Menai Bridge, Ynys Môn LL59 5EY, U.K.*
[b]*College of Marine Studies, University of Delaware, Newark, DE 19716, U.S.A.*
[c]*Scottish Office Agriculture Environment and Fisheries Department, Marine Laboratory, PO Box 101, Victoria Road, Aberdeen AB9 8DB, U.K.*

Received 9 February 1996 and accepted in revised form 27 September 1996

In April/May 1995, five satellite-tracked drifters, drogued at 15 m depth, were deployed in the southern part of the channel (the Minches) between the mainland of Scotland and the Outer Hebridean islands. Drifter trajectories provide direct evidence for a near-surface, cyclonic flow around the South Minch consistent with a baroclinic flow of buoyant, fresh coastal water around a tongue of dense, saline Atlantic water which extends into the centre of the channel from the south. This results in the southward recirculation of part of the north-flowing Scottish coastal current which is then diverted to flow to the west of the Outer Hebridean island chain. The results point to the necessity to include baroclinicity in hydrodynamic models of the region. The circulation pattern also has implications for the dispersal of contaminants and planktonic larvae, including those of the commercially important shellfish, Norway lobster (*Nephrops norvegicus*).

Keywords: drifters; density-driven; baroclinic; recirculation; Norway lobsters; Scottish coastal current; Minch; Scotland west coast

Introduction

Drifter releases, especially if targeted upon well-defined density structures, can reveal valuable information about the dynamics of shallow coastal seas. This paper describes the results of one such Lagrangian experiment, conducted west of Scotland (Figure 1), which provides the first direct confirmation of an aspect of the circulation implied by tracer fields and initially referred to by Craig (1959). The results are of wider significance because they point to a generic form of circulation which may be found in other shelf sea areas.

The experiment was conducted in the southern part of the channel between the Scottish mainland and the Outer Hebridean island chain (Figure 1). From its narrowest part northward, the channel is usually referred to as the Minches (Little Minch and North Minch). This paper will use the name ' South Minch ' to refer to the region bounded by a line from Barra Head to Tiree in the south and extending to the Little Minch in the north (Figure 1). The same region is sometimes referred to as the northern Sea of the Hebrides (McKinley *et al.*, 1981). Bottom topography in the South Minch [Figure 2(a)] is complex, on account of a series of shallow banks on its eastern side. West of these banks, however, the water is deep (>250 m south-east of Barra) with the bottom rising very steeply towards the eastern coasts of the Outer Hebrides.

The oceanography of Scottish coastal waters has been described by Craig (1959), Ellett (1979) and Ellett and Edwards (1983). High salinity (>35·0) water of Atlantic Ocean origin is found on the deeper (>100 m) outer parts of the shelf (Figure 3). Inshore, the low-salinity (<35·0) Scottish coastal current flows northward carrying a mixture of Irish and Clyde Sea waters from the North Channel. These waters are subject to further slight dilution by inputs of fresh water from the fjordic sea-lochs along the Scottish west coast (Craig, 1959; McKay *et al.*, 1986).

The distinctive feature of the salinity field in the South Minch, and the subject of this paper, is the pronounced meander in the surface isohalines (e.g. Figure 3). This feature, remarked upon by Craig (1959), is a persistent feature from year to year (e.g. Ellett, 1979; McKinley *et al.*, 1981; Simpson & Hill, 1986). Freshwater discharge from the Outer Hebrides

0272–7714/97/040473+12 $25.00/0/ec960198

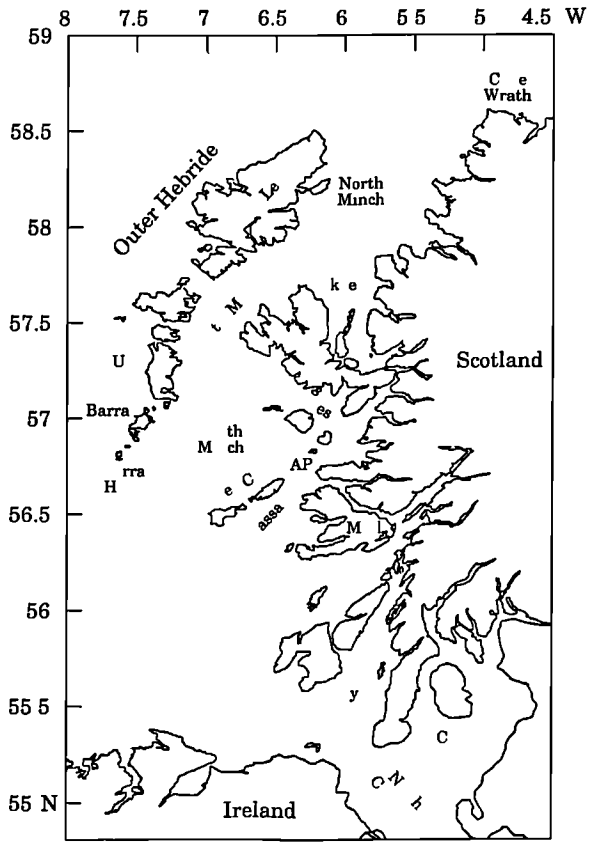

FIGURE 1. Location map. AP, (Ardnurmurchan Point .

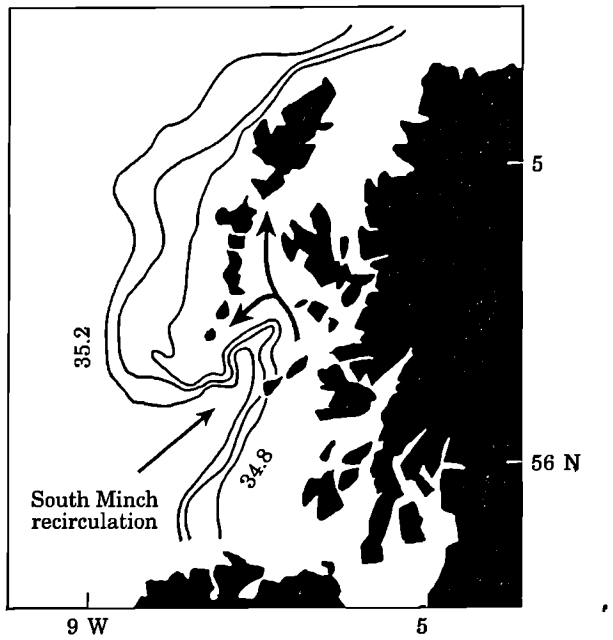

FIGURE 3. Surface (5 m alinity di tribution on th Hebridean shelf in May 1982 adapted fr m Simp n & Hill, 1986 .

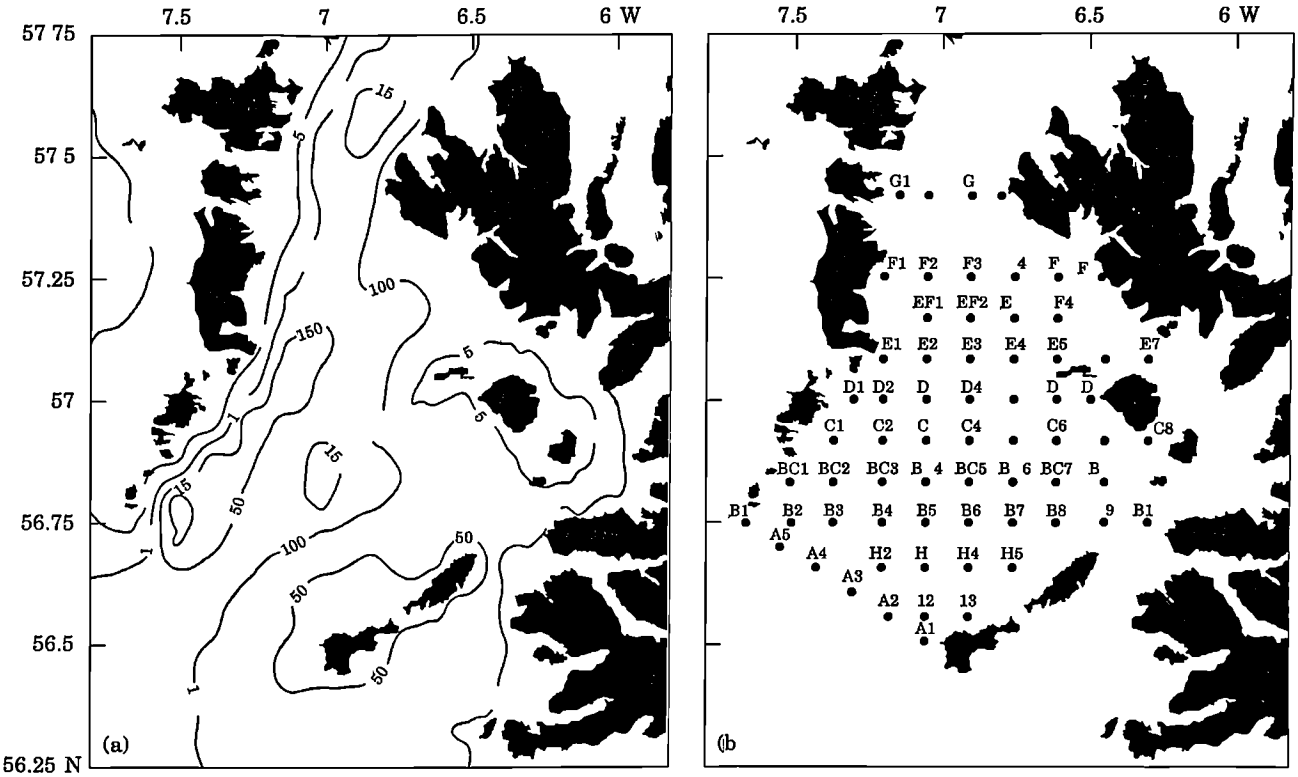

FIGURE 2. (a) Depth contours m), and b CTD stations occupied in the South Minch during *Clupea* Cruises 1 and 2.

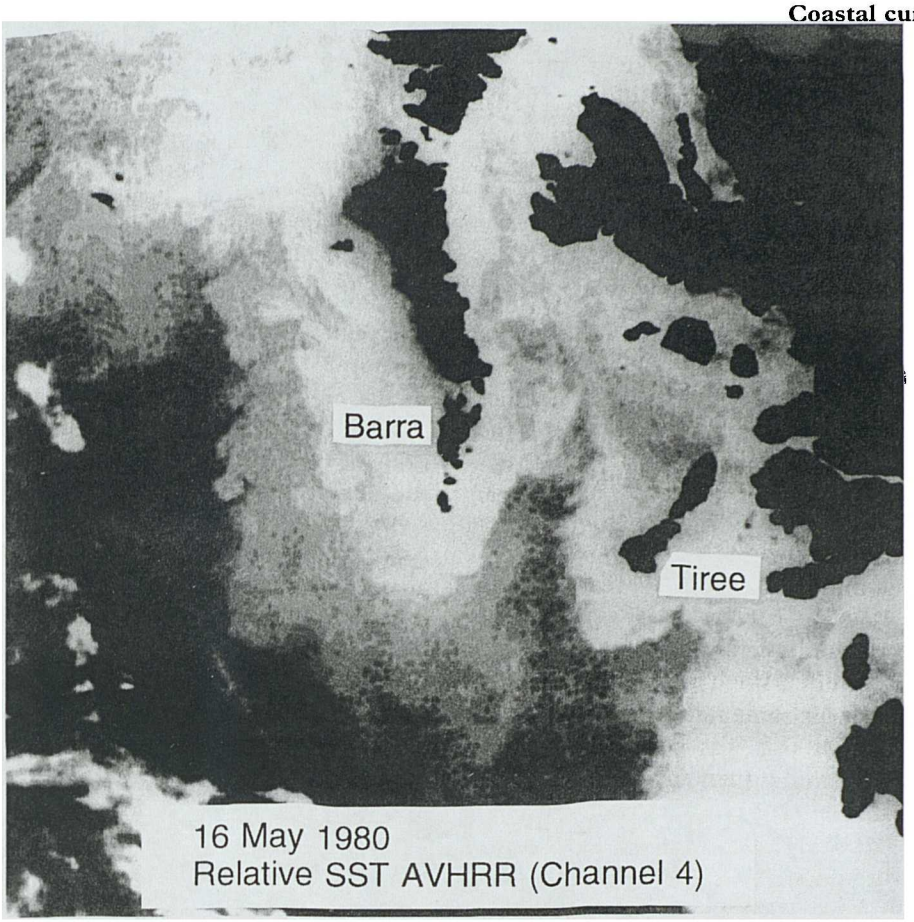

FIGURE 4. Satellite infra-red image of the Sea of the Hebrides including the South Minch, 16 May 1980.

is small, $\sim 32\ m^3\ s^{-1}$ (Craig, 1959), indicating a non-local source for the low-salinity water close to the outer islands. Crucially, the same isoline meander is visible in maps of radio-caesium (McKinley *et al.*, 1981; McKay *et al.*, 1986) which confirms that the Irish Sea (into which ^{137}Cs is discharged from the Sellafield nuclear reprocessing plant) is the origin of these waters.

The following advective interpretation can be placed upon the salinity distribution; the coastal current branches as it enters the South Minch with part of the flow continuing northward through the Little Minch and the remainder diverted to the western side of the channel, then flowing southward down the east coast of the outer islands, rounding Barra Head and resuming its northward course along the western side of the outer islands. This was the interpretation given by Craig (1959) who suggested that flow bifurcation in the South Minch resulted in a coastal water volume transport partition in the ratio 2:3 passing respectively through the Little Minch and west of the outer islands. In contrast, budget calculations by McKay *et al.* (1986), based on a comprehensive survey of the surface ^{137}Cs distribution in July 1981 and a single current meter record west of the outer islands, were used to infer that the coastal current divided into $9 \times 10^4\ m^3\ s^{-1}$ and $2 \times 10^4\ m^3\ s^{-1}$ passing through the Little Minch and west of the Outer Islands, respectively. Their overall estimate of coastal current transport, $11 \times 10^4\ m^3\ s^{-1}$, agreed with that of Craig (1959).

An alternative interpretation, consistent with the same tracer distributions, is that the fresh coastal water flows northward through the South Minch and, on approaching the narrow constriction of the Little Minch, some of the fresh coastal water diffuses down the east coasts of the Outer Hebridean islands (i.e. there may not necessarily be a southward flowing current down the eastern side of the outer islands). The meander-like structure is also visible in satellite infra-red images such as that from 16 May 1980 (Figure 4) which shows cold surface waters on both the eastern and western sides of the South Minch, with warmer water along the central axis. The cold water against the eastern coasts of the Outer Hebrides cannot be locally produced by tidal stirring because

close to these coasts, the water is expected to stratify in spring–summer owing to the large water depth and weak tidal currents (e.g. Pingree & Griffiths, 1978). This reinforces the interpretation that the cold water against the east coasts of Barra and South Uist is transported there either by horizontal advection or diffusion.

Sections across the South Minch in April–May 1995 (e.g. Figures 7 and 9 later) show the isohaline meander to be the surface manifestation of a dome of saline Atlantic water which extends into the deep channel from the south and which is flanked on either side by wedges of fresher, colder coastal water. It is the temperature contrast that enables the meander structure to be seen in infra-red imagery. From historical data, it would appear that this structure is most pronounced during spring, is fairly well developed in autumn, but in summer the isopycnals are more horizontal (Hill, 1987). McKinley *et al.* (1981) pointed out that the radio-caesium content of the saline water in the South Minch was slightly higher than that of water with the same salinity further south, and they suggested that this was consistent with a fairly static saline dome rather than an active incursion into the channel of Atlantic water. If the dense dome is indeed static (Garrett & Loder, 1981; Hill, 1996), the expected flow required to maintain the density field in geostrophic balance would be cyclonic (anticlockwise) at the surface, consistent with the hypothesized circulation around the South Minch.

In spite of the indirect evidence, there are almost no direct measurements of currents in this region except for a reported southward residual flow of order 0·05 m s^{-1} against the east coast of South Uist based on a 10-day current meter record obtained in July 1983 (Simpson & Hill, 1986). To test the existence of the suggested flow pattern, satellite-tracked drifters were released into the South Minch on two occasions during the Spring 1995.

Methods

The study was conducted from the Fisheries Research Vessel *Clupea* during Cruises 6/95 (12–21 April, Julian days 102–111, 1995; hereafter termed Cruise 1) and 8/95 (1–10 May, Julian days 121–130, 1995; hereafter termed Cruise 2). On both cruises, hydrographic variables were measured on the grid of stations shown in Figure 2(b) using a Seabird Sealogger CTD calibrated with water samples and reversing thermometers. On Cruise 1, the grid, with the exception of Lines BC and EF, was sampled from 14 to 20 April, and on Cruise 2, the complete grid was occupied from 1 to 8 May. All salinities quoted have been determined using the practical salinity scale (Unesco, 1978).

The drifter used was composed of a surface buoy and a holey sock drogue, 0·7 m diameter and 2·5 m long. All drogues were centred at a depth of 15 m below the sea surface (chosen to avoid grounding on some of the shallower banks). The drogue was suspended from its own float which was in turn tethered horizontally to the surface buoy with a 2 m long line. This arrangement reduces wave rectification by decoupling the drogue from the surface buoy displacements. The surface buoy derived its buoyancy from four floats attached to spars through the cylindrical body of the buoy. This arrangement is patterned after the Davis CODE drifter and has been shown to reduce wave rectification (Davis *et al.*, 1982). The drag area ratio for the system is $R=48$ which is expected to reduce the wind slip below 0·01 m s^{-1} in a wind of 10 m s^{-1} (Niiler *et al.*, 1995). The buoy was equipped with a System Argos transmitter, a conductivity sensor and a thermistor that permitted measurement of water conductivity and temperature at 1 m depth.

The observed density field obtained on Cruise 1 was used to guide the first batch of drifter deployments on 19 April (Julian day 109) 1995. Four of these were repositioned at new locations on 2–3 May (Julian days 122–123) 1995, at the beginning of Cruise 2. All drifters, except Drifter 4, were finally recovered on 7 May (Julian day 127) 1995. The remaining drifter travelled to the north of Cape Wrath (58°52.3'N, 5°00.2'W; Figure 1) before an automatic internal switch-off mechanism was activated 65 days after deployment; the drifter was eventually recovered off the Orkney Islands.

A wind record at 12 m altitude from Tiree covering the period 10 April to 12 May 1995 was obtained from the Glasgow Weather Centre (Figure 5). Tiree is a low, relatively flat island (<75 m above the sea level) so that the wind direction is representative of that over the wider area of interest. The durations of the first and second drifter deployments, DD1 and DD2, respectively, are indicated on the figure, which presents stick vectors of 3 hourly mean winds using the oceanographic convention.

Results

Drifter deployment 1 (12–21 April 1995)

Figure 6(a) shows that the four drifters, deployed on 19 April on the eastern side of the South Minch, crossed to the western side, travelled southwards and then rounded Barra Head before moving northwards

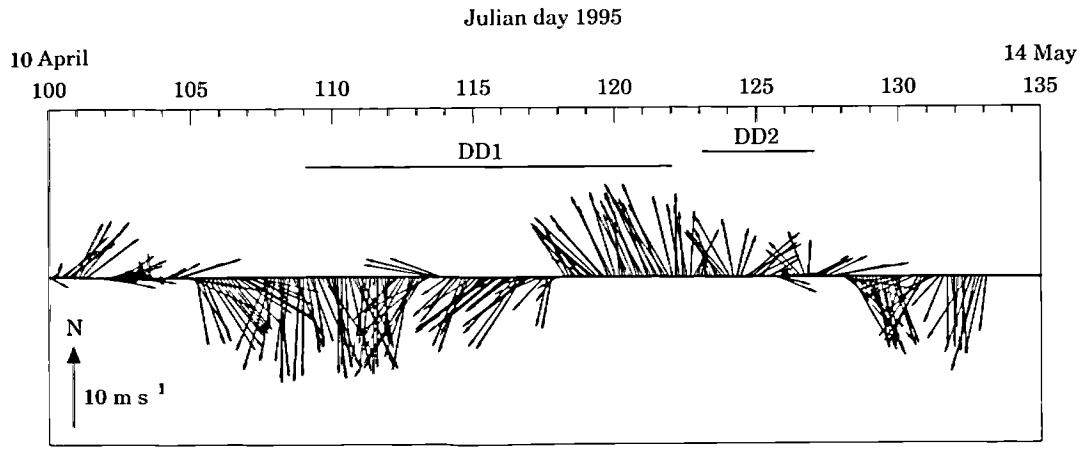

FIGURE 5. Wind vectors (3 h averages) at an altitude of 12 m at Tiree. The durations of the two sets of drifter deployments referred to in the text are denoted by DD1 and DD2.

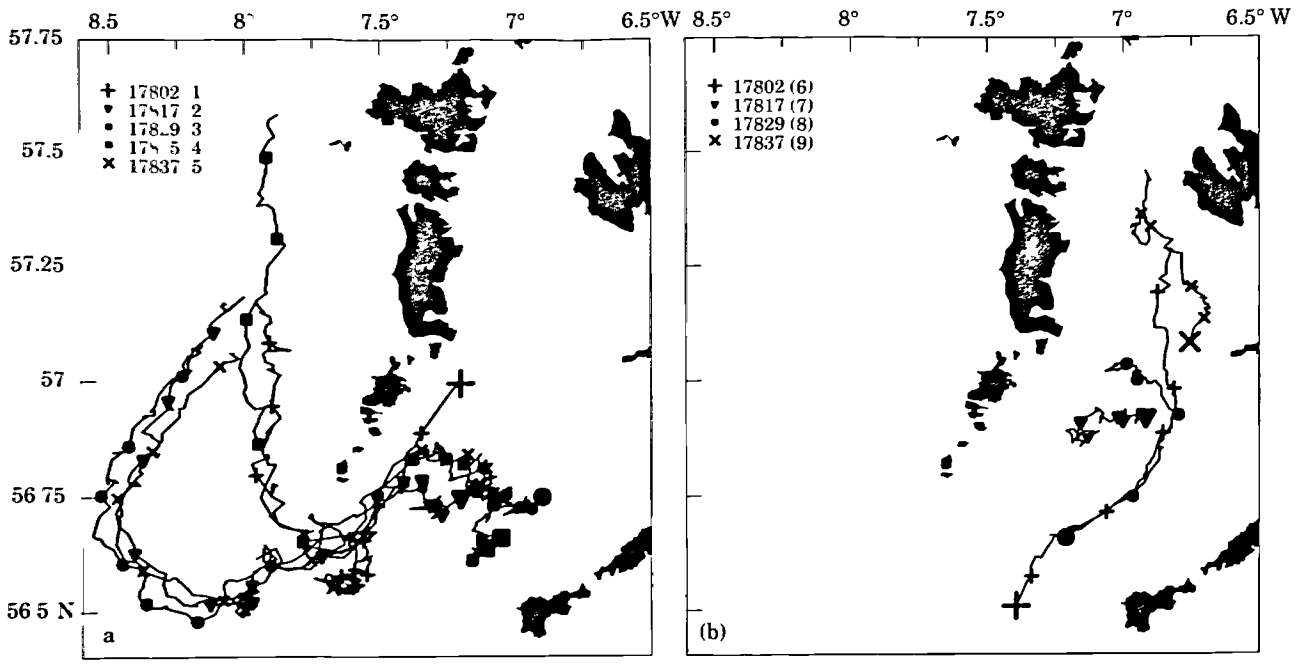

FIGURE 6. Drifter trajectories. Large symbols indicate release sites, and small symbols along each track are at daily intervals. Numbers in brackets are drifter numbers referred to in the text. All drifters were drogued at 15 m depth. (a) five drifters released on 19 April (Julian day 109), four of which were recovered on 2 May 1995. The track of Drifter 4 is shown truncated on 2 May 1995 (Day 122) but it continued to drift northwards reaching (58°52.2'N, 5°W) before automatic switch-off on Day 174, 1995. (b) Four drifters released on 2–3 May (Julian day 122 123) and recovered on 7 May (Day 127) 1995.

on the western side of the Outer Hebridean islands. The symbols along each track are at daily intervals and so give an indication of drifter speed. The congruence of near-neighbour tracks (e.g. Drifters 2, 3 and 5) is remarkable and shows little evidence of diffusion. Drifter 1, deployed east of Barra, moved quickly southwards with a mean speed of $\sim 0{\cdot}4$ m s^{-1} between Julian days 109 and 111. The drifter was arrested between Julian days 111 and 116 south of Barra Head, apparently caught in an eddy. The drifter travelled northwards away from the eddy between Julian Days 116 and 117, thus its ejection from the eddy preceded the shift in wind direction which occurred on Julian day 118 (Figure 5). After its ejection, this drifter, along with Drifter 4, appeared to take a more inshore route northwards on the western side of the islands, where as Drifters 2, 3 and 5 travelled to about 8°30'W, then turned north-eastwards, before they finally converged on the tracks of the others.

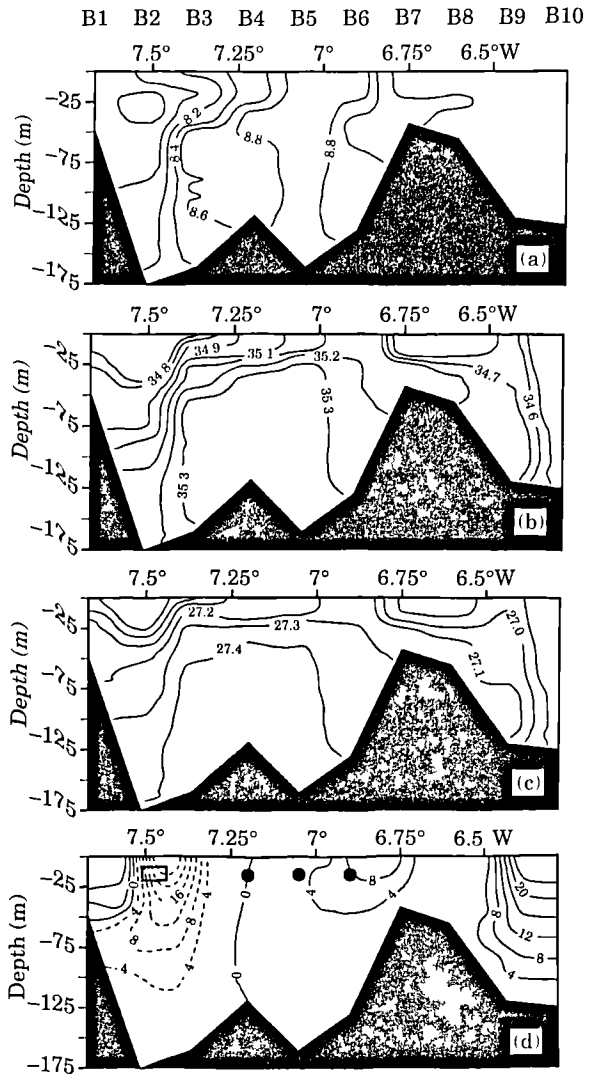

FIGURE 7. Section B at 56°45'N [Figure 2(b)] occupied from 14 to 15 April 1995 during Cruise 1 (a) temperature (°C), (b) salinity, (c) density (σ_t) and (d) geostrophic velocity (cm s $^{-1}$) relative to an assumed level of no motion at the sea-bed. In (d), solid and dashed contours represent northward (into page) and southward (out of page) flows, respectively. The centres of drogues released close to this section on 19 April 1995 are shown as solid circles projected onto the section. The rectangular box shows where all five drifters crossed B-section moving southwards.

Figure 7 shows the B-section [Barra Head to Ardnurmurchan Point; for location see Figures 1 and 2(b)] at latitude 56°45'N, sampled on 14–15 April 1995. This section was chosen for presentation because of the number of drifter trajectories that passed across it. Temperature variation across the section [Figure 7(a)] was fairly small (<1 °C) and the most pronounced feature was the dome of saline (>35·0) water centred on Station B4 which was flanked by wedges of fresher water on either side [Figure 7(b)]. The density field was controlled by salinity and consequently also had a dome structure [Figure 7(c)].

Geostrophic velocities normal to the section were calculated relative to an assumed level of no motion at the sea-bed and are shown in Figure 7(d). Solid and dashed contours indicate flow into the page (northward) and out of the page (southward), respectively. The chosen reference level is consistent with the notion, referred to previously, that the dense, saline dome is static. Consequently, the geostrophic calculations might be expected to characterize the flow best above the dome (between Stations B2 and B6, say). Four of the 19 April drifter releases (Drifters 2–5) were clustered close to B-section and the solid circles in Figure 7(d) represent meridional projections of the drogue centres onto the section (only three circles appear on the diagram because Drifter 5 was released due north of Drifter 4, hence both of these release sites project onto the middle circle near 7°W). Three of the drifters were located in the region of weak northward geostrophic flow and did indeed move initially northward [Figure 6(a)], although it must be remembered that the CTD section was not contemporaneous with the drifters crossing the section. Drifter 2 was located above the stagnation zone and initially moved very slowly before moving westwards. The rectangular box on Figure 7(d) shows where all five drifter tracks crossed B-section moving southwards and corresponded well to the location of the predicted (0·2 m s $^{-1}$) southward geostrophic flow down the western side of the channel. The ensemble mean Lagrangian southward velocity component of all five drifters (averaged over 24 h) as they crossed the B-section in April 1995 [Figure 6(a)] was 0·2 m s $^{-1}$ which is comparable with the computed geostrophic current.

The drifter trajectories have been superimposed upon a map showing the height above 175 m depth of the density (σ_t)=27·3 isopycnal which can be used to provide a picture of the spatial extent of the dome for both survey periods (Figure 8). The drifter tracks corresponded reasonably well to contours of this parameter, and the southward flow in April down the east coasts of the outer islands matched particularly well with the steeply sloping western flank of the dome [Figure 8(a)].

Drifter deployment 2 (1–10 May 1995)

Figure 6(b) shows trajectories from the second, shorter, drifter deployment which began on 2–3 May 1995. Guided by the first set of results, the second batch of drifters was released over a wider extent of the eastern margin of the saline dome in order to

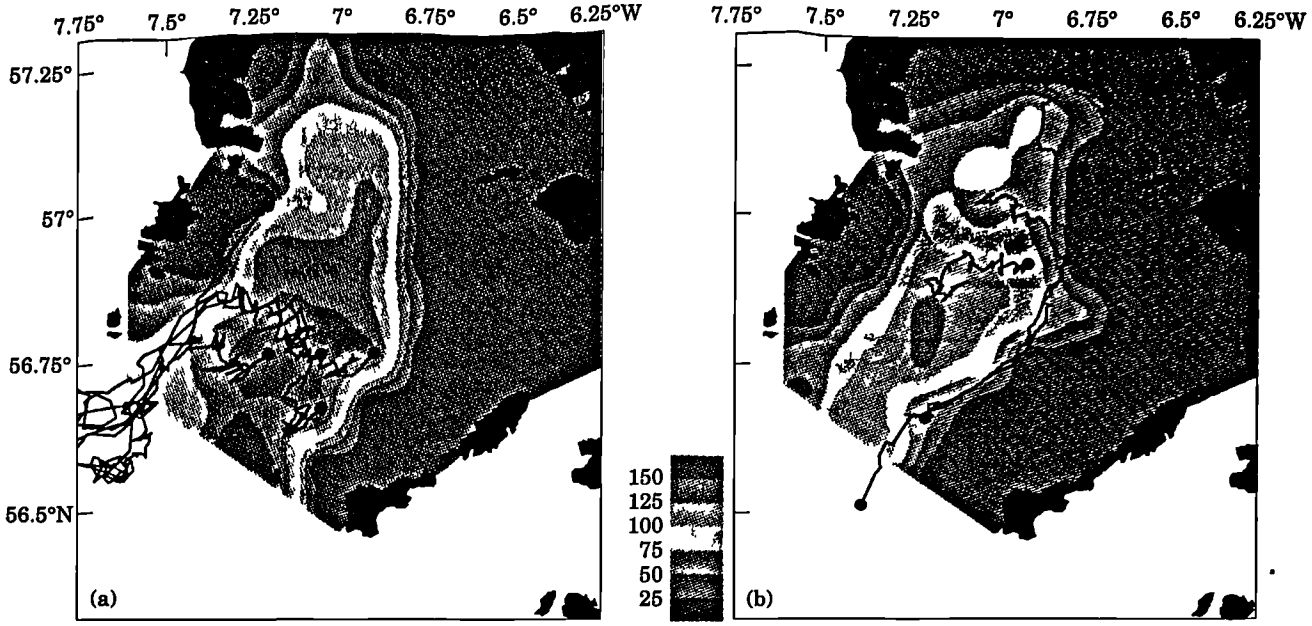

FIGURE 8. (a) height above 175 m depth of the density (σ_t)=27·3 isopycnal. (a) between 12 and 21 April 1995 with the batch 1 drifters superimposed, (b) between 1 and 10 May 1995 with the batch 2 drifters superimposed. Regions where the σ_t=27·3 isopycnal is absent or deeper than 175 m are indicated by zero (blue shading).

examine: (1) whether drifters released further north would also recirculate southwards; and (2) whether drifters released further to the south would enter the region. During this deployment, the B-section was sampled for the second time on 5–7 May 1995 (Figure 9) and showed a broadly similar saline dome structure, although with gentler isopycnal slope on the western side of the channel [Figure 9(c)] and correspondingly weaker geostrophic flow [Figure 9(d)]. In May, two drifters (7 and 8) showed a tendency to turn westwards. The remaining two drifters travelled northwards, towards the Little Minch, confirming the branching of the coastal current. The northward movement of Drifter 6 into the region from an initial position west of Tiree [Figure 6(b) and 8(b)] is also consistent with the view of Ellett (1979) and McKay *et al.* (1986) that the coastal current enters the Minch both through the Tiree Passage and by a route west of the islands of Tiree and Coll. The location where Drifters 6 and 8 crossed the B-section moving northwards is indicated by the square in Figure 9(d) and corresponded with the region of maximum predicted northward geostrophic flow. The drifter tracks corresponded well with the topography of the σ_t=27·3 isopycnal, particularly in showing the location of the branching region [Figure 8(b)].

Analysis of drifter response to winds

To assess the influence of the local wind drift upon the motion of the drifters, the authors examined to what extent the observed trajectories resemble those expected if the drifters behaved merely as wind-driven objects. In a region such as the Minch, the wind-driven flow will exhibit a complex dependency on topography, bathymetry and flow direction. Consequently, a relatively simple approach was adopted which can be justified *a posteriori* by the poor agreement between actual tracks and the predicted wind-driven trajectory. It is assumed that the drifters are subject to a drift law of the form, $u(t+\delta t)=fW(t)\cos a$, where u and W are drifter and local wind speeds, respectively. Here, t is time, δt is the lag in current with respect to the wind, f is the wind to water transfer coefficient, and a is the angular deflection of the drift velocity with respect to the wind. For the first deployment, DD1, the authors have taken a=0 (as in Brown, 1991), varied f between 0·01 and 0·04, and plotted the predicted trajectories in Figure 10. Lag times, δt, between 0 and 48 h were applied and the optimal track (which most closely resembled the actual track) shown in Figure 10 was obtained with δt=0 h and $f\sim$0·01. The authors chose to present drifter 1 from Figure 6(a) since it is the only drifter which resembles the virtual trajectory predicted by the above law, and thus shows the clearest indication of a possible wind-driven contribution. In contrast, the other four drifter trajectories for the same period bear no resemblance at all to the virtual track in Figure 10. Moreover, if the observed drifter trajectories were merely due to local wind drift, all drifter trajectories would have the same shape. The difference in shape between

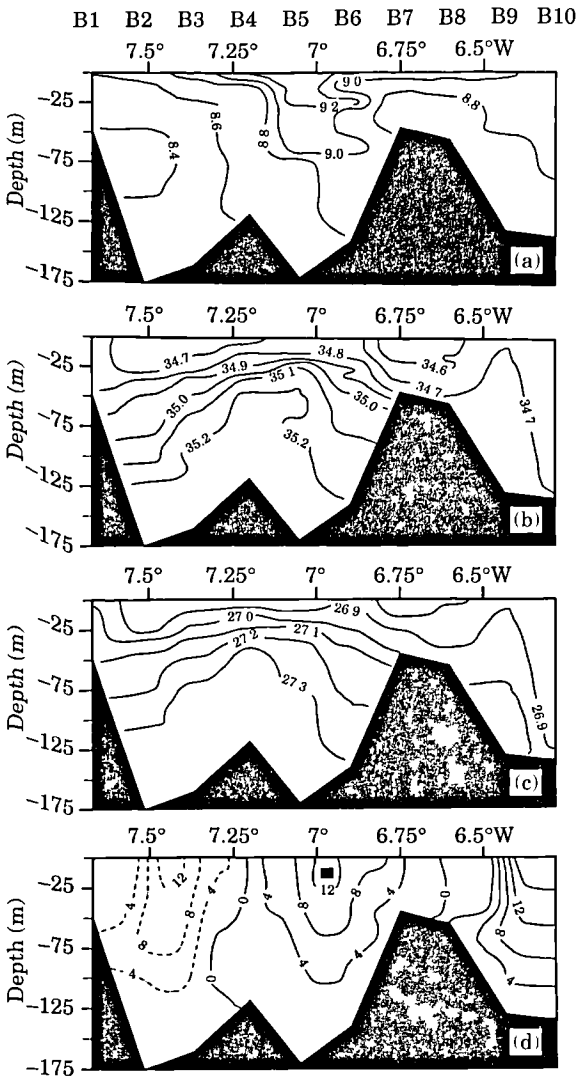

FIGURE 9. Section B occupied on 5–7 May 1995 during Cruise 2. The square shows where Drifters 6 and 7 both crossed the section travelling northwards. (a) Temperature (°C), (b) salinity, (c) density and (d) geostrophic velocity (cm s $^{-1}$).

individual trajectories thus provides the most compelling argument that the drifters do not simply respond to the local wind, but are subject to an underlying spatially varying flow pattern.

In May, the surface wind drift response produced a generally northward movement but did not account for the westward-turning tendency of Drifters 7 and 8 [Figure 6(b)]. In order for the virtual track to account for the motion of Drifter 6 in May, a value $f>0{\cdot}04$ would be required. The difference in the best-fit values of f between deployments provides further evidence that processes other than the local winds affected drifter motion. Table 1 shows the results of a correlation between fluctuations in wind speed and fluctuations in drifter speed, $<u-\bar{u}, W-W>$, where overbars indicate means, calculated over the entire duration that drifters remained within the South Minch (i.e. Julian days 109–114 for Cruise 1 and 122–127 for Cruise 2). Drifter velocity components, u, were calculated between successive Argos fixes, and W is the mean wind calculated over the same temporal interval (for zero lag). The poor correlations further demonstrate that local wind drift has only a small influence.

Discussion

There are two competing hypotheses for how low-salinity Scottish coastal water might be transported to the western side of the Outer Hebridean islands. The tracer plume might simply broaden (by diffusion) as it spreads northward along the Scottish coast until it is sufficiently wide for tracer to reach west of the Outer Hebridean island chain. This tracer behaviour was demonstrated in a numerical simulation of ^{137}Cs dispersal (Prandle, 1984). However, the 30 km resolution of that model, which covered the entire north-west European shelf, only just resolved the Minch. The high resolution (1/12° × 1/12°) model of Davies and Xing (1996) shows that it is possible for tracer to be carried directly outside the island chain without entering the Minch. On the other hand, detailed observations of caesium and salinity tracer fields (McKinley *et al.* 1981) suggest that, during spring at least, there is a recirculation of the coastal current within the South Minch. Tracer fields alone do not distinguish between advective and diffusive processes. These observations now provide unequivocal support for the view that meandering of isohalines in the South Minch is due to a genuine recirculation (advection). The significance of a transport path west of the islands is that water of inshore origin (labelled with anthropogenic contaminants) is brought into close proximity with the continental shelf edge, thereby increasing the potential for exchange with the open ocean. Prandle (1984) suggested that up to one-third of radio-caesium discharged into the Irish Sea could be lost from the shelf seas to the deep ocean north west of Scotland.

The candidate mechanisms for driving the cyclonic recirculation in the South Minch include two barotropic processes, tidal rectification and topographic steering of larger scale (e.g. wind-driven) flows. A third driving mechanisms is the baroclinic pressure gradient associated with the observed dome of dense, saline Atlantic water. Davies and Xing (1996) have used a three-dimensional model to investigate the response of the Malin-Hebrides shelf to forcing

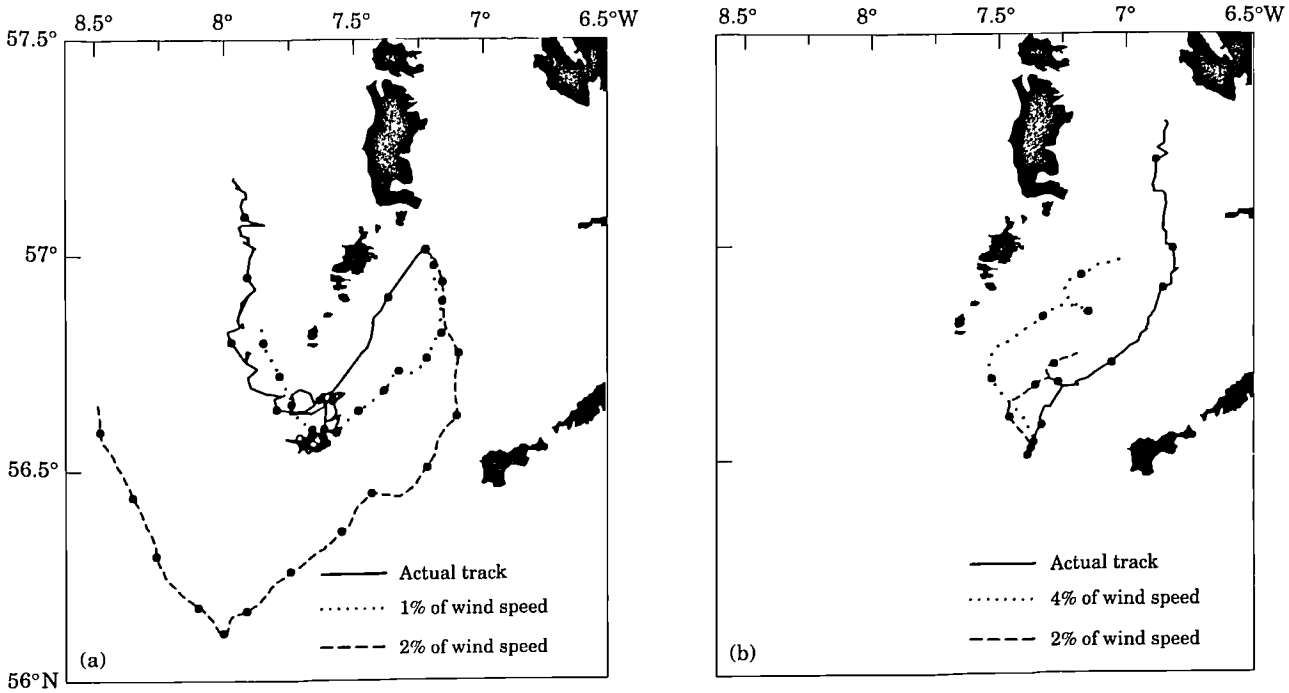

FIGURE 10. Virtual drifter trajectories determined from an assumed surface drift velocity in the direction of the wind with magnitude given by a fixed percentage of the wind speed. Winds at Tiree have been used. Solid circles indicate daily intervals. In (a), the solid line shows the actual trajectory of Drifter 1 during the first deployment [Figure 6(a)]; in (b), the solid curve shows the track of Drifter 6 during the second deployment [Figure 6(b)].

by tides, local winds and upstream inflows. The barotropic model (i.e. no horizontal density gradients included) shows negligible Eulerian tidal residuals in the deep waters of the South Minch. The model shows the wind-driven, near-bottom circulation to exhibit a southward recirculation in the South Minch for winds blowing from the west or south; a wind stress of $0{\cdot}1\ \mathrm{N\ m^{-2}}$ (equivalent to a characteristic wind speed of $\sim 10\ \mathrm{m\ s^{-1}}$) produces currents with speeds of order $0{\cdot}02\ \mathrm{m\ s^{-1}}$. A uniform inflow of $0{\cdot}01$–$0{\cdot}1\ \mathrm{m\ s^{-1}}$ through the North Channel (representing the effect of non-local, upstream forcing) generates a similar recirculation with flow speeds also of order $0{\cdot}01$–$0{\cdot}1\ \mathrm{m\ s^{-1}}$. Although the spatial pattern of flow in the South Minch can be partly accounted for by barotropic-forcing mechanisms, the observed (Lagrangian) drifter velocities are much larger ($\sim 0{\cdot}2\ \mathrm{m\ s^{-1}}$) than the characteristic (Eulerian) velocities predicted by the model. Given the small tidal current amplitudes in the deep South Minch, the tidal Stokes drift is unlikely to account for the difference. The discrepancy in flow magnitude is almost certainly accounted for by baroclinicity as indicated by the geostrophic estimates [Figure 7(d) and 9(d)].

The following hypothesis is proposed for the establishment of the South Minch circulation regime. Weak barotropic circulation in the South Minch encourages the initial cyclonic transport of fresh coastal water around the dense, saline Atlantic water which occupies the deep entrance to the Minch. In so doing, the barotropic circulation establishes the baroclinic density field. Geostrophic adjustment between the fresh coastal water and the saline Atlantic water leads to a dome-like density structure flanked by wedges of fresh water. Once this structure is formed, the resulting, stronger baroclinic circulation reinforces the original barotropic motion and is able to co-exist with it, maintaining the dome in thermal wind balance. The process described above may be relevant in other shelf seas, for example, the northern North Sea where the Dooley current (which has an important baroclinic component) may be maintained by large-scale topographically steered flow along the 100 m isobath south of the Fladen Ground (Figure 11; e.g. Turrell *et al.*, 1990, 1992; Hill, 1993). A more detailed examination of this hypothesis and the density-driven dynamics of the South Minch will require the application of a fully three-dimensional baroclinic coastal ocean model (e.g. Backhaus, 1985; Blumberg & Mellor, 1987).

There are other shallow sea locations where dome-like density structures drive intense cyclonic surface circulations. Hill (1993) and Hill *et al.* (1994), for example, have described a closed cyclonic gyre in the

TABLE 1. Correlation coefficients, ρ, between fluctuating parts of wind and drifter velocities (u and v denote eastward and northward components of velocity, respectively)

Lag (h)	Drifter	1	2	3	4	5
Cruise 1						
0	ρ_u	−0·06	0·06	0·01	−0·14	0·24
	ρ_v	0·30	0·06	0·19	0·04	−0·02
12	ρ_u	−0·16	0·15	0·07	0·07	0·31
	ρ_v	0·12	−0·06	0·03	0·01	−0·35
24	ρ_u	−0·14	0·19	0·14	0·10	0·35
	ρ_v	−0·15	−0·19	−0·19	−0·09	−0·21
n-2		72	61	72	62	55
5%		0·23	0·25	0·23	0·25	0·26
1%		0·30	0·32	0·30	0·32	0·34
Cruise 2						
0	ρ_u	0·00	−0·04	−0·29	−0·02	
	ρ_v	0·16	−0·04	0·11	−0·22	
12	ρ_u	−0·19	−0·12	−0·18	−0·19	
	ρ_v	0·05	0·00	0·16	0·11	
24	ρ_u	−0·09	−0·17	0·03	−0·19	
	ρ_v	0·14	0·01	0·18	0·24	
n-2		74	54	67	54	
5%		0·22	0·26	0·24	0·26	
1%		0·29	0·34	0·31	0·34	

Correlations were determined between Julian days 109 and 114 for Cruise 1 and Julian days 122–127 for Cruise 2. Values presented are for drifter velocity fluctuations lagging the wind by 0, 12 and 24 h. n-2 is the degrees of freedom, and 5% and 1% significance points are shown.

Irish Sea where an isolated, static dome of cold, dense bottom water forms each summer as winter water is trapped beneath the thermocline after the onset of thermal stratification. Unlike the Irish Sea system, the South Minch circulation is not a closed circulation because the saline water mass that controls it has the form of an elongated tongue rather than an isolated lens. The density structure at the shallow head of the Gulf of California (Mexico) also has a dome-like form (Bray, 1988) and probably drives a similar cyclonic surface circulation.

This study has implications for the environmental management of the Minch. The shoreline of the Minch contains wilderness areas of outstanding natural beauty; there are over 60 designated sites of special scientific interest and numerous areas important to cetaceans, seals and seabirds including three areas designated as of international importance to birds. These results highlight that inclusion of the baroclinic circulation will be essential in order to obtain satisfactory predictions from oil and chemical spill models in the South Minch.

There are important fisheries in the Minch, particularly for the benthic decapod, Norway lobster (*Nephrops norvegicus*), which inhabits the extensive mud substrates of the region (Figure 11). Adult females release planktonic larvae into the water column each year from March to July. Settlement onto mud of juvenile *Nephrops* is thought to be essential for survival (Bailey *et al.*, 1995). The circulation regime can thus be expected to play an important role in controlling the numbers of larvae present over particular *Nephrops* grounds at settlement time.

In the South Minch, *Nephrops* larvae released into the flow stagnation zone above the saline dome [see Figures 7(c) and 9(c), for example] could be retained above the mud substrate from which they were hatched, and eddies, such as the one that trapped Drifter 1, might also assist the retention of some larvae close to their hatching sites. However, many larvae entrained into the recirculating branch of the coastal current are likely to be lost to the South Minch population. The drifter tracks suggest that the small *Nephrops* ground south-west of Barra (Figure 11) could be seeded by larvae originating in the South Minch. Moreover, on the basis of the track of Drifter 4 (and its last recorded position off Cape Wrath), it also appears that it would be possible (within the known larval duration) for some of the larvae that are carried west of the islands to ultimately enter the North Minch ground, or even the Noup ground (Figure 11).

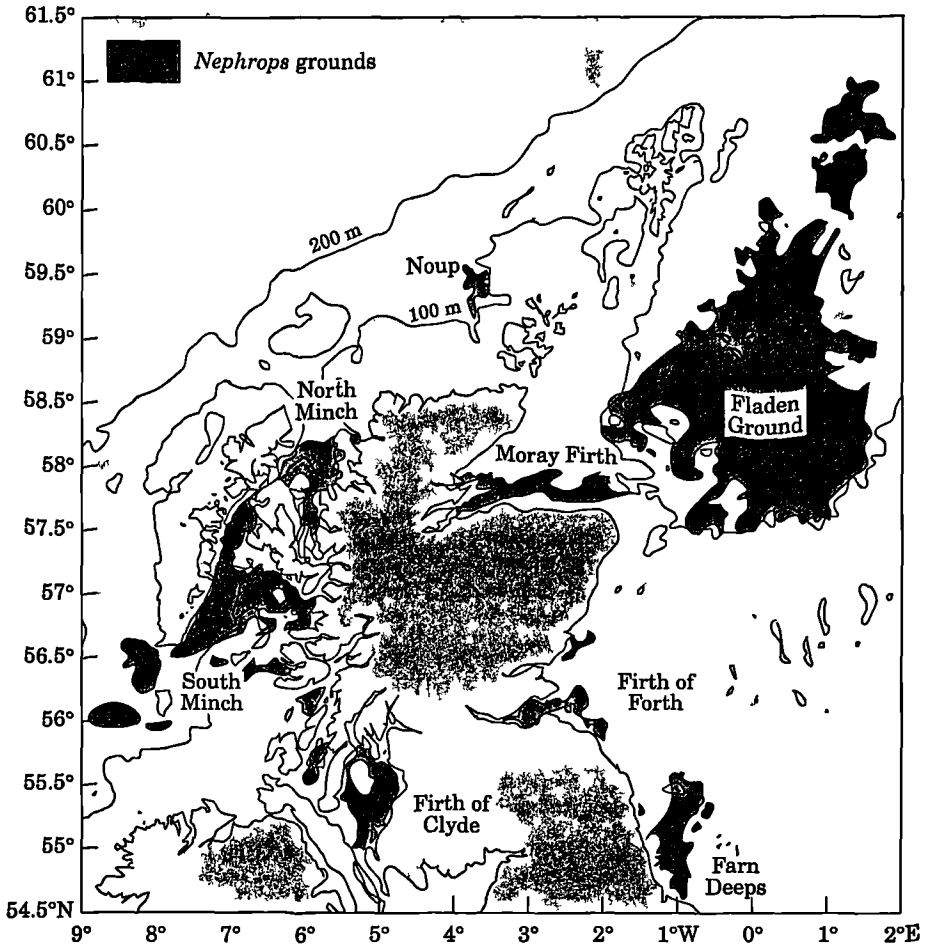

FIGURE 11. *Nephrops norvegicus* grounds around Scotland.

The previous discussion assumes *Nephrops* larvae behave as passive tracers whereas, in common with many marine larvae, active vertical migration could also affect dispersal (e.g. Hill, 1995). The application of a baroclinic coastal ocean model, with *Nephrops* larval transport represented by particle tracking (perhaps incorporating vertical migratory behaviour), would assist a more quantitative examination of these questions.

Although the drifter observations presented are limited in duration and are confined to the spring regime, they constitute the first direct current measurements within the region and provide confirmation of a bifurcation and partial recirculation of the Scottish coastal current in the South Minch. However, it would be unwise to infer a permanent circulation solely on the basis of relatively short drifter deployments, although the consistency with indirect inferences about the circulation is encouraging. Further deployments in the region over the entire seasonal cycle are obviously desirable. The observations point strongly to the importance of horizontal density gradients in driving the flow and the observations are sufficient to demonstrate that any future modelling approach in this region must take full account of baroclinic dynamics.

Acknowledgements

The authors are grateful to Captain George Geddes and the officers and crew of the FRV *Clupea*. Technical assistance was provided by Dave Boon and Anne Hammerstein. RWG participated in this work whilst on sabbatical leave from the University of Delaware and received support from the US National Science Foundation under Grant INT-9413299 and the Sir Kirby Laing Fellowship of the School of Ocean Sciences, University of Wales, Bangor. The study was partly funded by an award, GR3/9601, to AEH from the UK Natural Environment Research Council and by a Collaborative Research Grant, 940566, from NATO to RWG and AEH.

References

Backhaus, J. O. 1985 A three-dimensional model for the simulation of shelf sea dynamics. *Deutsche Hydrogrographische Zeitschrift* **38**, 165 187.

Bailey, N, Chapman, C. J., Alfonso-Dias, M. & Turrell, W. R. 1995 The influence of hydrographic factors on *Nephrops* distribution and biology. *ICES CM 1995/Q:17 Poster (mimeo)*.

Blumberg, A. F. & Mellor, G. L. 1987 A description of a three-dimensional coastal ocean model. In *Three Dimensional Coastal Ocean Models* (Heaps, N. S. ed.). Coastal and Estuarine Sciences No. 4, American Geophysical Union, Washington, 208 pp.

Bray, N. A. 1988 Thermohaline circulation in the Gulf of California. *Journal of Geophysical Research* **93**, 4993 5020.

Brown, J. 1991 The final voyage of the Rapaiti. A measure of sea surface drift velocity in relation to the surface wind. *Marine Pollution Bulletin* **22**, 37–40.

Craig, R. E. 1959 Hydrography of Scottish coastal waters. *Marine Research 1958 (2)*, 30 pp.

Davis, R. E., Dufour, J. E. Parks, G. P. & Perkins, M. R. 1982 Two inexpensive current-following drifters. Scripps Institution of Oceanography Reference No. 82–28.

Ellett, D. J. 1979 Some oceanographic features of Hebridean waters. *Proceedings of the Royal Society of Edinburgh* **77B**, 61–74.

Ellett, D. J. & Edwards, A. 1983 Oceanography and inshore hydrography of the Inner Hebrides. *Proceedings of the Royal Society of Edinburgh* **83B**, 143 160.

Garrett, C. J. R. & Loder, J. W. 1981 Dynamical aspects of shallow sea fronts, *Philosophical Transactions of the Royal Society of London* **A 302**, 653 681.

Hill, A. E. 1996 Spin-down and the dynamics of ' dense pool ' gyres in shallow seas. *Journal of Marine Research* **54**, 471–486.

Hill, A. E. 1995 The kinematical principles governing horizontal transport induced by vertical migration in tidal flows. *Journal of the Marine Biological Association of the UK* **75**, 3–13.

Hill, A. E. 1993 Seasonal gyres in shelf seas. *Annales Geophysicae* **11**, 1130–1137.

Hill, A. E. 1987 *The Dynamics and Variability of the Scottish Coastal Current*. PhD Thesis, University of Wales, Bangor, U.K.

Hill, A. E., Durazo, R. & Smeed, D. A. 1994 Observations of a cyclonic gyre in the western Irish Sea. *Continental Shelf Research* **14**, 479–490.

McKay, W. A., Baxter, M. S. Ellett, D. J. & Meldrum, D. T. 1986 Radiocaesium and circulation patterns west of Scotland. *Journal of Environmental Radioactivity* **4**, 205–232.

McKinley, I. G., Baxter, M. S., Ellett, D. J. & Jack, W. 1981 Tracer applications of radiocaesium in the Sea of the Hebrides. *Estuarine, Coastal and Shelf Science* **13**, 69–82.

Niiler, P. P., Sybrandy, A. S., Bi, K., Poulain, P. M. & Bitterman, D. 1995 Measurement of the water-following capability of holey sock and tristar drifters. *Deep Sea Research I* **42**, 1951–1964.

Pingree, R. D. & Griffiths, D. K. 1978 Tidal fronts on the shelf seas around the British Isles. *Journal of Geophysical Research* **83**, 4615–4622.

Prandle, D. 1984 A modelling study of the mixing of ^{137}Cs in the seas of the European continental shelf. *Philosophical Transactions of the Royal Society of London* **A 310**, 407–436.

Simpson, J. H. & Hill, A. E. 1986 The Scottish coastal current. In *The Role of Freshwater Outflow in Coastal Marine Ecosystems* (Skreslet, S., ed.) NATO ASI Series, Vol. G7: 295–308. Springer-Verlag, Berlin, Heidelberg.

Turrell, W. R., Henderson, E. W. & Slesser, G. 1990 Residual transport within the Fair Isle Current during the Autumn Circulation Experiment (ACE). *Continental Shelf Research* **10**, 521–543.

Turrell, W. R., Henderson, E. W. Slesser, G. Payne, R. & Adams, R. D. 1992 Seasonal changes in the circulation of the northern North Sea. *Continental Shelf Research* **12**, 257–286.

Unesco 1978 Eighth report of the joint panel on oceanographic tables and standards. *Unesco Technical Papers in Marine Science*, No 28.

Xing, J. & Davies, A. M. 1996 A numerical model of the long term flow along the Malin-Hebrides shelf. *Journal of Marine Systems* **8**, 191–218.

APPENDIX 4

Reprint of :

Horsburgh, K.J., A.E. Hill and J. Brown (1998) A summer jet in the St George's Channel of the Irish Sea. *Estuarine Coastal and Shelf Science,* **47**, 285-294.

Estuarine, Coastal and Shelf Science (1998) 47, 285 294
Article No. ec980354

A Summer Jet in the St George's Channel of the Irish Sea

K. J. Horsburgh[a], A. E. Hill[a] and J. Brown[b]

[a]*School of Ocean Sciences, University of Wales, Bangor, Marine Science Laboratories, Menai Bridge, Ynys Môn LL59 5EY, U.K.*
[b]*Centre for Environmental Fisheries and Aquaculture Science (CEFAS), Pakefield Road, Lowestoft, Suffolk, NR33 0HT, U.K.*

Received 1 December 1997 and accepted in revised form 16 March 1998

Satellite-tracked drifters released in summer 1997 have revealed a fast, northward flowing jet on the eastern side of St George's Channel, between the Celtic and Irish Seas. There is also evidence of a weaker, southward flowing current on the western side of the channel. Satellite imagery and hydrographic measurements support the interpretation that the current is density driven and associated with a meander in the Celtic Sea tidal-mixing front. The jet has implications for fluxes of heat, tracers and contaminants between the Irish and Celtic Seas. It also adds to a growing body of evidence that in summer, on the northwest European shelf, there is a widespread system of localized but intense baroclinic flows associated with the margins of dense bottom-water pools.

Keywords: jet; density driven; baroclinic; drifters; satellite observations; pollutant dispersal; Irish Sea; Celtic Sea

Introduction

The North Channel and the St George's Channel connect the Irish Sea to the open continental shelf at its northern and southern boundaries, respectively (Figure 1). Since property budgets and local area numerical models for the Irish Sea require knowledge of the fluxes through these two passages, estimation of the flow in both regions is of long-standing interest. It is generally accepted from tracer distributions (Bowden, 1950; Wilson, 1974) that there is a long-term sectionally-averaged northward drift of about $0{\cdot}4\ \mathrm{cm\ s^{-1}}$ through St George's Channel (corresponding to a volume transport of $3 \times 10^4 \mathrm{m^3\ s^{-1}}$). Surprisingly, in spite of the obvious importance of this key choke region, very few direct observations of currents are available and there is little knowledge of the detailed spatial and temporal variability of flow across this section. In contrast, intensive campaigns of flow measurement have been made across other important European shelf channels such as the North Channel of the Irish Sea (Brown & Gmitrowicz, 1995; Howarth *et al.*, 1995) and the Straits of Dover (Prandle *et al.*, 1993).

Winds are clearly important to the dynamics of the St George's Channel as shown by several experiments with barotropic hydrodynamic models (Thomson & Pugh, 1986; Pingree & Le Cann, 1989; Davies & Jones, 1992). Furthermore, in winter, wind-driven current surges of up to $10\ \mathrm{cm\ s^{-1}}$ have been recorded in the deep water ($\sim$90 m) section of St George's Channel (Howarth, 1975). An important consideration regarding the St George's Channel (which distinguishes it from the North Channel, for example) is that, during summer (May–October) each year, a tidal-mixing front (the Celtic Sea front) is located across the entrance to the passage, separating the stratified Celtic Sea from the tidally mixed Irish Sea (Simpson, 1976). The implication is that, during summer, there may also be baroclinic (density driven) components of flow in the region.

Here the authors report results from a release of satellite-tracked drifters in the Celtic Sea in July 1997. Although limited in number, taken together with contemporaneous satellite infrared imagery and hydrographic data from previous years, they provide compelling evidence for the existence of a density-driven flow associated with the Celtic Sea front and show that this flow may be responsible for significant transport.

Methods

Three satellite-tracked Argos drifters were deployed along the Celtic Sea front by the RV *Cirolana* on 2 July (year day 183) 1997. The drifter design comprised a 1 m long, cylindrical, spar-type surface drifter and a

0272 7714/98/030285+10 $30.00/0

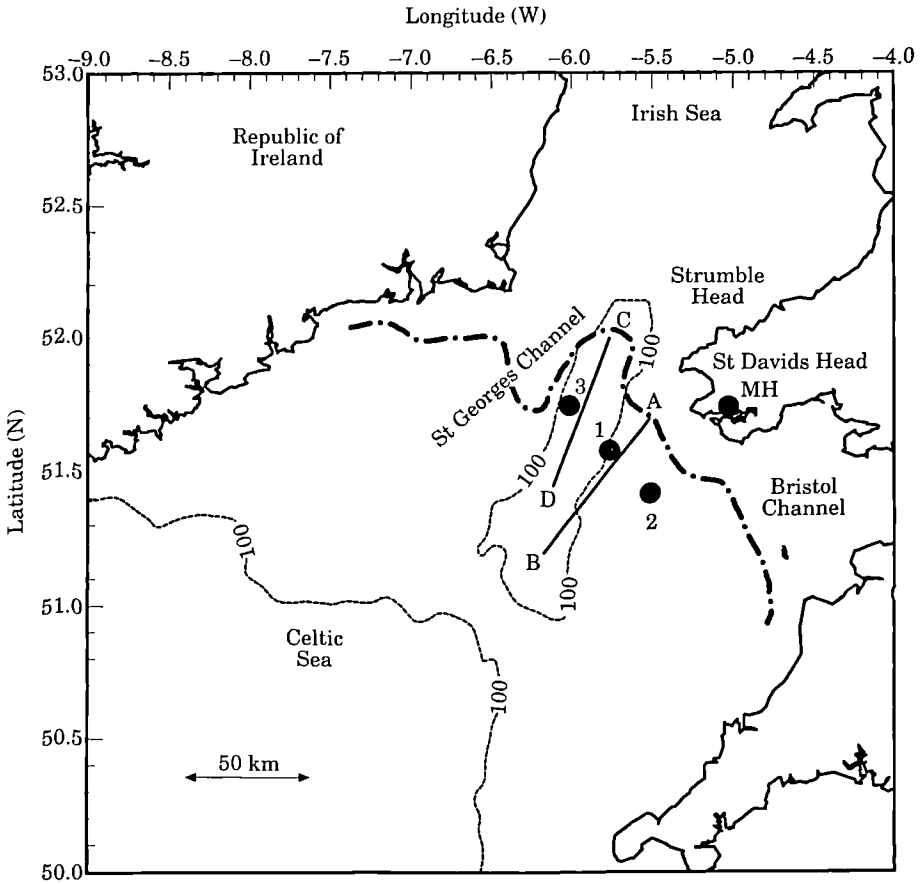

FIGURE 1. Location map showing places referred to in the text. The solid black circles numbered 1–3 denote the release positions of drifters (2 July 1997). Lines AB and CD show the hydrographic sections taken from observations on 27–28 June 1995. The broken-dashed line is the average position of the 13 °C isotherm from a composite image of sea-surface temperature for July 1997, taken to define the mean position of the surface front. The 100 m isobath is also shown as a dashed line. MH is Milford Haven.

neutrally buoyant holey-sock drogue 1·2 m in diameter and 5 m long. To reduce wave rectification, the drogue was attached to a small surface float which was then tethered to the drifter. The drag area ratio for the system was greater than 50 which restricts wind slip to less than 1 cm s^{-1} for winds of 10 m s^{-1} (Niiler *et al.*, 1995).

Deployment positions were guided by an archive of satellite infrared images, historical hydrographic measurements (Horwood, 1993) and measurements made in 1995 along two transects (denoted AB and CD in Figure 1). These hydrographic measurements were made on 27 and 28 June 1995 from the RV *Prince Madog* using a Neil Brown Mk III CTD, calibrated with reversing thermometers and water samples. All salinities quoted in the remainder of the text were determined on the practical salinity scale (Unesco, 1978).

Geostrophic calculations relative to an assumed level of no motion at the sea bed (see Figure 5 later) suggested that any frontal-jet flow would be located at the base of the thermocline, above the bottom front, on the stratified side some 10–20 km away from the surface front. Deployment positions were thus selected accordingly, relative to the surface front revealed by the satellite images, and the centre of each drogue was set at 30 m depth. The deployment positions for the drifters are designated by the solid circles (numbered 1–3) in Figure 1. Daily mean drifter positions are presented to remove fluctuations due to semi-diurnal tidal excursions. This simple approach to the removal of tides was found to be effective because the resulting smoothed track differed little from that derived using a lowpass, finite impulse response filter (Proakis & Manolakis, 1992).

A 6 hourly wind record for the period of 29 June–31 July (days 180–212) 1997 (Figure 2) was obtained from a Meteorological Office mesoscale model used in operational forecasting (Cullen, 1993) which has been validated against an offshore meteorological buoy in

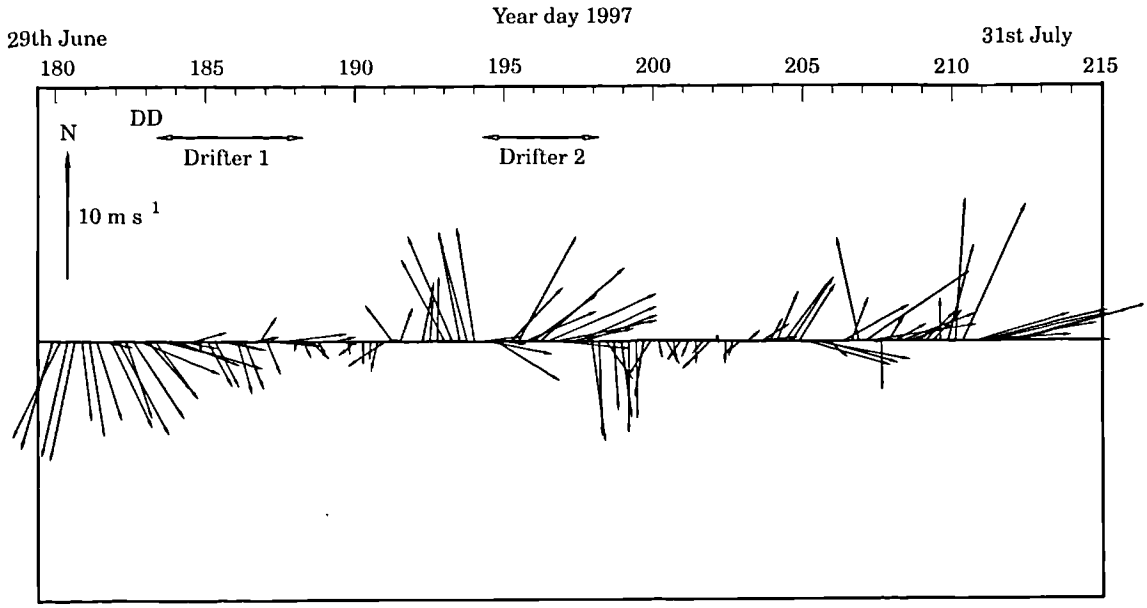

FIGURE 2. Modelled winds at 10 m above sea level at position 51°48'N, 5°30'W (close to position A in Figure 1) from a mesoscale meteorological model (Cullen, 1993). DD marks the date of drifter deployment and the two horizontal arrows show times when the indicated drifters moved northwards rapidly.

this region. Modelled winds were used because the closest terrestrial weather station was sheltered from south-westerly winds. The modelled winds are for 10 m above sea level at position 51°48'N, 5°30'W, which corresponds approximately to the northern end of hydrographic section AB. The day the drifters were deployed is denoted DD in Figure 2.

Cloud free, atmospherically corrected Advanced Very High Resolution Radiometer (AVHRR) images for the period of the experiment were obtained from the Natural Environment Research Council Remote Sensing Data Analysis Service (NERC-RSDAS) at Plymouth, U.K.

Results

Drifters

Drifter 1 moved rapidly northwards immediately after deployment and was recovered 11 days later (Figure 3). Between days 183–188 its average speed was 11 km day^{-1} (13 cm s^{-1}) with a maximum speed over a 24 h period of 24 cm s^{-1} on day 185. On this day the drifter encountered the region of shallow banks known as The Smalls (Figure 3). These banks, which in places are only 2 m below Chart Datum, are separated by deep channels where currents reach 2·5 ms ^{1} at spring tides. Drifter 1 passed through one such channel and by day 186 had continued its northward motion. On recovery the drogue was found to be intact and hence the authors can be confident that the fast current measured was not an artifact of the drifter having lost its drogue.

Drifter 2 moved initially north-westwards along the approximate locus of the Celtic Sea front (see Figure 4) at speeds of ~3 km day^{-1} (4 cm s^{-1}). After 11 days (on day 194) it reached the position at which drifter 1 had originally been deployed and then moved rapidly northwards with maximum speeds of 28 cm s^{-1} during days 195–197. On day 198, at latitude 52°10'N, the rapid northward motion ceased and the drifter thenceforth had only a small residual speed (~2 cm s^{-1}) until day 208 when the drifter moved north-westwards once more, describing a single cyclonic loop before transmission ceased on day 244.

Drifter 3 took a different path, moving in a south-west direction throughout its 25 day deployment. Cyclonic motions with loop diameters of about 8 km and a rotation period of approximately 5 days can be discerned between days 183–199 (that part of the track enclosed by the square box in Figure 3). After this, drifter 3 continued moving south-westwards at speeds of 6 cm s^{-1}.

The drifter deployments took place 4 days prior to the spring tides of 6 July. The maximum northward speed of drifter 1 occurred on day 185 (4 July), 2 days prior to the spring tide. In contrast, the maximum speed for drifter 2 occurred on day 195 (14 July) which was a neap tide.

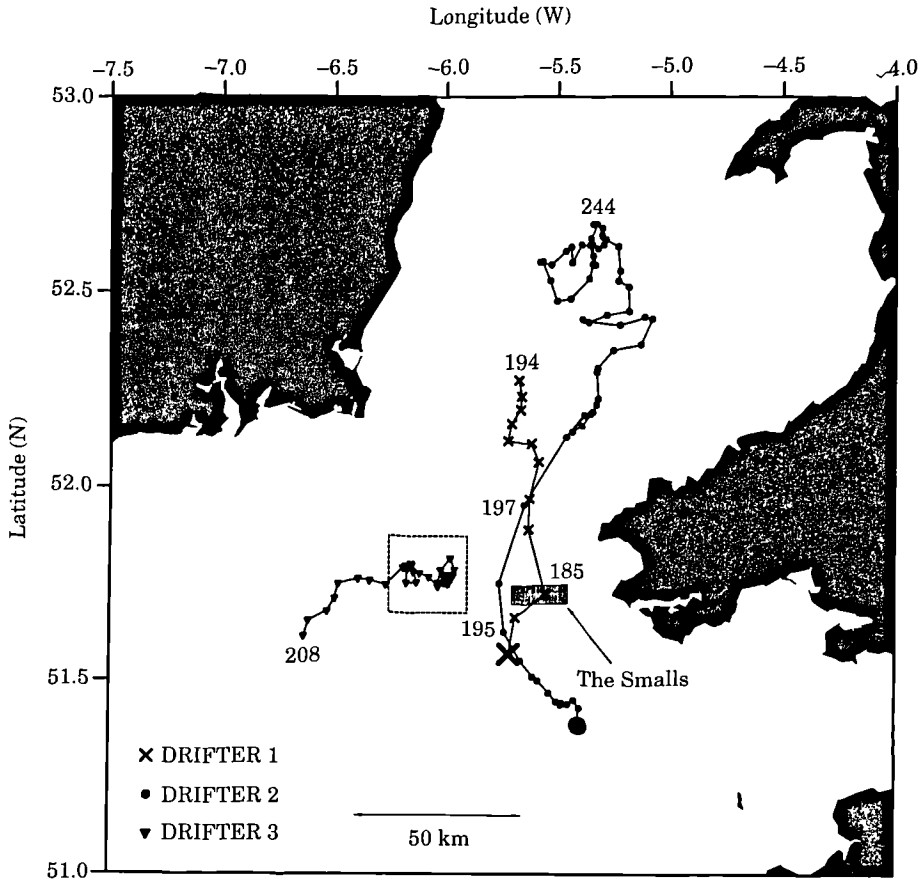

FIGURE 3. Drifter trajectories. Drifters are referred to in the text by their numbers (1–3) which relate to the symbols used here as shown in the legend. Large symbols indicate release sites and small symbols along each track are mean daily positions. Numbers alongside these indicate the day to which that position applies. The area enclosed by the dotted line contains the first part of the track of drifter 3 and shows cyclonic eddies of 8 km diameter. All drifters were drogued at 30 m depth. The shaded rectangle denotes The Smalls, a region of shallow banks where tidal currents reach 2·5 m s^{-1} at spring tides.

Satellite images

Two cloud-free satellite infrared images coincided with the drifter deployments and the drifter trajectories have been superimposed on these (Figure 4). The segments of each track, which are contemporaneous to within 24 h of the images, are identified by the white squares in Figure 4. The surface fronts in the images represent sea-surface temperature gradients of about 4 °C over 20–25 km (note that the temperature colour scales differ).

The initial slow movement of drifter 2 (days 183–194) was on the stratified side of, and directed parallel to, the surface front located south-west of St David's Head. However, the segments of the tracks of both drifters 1 and 2 corresponding to fast northward flow (days 183–187 and days 194–198 respectively) coincided with the eastern edge of what appears to be a ribbon-like intrusion of warm Celtic Sea surface water through St George's Channel into the Irish Sea. The warm ribbon extended up to 100 km through the channel north of the mean locus of the Celtic Sea front [Figure 4(b)]. Similarly, at a longitude of approximately 6°W, the track of drifter 3 coincides with a tongue of relatively cool surface water which appears to have intruded southwards into the Celtic Sea.

Along the margin of the cool water intrusion [Figure 4(b)], perturbations with a length scale of approximately 10 km are visible between the 17 °C (green) and 18 °C (yellow) waters (the cyclonic eddies observed in the trajectory of drifter 3 had diameters of approximately 8 km). Pingree (1978) has previously identified cyclonic eddies in the Celtic Sea and suggested baroclinic instability as the mechanism for their formation. The characteristic scale for a baroclinic disturbance is given by the Rossby radius of deformation, $R_d=[g'H]^{1/2}/f$ where $g'=g\delta\rho/\rho$ is the reduced gravity, H is depth of the baroclinic zone and f is the Coriolis parameter. From the hydrographic sections (presented later) the authors take ($\Delta\rho=1{\cdot}6$ kg m^{-3},

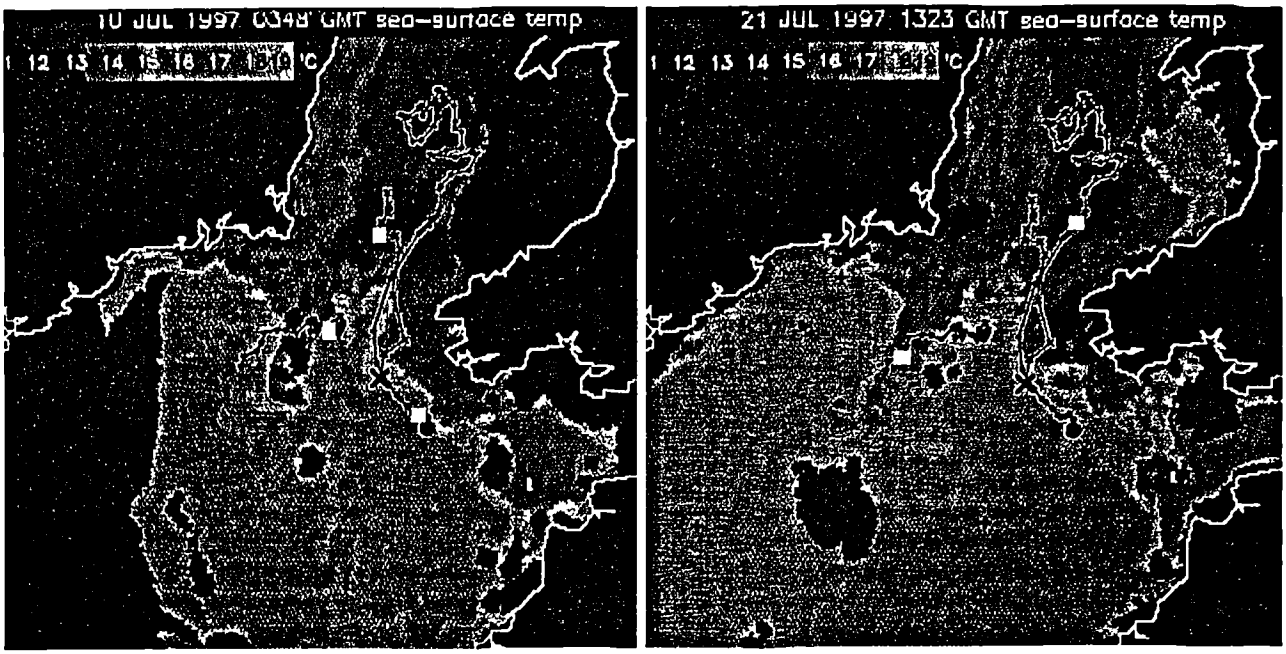

FIGURE 4. Corrected sea temperature (SST) from channel 4 of AVHRR for the region of St George's Channel. (a) 10 July 1997 and (b) 21 July 1997 (note that the temperature colour scales differ). The complete drifter tracks are superimposed on both images; white squares indicate those segments corresponding to drifter trajectories on the day of the image. Land areas and cloud are shown as black.

H=30 m which gives R_d=7 km, consistent with the scale of both the frontal perturbations and the observed cyclonic motions in the drifter trajectory.

The existence of a semi-permanent perturbation of the Celtic Sea front over the relatively deep (>100 m) trough in the central St George's Channel is well documented (Simpson & Pingree, 1977; Pingree, 1978; Pingree, 1979). Indeed, the characteristic pattern seen in Figure 4 of the northward meander of the front (and hence isotherms) into the channel was visible in 101 out of 111 cloud-free images examined for the period 1 June–21 September 1996 and 1997. The same feature is also visible in the analysis of frontal positions derived from satellite imagery by Simpson and Bowers (1981).

Dynamics of the flow

In order to examine the possible driving forces for the observed currents the authors consider in turn the possible influence of tides, winds and density gradients.

To assess whether the observed trajectories could merely be the result of Lagrangian tidal residual motion, a particle-tracking model was constructed from a database of M_2 and S_2 tidal streams on an 8 km resolution grid which has been used previously for oil-spill tracking (Elliott, 1991). A particle at time, t, was advected with a velocity bilinearly interpolated from the four model points surrounding its position at that time. Particles were released at 30 min intervals over a tidal cycle then advected for 15 days with a time step of 30 min. The maximum displacement vector (taken as the Lagrangian residual) for a release position corresponding to the deployment position of drifter 2 was 9 km in 15 days, corresponding to a residual current of less than 1 cm s^{-1}. Lagrangian tidal residual currents cannot, therefore, explain the observed along-front flows to the south of St David's Head or in the track of drifter 3.

The 8 km grid tidal database is, however, unable to resolve the spatial variability in tidal current in the shallow-water region of The Smalls. The Lagrangian mean velocity is the sum of the local, Eulerian residual and a Stokes velocity, U_s, which is generally of the order $\bar{u}^2T/L$, where T and L are typical time and length scales of the variation in the velocity field (Longuet-Higgins, 1969). A suitable estimate for the Stokes velocity in this instance can be obtained from $U_s = U^2/2c$ where U is the tidal current amplitude and c is the phase speed of the tidal wave. Taking U as 2·5 m s^{-1} and c as 20 m s^{-1} suggests Stokes velocities of the order 16 cm s^{-1}. Whilst it is possible that Lagrangian tidal residuals may contribute significantly to the maximum speed of drifter 1 as it moved through this area, they cannot explain the larger-scale

TABLE 1. Correlation coefficients, ρ, between fluctuating parts of wind and drifter velocities (u and v denote northward and eastward components of velocity, respectively)

Lag (h)	Drifter	1	2	3
0	ρ_u	0·17	0·62	0·06
	ρ_v	−0·13	0·48	0·05
12	ρ_u	0·31	0·59	0·02
	ρ_v	−0·20	0·51	0·00
24	ρ_u	0·34	0·48	0·04
	ρ_v	−0·41	0·47	−0·01
n-2		9	15	15
5%		0·60	0·48	0·48
1%		0·73	0·61	61

Correlations were determined between days 183 and 200 (183 and 194 for drifter 1) for drifter velocity fluctuations lagging the wind by 0, 12 and 24 h. n-2 is the degrees of freedom and the 5 and 1% significance points are given.

pattern of flow. Residual transports induced by islands have been shown to diminish to negligible values at a distance of one island diameter (Pingree & Maddock, 1985). By day 186, drifter 1 had escaped the region of influence but still had rapid northward movement. Furthermore, the tidal currents in this area rotate in an anticlockwise sense and this should give rise to anticlockwise residual transport (Pingree & Maddock, 1985) around The Smalls. There is some evidence of anticlockwise motion in the raw data track of drifter 1 before it passed through a gap between the shallow banks but drifter 2 moved continuously northward, passing to the west of The Smalls where southward motion should result from an anticlockwise residual current field. Even if drifter 2 was close enough to be influenced by the residual field then some opposing driving force must also have been present.

The simplest and strongest evidence that the observed motion is not simply a response to local winds is the basic difference in orientation and shape of the trajectory of drifter 3 compared with the other two drifter tracks. Since the spatial scale of wind forcing over the duration of these deployments would be expected to be much greater than the separation scale of individual tracks, the implication is that the difference between trajectories is due to an underlying, spatially-varying flow field and not the local wind. Nevertheless, Table 1 presents results of the correlation, $\langle u-\bar{u}, W-\bar{W}\rangle$, between fluctuations in drifter velocity, u, and the wind velocity, W. Here overbars denote time averages, calculated between day 183 when the drifters were released and day 200 when drifter 2 had ceased moving northwards at speeds greater than 5 cm s^{-1}. Since tides are strong (1 m s^{-1}) and would otherwise dominate the correlation, mean 24 hourly drifter velocity components were computed and the mean wind calculated over the same time interval. Drifter 1 is anti-correlated with the northward component of the wind (Table 1), moving northwards with speeds of up to 24 cm s^{-1} between days 183 and 188 despite winds blowing consistently from the north/north-west during that period and blowing strongly (>10 m s^{-1}) from the north immediately prior to the deployment (Figure 2). Drifter 3 shows no significant correlation with wind and its track is markedly different to the other two drifters. With the exception of drifter 2, the low correlation coefficients confirm that local wind forcing has little influence on the trajectories.

The non-local influence of wind-forcing is represented by the surge current. Howarth (1975) measured currents at three depths (in unstratified conditions) over a 32 day winter period at a location close to position C in Figure 1. He found time-averaged currents of 10 cm s^{-1} in response to winds of 10 m s^{-1} and maximum currents of 30 cm s^{-1} were sustained for only 2–3 h. Howarth (1975) also reported a distinctly two-phase response to winds with a strong south-westward flow preceding a north-eastward return flow when winds blew from the north-west. The drifter trajectories imply that the fast northward flow was sustained over a duration considerably longer than just a few hours (i.e. observed for durations of 5 days by drifter 1 and for 4 days by drifter 2, separated by an interval of 6 days). Moreover, barotropic models of the region do not suggest that flows driven by large-scale wind forcing produce a spatially varying pattern of wind-driven flow of the kind revealed by the drifter tracks (Davies & Jones, 1992).

The outstanding candidate for forcing the observed flow is thus the baroclinicity of the density field which would certainly show spatial variability on the observed scales. This is reinforced by the relationship between drifter tracks and the temperature field shown in the satellite images (Figure 4). The density structure across the Celtic Sea front in June 1995 is shown in section AB (Figure 5, see Figure 1 for location). On the tidally-mixed side of the front, the water had temperature and salinity values of ~12 °C and 34·9, respectively. On the stratified side, however, the vertical temperature difference was 5 °C and the bottom-water salinity was 35·3, indicative of its North Atlantic origin. Temperature was thus responsible for just over half the vertical density stratification of 1·6 kg m^{-3} seen in Figure 5(c) but, where the horizontal density gradient was sharpest (0·4 kg m^{-3} in ~10 km), it was predominantly due to the lateral

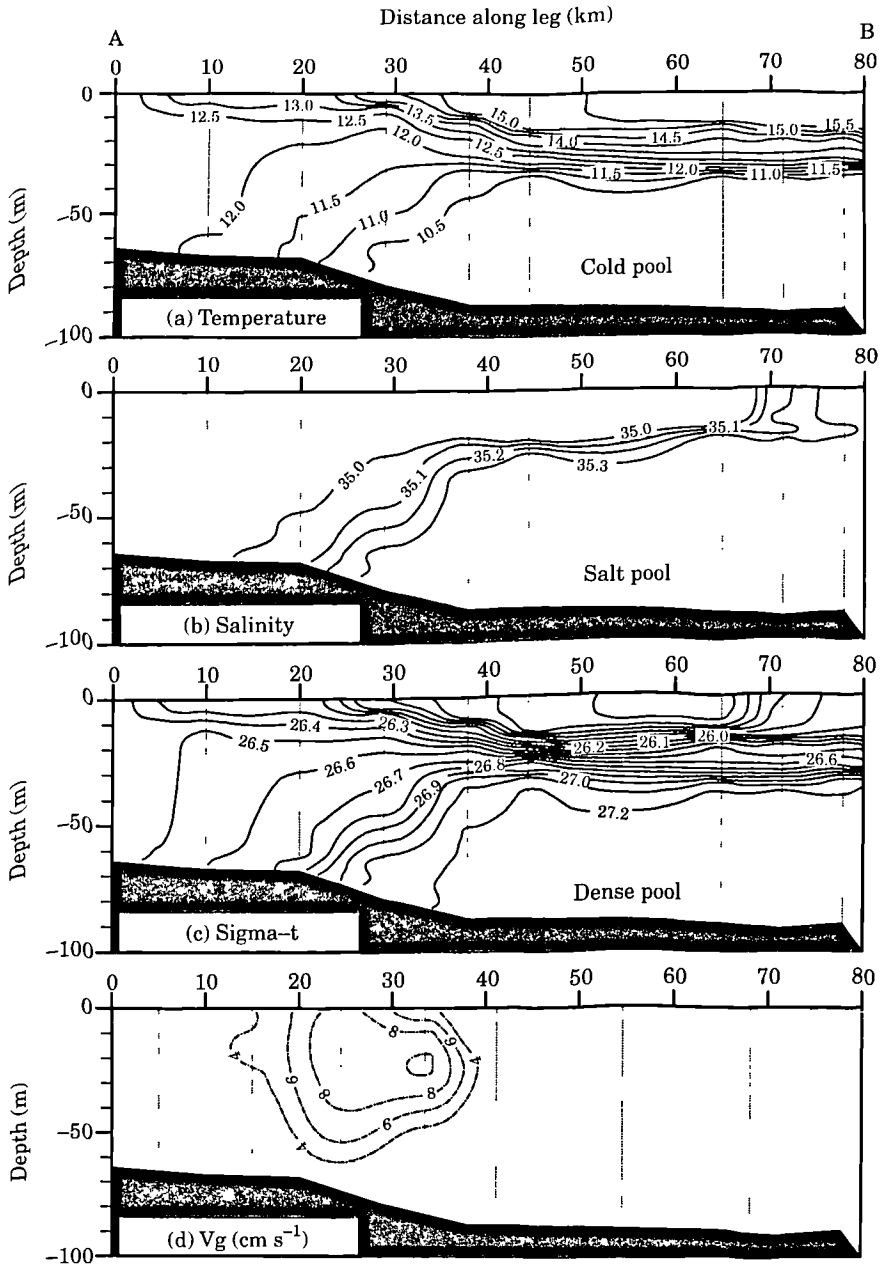

FIGURE 5. Section AB occupied on 27 June 1995. (a) Temperature, °C; (b) salinity; (c) density, σ_t; and (d) geostrophic velocity (cm s^{-1}) relative to an assumed level of no motion at the sea bed. The contours in (d) represent flow out of the page.

gradient of salinity. The key features to note from the density section are: (1) the pool of dense (cold, saline) water beneath the pycnocline is separated from the adjacent tidally-mixed waters by bottom fronts; (2) the frontal system is bottom-dominant in that the strongest horizontal density gradients are associated with the bottom rather than the surface front; and (3) the location of the bottom and surface fronts do not coincide along the horizontal axis (Figure 5).

Estimates of geostrophic velocity normal to AB section were calculated relative to an assumed level of no motion at the seabed and predicted an along-front flow of ~ 10 cm s^{-1} in a narrow (~ 20 km wide) core, centred at 30 m depth, coincident with the base of the pycnocline [Figure 5(d)]. Section CD (Figure 1), occupied on 28 June 1995 (not shown), displayed essentially similar hydrographic features, including the importance of horizontal salinity gradients, but exhibited rather higher geostrophic speeds (~ 25 cm s^{-1}). The key aspect of the geostrophic calculations is that they imply that the frontal jet is driven by the near-bottom density gradients at the margin of the dense

pool and that the surface front, whilst visible in satellite imagery, plays only a minor dynamical role with regard to flow generation (Garrett & Loder, 1981; Hill *et al.*, 1997*a*). Apart from uncertainty concerning the reference level, and the fact that hydrographic sections and drifter tracks are not contemporaneous, there is also uncertainty as to whether the hydrographic sections were orientated perpendicular to the maximum density gradients. A section oblique to the bottom front would lead to an underestimate of the along-front geostrophic speed. In spite of these uncertainties, the density gradients measured in the vicinity of the Celtic Sea front demonstrate that baroclinicity can generate mean currents of a magnitude consistent with the measured flows (~ 10 25 cm s ^{1}).

Discussion

For the first 11 days of its motion, drifter 2 moved parallel to the observed surface front (and presumably above the bottom front) in what might be considered a simple geostrophic regime. The fastest flows, however, were associated, not merely with the front, but with the northward perturbation of the front off St David's Head. Here, the spatial variability of both bathymetry and tidal currents can contribute a tidal residual component to the observed flows. Nevertheless, the same spatial variability in tidal-mixing power will ensure strong lateral gradients of density which can drive a significant baroclinic current.

The reason for the persistent meander observed on the Celtic Sea front may partly be explained by variations in the level of tidal-mixing along the axis of St George's Channel, reflected in a northward displacement of h/u^3 (Simpson & Hunter, 1974) contours over the deep (>100 m) trough there. Thinning of the tidal boundary layer due to local enhancement of the anticlockwise rotary tidal component (Soulsby, 1983) could also contribute to locally reduced mixing (Simpson & Sharples, 1994). Whilst the surface front may experience baroclinic instability (Griffiths & Linden, 1982) sharp gradients near the bed have been shown to be more stable (Flagg & Beardsley, 1978; James, 1989). Qualitatively, from the satellite images, the meander has the appearance of an inertial filament which intrudes through the St George's Channel. Satellite imagery alone, however, does not allow us to distinguish between advection or diffusion (as a result of eddy generation and subsequent intense mixing) as the cause of the incursion of warm surface water. The fast northward flow in the eastern part of St George's Channel seen in the drifter tracks, however, lends direct support to an advective explanation for the both the warm water ribbon and provides at least a partial explanation for the distortion of the Celtic Sea front, as has been suggested by Pingree (1984).

Both drifters 1 and 2 eventually departed from a trajectory parallel to the strongest frontal gradients and entered the mixed waters of the Irish Sea whereupon their speed dramatically diminished. Numerous candidate instability mechanisms (see Huthnance, 1995, for a review) are applicable to baroclinic flows moving over complex topography, any one of which may cause departure from geostrophic flow. Another possibility is that the curvature of the distorted front introduces significant ageostrophic motion.

Since the characteristic meander-like frontal pattern has been observed during the heating season over many years, the associated flows might be expected to be important (at least during summer) in the budgets of heat, salt and nutrients for both the Celtic and Irish Seas. Taking the width of the warm ribbon as 20 km and assuming that flows of 20 cm s^{-1} are present in the top 30 m (i.e. above the drogue depth) gives a northward transport of $1{\cdot}2 \times 10^5$ m^3 s^{-1} which is considerably larger than the annual-mean section-average transport given by Bowden (1950) and is comparable with the most recent estimates ($1{\cdot}1$–$1{\cdot}4 \times 10^5$ m^3 s^{-1}) of mean volume transport through the North Channel (Brown & Gmitrowicz, 1995). Although this transport may not be persistent over long time-scales, it does show the capacity for significant temporal and spatial variability of the flux.

An improved understanding of the spatial extent and temporal duration of these mean currents and transports is necessary for several reasons. Some numerical models of the Irish Sea (e.g. Xing & Davies, 1995) use St George's Channel as an open boundary at which tidal elevations and flow must be prescribed. Density-advecting models which are prognostic in temperature and salinity (e.g. Blumberg & Mellor, 1987; Proctor & James, 1996) further require accurate prescriptions of heat and salt fluxes across open boundaries.

The existence of strong subtidal flows has obvious implications for the transport of pollutants. Following the grounding of the oil tanker *Sea Empress* in February 1996 (Mair, 1997) 72 000 tonnes of oil were spilled into the sea near the entrance to Milford Haven (MH in Figure 1). Numerical simulations (SEEEC, 1996) predicted a significant quantity of surface oil over an area including the start position of drifter 2 and a considerable segment of the mean July frontal position. The fact that no oil was reported north of St George's Channel (SEEEC, 1996) reinforces the supposition that the density-driven currents reported here are summertime features only and

were either not present or were insignificant in winter conditions. However, had the spill occurred during summer, the strong flow shown by drifters 1 and 2 would have been an important factor in oil spill tracking and clean-up planning. More generally, the Bristol Channel is a source of anthropogenic contaminants with elevated average concentrations compared to the open Celtic and Irish Seas (e.g. Owens, 1984) and the observed jet provides a pathway for these to enter the Irish and Celtic Seas in summer. The above considerations emphasise that intense, localized baroclinic jets associated with tidal-mixing fronts are likely to be important for the dispersal of contaminants in summer and highlights the necessity of incorporating baroclinic effects in the next generation of water quality and oil- and chemical-spill models.

Taken in isolation, the drifter trajectories are a rather limited data set and clearly an expanded programme of hydrographic measurements in the region would be desirable. Nevertheless, the drifters provide striking evidence of a fast summer jet on the eastern side of St George's Channel which has not previously been revealed by other methods. Recently, more extensive, drifter releases have been undertaken in the Irish Sea (e.g. Hill *et al.*, 1997*a*) and on the Hebridean shelf (Hill *et al.*, 1997*b*), and were also carefully targeted on dense-pool bottom fronts. These results show the same two basic characteristics that have again been revealed by the present study: namely (1) the existence of fast currents (up to 20 cm s^{-1}); and (2) pronounced congruence in drifter tracks suggesting coherent, spatially confined flows. In this wider context, therefore, the results presented in this paper contribute to an emerging picture of an intense, readily measurable, component of organized jet-like flow, particularly associated with the margins of dense bottom-water pools, in the shelf seas of north-west Europe during summer.

Acknowledgements

We would like to thank the Captains and crew of the RV *Cirolana* and RV *Prince Madog* for deploying and recovering the drifters. Technical support was provided by Anne Hammerstein and John Read. The 1995 hydrographic data was collected by Grant Fulton and Gillian Scott on board the RV *Prince Madog*. Satellite images were processed by the NERC Remote Sensing Data Analysis Service, Plymouth, U.K. The study was partly funded by an award, GR3/9601, to AEH from the U.K. Natural Environmental Research Council. JB was funded by the Ministry of Agriculture, Fisheries and Food. The authors are grateful to two anonymous referees for their helpful comments.

References

Blumberg, A. F. & Mellor, G. L. 1987 A description of a three-dimensional coastal ocean circulation model. In *Three Dimensional Coastal Ocean Models* (Heaps, N. S., ed.). Coastal and Estuarine Sciences No. 4, American Geophysical Union, Washington, 208 pp.

Bowden, K. F. 1950 Processes affecting the salinity of the Irish Sea. *Monthly Notices of the Royal Astronomical Society*. Geophysical Supplement **6**, 63 90.

Brown, J. & Gmitrowicz, E. M. 1995 Observation of the transverse structure and dynamics of the low frequency flow through the North Channel of the Irish Sea. *Continental Shelf Research* **15**, 1133 1156.

Cullen, M. J. P. 1993 The unified climate/forecast model. *Meteorological Magazine* **122**, 81 94.

Davies, A. M. & Jones, J. E. 1992 A three-dimensional wind driven circulation model of the Celtic and Irish Seas. *Continental Shelf Research* **12**, 159–188.

Elliott, A. J. 1991 EUROSPILL: Oceanographic processes and NW European shelf databases. *Marine Pollution Bulletin* **22**, 548–553.

Flagg, C. N. & Beardsley, R. C. 1978 On the stability of the shelf water slope water front south of New England. *Journal of Geophysical Research* **83**, 4623–4631.

Garrett, C. J. R. & Loder, J. W. 1981 Dynamical aspect of shallow sea fronts. *Philosophical Transactions of the Royal Society of London* **A302**, 563 581.

Griffiths, R. W. & Linden, P. F. 1982 Laboratory experiments on fronts. *Geophysical and Astrophysical Fluid Dynamics* **19**, 159 187.

Hill, A. E., Brown, J. & Fernand, L. 1997*a* The summer gyre in the western Irish Sea: shelf sea paradigms and management implications. *Estuarine, Coastal and Shelf Science* **44(A)**, 83–95.

Hill, A. E., Horsburgh, K. J., Garvine, R. W., Gillibrand, P. A., Slesser, G., Turrell, W. R. & Adams, R. D. 1997*b* Observations of a density-driven recirculation of the Scottish Coastal Current in the Minch. *Estuarine, Coastal and Shelf Science* **45**, 473–484.

Horwood, J. 1993 The Bristol Channel Sole (*Solea solea*): a fisheries case study. *Advances in Marine Biology* **29**, 215–367.

Howarth, M. J. 1975 Current surges in St George's Channel. *Estuarine, Coastal and Shelf Science* **3**, 57—70.

Howarth, M. J., Harrison, A. J., Knight, P. J. & Player, R. J. J. 1995 Measurement of net flow through a channel. In *IEEE Fifth Working Conference on Current Measurement* (Anderson, S. P., Appell, G. F. & Williams, A. J., eds), pp. 121 126.

Huthnance, J. M. 1995 Circulation, exchange and water masses at the ocean margin: the role of physical processes at the shelf edge. *Progress in Oceanography* **35**, 353–431.

James, I. D. 1989 A three-dimensional model of circulation in a frontal region in the North Sea. *Deutsche Hydrographische Zeitschrift* **42**, 231 247.

Longuet-Higgins, M. S. 1969 On the transport of mass by time-varying current. *Deep Sea Research* **16**, 431–447.

Mair, H. 1997 Further leaks occur in *Sea Empress* saga. *Marine Pollution Bulletin* **34**, 222.

Niiler, P. P., Sybrandy, A. S., Bi, K., Poulain, P. M. & Bitterman, D. 1995 Measurement of the water-following capability of holey sock and tristar drifters. *Deep Sea Research* **42**, 1951 1964.

Owens, M. 1984 Severn Estuary an appraisal of water quality. *Marine Pollution Bulletin* **15**, 41 47.

Pingree, R. D. 1978 Cyclonic eddies and cross frontal mixing. *Journal of the Marine Biological Association of the UK* **58**, 955 963.

Pingree, R. D. 1979 Baroclinic eddies bordering the Celtic Sea in late summer. *Journal of the Marine Biological Association of the UK* **59**, 689 698.

Pingree, R. D. 1984 Some applications of remote sensing to studies in the Bay of Biscay, Celtic Sea and English Channel. In *Remote Sensing of Shelf Sea Hydrodynamics* (Nihoul, J. C. J., ed.). Elsevier Science, London, pp. 287 330.

Pingree, R. D. & Le Cann, B. 1989 Celtic and Armorican slope and shelf residual currents. *Progress in Oceanography* **23**, 303 338.

Pingree, R. D. & Maddock, L. 1985 Stokes, Euler and Lagrange aspects of residual tidal transports in the English Channel and the Southern Bight of the North Sea. *Journal of the Marine Biological Association of the UK* **65**, 969–982.

Prandle, D., Loch, S. D. & Player, R. 1993 Tidal flow through the Straits of Dover. *Journal of Physical Oceanography* **23**, 23–37.

Proakis, J. G. & Manolakis, D. G. 1992 *Digital Signal Processing: Principles, Algorithms and Applications, Second edition*. Macmillan Publishing Company, New York, 969 pp.

Proctor, R. & James, I. D. 1996 A fine resolution three dimensional model of the southern North Sea. *Journal of Marine Systems* **8**, 285–295.

SEEEC 1996 *Sea Empress* Environmental Evaluation Committee initial report, July 1996. SEEEC, The Welsh Office, Cardiff, 27 pp.

Simpson, J. H. 1976 A boundary front in the summer regime of the Celtic Sea. *Estuarine and Coastal Marine Science* **4**, 71 81.

Simpson, J. H. & Hunter, J. R. 1974 Fronts in the Irish Sea. *Nature, London* **250**, 404–406.

Simpson, J. H. & Pingree, R. D. 1977 Shallow sea fronts produced by tidal stirring. In *Oceanic Fronts in Coastal Processes* (Bowman, M. J. & Esaias, W. E., eds). Springer-Verlag, Berlin, pp. 29–42.

Simpson, J. H. & Bowers, D. 1981 Models of stratification and frontal movement in shelf seas. *Deep-Sea Research* **28A**, 727–738.

Simpson, J. H. & Sharples, J. 1994 Does the Earth's rotation influence the location of the shelf sea fronts? *Journal of Geophysical Research* **99(C2)**, 3315 3319.

Soulsby, R. L. 1983 The bottom boundary layer of the shelf sea. In *Physical Oceanography of Coastal and Shelf Seas* (Johns, B., ed.). Elsevier, New York, pp. 189 266.

Thomson, K. R. & Pugh, D. T. 1986 The subtidal behaviour of the Celtic Sea: part II, Currents. *Continental Shelf Research* **5**, 321 346.

Unesco 1978 Eighth report of the joint panel on oceanographic tables and standards. *Unesco Technical Papers in Marine Science*, No. 28.

Wilson, T. R. S. 1974 Caesium-137 as a water movement tracer in St George's Channel. *Nature, London* **248**, 125–127.

Xing, J. & Davies, A. M. 1995 Application of three dimensional turbulence energy models to the determination of tidal mixing and currents in a shallow sea. *Progress in Oceanography* **35**, 153 205.